Analysis of $W^{\pm}$ bosons with ALICE: Effect of alignment on $W^{\pm}$ bosons analysis

by

Pieter Johannes Wynand du Toit

Department of Physics

University of Pretoria

and

iThemba LABS, Somerset West

SA-CERN for the ALICE Collaboration

Submitted in partial fulfilment of the requirements for the degree

Magister Scientiae

in the Department of Physics

in the Faculty of Natural and Agricultural Sciences

University of Pretoria

Pretoria

30 April 2013

Analise van W± bosone met ALICE: Effek van oplyning op W± bosone analise

deur

Pieter Johannes Wynand du Toit

Fisika Departement

Universiteit van Pretoria

en

iThemba LABS, Somerset-Wes

SA-CERN vir die ALICE Medewerking

Voorgelê ter vervulling van 'n deel van die vereistes vir die graad

Magister Scientiae

in die Fisika Departement

in die Natuur- en Landbouwetenskappe Fakulteit

Universiteit van Pretoria

Pretoria

30 April 2013

Declaration

I, Pieter Johannes Wynand du Toit, declare that the dissertation, which I hereby submit for the degree Magister Scientiae (Physics) at the University of Pretoria, is my own work and has not previously been submitted by me for a degree at this or any other tertiary institution.

SIGNATURE: .....

DATE: .....

SUPERVISOR: Prof C. Theron

CO-SUPERVISORS: Dr S. V. Förtsch

Dr E. Z. Buthelezi

Verklaring

Ek, Pieter Johannes Wynand du Toit, verklaar dat die verhandeling wat ek hiermee vir die graad Magister Scientiae (Fisika) aan die Universiteit van Pretoria indien, my eie werk is en nie voorheen deur my vir 'n graad aan hierdie of 'n ander tersiêre instelling ingedien is nie.

HANDTEKENING: .....

DATUM: .....

PROMOTOR: Prof C. Theron

MEDE-PROMOTORS: Dr S. V. Förtsch

Dr E. Z. Buthelezi

Abstract

Analysis of $W^{\pm}$ bosons with ALICE: Effect of alignment on $W^{\pm}$ bosons analysis

by

Pieter Johannes Wynand du Toit

Supervisor: Professor C. Theron

Co-supervisors: Doctor S. V. Förtsch and Doctor E. Z. Buthelezi

The ALICE (A Large Ion Collider Experiment) detector at the CERN Large Hadron Collider (LHC) is dedicated to studying the deconfined medium called the quark-gluon plasma (QGP), which is formed at extreme energy densities in heavy-ion collisions. ALICE can study hadrons, photons, electrons and muons up to the highest multiplicities expected at the LHC and down to very low transverse momentum ($p_T \sim$ 30 MeV/c) by employing excellent particle identification (PID) and tracking over a broad momentum range ($p \sim$ 100 MeV/c – 100 GeV/c). It consists of the central barrel which covers mid-rapidity ($|y| < 0.9$) and the Muon Spectrometer covering the forward rapidity region ($2.5 < y < 4$). The Muon Spectrometer detects dimuons decaying from heavy quarkonia (e.g. J/Ψ) which are hard, penetrating probes as well as high-p_T single muons from $W^{\pm}$ bosons which are initial-state observables. These probes are essential tools for determining medium induced effects and studying the initial conditions of the interaction.

The $W^{\pm}$ boson has a high mass of M_W = 80.385 ± 0.015 GeV and is therefore formed in the early stages of the collision. It decays to single muons ($\mu^{\pm} \leftarrow W^{\pm}$) which are detected in the high-p_T region (30 – 80 GeV/c). The high centre-of-mass energies ($\sqrt{s}$) obtained during proton-proton (pp) and lead-lead (Pb-Pb) collisions at the LHC are sufficient for the formation of the $W^{\pm}$ boson. Due to the increase in luminosity for the LHC in 2011 it is now thought possible to perform a data analysis of the $W^{\pm}$ boson in ALICE. The results can then be compared to previous performance studies and to results from other LHC experiments (ATLAS, CMS and LHCb).

As a first requirement of the analysis, the effect of the alignment of the Muon Spectrometer has to be determined. Misalignment of the Muon Spectrometer could result in a systematic uncertainty in the measurement of the muon track, thereby influencing the efficiency of the detector. By analysing simulations of $W^{\pm}$ boson signals generated with PYTHIA in pp collisions at $\sqrt{s}$ = 8 TeV with ideal and residual misalignment configurations of the detector, these alignment effects on the p_T and pseudorapidity (η) distributions, as well as the ratio $\frac{\mu^+ \leftarrow W^+}{\mu^- \leftarrow W^-}$ (charge asymmetry) were studied using the AliROOT framework. It was found that the misalignment does cause a systematic uncertainty in the p_T distributions and charge asymmetry, especially in the region p_T > 40 GeV/c where the systematic uncertainty grows above 50 %.

Analyses of Pb-Pb collisions conducted in 2011 at $\sqrt{s_{NN}}$ = 2.76 TeV were then performed on data reconstructed with original alignment information and data refitted with improved alignment information. They were compared to establish the effect of alignment on the single muon distributions. The improved alignment has a limited effect in the high-p_T region and therefore also on possible $W^{\pm}$ boson studies. Due to lack of statistics at high-p_T the $W^{\pm}$ boson signal and the nuclear modification factor (R_{AA}) could not be extracted, but it is foreseen that the extraction will later be possible with the use of 2012 pp and Pb-Pb data.

Samevatting

Analise van $W^{\pm}$ bosone met ALICE: Effek van oplyning op $W^{\pm}$ bosone analise

deur

Pieter Johannes Wynand du Toit

Promotor: Professor C. Theron

Mede-promotors: Doktor S. V. Förtsch en Doktor E. Z. Buthelezi

Die ALICE ("A Large Ion Collider Experiment") detektor by CERN se Groot Hadron Versneller ("LHC") is toegewy tot die bestudering van die onbeperkte medium bekend as die kwark-gluon plasma (KGP), wat by uiterste energie digthede in swaar-ioon botsings gevorm word. ALICE kan hadrone, fotone, elektrone en muone bestudeer tot by die hoogste verwagte meervoudighede by die LHC en tot by baie lae transversale momentum ($p_T \sim$ 30 MeV/c) deur gebruikmaking van uitstekende deeltjie identifikasie ("PID") en sporing oor 'n wye momentum streek ($\sim$ 100 MeV/c – 100 GeV/c). Dit bestaan uit die sentrale loop wat die middel-rapiditeitsreeks ($|y| < 0.9$) dek en die Muon Spektrometer wat die voorwaartse rapiditeitsreeks ($2.5 < y < 4$) dek. Die Muon Spektrometer neem dimuone waar afkomstig van swaar kwarkonia (bv. J/Ψ) wat hard, indringende waarneembares is, sowel as hoë-p_T enkel muone vanaf $W^{\pm}$ bosone wat begintoestand waarneembares is. Hierdie waarneembares is noodsaaklik vir die bepaling van medium geïnduseerde effekte en die bestudering van die aanvanklike voorwaardes van die interaksie.

Die $W^{\pm}$ boson het 'n hoë massa van M_W = 80.385 ± 0.015 GeV en word daarom in the vroeë stadiums van die botsing gevorm. Dit verval na enkele muone ($\mu^{\pm} \leftarrow W^{\pm}$) wat in die hoë-$p_T$ streek (30 - 80 GeV/c) waargeneem word. Die groot massamiddelpunt energieë ($\sqrt{s}$) wat behaal word tydens die proton-proton (pp) en lood-lood (Pb-Pb) botsings by die LHC is voldoende vir die vorming van $W^{\pm}$ bosone. As gevolg van die toename in luminositeit in 2011 vir die LHC word dit verwag dat dit nou moontlik is om 'n $W^{\pm}$ boson data-analise uit te voer in ALICE. Die resultate kan dan vergelyk word met vorige werkverrigtingstudies en met resultate van ander LHC eksperimente (ATLAS, CMS en LHCb).

As 'n eerste vereiste vir die analise moet die effek van die oplyning van die Muon Spektrometer bepaal word. Afwyking van die Muon Spektrometer se oplyning kan moontlik 'n sistematiese fout in die bepaling van die muon se p_T veroorsaak en daardeur die doeltreffendheid van die detektor beïnvloed. Deur simulasies te analiseer van $W^{\pm}$ boson seine in pp botsings teen $\sqrt{s}$ = 8 TeV wat met PYTHIA gegenereer is vir ideale en residuele oplyningsfout konfigurasies van die detektor, is hierdie effekte op the p_T en pseudorapiditeit (η) verspreidings, sowel as die verhouding $\frac{\mu^+ \leftarrow W^+}{\mu^- \leftarrow W^-}$ (lading asimmetrie) bestudeer met die gebruik van die AliROOT raamwerk. Daar is bevind dat die

oplyningsfout wel ‘n sistematiese fout in the bepaling van die p_T verspreidings en lading asimmetrie veroorsaak, veral in die streek p_T > 40 GeV/c waar die sistematiese fout groter as 50% word.

Analises van Pb-Pb botsings wat in 2011 uitgevoer is teen $\sqrt{s_{NN}}$ = 2.76 TeV is daarna voltooi op data gerekonstrueer met oorspronklike oplyning informasie en data aangepas tot verbeterde oplyning informasie. Die twee gevalle is vergelyk om die effek van die oplyning op enkele muon verspreidings te bepaal. Die verbeterde oplyning het 'n beperkte uitwerking in die hoë-p_T streek en dus ook op moontlike $W^{\pm}$ boson studies. Weens 'n gebrek aan statistiek by hoë-p_T is die W ± boson sein en die kernwysigingsfaktor (R_{AA}) nie onttrek nie, maar daar word voorsien dat die onttrekking later sal moontlik wees met die gebruik van 2012 pp en Pb-Pb data.

Acknowledgements

I would like to thank everyone who supported me during my studies. Thanks to Dr Zeblon Vilakazi, Dr Zinhle Buthelezi, Dr Siegfried Förtsch and Dr Deon Steyn at iThemba Laboratory for Accelerator Based Sciences (LABS), Somerset West for all their help and for giving me the opportunity to experience the wonderful field of Particle Physics. Thank you also to Dr Francesco Bossù and my fellow M.Sc. student, Johnson Senosi for all their helpful discussions during the writing of this dissertation.

Thanks to everyone from Subatech at Ecole des Mines de Nantes for their help. Especially to Dr Diego Stocco, Dr Philippe Pillot and Dr Gines Martínez-García for their time and for helping me understand the analysis techniques, workings of the Muon Spectrometer and the theoretical background. Also a word of thanks to Dr Nicole Bastid and the rest of the PWG-HF group for all their valuable insights.

I would like to thank everyone at ALICE who helped me during my training as shifter at Point 2 and for the wonderful opportunity I received to work on such an intriguing experiment.

To Dr Andrew Hamilton from the University of Cape Town who was willing to give me a course on Particle Physics in his spare time, I would like to extend my sincere gratitude.

Without the financial help of the National Institute of Theoretical Physics (NITheP) and the National Research Foundation (NRF) I would not have been able to study Particle Physics. Thank you also to Prof Antonino Zichichi and the World Federation of Scientists (WFS) for the scholarship they made available to me and the University of Pretoria for the postgraduate bursaries I received.

I am very indebted to my family, especially my parents, for their love and encouragements throughout the last two years.

To the love of my life, Imonay, I would like to say thank you for uplifting my spirit when I was discouraged or dismayed. Thank you for your support and for believing in me, and for waiting for me.

Most of all I want to thank my Lord and Saviour for the strength and talents He has given me and the path He has laid out for me.

Table of Contents

Declaration ii
Verklaring iii
Abstract iv
Samevatting vi
Acknowledgements viii

List of Figures xiii
List of Inserts xvii
List of Tables xvii
List of Abbreviations used xviii

Chapter I. Introduction 1
A. Studying the Quark Gluon Plasma in Heavy Ion Collisions 1
1. From AGS and SPS to RHIC and LHC 1
2. Heavy quarks and quarkonia as hard probes 3
B. Physics Motivations for Studying the $W^{\pm}$ boson? 4
1. $W^{\pm}$ boson production as medium-blind reference 5
2. Production of $W^{\pm}$ bosons at LHC energies 5
3. "Standard candles" for luminosity measurements 6
4. Information on PDFs in pp collisions 6
5. Study of cold nuclear matter effects in p-A collisions 7
6. Check nuclear modification effects in A-A collisions 7
7. How can we measure the $W^{\pm}$ boson? 7
C. ALICE and the Muon Spectrometer 8
D. Aims of this Study 9
E. Outline 10

Chapter II. Theoretical Overview 12
A. The Standard Model of elementary particles 12

Table of Contents

B. Quantum Chromodynamics (QCD) 12
1. Confinement & Asymptotic freedom 12
2. Chiral symmetry restoration 14
3. QCD matter phase diagram 15
4. Lattice QCD (lQCD) 15
C. The Quark-Gluon Plasma (QGP) 16
1. Formation of the QGP 16
2. Experimental Observables 17
D. Heavy Flavour Physics 19
1. Heavy quark and quarkonium formation and decay times 19
2. Heavy Flavour production in nucleon-nucleon (pp) collisions 20
3. Heavy Flavour production in p-A collisions: cold nuclear matter effects 21
4. Heavy Flavour production in A-A collisions: hot nuclear matter effects 21
5. Nuclear modification factor (R_{AA}) 22
E. Electroweak Theory and the $W^{\pm}$ boson 23
1. The Electroweak Theory 23
2. Feynman diagrams for the $W^{\pm}$ boson 24
3. $W^{\pm}$ boson production cross sections 25
4. Charge asymmetry of $W^{\pm}$ boson production 27
5. Parity violation in $W^{\pm}$ boson leptonic decays 28
F. Muon Sources at LHC energies 29

Chapter III. The Experiment 33
A. The LHC 33
B. ALICE 34
1. Global detectors 34
2. Central barrel detectors 36
C. The Muon Spectrometer 38
1. The Absorbers 38
2. Dipole Magnet 40
3. The Muon Tracker 40
4. The Muon Trigger 43
5. Alignment of the Muon Spectrometer 45
6. Acceptance and efficiency: effect of alignment 46

Table of Contents

D. ALICE Online Data Taking 47
1. Central Trigger Processor (CTP) 47
2. Data Acquisition (DAQ) and High Level Trigger (HLT) 47
3. Detector Control 49
4. ALICE and the LHC: LHC beam modes, Handshakes and Filling Schemes 50

Chapter IV. Simulation and Analysis 55
A. AliROOT: Offline Framework 55
1. Simulation 55
2. Reconstruction 57
3. Analysis 60
4. The ALICE Grid 62
B. Alignment Study using Simulation 63
1. Simulation Sample 63
2. Alignment Analysis of Simulation 67
C. Alignment Study on Pb-Pb Data 68
1. Experimental Measurements 68
2. $W^{\pm}$ Boson Data-Analysis 71

Chapter V. Results and Discussion 73
A. Alignment Study from pp Simulation 74
1. Transverse momentum (p_T) distributions 74
2. Charge asymmetry 79
3. Pseudorapidity (η) distributions 81
4. Summary 85
B. Alignment Study on Pb-Pb data 86
1. Transverse momentum (p_T) distributions 86
2. Charge asymmetry 91
3. Pseudorapidity (η) distribution 93
4. Possible $W^{\pm}$ boson extraction 95
5. Summary 95

Table of Contents

Chapter VI. Summary and Conclusions 96
A. Summary 96
B. Conclusions 98
C. Outlook 99

Appendix A. Simulation and Reconstruction files A-1
A. Configuration file (Config.C) used in Ideal Case A-1
B. Simulation file (sim.C) used in Ideal Case A-10
C. Reconstruction file (rec.C) used for Ideal Case A-11
Appendix B. Quality Assurance (QA) Run Lists A-12
Appendix C. Analysis task A-14

References R-1

List of Figures

Figure 1: Representation of the Quantum Chromodynamics (QCD) phase diagram. The regions where RHIC and LHC study the transition to the quark-gluon plasma (QGP) are shown in blue and green, respectively. Figure taken from [BNL12].....1
Figure 2: Bjorken-x values accessible at SPS, RHIC and LHC as a function of mass squared ($M2$), centre-of-mass energy (sNN) and rapidity (y). The blue line shows the limit on sNN for the LHC, while the dashed lines indicate constant rapidity. The area circled in red shows the small Bjorken-x region the LHC is able to reach, beyond the reach of SPS and RHIC. Picture taken from [Ian11].....3
Figure 3: The CTEQ6M Parton Distribution Function (PDF) of the proton at Q = 100 GeV. Figure taken from [PS+02].....6
Figure 4: QCD coupling constant. Figure taken from [Bet07].....13
Figure 5: Energy density (ε) as a function of the temperature (T) of the system. Different cases for the number of flavours are considered. The Steffan-Boltzmann limit for an ideal QGP is indicated by the arrows to the right-hand side. Figure taken from [Kar01].....16
Figure 6: The evolution of a heavy-ion collision. The disks represent the colliding nuclei. The figure shows (a) the moments just before the collision, (b) the fireball and the formation of the QGP at a high enough energy density, (c) hadronization of the medium and (d) free-streaming of the hadrons. Figure taken from [Han01].....18
Figure 7: Schematic light-cone representation of the various phases of a heavy-ion collision. Figure taken from [STA10].....18
Figure 8: Nuclear modification factor of muons from heavy flavour decays as function of transverse momentum (pT) in Pb-Pb collisions at sNN =2.76 TeV as measured at ALICE. The data is also compared to different models of energy loss and shadowing. Figure taken from [ALI13b].....23
Figure 9: Feynman diagram of the Wf_1f_2 vertex, where f indicates the fermions, either quarks of leptons. Rules for the vertex construction are also given.....24
Figure 10: Feynman diagram of the production and semi-muonic decay of the $W+$ boson.....25
Figure 11: Lowest order Feynman diagram for $W\pm$ boson production.....25
Figure 12: Second order diagrams for $W\pm$ boson producton.....26
Figure 13: Flavour decomposition of the $W\pm$ cross sections at LO. Figure taken from [MRST00].....27
Figure 14: Sketch of $W+$ and $W-$ boson muonic decay in their rest frames. The long thin arrows indicate the momenta and the thick shorter arrows the spins.....29
Figure 15: Properties and decay modes of the $W\pm$ boson. The leptonic decay mode has a branching ratio of 10.8 %. Figure taken from the Particle Data Group (PDG) report [B+12].....30
Figure 16: Predicted number of reconstructed muons as a function of pT for simulated pp collisions at 14 TeV (above) and for Pb-Pb collisions at 5.5 TeV (below). Figures taken from [CdV07].....31
Figure 17: Predicted single muon charge asymmetry (ratio of $\mu+\mu-$) as a function of pT for simulated pp (above) and Pb-Pb (below) collisions in the ALICE Muon Spectrometer acceptance. The sum of all different sources and also the W contribution are plotted. Figure taken from [CdV07].....32

List of Figures

Figure 18: The CERN accelerator complex. Figure taken from [CER09a].....33
Figure 19: The ALICE detector. The insert shows the Inner Tracking System (ITS) and forward detectors. Figure taken from [ALI13b]. 35
Figure 20: Schematic representation of the Muon Spectrometer showing the absorbers, dipole magnet and the tracker and trigger chambers. Figure taken from [Das13] 39
Figure 21: The Front absorber. Figure taken from [ALI00]. 40
Figure 22: The Dipole magnet. Figure taken from [CER04]. 41
Figure 23: Cathode Pad Chamber layout. Figure taken from [CdV07]. 41
Figure 24: Tracking chamber quadrant. Figure taken from [CDS07]. 42
Figure 25: Tracking chamber slat. Figure taken from [CDS02]. 43
Figure 26: Resistive Plate Chamber (RPC). 44
Figure 27: The trigger principle for the Muon Trigger chambers. Tracks with infinite pT would show no deviation. Therefore a larger deviation in the y-direction indicates a lower pT for the track. Figure taken from [ALI08] 44
Figure 28: The Geometry Monitoring System (GMS). The red lines are optical lines. Figure taken from [TG+05]. 45
Figure 29: The Data Acquisition (DAQ) architecture. Figure from [ALI10] 48
Figure 30: The ALICE Control System context. Picture from [ALI03] 49
Figure 31: Representation of three of the four states of the Muon Tracker (MCH) and commands of the Detector Control Agent (DCA). 50
Figure 32: Magnetic field of the LHC during operation with some of the beam phases shown. When the magnets are ramped up the beam energy increases and when they are ramped down the beam energy decreases. Figure taken from [LHC12].....52
Figure 33: LHC Beam modes with some ALICE responsibilities 54
Figure 34: The AliROOT framework. Figure taken from [ALI11a] 56
Figure 35: Schematic of the data processing in AliROOT. Figure taken from [ALI11a].....57
Figure 36: Simulation Framework. Figure from [ALI11a].....58
Figure 37: The Virtual Monte Carlo (VMC). Figure taken from [ALI11b] 58
Figure 38: Reconstruction Framework. Figure taken from [ALI11a] 59
Figure 39: Pb-Pb event from the LHC in 2011 detected and reconstructed by ALICE. The grey cylindrical transparent object represents the TPC. Tracks detected by the TPC are shown in red and tracks detected by the SPD in white. Figure taken from [ALI13b]. 59
Figure 40: Schematic of the Muon Spectrometer showing the Distance of Closest Approach (DCA). Figure from [Sto10] 62
Figure 41: The ALICE Grid structure. Figure taken from [A+08]. 63
Figure 42: Integrated trigger events (above) and integrated luminosity (below) for different triggers during LHC11h. The orange line shows the Integrated MSH trigger events and luminosity measurements. Figures taken from [TOA11]. 69
Figure 43: Simulation of the pT distributions of different $\mu \pm$ sources for an ideal case carried out with PYTHIA at sNN = 8 TeV. 75
Figure 44: Simulation of the pT distributions of different $\mu \pm$ sources for the residual case carried out with PYTHIA at sNN = 8 TeV.....76
Figure 45: The pT distributions of $\mu+\leftarrow W+$ simulated in pp collisions at sNN = 8 TeV using PYTHIA. The red markers show the ideal case, while the other coloured markers are for the 11 different misalignment cases. 77

List of Figures

Figure 46: The pT distributions of $\mu-\leftarrow W-$ simulated in pp collisions at sNN = 8 TeV using PYTHIA. The red markers show the ideal case, while the other coloured markers are for the 11 different misalignment cases. 77
Figure 47: The pT distributions of $W\pm$ muonic decays simulated in pp collisions at s = 8 TeV using PYTHIA. 78
Figure 48: Predicted differential production cross section from $W\pm$ muonic decays in the ALICE Muon Spectrometer acceptance as a function of pT in pp collisions at s = 14 TeV. Squares represent $\mu+$ and triangles $\mu-$. Figure taken from [CMAF06]. 79
Figure 49: The ratio $\mu+\leftarrow W+\mu-\leftarrow W-$ (charge asymmetry) as a function of transverse momentum (pT) simulated in pp collisions at sNN = 8 TeV using PYTHIA. The red markers show the ideal case, while the other coloured markers are for the 11 different misalignment cases. 80
Figure 50: A magnification of the ratio $\mu+\leftarrow W+\mu-\leftarrow W-$ (charge asymmetry) as a function of transverse momentum (pT) simulated in pp collisions at sNN = 8 TeV using PYTHIA. Only the range 0 < pT < 80 GeV/c is shown to clarify the charge asymmetry in this region. Note that some points fall outside of the charge asymmetry range (0, 4) from pT > 40 GeV/c. 80
Figure 51: The single muon charge asymmetry for $W\pm$ in the ALICE Muon Spectrometer acceptance as a function of pT for pp collisions at s = 14 TeV. Figure from [CMAF06]. 81
Figure 52: The η distributions of $\mu\pm\leftarrow W\pm$ for the ideal case simulated in pp collisions at sNN = 8 TeV using PYTHIA. 82
Figure 53: The η distributions of $\mu\pm\leftarrow W\pm$ for the residual case simulated in pp collisions at sNN = 8 TeV using PYTHIA. 83
Figure 54: Predicted differential production cross section of $\mu\pm\leftarrow W\pm$ as a function of rapidity (y) in pp collisions at s = 14 TeV. Figure from [CMAF06]. 83
Figure 55: The η distributions of $\mu+\leftarrow W+$ simulated in pp collisions at sNN = 8 TeV using PYTHIA. The red data points show the ideal case, while the other coloured markers are for the 11 different misalignment cases. 84
Figure 56: The η distribution for $\mu-\leftarrow W-$ simulated in pp collisions at sNN = 8 TeV using PYTHIA.. The red data points show the ideal case, while the other coloured markers are for the 11 different misalignment cases. 85
Figure 57: The *Pass 1* (blue) and *Pass 2* (red) pT distributions of $\mu\pm$ for Pb-Pb data collected at sNN = 2.76 TeV from data taking period LHC11h. The ratio $Pass\,2Pass\,1$ is shown in purple. 87
Figure 58: Ratio of $Pass\,2Pass\,1$ for the the pT distributions of $\mu\pm$ for Pb-Pb data collected at sNN = 2.76 TeV from data taking period LHC11h. 87
Figure 59: Estimated number of reconstructed muons as a function of pT for Pb-Pb collisions at 5.5 TeV. Figure taken from [CMAF06]. 88
Figure 60: The *Pass 1* (blue) and *Pass 2* (red) pT distributions of $\mu+$ for Pb-Pb data collected at sNN = 2.76 TeV from data taking period LHC11h. The ratio $Pass\,2Pass\,1$ is shown in purple. 89
Figure 61: Ratio of $Pass\,2Pass\,1$ for the the pT distributions of $\mu+$ for Pb-Pb data collected at sNN = 2.76 TeV from data taking period LHC11h. 89
Figure 62: The *Pass 1* (blue) and *Pass 2* (red) pT distributions of $\mu+$ for Pb-Pb data collected at sNN = 2.76 TeV from data taking period LHC11h. The ratio $Pass\,2Pass\,1$ is shown in purple. 90

List of Figures

Figure 63: Ratio of $Pass\ 2 Pass\ 1$ for the the pT distributions of $\mu -$ for Pb-Pb data collected at sNN = 2.76 TeV from data taking period LHC11h.....90
Figure 64: The ratio of $\mu + \mu -$ (charge asymmetry) as a function of pT for LHC11h *Pass 1* (blue) and for *Pass 2* (red). The ratio $Pass\ 2 Pass\ 1$ is shown in purple.....91
Figure 65: Ratio of $Pass\ 2 Pass\ 1$ for the the charge asymmetry of $\mu -$ for Pb-Pb data collected at sNN = 2.76 TeV from data taking period LHC11h. 92
Figure 66: Single muon charge asymmetry (ratio of $\mu + \mu -$) as a function of pT for Pb-Pb collisions at sNN = 5.5 TeV in the ALICE Muon Spectrometer acceptance. Figure from [CdV07].....92
Figure 67: The *Pass 1* (blue) and *Pass 2* (red) η distributions of $\mu \pm$ for Pb-Pb data collected at sNN = 2.76 TeV from data taking period LHC11h.....93
Figure 68: The *Pass 1* (blue) and *Pass 2* (red) η distributions of $\mu +$ for Pb-Pb data collected at sNN = 2.76 TeV from data taking period LHC11h.....94
Figure 69: The *Pass 1* (blue) and *Pass 2* (red) η distributions of $\mu -$ for Pb-Pb data collected at sNN = 2.76 TeV from data taking period LHC11h.....94

List of Inserts

Insert 1: Extracts of the Config.C file used to steer and configure the Simulation of the pp collisions. 65
Insert 2: Extracts from the sim.C file used to run the simulation for the Ideal case. 65
Insert 3: Extracts of the rec.C file used to run the reconstruction for the ideal case. 66
Insert 4: Line of code to implement the selection cuts in the analysis using AliMuonTrackCuts. 67

List of Tables

Table 1: Summary of the number of modules (half chambers) and detection elements (quadrants and slats) in the Muon Tracker. 42
Table 2: Triggers available for the Muon Trigger system. 44
Table 3: Some of the Beam modes of the LHC relevant to ALICE. Table adapted from [LHC11a]. 51
Table 4: Selection cuts applied to events and tracks in the analysis of the simulation of pp collisions at sNN = 8 TeV and of Pb-Pb data collected at sNN = 2.76 TeV. 61
Table 5: Resolution of the alignment of the detector elements (DEs) of the Muon Spectrometer. Table courtesy of J. Castillo [Cas12] 67
Table 6: Resolution of the alignment of the chambers of the Muon Spectrometer. Table courtesy of J. Castillo [Cas12]. 67
Table 7: Number of events in the *Pass 1* and *Pass 2* data samples during the different stages of the analysis. 68
Table 8: Conditions of the Quality Assurance (QA) imposed on runs from LHC11h. 70
Table 9: The Muon Trigger and Muon Tracker Chamber efficiencies for data taking period LHC11h for *Pass 1* and *Pass 2*. 71
Table 10: Systematic uncertainties in the measurements in Pb-Pb collisions for 2011. 71
Table 11: Total number of tracks which satisfy the cuts in the analysis 87

List of Abbreviations used

A-A	Nucleus-nucleus
ACR	ALICE Control Room
AGS	Alternate Gradient Synchrotron
ALICE:	A Large Ion Collider Experiment
AliEn	Alice Environment
AliROOT	ALICE offline framework using ROOT
AOD	Analysis Object Data
ATLAS	A Toroidal Large ApparatuS
Au	Gold
BDMPS	Baier-Mueller-Peigné-Schiff formalism
BNL	Brookhaven National Laboratory
BRAHMS	Broad Range Hadron Magnetic Spectrometers Experiments at RHIC
CEM	Colour Evaporation Model
CERN	European Organization for Nuclear Research
CGC	Colour Glass Condensate
CMS	Compact Muon Solenoid
CPC	Cathode Pad Chambers
CROCUS	Concentrator Read Out Cluster Unit System
CSM	Colour Singlet Model
CTP	Central Trigger Processor
DAQ	Data Acquisition
DCA	Distance of Closest Approach
DCS	Detector Control System
DDL	Detector Data Links
DE	Detector Element
DQM	Data Quality Management
ECR	Electron Cyclotron Resonance
ECS	Experimental Control System
EKS	Eskola-Kolhinen-Salgado shadowing model
EMCal	Electromagnetic Calorimeter
ESD	Event Summary Data
FEE	Front-End Electronics
FEP	Front End Processors
FERO	Front-End Read Out
FMD	Forward Multiplicity Detector
FSM	Finite State Machines
GDC	Global Data Collector
GMS	Geometry Monitoring System
HF	Heavy Flavour
HIC	Heavy-Ion Collision
HLT	High Level Trigger
HMPID	High Momentum Particle Identification
IP	Interaction Point
iThemba LABS	iThemba Laboratory for Accelerator Based Sciences
ITS	Inner Tracking System
LDC	Local Data Concentrator
LEIR	Low Energy Ion Ring

List of Abbreviations used

LHC	Large hadron Collider
LHCb	The Large Hadron Collider beauty experiment
LINAC	LINear Accelerator
LO	Leading Order
lQCD	Lattice Quantum ChromoDynamics
LTU	Local Trigger Units
LUT	Look-Up Tables
MANAS	Multiplexed ANAlogic Signal
MANU	MANAS Numérique
MC	Monte Carlo
MCH	Muon Tracking Chambers
MRPC	Multi-gap Resistive Plate Chambers
MTR	Muon Trigger Chambers
MWPC	Multi-Wire Proportional Chamber
NLO	Next-to-Leading Order
NN	Nucleon-Nucleon
NNLO	Next-to Next-to-Leading Order
OCDB	Offline Condition Database
pp	Proton-proton
p-A	Proton-nucleus
PATCH	Protocol for the ALICE Tracking CHamber
Pb-Pb:	Lead-lead
PDF	Parton Distribution Function
PHENIX	Pioneering High Energy Nuclear Interaction eXperiment
PHOBOS	Experiment at RHIC named after moon on Jupiter
PHOS	Photon Spectrometer
PID	Particle Identification
PMD	Photon Multiplicity Detector
PQM	Parton Quenching Model
PS	Proton Synchrotron
PSB	Proton Synchrotron Booster
QA	Quality Assurance
QCD	Quantum ChromoDynamics
QED	Quantum ElectroDynamics
QGP	Quark Gluon Plasma
QQ	Heavy quark pair
RHIC	Relativistic Heavy Ion Collider
RICH	Ring Imaging Cherenkov
RORC	Read-Out Receiver Card
RPC	Resistive Plate Chambers
SPD	Silicon Pixel Detectors
SPS	Super Proton Synchrotron
STAR	Solenoidal Tracker At RICH
SUSY	Super Symmetry
TPC	Time Projection Chamber
TRD	Transition Radiation Detector
VMC	Virtual Monte Carlo
ZDC	Zero Degree Calorimeter

Chapter I. Introduction

A. Studying the Quark Gluon Plasma in Heavy Ion Collisions

1. From AGS and SPS to RHIC and LHC

According to the theory of Quantum Chromodynamics (QCD), which describes the strong colour force, coloured quarks and gluons are confined inside colour neutral hadrons. But calculations which evaluate the QCD theory at discrete points on a 3D lattice (lattice QCD) predict that under conditions of extreme energy densities and temperatures a state of strongly interacting matter can be formed, where quarks and gluons are no longer confined [Kar06]. This deconfined state of matter is known as the quark-gluon plasma (QGP). The transition to this deconfined state is expected to be accompanied by the restoration of the chiral symmetry of the strong interaction, which is spontaneously broken at low energies [Cre11]. The restoration of this symmetry is also a sufficient condition for a phase transition [NO06]. Therefore the hot and dense QGP is expected to have properties different to that of the cold confined hadronic phase. Figure 1 shows a representation of the QCD phase diagram as a function of Temperature (T) and baryon density (μ).

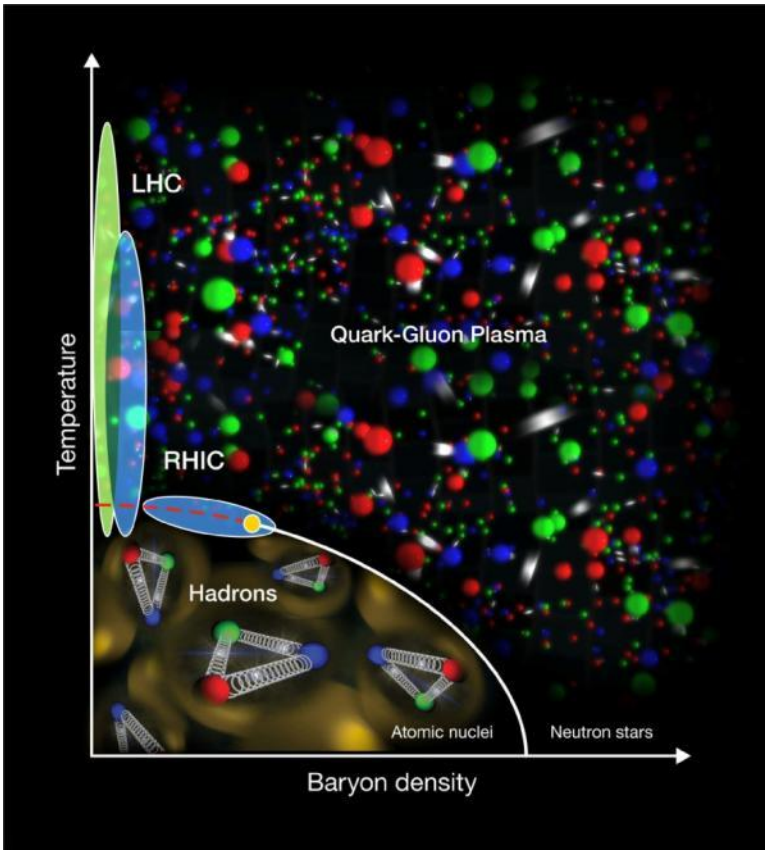

Figure 1: Representation of the Quantum Chromodynamics (QCD) phase diagram. The regions where RHIC and LHC study the transition to the quark-gluon plasma (QGP) are shown in blue and green, respectively. Figure taken from [BNL12].

I. Introduction

Relativistic heavy-ion collisions provide the necessary conditions of extreme energy density (ε) higher than the critical energy density ($\varepsilon_c \approx 1$ GeV/fm^3) which enable the formation of the QGP in a large volume (V) to study it experimentally. The Alternate Gradient Synchrotron (AGS) at the Brookhaven National Laboratory (BNL) in the USA has been able to accelerate heavy ions, such as gold (Au) and iron (Fe) ions since the 1960s. When the AGS Booster was constructed in 1991 the AGS was able to accelerate Au ion beams to even higher energies onto fixed Au targets, reaching centre-of-mass energies per nucleon-nucleon collision of $\sqrt{s_{NN}}$ = 5 GeV [A+94]. Unfortunately the energy densities attained ($\varepsilon \approx 1.5$ GeV/fm^3) were insufficient to study the QGP. During the same period the CERN Super Proton Synchrotron (SPS) was able to accelerate lead (Pb) ions to $\sqrt{s_{NN}}$ = 17.2 GeV, obtaining higher energy densities of $\varepsilon \approx 2.9$ GeV/fm^3 where the formation of a new state of matter was observed [HJ00].

More recently in the 2000s the Relativistic Heavy Ion Collider (RHIC) at BNL achieved $\sqrt{s_{NN}}$ = 130 and 200 GeV in Au-Au collisions, reaching energy densities of $\varepsilon \approx 2 - 15$ GeV/fm^3, which were sufficient for the formation of the QGP [Bay02]. The RHIC experiments, STAR [A+05a], PHENIX [A+05b], BRAHMS [A+05c] and PHOBOS [B+05] all agreed that a strongly interacting matter had been observed. They studied the effects of the medium on the surrounding matter by measuring various observables, e.g. RHIC measurements showed the suppression of high transverse momentum (p_T)[1] particles which suggested that particles traversing the QGP loses a large amount of energy due to a high gluon density found inside the deconfined medium [Mar06a].

The CERN Large Hadron Collider (LHC) has been built to deliver much higher centre-of-mass energies and energy densities ($\varepsilon \approx 4 - 40$ GeV/fm^3) than RHIC [Mar06a]. The nominal centre-of-mass energies at the LHC are $\sqrt{s}$ = 14 TeV for proton-proton (pp) collisions, $\sqrt{s_{NN}}$ = 5.5 TeV for lead-lead (Pb-Pb) collisions and $\sqrt{s_{NN}}$ = 8.8 TeV for proton-lead (p-Pb) collisions. At present the LHC has delivered up to $\sqrt{s}$ = 8 TeV for pp collisions, $\sqrt{s_{NN}}$ = 2.76 TeV for Pb-Pb collisions and $\sqrt{s_{NN}}$ = 5.0 TeV for p-Pb collisions. This enables further studies into the properties of the QGP and chiral symmetry restoration due to the increase in energy densities and also because the lifetime of the QGP will be significantly longer than at RHIC. These studies at higher energy density could even lead to the discovery of new and unexpected physics. Figure 1 shows the regions where the LHC can study the QCD phase diagram, which RHIC could not.

The LHC is also able to probe a new range of small Bjorken-x values previously inaccessible by RHIC and SPS. The Bjorken-x values, x_1 and x_2 give the fraction of longitudinal momentum carried by the two interacting partons and can be determined by the following equation [TCG05, Coo05]:

$$x_{1,2} = \frac{M}{\sqrt{s}} e^{\pm y} \qquad \text{(I—1)}$$

[1] If p_x, p_y and $p_z$are the momenta in the x, y and z directions, where z is the collision (beam) axis, then the transverse momentum (p_T) is given by $p_T = \sqrt{{p_x}^2 + {p_y}^2}$.

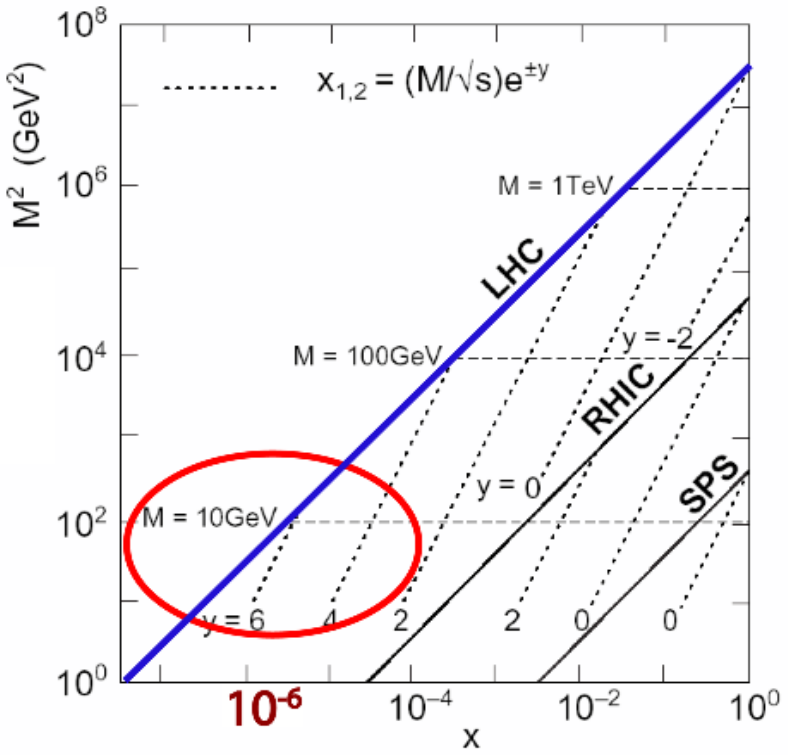

Figure 2: Bjorken-x values accessible at SPS, RHIC and LHC as a function of the mass squared (M^2), centre-of-mass energy ($\sqrt{s}$) and rapidity (y). The blue line shows the limit on $\sqrt{s}$ for the LHC, while the dashed lines indicate constant rapidity. The area circled in red shows the small Bjorken-x region the LHC is able to reach, beyond the reach of SPS and RHIC. Picture taken from [Ian11]

Where M is the mass of the $W^{\pm}$ boson, y is the rapidity[2] and $\sqrt{s}$ the centre-of-mass energy per nucleon-nucleon collision. Figure 2 shows Bjorken-x values within reach at the different heavy-ion colliders and shows circled in red the new range ($10^{-6} < x < 10^{-4}$) the LHC is able to probe.

2. Heavy quarks and quarkonia as hard probes

Earlier it was mentioned that the properties of the QGP can be investigated by measuring different observables. One of the tools available to study the QGP is the production of charm (c) and bottom (b) heavy quarks and subsequently the production of heavy quarkonia (flavourless mesons consisting of a heavy quark and its own anti-quark ($Q\bar{Q}$) such as the charmonium ($c\bar{c}$) J/Psi meson (J/ψ) and the bottomonium ($b\bar{b}$) Upsilon meson (Υ). Due to their large mass heavy quarks are produced in the early stages of the collision by gluon fusion ($gg \rightarrow Q\bar{Q}$) and are hard, penetrating probes which carry information about the QGP and the transition stages of the hot and dense matter [Sat07].

a) In nucleus-nucleus (A-A) collisions

By measuring the decay of heavy flavour to single leptons[3] or lepton pairs (dileptons) in nucleus-nucleus (A-A) collisions the effects caused by the hot matter (hot nuclear matter effects) on heavy

[2] For a particle with 4-momentum $(E, \vec{p})$ where E is the energy of the particle and $\vec{p}$ its momentum, rapidity is given by $y = \frac{1}{2}\log\left(\frac{E+p_z}{E-p_z}\right)$ where p_z is the momentum of the particle in the beam direction (z-direction).

[3] See Chapter II.A "The Standard Model of elementary particles" for a description of leptons and the other elementary particles.

flavour can be studied by measuring the nuclear modification factor, R_{AA}. The nuclear modification factor is defined as the ratio of the measured number of particles produced in A-A collisions to what is expected from the proton-proton (pp) collisions basis, scaled by the average number of binary nucleon-nucleon (NN) collisions during the A-A collisions. Therefore if there were no effects caused by the hot and dense matter, the nuclear modification factor should be one ($R_{AA} = 1$), but since there are effects, they will influence the R_{AA} measurement, so that $R_{AA} \neq 1$ (See discussion in Chapter II.D.5 for more details). These hot nuclear matter effects include heavy quark energy loss, quarkonia suppression [MS86] and quarkonia recombination [GRB04], which will be discussed in Chapter II.D.4.

b) In proton-nucleus (p-A) collisions

In addition to heavy flavour measurements in A-A collisions, heavy flavour production also needs to be measured in proton-nucleus (p-A) collisions to determine effects caused by the high density of partons inside the nucleus (cold nuclear matter effects). Cold nuclear matter effects include effects such as nuclear shadowing [EKS99, GdC07, BBB+03] and nuclear absorption [CF07] that modify the initial or final distributions of heavy flavour production. Nuclear shadowing comes about due to the modification of the gluon PDF, leading to less heavy flavour production. This can also be seen as a reduction of the corresponding cross sections owing to the phenomenon of multiple scattering between the nucleons in the nucleus. There can also be nuclear absorption if the $Q\bar{Q}$ resonance collides repeatedly with the other nucleons in the nucleus. Together with the hot nuclear matter effects, cold nuclear matter effects are responsible for the fact that the heavy flavour production in A-A do not scale with the number of pp collisions ($R_{AA} \neq 1$). Cold nuclear matter effects need to be studied because the hot matter effects in A-A collisions can only be fully understood once the initial conditions are known.

c) In proton-proton (pp) collisions

In proton-proton (pp) collisions heavy flavour is utilized to test theoretical models, such as the Colour Evaporation Model (CEM) [AEGH97] and Colour Singlet Model (CSM) [BBB+03]. CEM is a statistical model describing the probability of the formation of charmonia states, while CSM makes use of the non-relativistic QCD (NRQCD) [CL86] approach. Lattice QCD (lQCD) calculations of heavy quark production can also be verified. Measurement of the heavy flavour yield in pp collisions is also the reference used in determining the nuclear modification factor R_{AA} in Pb-Pb collisions

B. Physics Motivations for Studying the W± boson?

There are various motivations for studying the production of $W^{\pm}$ bosons at LHC energies due to the fact that the $W^{\pm}$ boson is considered to be unaffected by the QGP and therefore a medium-blind reference. Also the production cross section of the $W^{\pm}$ boson carries valuable information in pp, p-Pb and Pb-Pb collisions. To confirm these statements it is necessary to first consider some of the properties of the $W^{\pm}$ boson, such as the qualitative formation and decay times of the $W^{\pm}$ boson and its production processes.

1. $W^{\pm}$ boson production as medium-blind reference

The LHC provides much higher centre-of-mass energies than RHIC which permits the production of $W^{\pm}$ bosons that have a large mass [B+12],

$$M_W = 80.385 \pm 0.015\ \mathrm{GeV/c^2}.$$

Because of this large mass it is formed early in the initial hard collisions with a production time (t_p):

$$t_p \sim \frac{1}{M_W} \sim 0.001\ \mathrm{fm/c} \qquad \text{(I—2)}$$

By definition the decay time is inversely proportional to its width (Γ_W):

$$t_d(W^{\pm} \to X) = \frac{1}{\Gamma_W} \backsimeq \frac{1}{2.085\ \mathrm{GeV}} = 0.09\ \mathrm{fm/c} \qquad \text{(I—3)}$$

Theoretical predictions estimate that at LHC energies the QGP will be formed in approximately 0.1 fm/ c and will last for at least 10 fm/ c [Mar06a]. Hence $W^{\pm}$ bosons are produced before the QGP is created and decays either before the formation of the QGP or during the lifetime of the QGP.

The $W^{\pm}$ boson is one of the mediators of the electroweak force (See Chapter II.E.1) and consequently does not interact strongly with the QGP. The leptonic decays of the $W^{\pm}$ boson also do not interact strongly, so they should similarly not be influenced by the QGP. Therefore, when using the leptonic decay channel of the $W^{\pm}$ boson it can safely be considered as a medium-blind reference, since it is insensitive to the strong interaction it will not interact with the medium even if it were produced later.

2. Production of $W^{\pm}$ bosons at LHC energies

$W^{\pm}$ bosons are produced in the leading order (LO) approximation by the quark (q) – anti-quark ($\bar{q}'$) annihilation process:

$$q + \bar{q}' \to W^{\pm}.$$

Other higher order processes, such as next-to-leading order (NLO) and next-to-next-to-leading order (NNLO) processes involve the radiation of gluons and photons in the initial and final states (QCD and QED radiation). The LO and NLO processes are shown in Chapter II.E.3.

The LO subprocess can be characterized by the scale:

$$Q^2 = {M_W}^2 \qquad \text{(I—4)}$$

where Q is the momentum transferred in the interaction and M_W is the mass of the $W^{\pm}$ boson; and also by the Bjorken-x values which can be calculated using Equation I—1.

Measuring the production cross-sections of $W^{\pm}$ bosons at this high scale $Q^2 = {M_W}^2$ and using the fact that the $W^{\pm}$ boson is a medium-blind reference will provide the following important information:

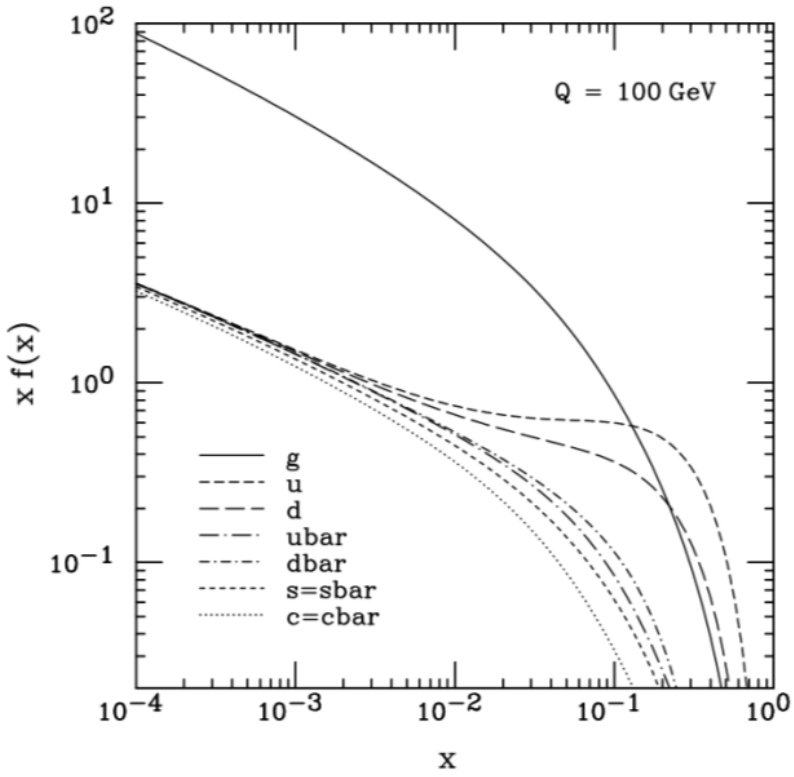

Figure 3: The CTEQ6M Parton Distribution Function (PDF) of the proton at Q = 100 GeV. Figure taken from [PS+02].

3. "Standard candles" for luminosity measurements

The production cross-sections of $W^{\pm}$ bosons are well known with a precision which is dependent on the uncertainties of the Parton Distribution Functions (PDFs) [FM04]. A PDF is defined as the probability density of finding a parton with a certain longitudinal momentum fraction of the proton momentum, x at a resolution scale Q^2 inside the proton. Figure 3 shows an example of the PDF of the proton at $Q = 100$ GeV. Therefore they could be used as "standard candles" in measurements of the luminosity (luminosity monitors). This is done by comparing the experimental cross section to the theoretical cross section calculated using the PDFs and the world averages for M_W and Γ_W, thereby determining the luminosity. These comparisons of the cross section measurements can then also be used to evaluate the performance of the detectors [TCG05, Coo05].

4. Information on PDFs in pp collisions

Figure 3 shows an example of a PDF with the Bjorken-x value on the x-axis at $Q = 100$ GeV. It shows the probability density for finding any one of the partons (g, u, d, etc.) within the proton. At values of $x \lesssim 1$ the proton will consist of only u and d quarks, while at values of $x \ll 1$ the probability of finding the $\bar{u}$ and $\bar{d}$ and strange and charm (s and c) quarks and anti-quarks ($\bar{s}$ and $\bar{c}$) increases and the gluons start to dominate.

$W^{\pm}$ bosons will be sensitive to the PDFs of quarks at the high scale $Q^2 \sim {M_W}^2$. Therefore in pp collisions, measurements of $W^{\pm}$ bosons will provide valuable information on the PDFs.

5. Study of cold nuclear matter effects in p-A collisions

Also at this same scale ($Q^2 \sim {M_W}^2$) in proton-nucleus (p-A) collisions nuclear modification effects will become accessible. Nuclear shadowing and nuclear absorption are cold nuclear matter effects which can be studied and were already mentioned before in the introduction of heavy flavour. Nuclear shadowing could be different for quarks and gluons [Mar06a], which would result in different effects on $W^{\pm}$ boson and heavy flavour studies. At leading order (LO) heavy quarks are produced via pair production, mostly by gluon-gluon fusion, whereas $W^{\pm}$ bosons are formed through quark anti-quark annihilation only. Therefore production of heavy quarks is sensitive to the gluon PDF and production of $W^{\pm}$ bosons to the quark PDF. Therefore comparing the cold nuclear matter effects for heavy flavour and the $W^{\pm}$ boson will provide interesting information on the differences between quarks and gluons.

6. Check nuclear modification effects in A-A collisions

It has been shown that the $W^{\pm}$ boson will be insensitive to the effects of the QGP, since it does not interact via the strong force and is therefore a medium-blind reference. Thus $W^{\pm}$ bosons can be used as reference when studying medium induced effects on other probes, like the suppression of high-p_T muons from heavy quarks. It has already been mentioned in Chapter I.A.a) that in nucleus-nucleus (A-A) collisions these effects can be described by the nuclear modification factor, R_{AA} (See Chapter II.D.5 for a detailed discussion).

In order to study R_{AA}, pp collisions are necessary as reference to the A-A collisions. It is also important to remember that the nuclear modification factor is not only influenced by effects caused by the hot matter (hot nuclear matter effects), but also those effects seen in p-A collisions which are caused due to the high parton density in the nucleus (cold nuclear effects).

The measurement of R_{AA} for $W^{\pm}$ bosons in Pb-Pb will thus be a very powerful tool for binary scaling cross-checks. Binary scaling assumes that by scaling the pp production cross section with the mean number of binary collisions $\langle N_{bin} \rangle_{AA}$ the total production cross sections in A-A collisions can be obtained. Therefore the validity of the Glauber scaling hypothesis [GM70] can be checked, which relates the number of binary collisions, N_{bin} to the nuclear overlap function, T_{AA} which is also sometimes used in R_{AA} calculations.

7. How can we measure the W± boson?

Therefore the physics motivations for studying the $W^{\pm}$ boson are:

- They can be used as “standard candles” for luminosity measurements and to evaluate detector performances.
- They can provide information on the quark PDFs in pp collisions at high Q^2.
- In p-Pb collisions they will enable the study of quark nuclear modification effects (cold matter effects) and comparison to gluon effects.
- Since they are insensitive to the surrounding medium they can be used as medium-blind references for medium induced effects (hot matter effects) in Pb-Pb collisions and to check binary scaling.

These are sufficient reasons to study the production of the $W^{\pm}$ boson in pp, p-Pb and Pb-Pb collisions at the LHC.

The $W^{\pm}$ boson can be measured via its semi-leptonic (or single leptonic) decay channels. The branching ratios for these single decay channels are 10.8 % and more specifically for the muonic decay channel:

$$W^{+} \rightarrow \mu^{+} + \nu_{\mu} \qquad W^{-} \rightarrow \mu^{-} + \overline{\nu_{\mu}}$$

it is 10.6 % [B+12]. Single muons decaying from $W^{\pm}$ bosons can be found in the high-p_T region (30 – 80 GeV/c) because there are only two decay products and therefore the $\mu^{\pm}$ carries away roughly half of the mass of the $W^{\pm}$ boson ($M_W/2 \approx 40$ GeV/c) due to the principle of conservation of energy and momentum.

The production cross section of the $W^{\pm}$ boson in pp collisions (σ_{pp}^{W}) can be found by experiment using the following equation [FM04]:

$$\sigma_{pp}^{W^{\pm}} = \frac{1}{BR_{W^{\pm}\rightarrow\mu^{\pm}\nu}} \frac{1}{\int \mathcal{L}\, dt} \frac{N_{\mu^{\pm}\leftarrow W^{\pm}}^{obs}}{A \times \varepsilon} \qquad \text{(I—5)}$$

where $BR_{W^{\pm}\rightarrow\mu^{\pm}\nu}$ is the branching ratio, $\int \mathcal{L}\, dt$ is the integrated luminosity, $N_{\mu^{\pm}\leftarrow W^{\pm}}^{obs}$ is the number of muons observed and $A \times \varepsilon$ is the acceptance and efficiency of the detector, which need to be determined from simulation, or data if possible [Sto08a]. From this it is clear that the efficiency of the detector needs to be well understood in order to make an accurate measurement of the production cross section. For Pb-Pb the situation is similar but nuclear shadowing effects also need to be taken into account.

The experimental production cross section can then also be compared to the theoretical predictions which will be discussed further in Chapter II.E.3.

C. ALICE and the Muon Spectrometer

There are four major experiments at the LHC: A Toroidal LHC Apparatus (ATLAS), the Compact Muon Solenoid (CMS) experiment, the Large Hadron Collider beauty (LHCb) experiment and A Large Ion Collider Experiment (ALICE) [CER09b]. While ATLAS and CMS are interested in a wide range of physics goals, including the search for the Higgs boson and supersymmetry (SUSY), and LHCb specializes in the study of asymmetry between matter and anti-matter, ALICE [A+08] is dedicated specifically to studying heavy ion collisions with the primary goal of investigating the properties of the QGP and probing the QCD phase diagram.

ALICE is unique with respect to the other LHC experiments in the fact that it is able to measure tracks at very low p_T (~ 30 MeV/c) and with momentum resolution ($\Delta p/p$) of 1 % at 20 GeV/c and 4 % at 100 GeV/c. It achieves this through the use of excellent particle identification (PID) and tracking over a wide momentum (~ 100 MeV/c – 100 GeV/c) range [A+08].

The ALICE detector consists of many subdetectors, which enable it to reach its goal of studying the properties of the QGP. These subdetectors are situated at various positions around the interaction

point (IP) and cover different regions of rapidity[4] (y). The central barrel covers a mid-rapidity region similar to ALTAS and CMS ($|y| < 2$) while the Muon Spectrometer [ALI00] complements this by covering the forward rapidity range of $2.5 < y < 4.0$ [A+08].

In the ALICE reference frame pseudorapidity (η) and rapidity are the same. Pseudorapidity is a spatial coordinate which describes the trajectory of the particle and is given by:

$$\eta = -\log(\tan\frac{\theta}{2}) \qquad \text{(I—6)}$$

where θ is the polar angle relative to the beam (z-) axis. Pseudorapidity is useful in relativistic collisions because it is invariant under Lorentz boosts in the beam direction (z-direction).

The Muon Spectrometer [ALI00] actually covers a negative η and y range in the ALICE reference frame because it is situated on the negative side of the beam-axis (z-axis) with the interaction point (IP) at z = 0 cm. But since for pp and Pb-Pb collisions rapidity and pseudorapidity are symmetric the positive notation can be used. This corresponds to a polar angle of $171° < \theta < 178°$ relative to the beam axis. The Muon Spectrometer is responsible for detecting and reconstructing single muons and muon pairs (dimuons) decaying from various particles, such as heavy flavour and $W^{\pm}$ bosons produced in the collisions.

The determination of the efficiency of the Muon Spectrometer is a crucial step in any single muon analysis [A+12a]. The efficiency of the detector can be influenced by a number of factors, including the status of the detector (the number of dead channels, the gain and pedestal, etc.) and the alignment of its chambers and detector elements (DEs). Therefore it is necessary to first conduct an investigation on any inefficiency caused by the misalignment of the Muon Spectrometer, before a comprehensive analysis of the $W^{\pm}$ boson can be done. Ongoing studies on misalignment effects in $W^{\pm}$ boson simulation analyses [LZ12a], have shown a significant systematic uncertainty in the shape of the p_T distributions of $\mu^{\pm} \leftarrow W^{\pm}$ and also of the ratio $\frac{\mu^{+}\leftarrow W^{+}}{\mu^{-}\leftarrow W^{-}}$ (charge asymmetry) in the high-p_T region.

D. Aims of this Study

In 2011 the LHC delivered much higher beam luminosities than in 2010. For example the luminosity delivered by the LHC to the ALICE experiment in Pb-Pb collisions increased from a maximum of approximately L = 30 $b^{-1}s^{-1}$ in 2010 to 450 $b^{-1}s^{-1}$ in 2011. This resulted in an integrated luminosity of $L_{int} = 143.6$ μb^{-1} in 2011 compared to 10 μb^{-1} delivered to ALICE by the LHC in 2010 [LPC12a, LHC13]. Due to this increase in the luminosity it is now thought possible to study the production of $W^{\pm}$ bosons with the 2011 data. This was not the case with the 2010 data due to the low statistics in the high-p_T region (30 – 80 GeV/c) of the ALICE Muon Spectrometer.

A previous performance study [CdV07, CMAF06] on the predicted production and measurement of $W^{\pm}$ bosons in heavy-ion collisions at the LHC using the AliROOT [ALI11a] framework and the PYTHIA 6.2 [SMS06] event generator showed that it is indeed feasible to study the $W^{\pm}$ boson in the ALICE

[4] Rapidity is useful in collisions at relativistic speeds because under Lorentz boosts in the beam direction it simply changes by an additive constant.

Muon Spectrometer via the single muon decay channel. In the high-p_T range the p_T distribution is dominated by the $\mu^{\pm} \leftarrow W^{\pm}$ decays and the ratio $\frac{\mu^+}{\mu^-}$ (charge asymmetry) could be used to provide evidence for the production of $W^{\pm}$ bosons.

That study looked at the methods employed to determine the acceptance and efficiency of the Muon Spectrometer in order to determine its expected performance. Although it was at first thought that the alignment of the Muon Spectrometer would not significantly influence its efficiency, further studies [Sto08a, LZ12a] have suggested that misalignment does affect the efficiency and results in a systematic uncertainty in the measurement of the p_T of single muons especially at high p_T.

One aim of this study is to determine these misalignment effects by first analysing simulations of $W^{\pm}$ boson signal in pp collisions generated with PYTHIA for ideal and several residual misalignment configurations of the detector. The p_T and η distributions, as well as the charge asymmetry of the single muons decaying from the $W^{\pm}$ boson will be extracted. The effects of the misalignment will then be determined by comparing the ideal and residual cases.

Information on the alignment of the Muon Spectrometer improved in 2012 and Pb-Pb data were refitted to the newly determined alignment of the 2011 data taking period. This study will analyse the p_T and η distributions and the charge asymmetry of the all the single muons reconstructed in the original (*Pass 1*) and refitted (*Pass 2*) data. A comparison between the original and refitted data will check the effect of the new improved alignment on single muon analyses in the high-p_T region.

Conclusions will then be drawn about the effect the alignment has on the simulation and data studies. If any effects are observed in the high-p_T region they could significantly influence the viability of a $W^{\pm}$ boson study. A further aim of this study is to compare the distributions obtained in this study to those predicted in the mentioned performance study. Finally the possibility of extracting the $W^{\pm}$ boson signal from the Pb-Pb data, by subtracting any background, will be considered, in order to determine the $W^{\pm}$ boson cross section and attempt a calculation of the nuclear modification factor R_{AA}.

E. Outline

In Chapter II: “Theoretical Overview” a short description of the Standard Model (SM) and Quantum Chromodynamics (QCD) is given. Confinement, asymptotic freedom and other peculiarities of QCD are presented. This is followed by a discussion on the QGP and signatures of its formation. A section on Heavy Flavour physics examines some of the properties of the heavy quarks and quarkonia and will elaborate on the hot and cold nuclear matter effects observed in heavy-ion collisions The next section gives an overview of the electroweak theory and discusses the production and decay processes of the $W^{\pm}$ boson. Other significant aspects such as charge asymmetry and parity violation are also discussed.

Chapter III: “The Experiment”, introduces the experimental setup. The LHC and ALICE are described and special attention is paid to the ALICE Muon Spectrometer. An account of the online systems at ALICE is given and lastly the data taking procedure is also described, again with emphasis on the Muon Spectrometer.

Chapter IV: “Simulation and Analysis” is dedicated to both the alignment analysis of simulations and the data analysis. But first it describes the offline AliROOT framework used for the simulation, reconstruction and analysis. It then details the simulation sample used and the analysis techniques followed in order to determine the effect of the alignment on the simulation of the $W^{\pm}$ boson signal in pp collisions at $\sqrt{s}$ = 8 TeV. Next the data sample from 2011 Pb-Pb data at $\sqrt{s_{NN}}$ = 2.76 TeV is discussed and also the method used to analyse the data reconstructed with original alignment information (*Pass 1*) and refitted to an improved alignment (*Pass 2*).

The “Results” for both analysis studies are shown and discussed in Chapter V. Comparisons are also made between the results of this study and the previous performance study. The viability of a full $W^{\pm}$ boson study is also considered.

I finish with Chapter VI: “Summary and Conclusion”, with a summary of this work and my conclusions about both the effects of the alignment of the Muon Spectrometer on the analyses and the possibility of a complete $W^{\pm}$ boson study. Further studies and comparisons are considered and also the way forward.

Chapter II. Theoretical Overview

A. The Standard Model of elementary particles

The Standard Model of elementary particles aims to provide the best description of all the phenomena found in particle physics, except those caused by gravity [Mar06b]. Elementary particles are defined as point-like objects and can be classified as fermions or bosons according to their spin. Fermions are particles with fractional spin, e.g. the electron with spin = $\pm\frac{1}{2}$., while the bosons have integer spin, e.g. the photon with spin = ± 1.

Fermions are classified according to their charge and each fermion has a corresponding anti-particle with opposite electric charge. Furthermore fermions consist of quarks and leptons. There are 6 quark flavours which can be grouped into pairs of the up and down (u, d), charm and strange (c, s) and top and bottom (t, b) quarks and their anti-quarks - $(\bar{u}, \bar{d})$, $(\bar{c}, \bar{s})$ and $(\bar{t}, \bar{b})$. The leptons can also be grouped in pairs of the electron and its neutrino (ν_e, e^-), the muon and its neutrino (ν_μ, μ^-) and the tauon and its neutrino (ν_τ, τ^-) and their anti-leptons - $(\overline{\nu_e}, e^+)$, $(\overline{\nu_\mu}, \mu^+)$ and $(\overline{\nu_\tau}, \tau^+)$. Furthermore the pairs of fermions can be grouped together to form three generations of fermions, e.g. Generation I: (u, d), $(\bar{u}, \bar{d})$, (ν_e, e^-) and $(\overline{\nu_e}, e^+)$.

Bosons mediate the fundamental interactions – the electromagnetic force is mediated by the massless photon (γ), the weak force by the massive W^+, W^- and Z^0 bosons, and the strong force by the gluons (g). The Higgs boson has spin 0 and explains the origin of mass in the theory.

Due to the strong interaction quarks are confined into bound states called hadrons. A hadron can either be a baryon, anti-baryon or a meson. Baryons are states with three quarks (qqq) e.g. the proton (uud), anti-baryons states with three anti-quarks $(\bar{q}\bar{q}\bar{q})$ e.g. the anti-proton $(\bar{u}\bar{u}\bar{d})$ and mesons are quark anti-quark states $(q\bar{q})$ such as the triplet of pions: π^- $(u\bar{d})$, π^0 $(u\bar{u}, d\bar{d})$ and π^+ $(d\bar{u})$.

B. Quantum Chromodynamics (QCD)

Quantum Chromodynamics (QCD) accurately describes the strong interaction by means of the postulated existence of the colour charge. Quarks can be in one of three colour charge states, either red (r), green (g) or blue (b) and anti-quarks can have one of three anti-colour charge states: anti-red $(\bar{r})$, anti-green$(\bar{g})$ or anti-blue$(\bar{b})$, while the eight gluons can have the combination of a colour and anti-colour state, e.g. red - anti-green$(r\bar{g})$.

1. Confinement & Asymptotic freedom

According to QCD, quarks always group together to form colour neutral states ($q_r q_g q_b$, $\bar{q}_{\bar{r}}\bar{q}_{\bar{g}}\bar{q}_{\bar{b}}$ and $q_r\bar{q}_{\bar{r}}$, $q_g\bar{q}_{\bar{g}}$, $q_b\bar{q}_{\bar{b}}$) and cannot be observed as free particles – this is known as colour confinement. This can be explained by examining the coupling (intensity) of the strong force. The coupling of the strong interaction (α_S) is influenced by vacuum polarization effects caused by quantum fluctuations. In quantum electrodynamics (QED) which describes the electromagnetic interaction, electrons

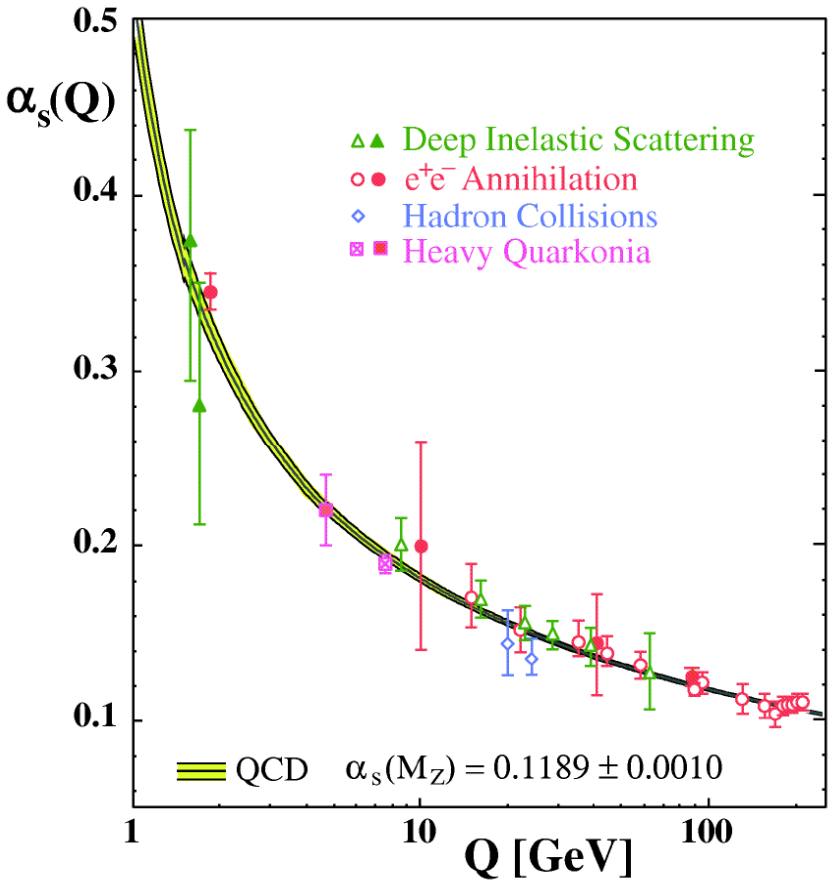

Figure 4: QCD coupling constant. Figure taken from [Bet07]

continually emit and reabsorb photons. If another electron is nearby it could also absorb the photon leading to one-photon exchange scattering. These quantum fluctuations are allowed as long as the violation of energy conservation can be justified by the uncertainty principle. The emitted photon could in turn also produce electron-positron (e^-e^+) pairs. It is due to these virtual processes that a screening effect is produced. Thus as seen from a distance, the charge and the strength of the interaction (α_{em}) will appear weaker while at short distances it will increase.

In QCD, analogously to QED, quarks and gluons also undergo quantum fluctuations and this causes a variation in α_S with distance. But in contrast to QED, there is not only a screening effect, but also a more important anti-screening effect. This is due to the fact that gluons can couple to other gluons, because they carry colour charge, but photons cannot couple to other photons because they do not carry electric charge. The anti-screening results in the strength of the strong interaction being weaker at short distances

This shows that the strong coupling constant, α_S is actually not constant (therefore sometimes called the running coupling constant) and is dependent on the distance at which the interaction occurs. The distance of the interaction is inversely proportional to the momentum transferred in the interaction Q and thus α_S can be given by:

$$\alpha_S(Q^2) = \frac{4\pi}{(11 - \frac{2}{3}n_f)\ln(\frac{Q^2}{\Lambda^2_{\mathrm{QCD}}})} \qquad \text{(II—1)}$$

where n_f is the number of flavours (e.g. 2 if considering only u and d quarks), Q^2 gives the scale of the interaction and Λ_{QCD} is the QCD scale parameter determined by experiments. Figure 4 shows the coupling constant as a function of Q compared to some experimental results.

At small values of Q^2 (for small energies and at large distances) the coupling becomes large, and therefore the quarks are confined to colour neutral states. At high energies the coupling weakens and it is possible that the quarks can become liberated from confinement and behave as quasi-free particles – a condition known as asymptotic freedom [GW73]. This transition between the confining and deconfining phases is related to a gauge symmetry of QCD. This deconfined phase is called the quark-gluon plasma (QGP).

2. Chiral symmetry restoration

QCD is a quantum field theory [Sre07] which represents quarks as fields and the dynamics of the quarks are given by the QCD Lagrangian. These quark fields can be separated into independent left-handed (ψ_L) and right-handed (ψ_R) quark fields. $SU(N_f)_L$ is the gauge group which describes the left-handed and $SU(N_f)_R$ describes the right-handed quarks field where N_f is the number of quark flavours. Chiral symmetry (See [Koc95] for an introduction) refers to the symmetry between these left- and right-handed quark fields and is represented by the $SU(3)_L \otimes SU(3)_R$ symmetry group in the QCD approximation with 3 quark flavours (u, d and s) of vanishing mass.

In this approximation of the QCD Lagrangian chiral symmetry is spontaneously broken in the vacuum. This means that although there is the underlying chiral symmetry in the QCD Lagrangian, the ground state does not also exhibit this symmetry and a chiral (or quark) condensate [Han01],

$$\langle \bar{\psi}\psi \rangle = \langle \bar{\psi}_L \psi_R + \bar{\psi}_R \psi_L \rangle \neq 0 \qquad \text{(II—2)}$$

is formed which contributes to the mass of the quarks inside hadrons. The spontaneous symmetry breaking results in the creation of massless modes called the Goldstone bosons which are the octet of pseudoscalar mesons ($\pi^+, \pi^0, \pi^-, K^+, K^0, K^-, \bar{K}^0, \eta_8$).

These mesons are however not really massless, but do have small masses caused by the fact that the quarks do actually have mass. The small masses of the u, d and s quarks results in an explicit breaking of the chiral symmetry in the QCD Lagrangian. The chiral symmetry was therefore only an approximate symmetry to begin with. But because the masses of the quarks are small compared to the energy scale of QCD the explicit symmetry breaking is much smaller than that of the spontaneous symmetry breaking and the assumption of a perfect chiral symmetry in the Lagrangian can be made.

At high energy densities and temperature we expect the restoration of approximate chiral symmetry [Han01]. This occurs at roughly the same temperature as where deconfinement is expected, but is an entirely different phenomenon and not directly linked with the QGP. The chiral condensate should melt inside of the hot and dense medium and the Goldstone bosons lose their special role, hence $\langle \bar{\psi}\psi \rangle = 0$ and the quarks recover their close to null mass. This restoration of a symmetry is a sufficient condition for a phase transition [NO06].

3. QCD matter phase diagram

The QCD matter phase diagram can be given as a function of temperature (T) and baryon density (μ). Baryon density is the net baryon number[5] of the system. Figure 1, p. 1 shows a representation of how the phase diagram could look like. Examining the phase diagram at null μ, when T is above a certain critical temperature, $T > T_C$ (lQCD calculations predict this to be in the region of $T_C \sim$ 170 - 192 MeV [Kar06]) the intensity of the strong force becomes weak enough and the quarks and gluons are no longer confined inside hadrons. This results in the transition to a new phase - the quark-gluon plasma (QGP). There are still interactions in the deconfined state, but the requirement of forming neutral bound states is now obsolete [MS86]. For $T < T_C$, the intensity of the strong force grows and quarks and gluons are confined inside hadrons - the hadronic gas phase is entered.

It is expected that chiral symmetry will be restored when the hadron gas changes into the QGP and thus a phase transition should occur. This is indicated in Figure 1 by the solid white line between the hadrons and the QGP. But as was mentioned earlier, chiral symmetry is not exactly restored due to the fact that the non-zero mass of the quarks ($m_{u,d} \neq 0$) explicitly breaks the symmetry. Therefore there is rather a cross-over region at low μ where matter goes through a rapid and continuous transition [Mar06a, Han01]. The dashed line in Figure 1 indicates this cross-over region. The conditions of low T and high μ are not discussed here, but are expected to occur in dense neutron stars.

4. Lattice QCD (lQCD)

Lattice Quantum Chromodynamics (lQCD) can be used to numerically calculate the properties of the strongly interacting matter at high temperature and at small values of the baryon density [Kar01]. Therefore it can characterize the transition from hadronic matter to the QGP phase by determining the critical behaviour of the QGP.

This critical behaviour can either be considered by examining the free quark energy or chiral symmetry. The free quark energy can be characterized by the average value of the Polyakov loop which gives rise to the order parameter L for deconfinement [Kar01, KL03]. At $T > T_L$ the transition to the deconfined phase occurs. Chiral symmetry (χ) is characterized by the quark condensate $\langle\bar{\psi}\psi\rangle$ described before and when $T > T_\chi$ the broken chiral symmetry is restored. T_L and T_χ can be computed with lQCD and results show that they coincide ($T_L \approx T_\chi$) and therefore both order parameters (L and χ) indicate a transition at the same critical temperature T_C.

Calculations at finite temperature and null baryon density suggest the value of the critical temperature to be $T_C \sim$ 170 -192 MeV [Kar06]. Figure 5 shows the energy density as a function of the temperature of the system for different cases. The rapid increase in the energy density at the critical temperature is due to the increase in the degrees of freedom of the system. The degrees of freedom changes when deconfinement sets in - from the 3 possible pions (in the 2 flavour case) to the number of quarks and gluons. The Steffan-Boltzmann limit for an ideal gas (and also the QGP) is given by:

[5] The baryon number, B is a quantum number associated to quarks. Quarks have a baryon number, $B = \frac{1}{3}$ and anti-quarks, $= -\frac{1}{3}$. The baryon numbers for baryons are then $= 1$, $B = -1$ for anti-baryons and $B = 0$ for mesons.

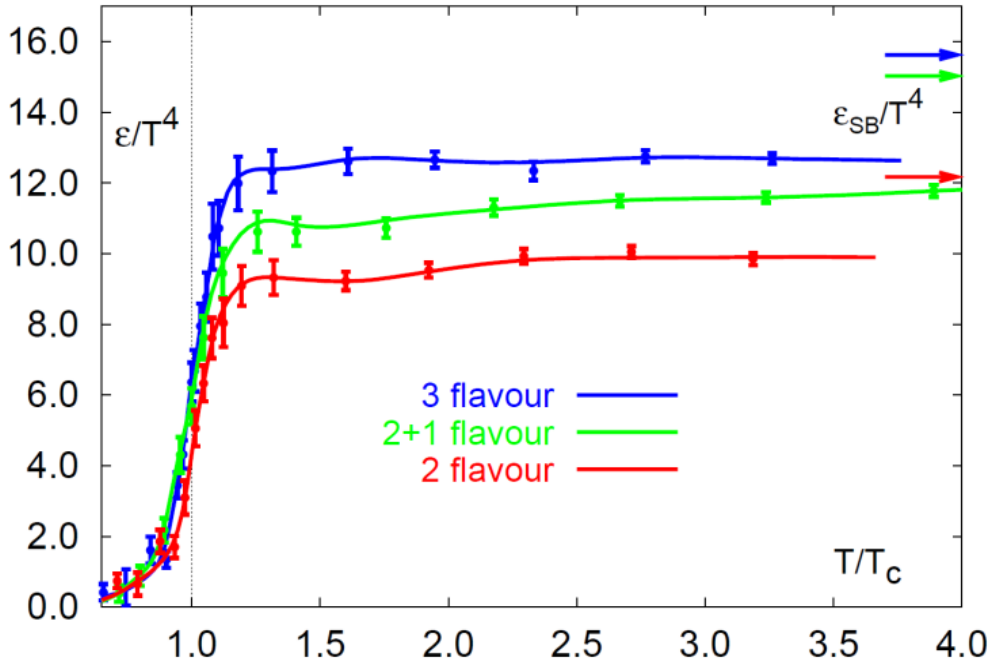

Figure 5: Energy density (ε) as a function of the temperature (T) of the system. Different cases for the number of flavours are considered. The Steffan-Boltzmann limit for an ideal QGP is indicated by the arrows to the right-hand side. Figure taken from [Kar01].

$$\varepsilon_{SB} = N \cdot \frac{\pi^2}{30} T^4 \qquad \text{(II—3)}$$

where N is the number of degrees of freedom. For the ideal hadron gas of massless pions $N = 3$ and $\varepsilon_\pi \simeq T^4$. While for the ideal QGP with 3 flavours:

$$\varepsilon_{QGP} = N \cdot \frac{\pi^2}{30} T^4 = \left\{ \left(3_f \cdot 2_s \cdot 2_q \cdot 3_c\right) \frac{7}{8} + \left(2_s \cdot 8_c\right) \right\} \frac{\pi^2}{30} T^4 = 15.6\, T^4 \qquad \text{(II—4)}$$

where the numbers with subscripts denote the number of flavours (f), spins (s), charge conjugates (q) and colours (c). The first term is for the quarks and the second for the gluons and the multiplication by $\frac{7}{8}$ is due to the different statistics for quarks and gluons.

C. The Quark-Gluon Plasma (QGP)

1. Formation of the QGP

The quark-gluon plasma (QGP) can be studied in relativistic heavy-ion collisions by reaching energy densities of at least 1 GeV/fm^3 [Mar06a]. Figure 6 shows the evolution of a heavy-ion collision. Under relativistic conditions the nuclei can be visualized as disks in the centre-of-mass frame due to Lorentz contraction [Han01]. Figure 6 (a) illustrates the ions just moments before the collision. The nuclei collide and in the initial phase, hard inelastic collisions occur between nucleons (protons and neutrons). During this first stage of the collision many partons (quarks and gluons) are released.

The time the nuclei take to cross (τ_{cross}) is thought to be much smaller than the characteristic time of the strong interaction (τ_{strong}):

$$\tau_{cross} \ll \tau_{strong} \approx \frac{1}{\Lambda_{\mathrm{QCD}}} \sim 1 \text{ fm/c} \qquad \text{(II—5)}$$

where Λ_{QCD} is the QCD scale. Therefore the nuclei pass through leaving behind the liberated partons in a pre-equilibrium phase. Because of the large density of the nuclear material the partons can rescatter several times, thereby depositing a significant part of the incident kinetic energy into the centre-of-mass frame. This thermalization of the partons causes a "fireball" to be created. If the energy density of this fireball exceeds the critical energy density ($\varepsilon > \varepsilon_c \rightleftharpoons T > T_c$) the QGP could be formed as is shown in Figure 6 (b).

The system expands due to the excess pressure with respect to the vacuum and cools down. When $T < T_c$ the system enters the mixed phase where hadrons are formed as depicted in Figure 6 (c). As soon as the energy density is too low to allow further inelastic scattering between partons the formation of new hadrons stops. This is called the chemical freeze-out phase and the hadron gas is formed. Then the system becomes even colder and elastic scattering between the hadrons become impossible. The kinetic properties of the hadrons are fixed - the kinetic (thermal) freeze-out phase. From here the hadrons stream away to the detectors Figure 6 (d). Figure 7 shows the light-cone scheme of the heavy-ion collision and the different phases it undergoes under the condition that the energy density is high enough to allow the formation of the QGP.

2. Experimental Observables

In order to study the properties of the deconfined medium we have to determine the kinematic and chemical properties of the emitted particles in the collision. In effect only pions (π), kaons (K), protons (p), electrons (e), muons (μ), neutrons (n) and photons (γ) can be measured by the ALICE detectors. Through different analysis techniques the particles produced in the collisions can be determined. These particles are then the probes used to deduce the characteristics of the medium and determine its effects on the surrounding matter. These different observables and probes are discussed below:

a) Global observables

Global observables provide information on the main characteristics of the collision such as the centrality, reaction plane, volume, expansion velocity and energy density [Mar06a]. This information can be obtained by measuring the charged particle multiplicity and the transverse energy at mid-rapidity. By measuring particle multiplicity and the energy carried away by participant and spectator nucleons of the collision, the reaction centrality can be obtained. Studies of the transverse energy as a function of centrality provide information about the initial energy density and the duration of the interaction.

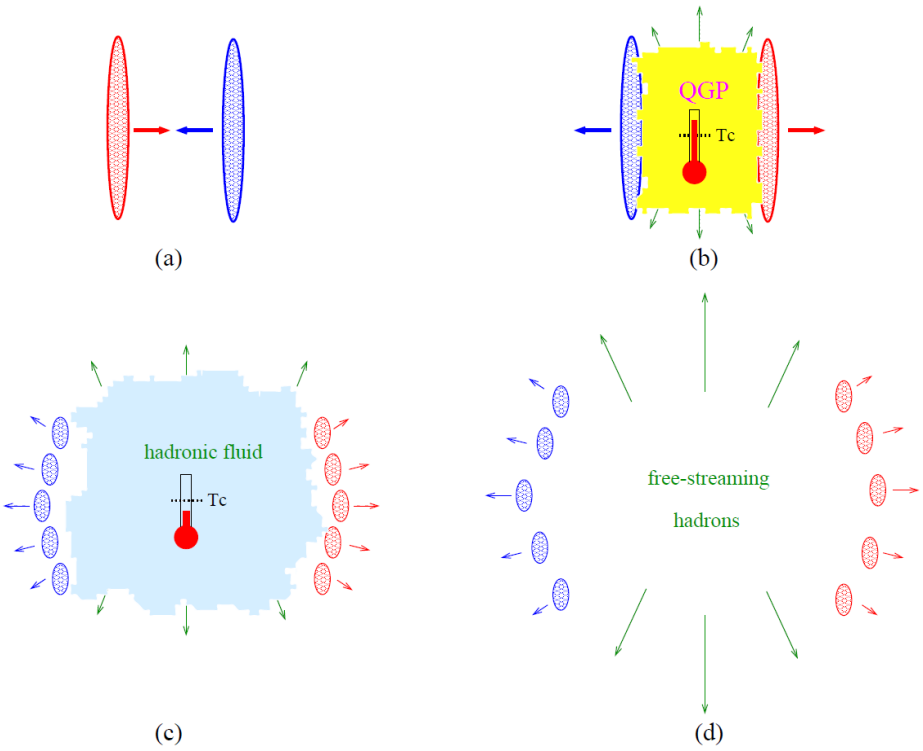

Figure 6: The evolution of a heavy-ion collision. The disks represent the colliding nuclei. The figure shows (a) the moments just before the collision, (b) the fireball and the formation of the QGP at a high enough energy density, (c) hadronization of the medium and (d) free-streaming of the hadrons. Figure taken from [Han01].

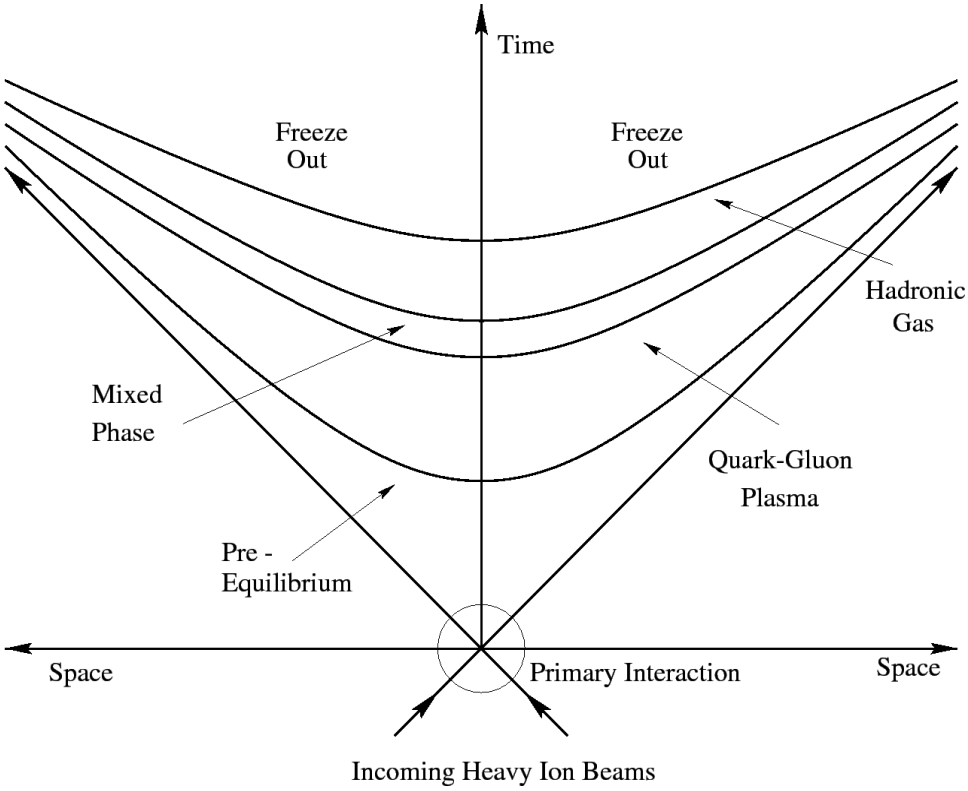

Figure 7: Schematic light-cone representation of the various phases of a heavy-ion collision. Figure taken from [STA10].

b) Final-state observables

Final-state observables provide information on the QGP and hadronic phases, e.g. the dynamical evolution of the expanding hadron gas and properties of the chemical and kinetic freeze-out phases, such as the temperature, baryon density and relative times between them. This information is given by measurements of the hadron yields and their kinematic properties. There are many such probes, such as the p_T distributions and relative yields of the different hadron species, the flow, event fluctuations and high-p_T particle correlations. Measurement of the yields of strange hadrons (for instance the K^0) gives information about the QGP because, due to chiral symmetry restoration which is expected to occur in the deconfined medium, strange quarks are supposed to become lighter than in the confined state and thus strange hadrons are more readily formed [Mar06a].

c) Hard probes

Hard probes are those that carry information on the first stages of the collision, the equilibrium process, the QGP and its transitions [Wie00]. They are produced in the early stages of the collision and their lifetimes are long enough to be sensitive to the formation of the QGP before they fragment. These penetrating probes include: high-p_T particles which allow studying the hot and dense medium via their interaction with the partons; low-p_T photons which can indicate the temperature of the medium; resonances with short lifetimes such as the ρ, ω and ϕ mesons which are produced and decay within the fireball because of their low mass and might be modified by chiral symmetry restoration; and heavy quarks and quarkonia that can probe the potential screening caused by the formation of the QGP [MS86] which will be discussed in the next section, Chapter II.D.

D. Heavy Flavour Physics

It was early on predicted that the suppression of heavy quarkonia states, which are bound states of a heavy quark and its anti-quark - $Q\bar{Q}$, e.g. $c\bar{c}$ (J/Ψ) or $b\bar{b}$ (Υ) could be used as a signature for the formation of the QGP in heavy-ion collisions[MS86]. In order to justify this statement the formation and decay times of heavy quarks and quarkonia with respect to that of the QGP need to be determined. It will also be interesting to look at some of the models used to describe the probability of the formation of open heavy flavour (mesons consisting of a heavy quark and a light quark) and quarkonium states in nucleon-nucleon collisions. Open charm mesons (D) are for instance the D^0, $D^{\pm}$, $D_s^{\pm}$ and $D^{*\pm}$) Finally the influence of the hot and cold nuclear matter effects mentioned in Chapter I on heavy quark and quarkonium production will be discussed.

1. Heavy quark and quarkonium formation and decay times

Heavy quarks and quarkonia are produced in the early stages of the collisions and are hard, penetrating probes of the QGP [Sat00]. At collider energies it is generally accepted that the production mechanism of heavy quarks is either gluon fusion: $gg \rightarrow Q\bar{Q}$, or quark – anti-quark annihilation $q\bar{q} \rightarrow Q\bar{Q}$. At high energies it is mainly the gluons and not the quarks that form these $Q\bar{Q}$ pre-resonance states in the initial hard collision [The94]. In most models of the formation of quarkonium [BBB+03] this pre-resonance will be formed in the characteristic production time t_p:

$$t_p(m_Q) \sim \frac{1}{m_Q} \qquad \text{(II—6)}$$

where m_Q is the mass of the heavy quark.

Therefore the production time of the charm and bottom pre-resonance pairs will be around

$$t_p(m_c) \sim \frac{1}{m_c} \approx \frac{1}{1.5\ \mathrm{GeV/c^2}} \approx 0.15\ \mathrm{fm/c}$$

$$t_p(m_b) \sim \frac{1}{m_b} \approx \frac{1}{5\mathrm{Gev/c^2}} \approx 0.05\ \mathrm{fm/c} \qquad \text{(II—7)}$$

This production time is much smaller than the characteristic time of the strong force $\tau_{strong} \sim 1$ fm/c and therefore they are travelling very close to each other at a relative distance $1/m_Q \ll 1$ fm. The pre-resonance pair therefore needs to expand to reach the characteristic size of a resonance and it is in this time that the pre-resonance "decides" which of the possible $Q\bar{Q}$ resonances it will form. For example the $c\bar{c}$ pre-resonance could either form a J/Ψ with mass $m_{J/\Psi}$ or a Ψ' with mass $m_{\Psi'}$. The time it takes to decide which resonance it will form can be calculated by [KT99]:

$$t_f(J/\Psi, E) \simeq \frac{2E}{m_{J/\Psi}^2 - m_{\Psi'}^2} \qquad \text{(II—8)}$$

where E is the energy of the pair. Thus depending on the energy, the formation time of the resonance could be anywhere between a fraction of a fm/c (0.36 fm/c for Υ with $E = 10$ GeV) to about 3 fm/c (formation time for J/Ψ with $E = 30$ GeV).

Later the unstable $Q\bar{Q}$ resonances will decay with a characteristic proper time inversely proportional to its width. The J/Ψ and Υ decay times would therefore be:

$$t_d(J/\Psi) \simeq \frac{1}{93\ \mathrm{keV}} = 2.1 \cdot 10^3\ \mathrm{fm/c}$$

$$t_d(\Upsilon) \simeq \frac{1}{54\ \mathrm{keV}} = 3.7 \cdot 10^3\ \mathrm{fm/c} \qquad \text{(II—9)}$$

Theoretical calculations show that at collider energies the QGP may be formed in around 0.1 fm/c and might last 10 fm/c or more [Sat06]. Therefore the $Q\bar{Q}$ pre-resonances are produced before the QGP is formed and the $Q\bar{Q}$ resonances (quarkonium) are formed either just before the formation of the QGP, or during its existence and may decay out of it. Quarkonium will therefore be sensitive to the formation of the QGP and this proves that heavy quark and quarkonium formation can be used as a hard probe of the strongly interacting medium.

2. Heavy Flavour production in nucleon-nucleon (pp) collisions

The production of quarkonia and open heavy flavour in nucleon-nucleon collisions can be predicted using several models. Results from pp collisions can then be used to test the theoretical predictions made by these models. Two examples of the models used to describe quarkonium production are the Colour Evaporation Model (CEM) [AEGH97] and the Colour Singlet Model (CSM) [BBB+03]. This study will not focus on these models, but the references can be studied for further details.

3. Heavy Flavour production in p-A collisions: cold nuclear matter effects

In p-A collisions quarkonium and heavy quark production may be influenced by the dense environment found in the nucleus. These effects are called cold nuclear matter effects and include nuclear shadowing [EKS99, GdC07, BBB+03] and nuclear absorption [CF07]. It is very important to determine these effects in p-A collisions in order to have a baseline for the nucleus-nucleus (A-A) collisions in which not only hot nuclear matter effects caused by the formation of the hot nuclear medium are present, but also cold nuclear matter effects caused by the cold dense nuclear medium. This study does not consider cold nuclear matter effects and will therefore not give further details on these effects.

4. Heavy Flavour production in A-A collisions: hot nuclear matter effects

In the hot and high energy density environments created in A-A collisions at relativistic energies, heavy quark and quarkonia are influenced by the strongly interacting medium. These hot nuclear matter effects include heavy quark energy loss, quarkonia suppression [Sat07, GV97, McL03] and quarkonia regeneration [1], which may decrease or increase the production rates of heavy quarks and quarkonia. In this study we will only look at heavy quark energy loss. For further details on quarkonia suppression and regeneration see the mentioned references.

Heavy quarks produced in A-A collisions which travel through the produced medium are subject to energy loss via various mechanisms. It was first predicted by Bjorken [Bjo82] that heavy quarks could lose energy due to elastic collisions with other partons in the medium, in a similar way to ionization of charged particles in ordinary matter. This was later shown to produce only relatively low energy loss.

The heavy quarks can also undergo radiative energy loss when interacting with the medium. Inelastic scattering occurs when the heavy quarks passing through the QGP interact with the medium and lose energy through medium induced gluon radiation. This is analogous to bremsstrahlung of charged particles crossing ordinary matter. One of the various approaches used to describe the energy loss of heavy quarks is the Parton Quenching Model (PQM) [DLP06]

The PQM is based on the Baier-Mueller-Peigné-Schiff (BDMPS) formalism [BDM+97] and includes the dead cone effect [DKT91, DK01] and a realistic collision geometry (the parton energy loss depends on the distance travelled in the medium). In the BDMPS formalism a parton produced in a hard collision suffers multiple scattering in the medium and in this process the gluons in the parton wave function pick up transverse momentum and may eventually de-cohere from the parton and be radiated.

The dead cone effect suppresses gluon bremsstrahlung from heavy quarks compared to light quarks. Due to destructive quantum interferences gluon bremsstrahlung cannot occur in the angular region $\theta < M/E$, where M is the mass of the quark and E its energy. Therefore for heavy quarks the “dead cone” will be larger than for light quarks and less gluons are radiated for heavy quarks than for a light quarks. Furthermore the PQM is a Monte Carlo model which takes into account a realistic energy density profile in the medium. It contains one single parameter which can be estimated from the data.

5. Nuclear modification factor (R_{AA})

The nuclear modification factor, R_{AA} is one of the observables which can be used to determine the effects of the medium on different probes. It is defined as the invariant yield ratio in nucleus-nucleus (*AA*) collisions versus nucleon-nucleon (*NN*) collisions, scaled by the mean number of nucleon-nucleon binary collisions in the nucleus-nucleus reaction $\langle N_{bin} \rangle_{AA}$

$$R_{AA}(p_T, \eta) = \frac{(d^2N/dp_T d\eta)_{AA}}{(d^2N/dp_T d\eta)_{NN}} \cdot \frac{1}{\langle N_{bin} \rangle_{AA}} \qquad \text{(II—10)}$$

where $\langle N_{bin} \rangle_{AA}$ is usually computed using a Glauber model [GM70] that assumes nucleons to travel in straight line trajectories. R_{AA} is close to unity when there are no medium induced effects and the production in *AA* and *NN* collisions are the same. $R_{AA} < 1$ reveals a suppression, and $R_{AA} > 1$ an enhancement of the invariant yield with respect to the reference and points out medium-induced effects. The smaller the R_{AA}, the higher the suppression.

Therefore depending on the degree of energy loss experienced by the probe, the R_{AA} may be different. For instance, the heavy quarks lose energy as they travel through the QGP via the inelastic (gluon radiation) and elastic (collisional energy loss) processes and thus a suppression is expected to be observed for the heavy open flavour D and B mesons. The suppression for light mesons (e.g. π) is expected to be even higher than for heavy flavour mesons. This is because the light mesons originate mostly from gluons which have a higher coupling-strength than quarks and therefore their energy loss in the medium should be higher. Also there will be a higher suppression for the D mesons originating from the lighter c quark ($m_c \approx 1.5$ GeV/c^2), than for the B mesons originating from the heavier b quark ($m_b \approx 5$ GeV/c^2), because of the dead cone effect which reduces the small-angle gluon radiation for heavy quarks as was discussed before. This all translates into:

$$R_{AA}(\pi) < R_{AA}(D) < R_{AA}(B) \qquad \text{(II—11)}$$

It is important to also remember that medium-induced effects are not only the hot matter effects caused by the dense and hot matter, but also the cold nuclear effects, such as nuclear shadowing which have to be checked in p-A collisions as mentioned before. Figure 8 shows the results of a recent study [A+12b] by ALICE on the nuclear modification factor for heavy flavour in Pb-Pb collisions at $\sqrt{s_{NN}} = 2.76$ TeV in the forward rapidity region $2.5 < y < 4$. The data shows a clear suppression of heavy flavour of around 60% in the centrality class 0-10%. Various predictions from models are also shown, e.g. the NLO (MNR) [MNR92] program for heavy flavour production with EPS09 [PES09] shadowing included and Salgado-Wiedemann multiple soft scattering (BDMPS-ASW) [ASW05] which takes into account radiative energy loss.

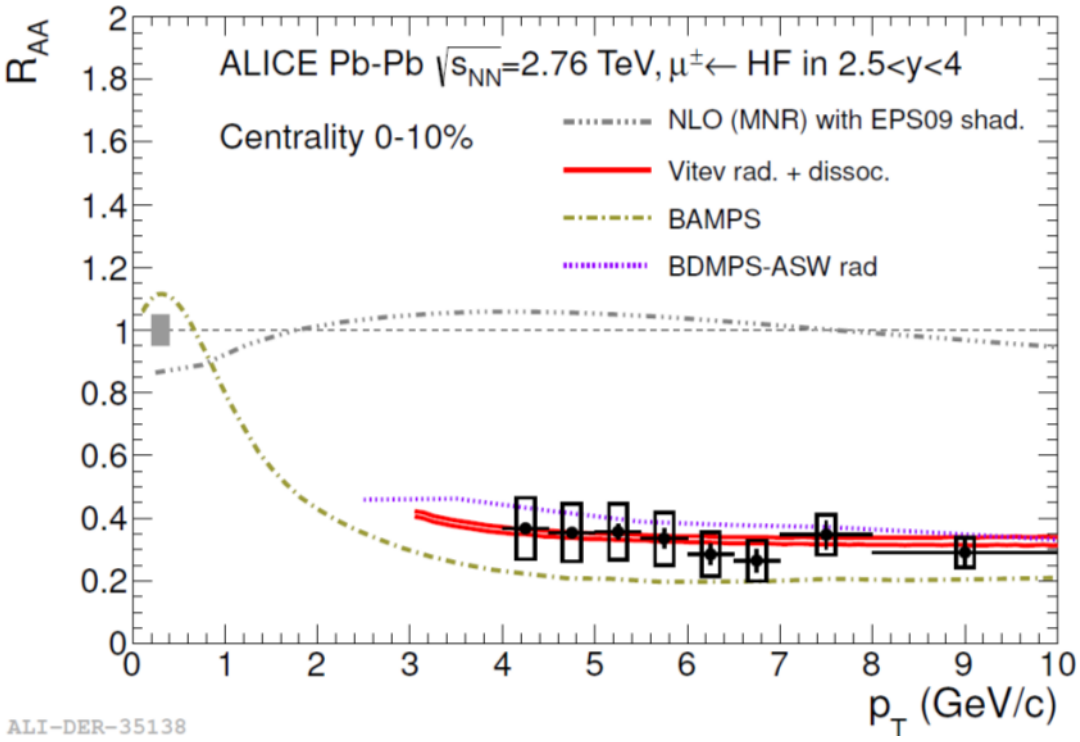

Figure 8: Nuclear modification factor of muons from heavy flavour decays as function of transverse momentum (p_T) in Pb-Pb collisions at $\sqrt{s_{NN}}$ =2.76 TeV as measured at ALICE. The data is also compared to different models of energy loss and shadowing. Figure taken from [ALI13b].

E. Electroweak Theory and the W± boson

This study focuses on the production and decay of the $W^{\pm}$ boson, which is one of the mediators of the electroweak force (the others being the Z^0 boson and the photon (γ)). We have determined already in Chapter I.B.1 that the $W^{\pm}$ boson is unaffected in the presence of the QGP and can therefore be used as a medium-blind reference when studying medium induced effects on other probes such as suppression of heavy quarks. It is necessary to now discussion the electroweak theory which is the unified theory of electromagnetic and weak interactions, in order to determine the characteristics of the $W^{\pm}$ boson. The processes which contribute to the production cross section of the $W^{\pm}$ boson are also very important and other concepts related to our study such as charge asymmetry and parity violation will also be examined.

1. The Electroweak Theory

In 1979, Sheldon Glashow, Steven Weinberg and Abdus Salam shared the Nobel Prize in Physics for the formulation of the electroweak theory [Nob13]. This theory predicted the existence of four mass-less gauge bosons with spin-1: a triplet and a single neutral particle. But the Standard Model also predicts the existence of the heavy spin-0 Higgs boson which is responsible for the mass-giving mechanism. This mechanism can break the symmetry of the postulated triplet, which then ultimately gives rise to the massive W^+, W^- and Z^0. Therefore the mediators of the electroweak force are the massive weak bosons, $W^{\pm}$ and Z^0, together with the massless photon (γ) [Gri04].

The theory of Quantum electrodynamics (QED) is described mathematically by the gauge group $U(1)_{em}$. where $U(1)$ is a unitary gauge group describing a phase rotation of a complex field. The

weak interaction is given by a $SU(2)_L$ gauge group and only acts on left-handed fermions: therefore there is parity violation of the weak interactions. The electroweak theory describes both the electromagnetic and weak interactions together, using a $SU(2)_L \otimes U(1)_Y$ symmetry, where $U(1)_Y$ is the gauge group describing the weak hypercharge (Y). The electromagnetic interaction now "sits across" the weak interaction and the weak hypercharge (Y) which is defined by:

$$Q = T^3 + \frac{Y}{2} \qquad \text{(II—12)}$$

where Q is the electromagnetic charge and T^3 is the third component of the fermion weak isospin charge. This $SU(2)_L \otimes U(1)_Y$ group (sometimes also referred to as a symmetry) is spontaneously broken to the $U(1)_{em}$ group of QED by the Higgs mechanism, which also generates the masses of the quarks and leptons.

In order to visualize and further investigate the $W^{\pm}$ boson and its interactions, it is necessary to understand its Feynman diagrams [Gri04].

2. Feynman diagrams for the W± boson

Feynman diagrams are pictorial representations of the mathematical expressions governing the behaviour of the elementary particles [Gri04]. This scheme is named after its inventor and Nobel Prize-winning American physicist, Richard Feynman, and was first introduced in 1948. Particle trajectories are represented by lines and the points where the lines connect are called the interaction vertexes. This is a simple way to study the mechanisms involved in particle physics.

The Feynman diagram for the $W^{\pm}$ boson vertex is shown in Figure 9, and the rules for the vertex construction are also given. Note that the weak interaction mixes the quark generations, but not the lepton generations. The $W^{\pm}$ boson vertex connects two different fermions and only couples with left-handed fermions and right-handed anti-fermions which is a consequence of the pure vector-axial (V-A) nature of the coupling of the charged weak currents.

In Figure 10 an example of a Feynman diagram is given, which shows the lowest order (LO) production of a W^+ boson from a u quark and $\bar{d}$ anti-quark and its subsequent semi-muonic decay into a μ^+ and its ν_μ.

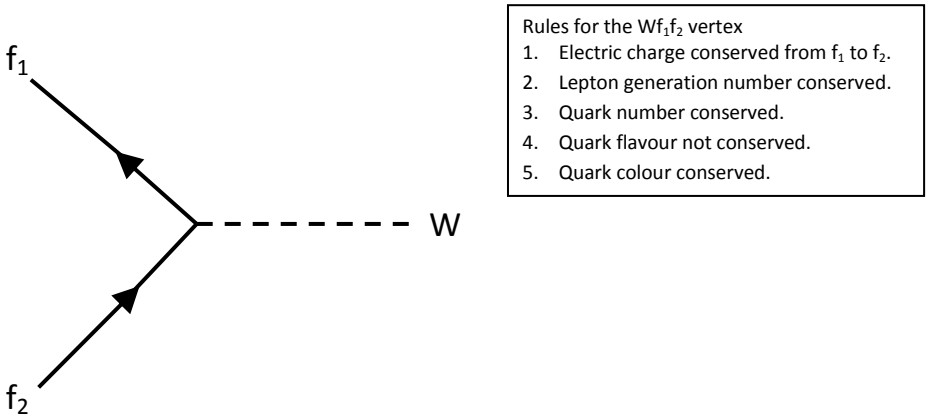

Figure 9: Feynman diagram of the Wf_1f_2 vertex, where f indicates the fermions, either quarks of leptons. Rules for the vertex construction are also given.

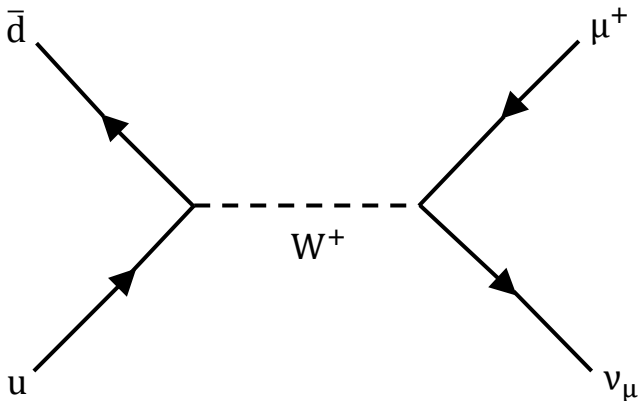

Figure 10: Feynman diagram of the production and semi-muonic decay of the W^+ boson.

3. W± boson production cross sections

The $W^{\pm}$ boson is produced in the initial hard collisions between partons, where the centre-of-mass energy is a maximum. This is because it is a massive particle requiring a high centre-of-mass energy for its formation. Only quarks (not gluons) participate in the production of $W^{\pm}$ bosons in the leading order (LO) approximation[6] shown in Chapter I.B.2. Figure 11 shows the Feynman diagram of the LO approximation of the production of $W^{\pm}$ bosons. The quarks are represented by f_i and $\overline{f_j}$

The next-to-leading order (NLO) processes are:

$$q + g \rightarrow W^{\pm} + q' \qquad q + \overline{q'} \rightarrow W^{\pm} + g$$

$$q + \gamma \rightarrow W^{\pm} + q' \qquad q + \overline{q'} \rightarrow W^{\pm} + \gamma$$

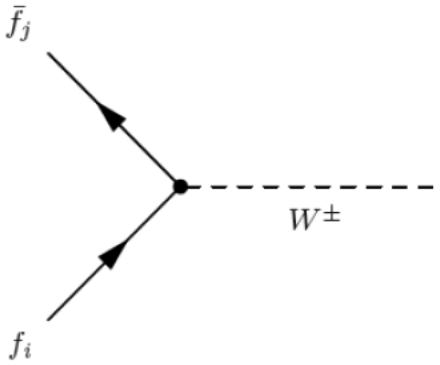

Figure 11: Lowest order Feynman diagram for $W^{\pm}$ boson production.

[6] Leading order (LO) processes are often referred to as the lowest order processes and the next-to-leading order (NLO) processes as second order processes. Also NLO and next-to-next-to-leading order (NNLO) are called higher order processes.

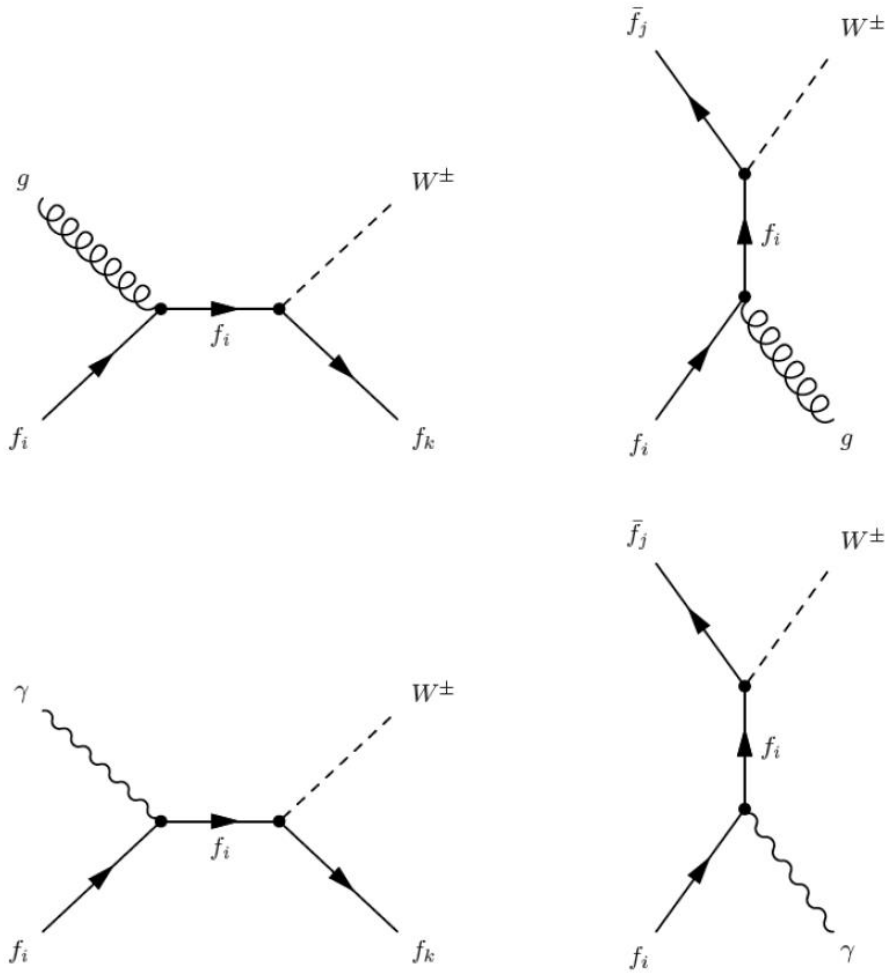

Figure 12: Second order diagrams for $W^{\pm}$ boson producton.

where a gluon or photon is radiated in the initial or final state. The NLO diagrams for the production of the $W^{\pm}$ boson are shown in Figure 12.

The total cross section for the $W^{\pm}$ boson can be computed by taking into account the LO, NLO and next-to-next-to leading order (NNLO) processes [ADMP04]. The NLO correction amounts to about 13 % of the total cross section at NLO, while corrections to the cross section at NNLO are small and dominated by the uncertainties in the Parton Distribution Functions (PDFs) used in the calculation. $W^{\pm}$ boson measurements at the LHC can therefore provide important information on the different sets of PDFs available.

The flavour decomposition of the production cross sections of $W^{\pm}$ bosons at LO as a function of centre-of-mass energy ($\sqrt{s_{NN}}$) is shown in Figure 13. For W^{+} (W^{-}) the dominant contribution to the total cross section is from $u - \bar{d}$ ($d - \bar{u}$) scattering, but there is also a ~17 % (~23 %) contribution from $c - \bar{s}$ ($s - \bar{c}$) scattering. The other processes only contribute between 1 – 3 % to the total cross section.

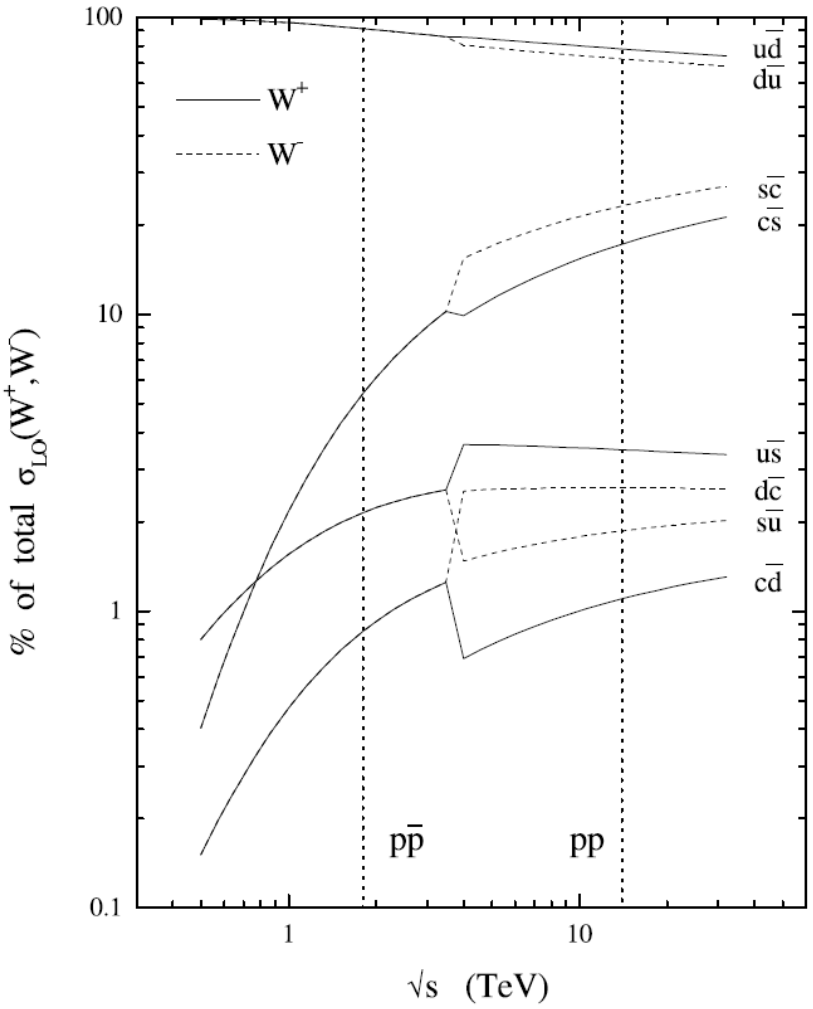

Figure 13: Flavour decomposition of the $W^{\pm}$ cross sections at LO. Figure taken from [MRST00].

4. Charge asymmetry of W± boson production

As can be seen from Figure 13 at LO, the W^+ (W^-) boson is produced primarily by the coupling of $u\bar{d}'$ ($d'\bar{u}$) and with smaller significance by the coupling of $c\bar{s}'$ ($s'\bar{c}$)[7]. This means that the isospin content (number of protons and neutrons) of the colliding nuclei influences the production of W^+ and W^- bosons. In pp and Pb-Pb collisions the net isospin of the colliding nuclei will not be zero, and thus there should be a difference in the number of W^+ and W^- produced.

Looking at Equation I—1, p. 2 which gives the Bjorken-x values as a function of M_W, y and $\sqrt{s_{NN}}$, the $W^{\pm}$ boson is produced at mid-rapidity by small values of x. The PDF shown in Figure 3, p. 6 then makes it clear that the $W^{\pm}$ boson is mainly produced by the interaction of the "sea" quarks with $x_{1,2} \ll 0.1$ with each other. While at high-rapidity the equation leads to at least one high value of $x \lesssim 1$, in which case the contributions from "valence" quarks are predominant.

[7] Here d' and s' are the Cabiddo-rotated quark states which are given by the rotation matrix and the Cabiddo angle, θ_C=13.1° determined from experiments [Mar06b].

Considering pp collisions at high rapidity: protons are made out of uud valence quarks ($N_u = 2N_d$) and so the production of W^+ over W^-will most likely be favoured (Figure 13 shows that the cross section for $u\bar{d}$ is higher than for $d\bar{u}$). Therefore at high rapidity we expect at most $N_{W^+} = 2N_{W^-}$.

For the Pb-Pb case protons (uud) and neutrons (udd) are involved in the collision. Therefore the number of u valence quarks is $N_u = 2Z + N$ and the number of d valence quarks is $N_d = Z + 2N$. At high-rapidity we have at most

$$\frac{N_{W^-}}{N_{W^+}} = \frac{Z + 2N}{2Z + N}$$

$$N_{W^-} = 1.15 N_{W^+} \qquad \text{(II—13)}$$

and therefore we expect to see slightly more W^- than W^+ produced in Pb-Pb collisions at high rapidity.

5. Parity violation in W± boson leptonic decays

The parity operator (P) deals with space inversion ($\vec{r} \to -\vec{r}$) of a state and has eigenvalues: ±1 which is called the intrinsic parity or just parity of the state. While scalars and axial-vectors (also called pseudovectors) have an associated parity of $P = +1$, pseudo-scalars and vectors have parity $P = -1$. The helicity (h) of a particle describes the projection of its spin ($\vec{S}$) on its momentum direction ($\vec{p}$):

$$h = \frac{\vec{S} \cdot \vec{p}}{|\vec{p}|} \qquad \text{(II—14)}$$

Spin is a axial-vector it has parity $P = +1$: $P(\vec{S}) = \vec{S}$. Momentum is a vector and has parity $P = -1$: $P(\vec{p}) = -\vec{p}$. Parity is a multiplicative quantum number and therefore the helicity will change sign under the parity operation: $P(h) = -h$. In the extreme relativistic limit and also in the case of massless particles, chirality (derived from the Greek word for “hand”) corresponds to the helicity of the particle [Gri04]. So for instance, an electron with negative helicity is left-handed (spin in opposite direction of its momentum), and an anti-neutrino with positive helicity is right-handed (spin in same direction of its momentum) .

It was first suggested by Lee and Yang in 1956, and later observed through experiment [WAH+57] that the weak interaction violates parity. It was seen from this experiment that the weak interaction only acts on left-handed fermions and right-handed anti-fermions, which clearly violates parity.

Thus by applying the fact that the weak interaction violates parity and the principle of angular momentum conservation, the helicity (polarization) of $W^\pm$ bosons produced in the hard collisions can be determined. $W^\pm$ bosons emitted at high-rapidity will be produced in parton-parton collisions with $x_1 \lesssim 1$ and $x_2 \ll 1$ as was mentioned in the previous section on charge asymmetry. The Parton Distribution Function (PDF) (Figure 3, p. 6) shows that partons with $x \sim 1$ (high momentum fraction) are more likely to be quarks, than anti-quarks. Remembering that the weak interaction only couples left-handed fermions to right-handed anti-fermions, the $W^\pm$ bosons is therefore predominantly produced by annihilation of a left-handed valence quark carrying a higher momentum fraction, and a right-handed sea anti-quark with a much smaller momentum fraction.

Figure 14: Sketch of W^+ and W^- boson muonic decay in their rest frames. The long thin arrows indicate the momenta and the thick shorter arrows the spins.

Looking at the LO diagram (Figure 11, p. 25), it then shows that due to angular momentum conservation, the $W^\pm$ boson tends to be left-handed (spin in the opposite direction of its momentum) and thus polarized in the same direction as the momentum of the anti-quark.

Next we consider the $W^\pm$ boson decay: Figure 14 shows a sketch of the muonic decays of the W^+ and W^- bosons in their rest frames. When the $W^\pm$ boson decays the fact that the anti-neutrino is right-handed and the neutrino is left-handed is essential. The emission of μ^- will be favoured in the opposite direction to the spin of the W^- boson and the emission of μ^+ in the same direction of the W^+ boson spin due to angular momentum conservation. Therefore, since we have shown that $W^\pm$ bosons tend to be left-handed, the W^+ boson will emit a μ^+ opposite to its momentum direction and the W^- boson will emit a μ^- in its momentum direction. This explains why the μ^+ distribution tends to be shifted to mid-rapidity and the μ^- to higher rapidity, resulting in wider rapidity distributions for μ^- than for μ^+.

F. Muon Sources at LHC energies

In order to determine the viability of measuring the $W^\pm$ boson, the various sources which will contribute to the muon spectra at LHC energies have to be determined. This was studied in detail in [CdV07] and in the present study only the main muon sources relevant to the $W^\pm$ boson study will be mentioned. Figure 16 shows the predicted contributions from the different muon sources found from simulation.

$W^\pm$ and Z^0 boson muonic decays

$W^\pm$ and Z^0 bosons have various decay modes, of which the muonic decays:

$$W^+ \to \mu^+ + \nu_\mu, \qquad W^- \to \mu^- + \overline{\nu_\mu}, \qquad Z^0 \to \mu^+ + \mu^-$$

play the most important role in the high-p_T range, with the muons being produced with a p_T of around half the mass of the boson ($\sim$ 40 GeV/c). Other decay modes of $W^\pm$ and Z^0 bosons, such as tau and charm decays will only produce muons to the low-p_T range, and can therefore be ignored in the high-p_T range. The different decay modes of the $W^\pm$ boson and their branching ratios are shown in Figure 15.

W $J = 1$

Charge $= \pm 1\ e$
Mass $m = 80.385 \pm 0.015$ GeV
$m_Z - m_W = 10.4 \pm 1.6$ GeV
$m_{W^+} - m_{W^-} = -0.2 \pm 0.6$ GeV
Full width $\Gamma = 2.085 \pm 0.042$ GeV
$\langle N_{\pi^\pm} \rangle = 15.70 \pm 0.35$
$\langle N_{K^\pm} \rangle = 2.20 \pm 0.19$
$\langle N_p \rangle = 0.92 \pm 0.14$
$\langle N_{\text{charged}} \rangle = 19.39 \pm 0.08$

W^- modes are charge conjugates of the modes below.

W^+ DECAY MODES		Fraction (Γ_i/Γ)	Confidence level	p (MeV/c)
$\ell^+ \nu$	[b]	(10.80 ± 0.09) %		–
$e^+ \nu$		(10.75 ± 0.13) %		40192
$\mu^+ \nu$		(10.57 ± 0.15) %		40192
$\tau^+ \nu$		(11.25 ± 0.20) %		40173
hadrons		(67.60 ± 0.27) %		–
$\pi^+ \gamma$		$< 8 \times 10^{-5}$	95%	40192
$D_s^+ \gamma$		$< 1.3 \times 10^{-3}$	95%	40168
cX		(33.4 ± 2.6) %		–
$c\bar{s}$		(31 $^{+13}_{-11}$) %		–
invisible	[c]	(1.4 ± 2.9) %		–

Figure 15: Properties and decay modes of the $W^\pm$ boson. The leptonic decay mode has a branching ratio of 10.8 %. Figure taken from the Particle Data Group (PDG) report [B+12].

Charm and bottom muonic decays

Due to the abundance of c- and b-quarks produced at LHC energies , they are the main contributors to the muon spectra at intermediate p_T [A+06].

Hadronic decays

Light flavour and strange hadrons (π/K) also produce muons but with relatively low p_T. In the Muon Spectrometer they should dominate p_T < 2-3 GeV/c.

Therefore in conclusion, the hadronic contribution dominates for p_T < 2, direct muons from charm decays are predominant in the low p_T range (2 < p_T < 4 GeV/c), for 4 < p_T < 30 GeV/c the beauty decays rule and for the high-p_T range (30, 80) GeV/c the $W^\pm$ boson has the greatest influence on the single muon spectra. This leads to the fact that $W^\pm$ boson production can be studied via the high-p_T muons.

The measured distributions will of course influenced by the acceptance and efficiency of the Muon Spectrometer during reconstruction and this has to be taken into account when comparing these predictions to experiment. Figure 16 shows the estimated muon spectra in the acceptance of the Muon Spectrometer for pp and Pb-Pb collisions. The charge asymmetry, shown in Figure 17, can be used to indicate the production of $W^{\pm}$ bosons. This study hopes to compare the p_T distributions and charge asymmetry trends from these predictions to new simulations and to real experimental data.

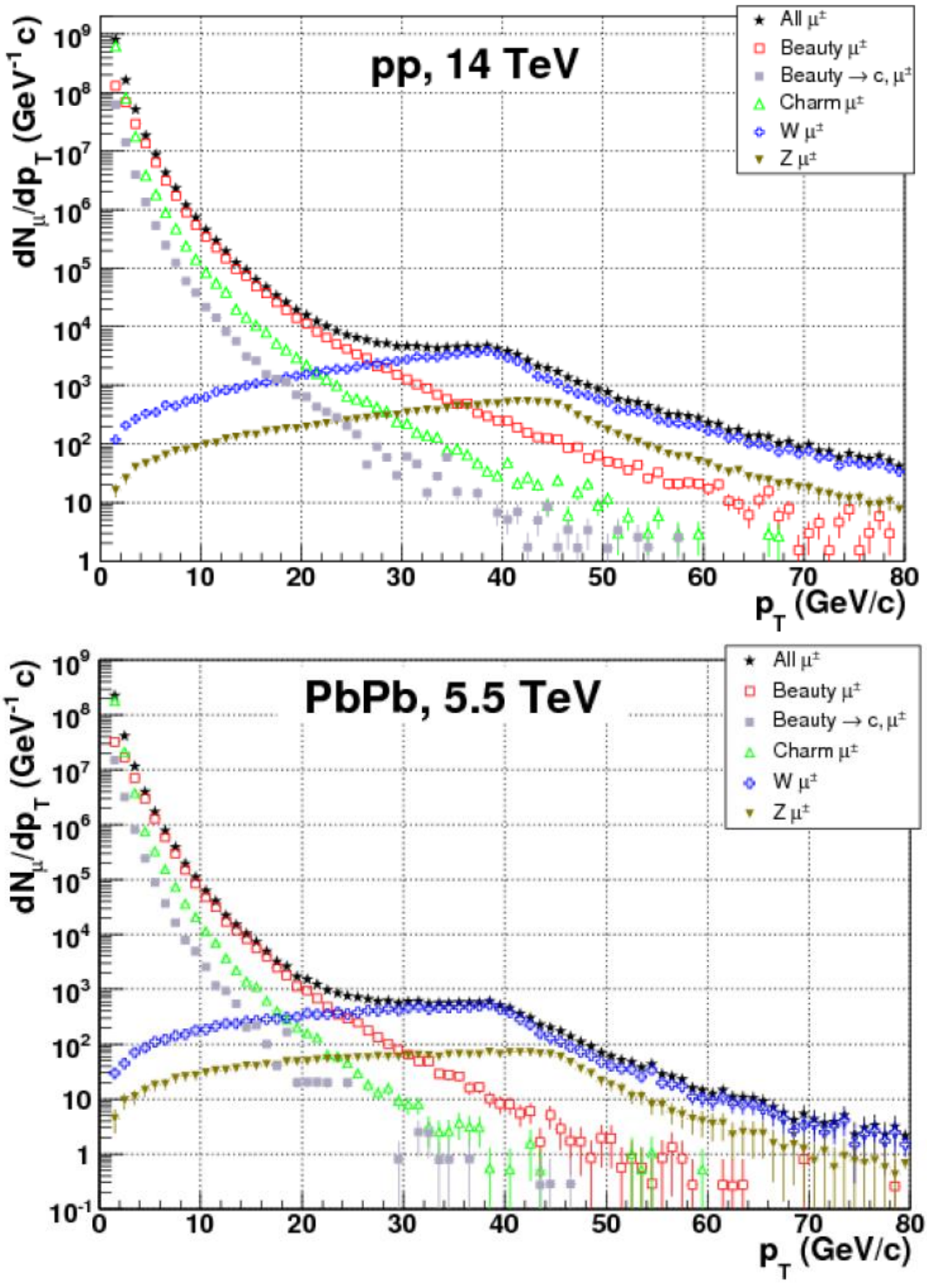

Figure 16: Predicted number of reconstructed muons as a function of p_T for simulated pp collisions at 14 TeV (above) and for Pb-Pb collisions at 5.5 TeV (below). Figures taken from [CdV07].

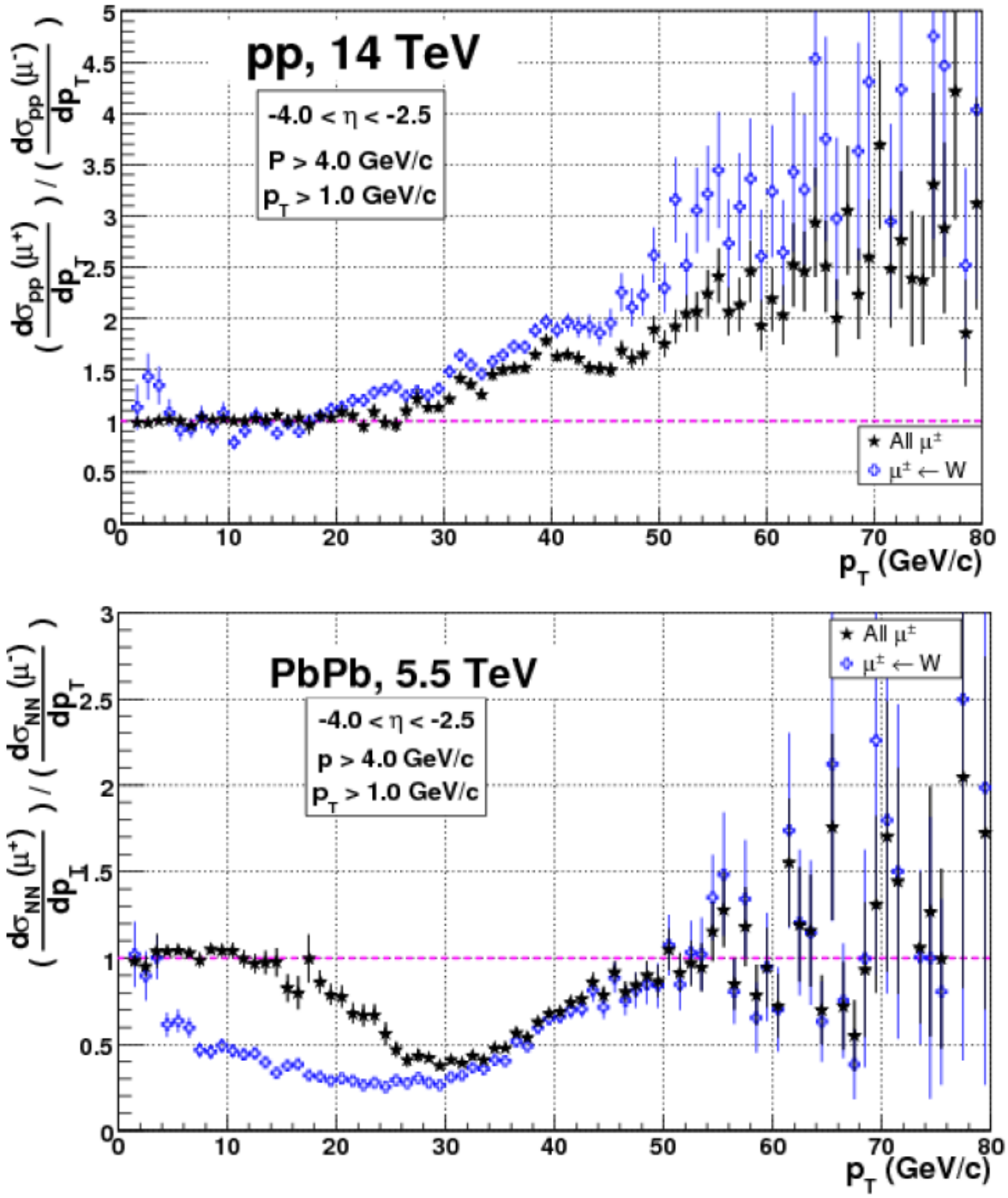

Figure 17: Predicted single muon charge asymmetry (ratio of $\frac{\mu^+}{\mu^-}$) as a function of p_T for simulated pp (above) and Pb-Pb (below) collisions in the ALICE Muon Spectrometer acceptance. The sum of all different sources and also the W contribution are plotted. Figure taken from [CdV07]

Chapter III. The Experiment

A. The LHC

The Large Hadron Collider (LHC) is the largest particle collider in the world. It is situated on the Swiss-France border between the Jura Mountains and Lake Geneva. It has a circumference of 27 km and lies between 70 and 100 m below ground. Beams of either protons or heavy ions (Pb^{82+}), are produced and accelerated in a chain of accelerators (Booster/Leir, PS, SPS) and then injected into the LHC where they are further accelerated presently to energies of 4 TeV for protons and 1.38 TeV for Pb. Thus generating head-on collisions in the centre-of-mass of $\sqrt{s_{NN}}$ = 8 TeV for pp and $\sqrt{s_{NN}}$ = 2.76 TeV for Pb-Pb collisions. In 2013 p-Pb collisions have also been performed at $\sqrt{s_{NN}}$ = 5 TeV. These energies are much higher than previously obtainable at accelerators such as RHIC. For Pb-Pb collisions the nominal LHC centre-of-mass energy of $\sqrt{s_{NN}}$ = 5.5 TeV will be larger by a factor of 30 [C+04] and the energy densities by a factor of 1 -10 than at RHIC [Mar06a]. Therefore new insights into particle and nuclear physics are provided by the LHC.

Figure 18 shows a representation of the CERN Accelerator Complex. The proton beam originates from the LINear ACcelerator 2 (LINAC 2) [LIN08]. The electrons orbiting the hydrogen atoms are

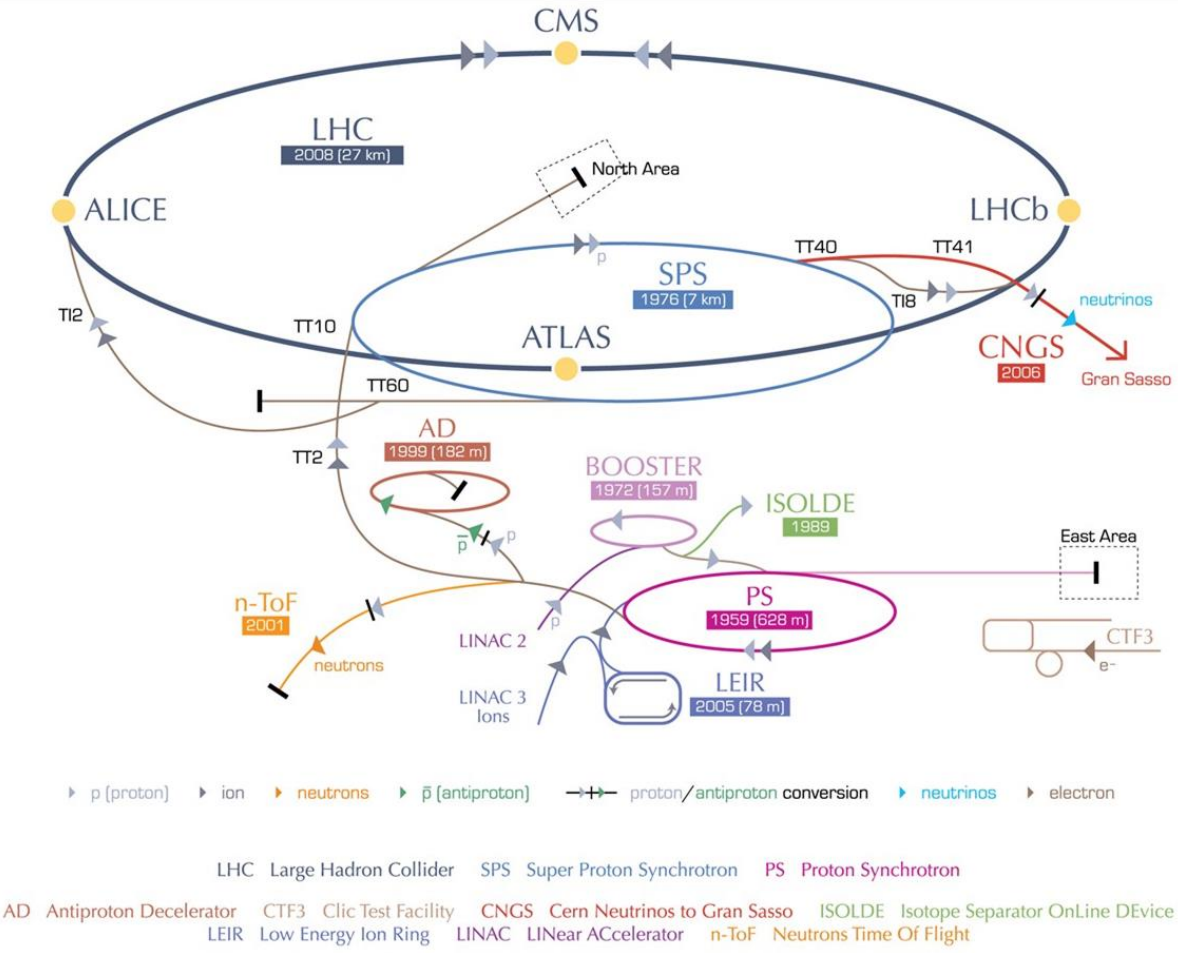

Figure 18: The CERN accelerator complex. Figure taken from [CER09a].

stripped off in the duoplasmatron source, creating the proton beam. This beam is then injected into the Proton Synchrotron Booster (PSB) at an energy of 50 MeV where it is accelerated to 1.4 GeV. The proton beam is then fed to the Proton Synchrotron (PS) where it is accelerated even further to 25 GeV. It is then injected into the Super Proton Synchrotron (SPS) and accelerated to 450 GeV. The protons are then finally transferred to the LHC where they are accelerated to the required energy.

The lead ions are produced by the Electron Cyclotron Resonance (ECR) sources of the LINAC 3, which are plasma devices that generate multi-charged ion states through the use of heat, magnetic fields and microwaves [Hil13]. This produces a sample of different charge states, with the maximum being Pb^{27+}. These ions are selected, accelerated and passed through a carbon foil stripping most of them to Pb^{54+}. The beam is then accumulated and accelerated in the Low Energy Ion Ring (LEIR). It is then sent to the PS where it is further accelerated, passed through another foil which fully strips it to Pb^{82+} and then transferred to the SPS. The SPS accelerates it even further and then injects it into the LHC, where it is accelerated to the nominal energy.

The four main experiments at the LHC are A Toroidal LHC Apparatus (ATLAS), the Compact Muon Solenoid (CMS) experiment, the Large Hadron Collider beauty (LHCb) experiment and A Large Ion Collider Experiment (ALICE) [CER09b]. ATLAS is a general purpose detector and its wide physics goals include the search for the Higgs boson and supersymmetry (SUSY) and extra dimensions. CMS has the same physics goals as ATLAS, but follows a different technical solution and design. LHCb specializes in the study of asymmetry between matter and anti-matter present in interactions of B-particles (particles containing the b quark). ALICE specializes in analyzing lead-ion collisions in order to study the properties of the QGP.

B. ALICE

A Large Ion Collider Experiment (ALICE) [A+08] is situated at Interaction Point 2 (IP2) on the LHC ring, near Saint-Genis-Pouilly, France. ALICE is specifically designed for the study of the quark-gluon plasma by analyzing heavy ion collisions and allows the study of various observables over a wide p_T and η range. It is able to track and identify particles in a large particle multiplicity environment using a number of detectors. These detectors can be divided into three groups: the global detectors, the central barrel and the Muon Spectrometer which all measure different experimental observables. Figure 19 shows the ALICE detector and its different components. The beam line travels along the z-axis and the interaction point (IP) is at z = 0 cm.

1. Global detectors

The global detectors measure the global observables - such as event particle multiplicity, the beam luminosity and event centrality. These detectors are the Forward Multiplicity Detector (FMD), the Photon Multiplicity Detector (PMD), the V0 and T0, and the Zero Degree Calorimeter (ZDC). The forward detectors are the T0, V0 and FMD. In the schematic of the ALICE detector (Figure 19) the forward detectors are shown with respect to the Inner Tracking System (ITS) in the insert.

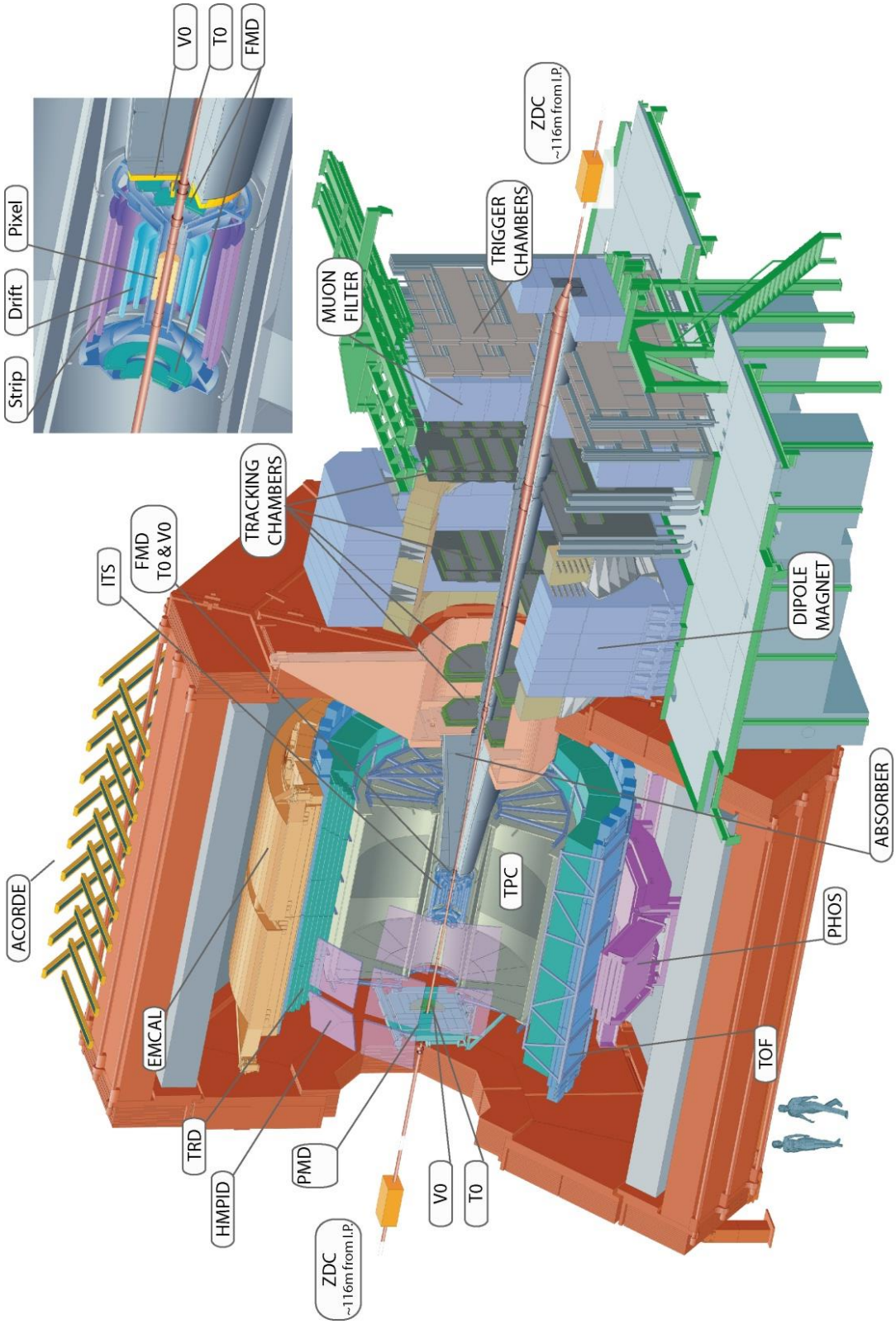

Figure 19: The ALICE detector. The insert shows the Inner Tracking System (ITS) and forward detectors. Figure taken from [ALI13b].

a) Forward Multiplicity Detector (FMD)

The Forward Multiplicity Detector (FMD) [A+08] consists of five rings of silicon strip detectors situated on both sides of the Inner Tracking System (ITS) at z = -75.2, -62.8, 75.2, 83.4, 340 cm relative to the IP and covers the pseudo-rapidity range -3.4 < η < -1.7 and 1.7 < η < 5.1. It evaluates the charged particle multiplicity in this range and helps to determine the reaction plane event-by-event. Together with the ITS, it provides an early charged particle multiplicity measurement for -3.4 < η < 5.1.

b) V0

The V0 detector [A+08] consists of two arrays of scintillator counters that are segmented into four rings and eight sectors. The one array, V0A, is located at z = 340 cm and the other, V0C, at z = -90 cm just in front of the muon absorber. Each scintillator counter is embedded with optical fibre to collect the light produced. A clear fibre then transmits the light to a photo-multiplier tube 3-5 m from the detectors. This ensures each counter has a time resolution better than 1 ns and can provide information on the time-of-flight and the charge of the signal. Therefore the V0 is a fast detector and provides a fast trigger signal and is used to validate the Muon Trigger signal by rejecting beam-gas interactions.

c) T0

The T0 detector [A+08] consists of two arrays of 12 Cherenkov counters per array. T0C is located at z = -70 cm and covers 3.3 < η < -2.9, while T0A at z = 350 cm covers 4.5 < η < 5. Each Cherenkov counter is based on a fine-mesh photo-multiplier tube optically connected to a quartz radiator. The time resolution of the T0 detector is about 50 ps and it can measure the vertex with a resolution of 1.3 cm. It provides a measurement of the collision time; generates a L0 trigger by means of a fast vertex position measurement; measures particle multiplicity and generates three possible trigger signals (minimum bias and two centrality triggers).

d) Photon Multiplicity detector (PMD)

The Photon Multiplicity Detector (PMD) [A+08] is located at z = 360 cm and covers 2.3 ≤ η ≤ 3.5. It measures event-by-event photon-multiplicity and spatial distribution of photons.

e) Zero Degree Calorimeter (ZDC)

The Zero Degree Calorimeter (ZDC) [A+08] determines the centrality of the interaction by measuring the number of the spectator nucleons and their energy.

2. Central barrel detectors

The following detectors are used to measure observables at central rapidity:

f) Inner Tracking System (ITS)

The Inner Tracking System (ITS) [A+08] has the main purpose of tracking and providing vertex measurements. It is made out of six cylindrical layers of silicon detectors covering $|\eta| \leq |0.9|$. The innermost two layers are Silicon Pixel Detectors (SPD), the following two layers are Silicon Drift Detectors (SDD) and the two external layers are Silicon micro-Strip Detectors (SSD). The ITS can

localize the primary vertex with a resolution smaller than 100 µm, reconstruct secondary vertexes and improve the Time Projection Chamber (TPC) measurements, extending the momentum coverage down to 100 MeV/c thereby improving the momentum resolution.

g) Time Projection Chamber (TPC)

The Time Projection Chamber (TPC) [A+08] is the main tracking detector of the central barrel. It is in charge of tracking and determining charged particle momentum to identify particles and evaluate the event vertex position. It can determine charged particles from 100 MeV/c up to 100 GeV/c. The TPC is a cylindrical cage and is positioned between z = ±255 cm. Its internal and external radius is 84 cm and 246 cm, respectively. It covers the pseudo rapidity range $|\eta| \leq 0.9$.

h) Time of Flight (TOF)

The Time of Flight detector (TOF) [A+08] also covers $|\eta| \leq 0.9$ and is responsible for particle identification in the intermediate momentum range between 0.2 and 2.5 GeV/c. It is made of 18 sectors of 5 segments each of Multi-gap Resistive Plate Chambers (MRPC). Together with the ITS and TPC it identifies pions (π), kaons (K) and protons (p).

i) Transition Radiation Detector (TRD)

The Transition Radiation Detector (TRD) [A+08] covers $|\eta| \leq 0.9$ and is positioned between the TPC and TOF detectors. It consists of 18 sectors and each sector is made of 6 layers and 5-fold segmentation along the beam axis. A module has a radiator of 4.8 cm thickness and a multi-wire proportional chamber (MWPC) with cathode pad readout. The MWPC's are filled with a Xe/CO2 gas mixture (85%/15%) and the pads are between 6 – 7 cm2. The detector resolution is around 400 µm and the momentum resolution is ≈ 2.5%. The main function of the TRD is to provide electron identification by rejection of π. Also because it is a fast tracker, it serves as a trigger for high p_T electrons and for electron pairs.

j) High Momentum Particle Identification (HMPID)

The High Momentum Particle Identification (HMPID) [A+08] is one of the outer detectors of ALICE. It is located at a radius of 5 m and has pseudo-rapidity coverage of $|\eta| \leq 0.6$. It is made of 7 modules of proximity focusing Ring Imaging Cherenkov (RICH) counters. When a charged particle crosses a dielectric medium at a speed higher than the speed of light in that medium the particle emits Cherenkov radiation. This is used to identify hadrons with p_T > 1 GeV/c and extends pion and kaon (π/K) discrimination to 3 GeV/c and kaon to proton (K/p) discrimination to 5 GeV/c on a track-by-track analysis.

k) Photon Spectrometer (PHOS)

The Photon Spectrometer (PHOS) [A+08] is situated at the bottom of the central barrel at 460 cm from the interaction point. It covers $|\eta| \leq 0.12$. It is composed of the charged particle veto (CPV) and the electromagnetic calorimeter (EMC). The CPV consists of multi-wire proportional chambers with an Ar/CO_2 gas mixture and cathode pad readout. The EMC is made of lead-tungsten crystals and read-out by Avalanche Photo-Diodes. If an electromagnetic shower is detected by the EMC but not by the CPV it is considered that a photon is detected. The time of flight measurement with

nanosecond precision enables discrimination between photons and baryons. Thus the PHOS provides photon and neutral meson (through the two photon decay channel) identification and also produces a fast trigger.

l) Electromagnetic Calorimeter (EMCal)

The electromagnetic calorimeter (EMCal) [Cor04] covers the $|\eta|$ < 0.7 region and 80° < ϕ < 187° in azimuth. It is able to provide even further electromagnetic calorimetry in the heavy-ion collision environment. It is used to improve the measurement of jets and can also be used as a trigger. The EMCal is a Pb-scintillator sampling calorimeter which is much larger than PHOS, but with lower energy resolution. In conjunction with the TPC and other barrel detectors it measures jet production rates and fragmentation functions [A+08].

C. The Muon Spectrometer

The Muon Spectrometer [ALI99, ALI00] is designed to detect dimuons decaying from the quarkonia J/ψ and Υ families, but also single muons decaying from heavy flavour as well as the $W^{\pm}$ boson. This study involves the measurement of these single muons and therefore emphasis will be placed on this subdetector. It is able to reconstruct muons in the angular range between 171° and 178°, which corresponds to a pseudorapidity interval of -4.0 < η < -2.5 in ALICE. The Muon Spectrometer consists of various elements which are used to achieve effective muon tracking and triggering. The front absorber, beam shield and muon filter are passive elements which reduce the background while the tracking and trigger chambers actively permit muon tracking and triggering. The muon trigger system also uses the V0 detector as a fast trigger to reduce background particles coming from interaction between the beam and gas in the beam-pipe (beam-gas). Figure 20 shows a schematic representation of the Muon Spectrometer and all its elements.

1. The Absorbers

a) Front Absorber

The front absorber (Figure 21) is 4 m in length and lies within the L3 solenoid magnet. It sits as close as possible to the interaction point, at z = 90 cm, in order to reduce mainly the background of muons decaying from π and K. It is made of carbon and concrete and can be divided into the central cone, the inner shield and the outer shield. The central cone's front part is made of concrete and low atomic number materials (carbon) to limit multiple scattering. The back part is made of high atomic number materials (lead, tungsten) in order to absorb particle showers, the secondary particles produced in the absorber itself, and low energy neutrons. The central cone also reduces background from photons and low energy electrons. The inner shield is composed of lead and tungsten and protects the detector from beam particles, while the outer shield is made of high density materials and protects the central barrel detectors from particles recoiling from the absorber.

b) Beam Shield

The beam shield is made of lead, tungsten and stainless steel and surrounds the beam pipe. It has an angular coverage aperture of 2° until it reaches a 30 cm diameter, which it keeps till the end of the spectrometer. The function of the beam shield is to protect the chambers from high rapidity particles and from secondary particles.

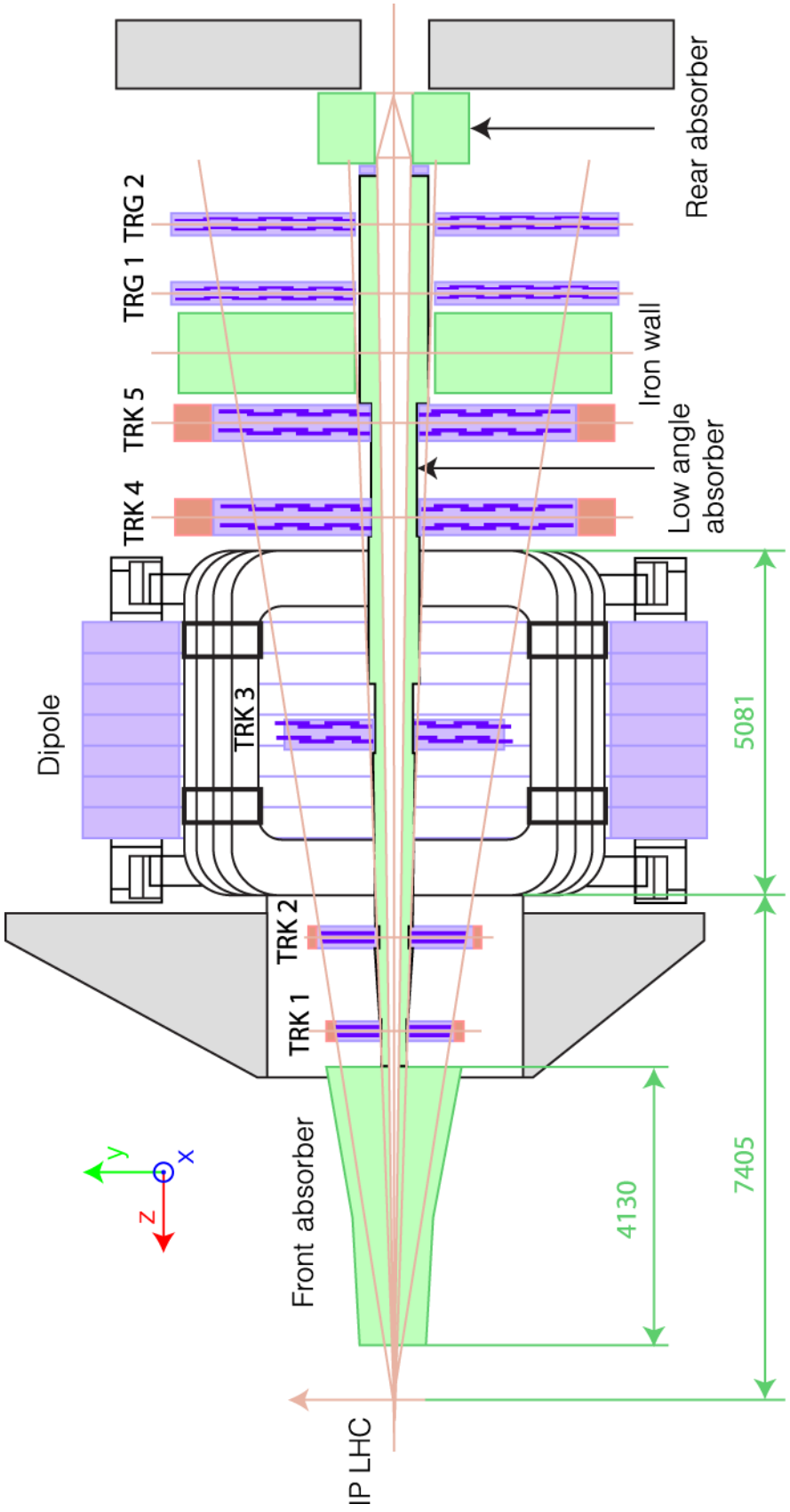

Figure 20: Schematic representation of the Muon Spectrometer showing the absorbers, dipole magnet and the tracker and trigger chambers. Figure taken from [Das13]

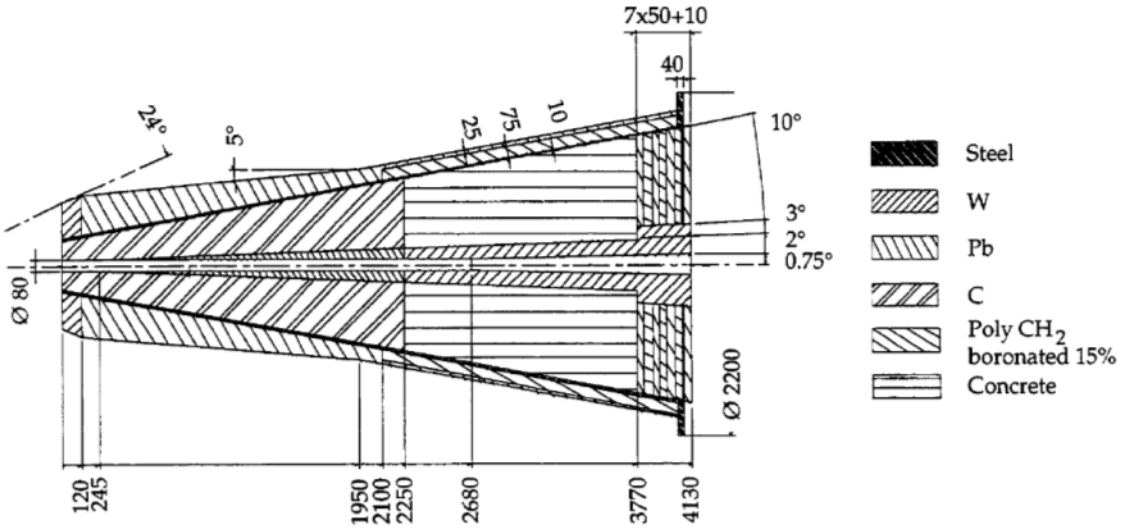

Figure 21: The Front absorber. Figure taken from [ALI00].

c) Iron Wall

The Muon Trigger chambers (see section 4) need further protection and therefore a 1.2 m thick iron wall is situated between the tracking and trigger chambers. This muon filter has dimensions of 5.6 m x 5.6 m x 1.2 m and reduces further the hadronic background on the Muon Trigger chambers.

2. Dipole Magnet

Charged particles are deflected when they pass through a magnetic field. Through measuring their curvature, the momentum and charge of the particles can be determined. The dipole magnet (Figure 22) is therefore an essential part of the Muon Spectrometer. It consists of resistive coils in a horseshoe shape and weighs 900 tons. It sits 7 m from the interaction vertex, is 9 m in height and has an acceptance in the polar angle of $171° < \theta < 178°$. The dipole magnet creates an axial magnetic field of up to 0.7 T and the field integral from the interaction point to the iron wall is 3 Tm.

3. The Muon Tracker

The Muon Tracking system [ALI99, ALI00] consists of five stations (see Figure 19 and Figure 20), with two planes of Cathode Pad Chambers (CPC) each, giving a total of 10 detection planes. Stations 1 and 2 are situated in front of the dipole magnet, Station 3 inside the dipole magnet and Stations 4 and 5 behind the magnet. The sizes of these stations range between a few square meters for Station 1 to more than 30 m^2 for Station 5.

Each chamber is made out of two planes (bending and non-bending) of cathode pads separated by 5 mm and a wire anode plane in between (Figure 23). The bending plane is the plane containing the horizontal read-out strips, which measure the bending deviation (in y-direction) due to the magnetic field of the dipole magnet. The non-bending plane is the plane with the vertical strips which measures the non-bending direction (x-direction). A potential difference of about 1650 V is applied over the planes creating an electric field in the active volume which is filled with an Ar/CO_2 (80%/20%) gas mixture. The gas mixture is ionized when a charged particle passes through the detector. The created electrons are driven to the anode wires by the electric field. An avalanche is

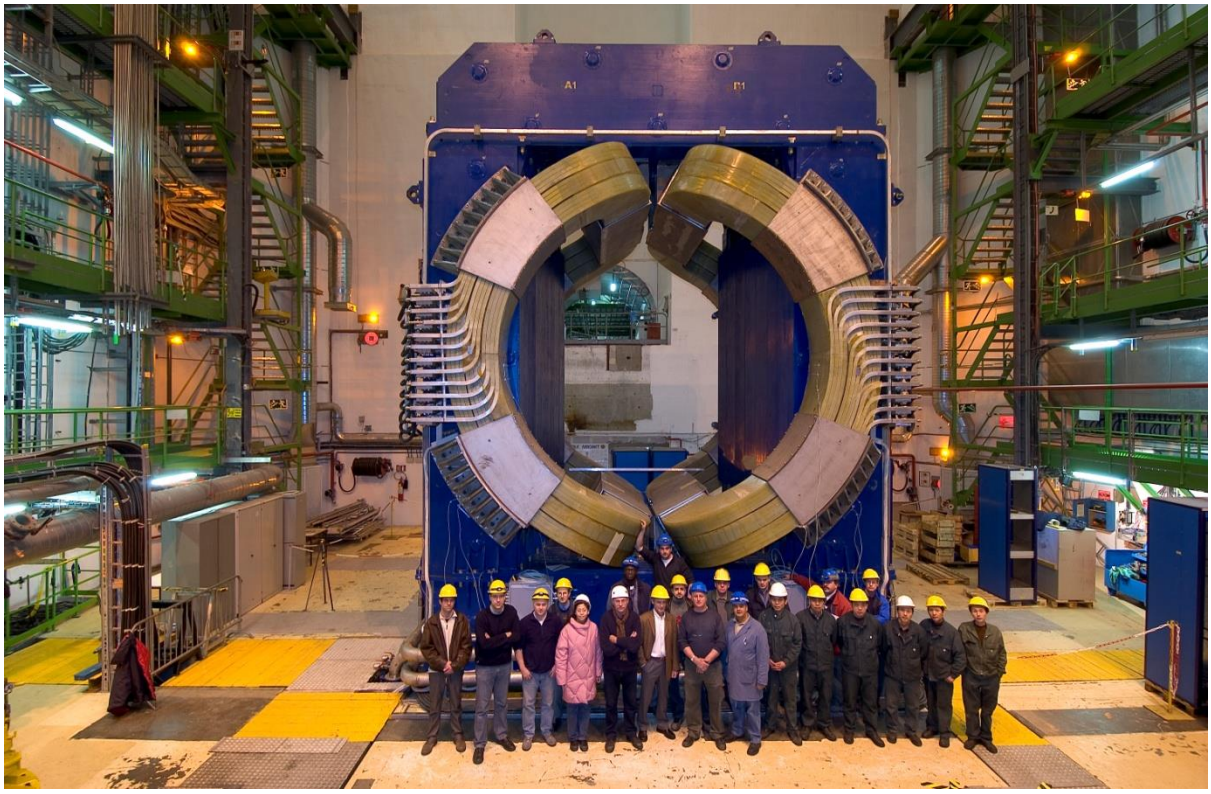

Figure 22: The Dipole magnet. Figure taken from [CER04].

created near the anode wires due to the higher electric field in this region. The sizes of the cathode pads corresponding to the bending plane are smaller than the pads of the non-bending plane.

Stations 1 and 2 are of quadrant type (Figure 24) and cover a small area affected by a high density particle flux. Stations 3, 4 and 5 are not exposed to a high density particle flux and are of the slat type (Figure 25). The slats are overlapped to avoid dead zones in the detector. These quadrants and slats are referred to as the detection elements (DEs) of the Muon Tracker. A summary of the half chamber modules and detection elements is given in Table 1. These are the moveable parts of the Muon Spectrometer.

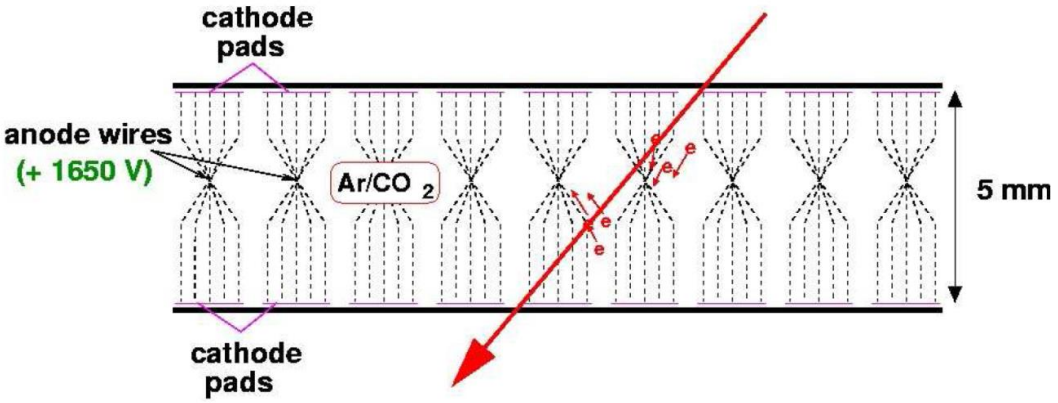

Figure 23: Cathode Pad Chamber layout. Figure taken from [CdV07].

The front-end electronics (FEE) of the tracking chambers consists of MANAS Numérique (MANU) cards, each with 4 Multiplexed ANAlogic Signal (MANAS) processor chips and 1 Muon Arm Readout Chip (MARC) chip. The Protocol for the ALICE Tracking CHamber (PATCH) buses is the connection between the MANU and Concentrator Read Out Cluster Unit System (CROCUS) crates, which in turn transmit the signal to the DAQ (Data Acquisition) for recording and monitoring. The TCI (Trigger Crocus Interface) cards give the trigger signal to the CROCUS crates for the readout of the tracking chambers.

Table 1: Summary of the number of modules (half chambers) and detection elements (quadrants and slats) in the Muon Tracker.

Station	Modules (Half-chambers)	Detection Elements
Station 1	2	4 Quadrants × 2
Station 2	2	4 Quadrants × 2
Station 3	4	18 Slats × 2
Station 4	4	18 Slats × 2
Station 5	4	18 Slats × 2
Total:	16	156

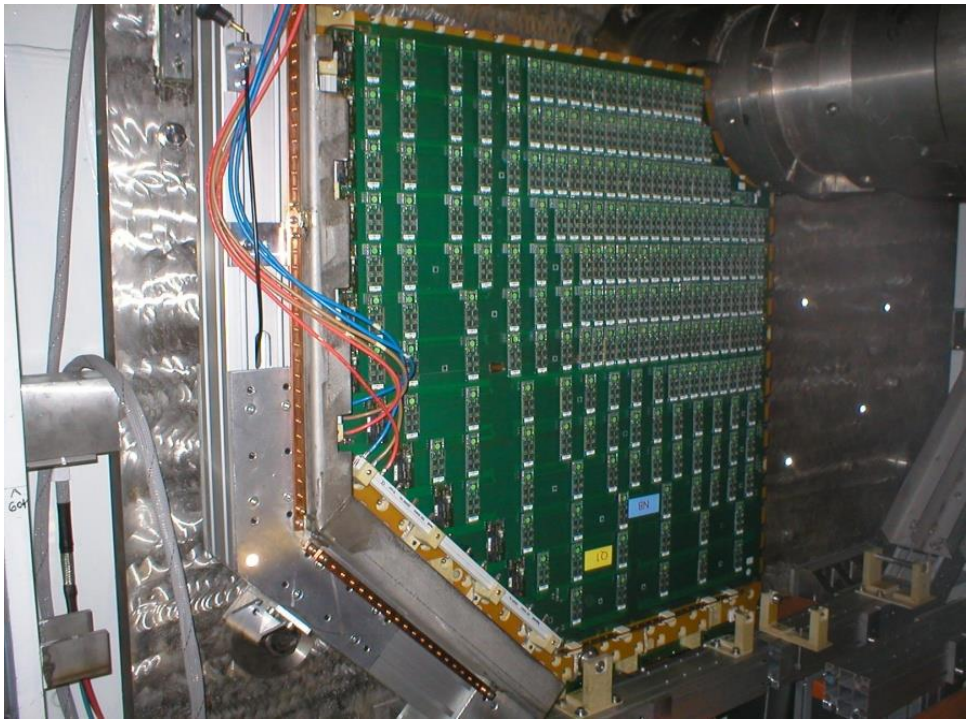

Figure 24: Tracking chamber quadrant. Figure taken from [CDS07].

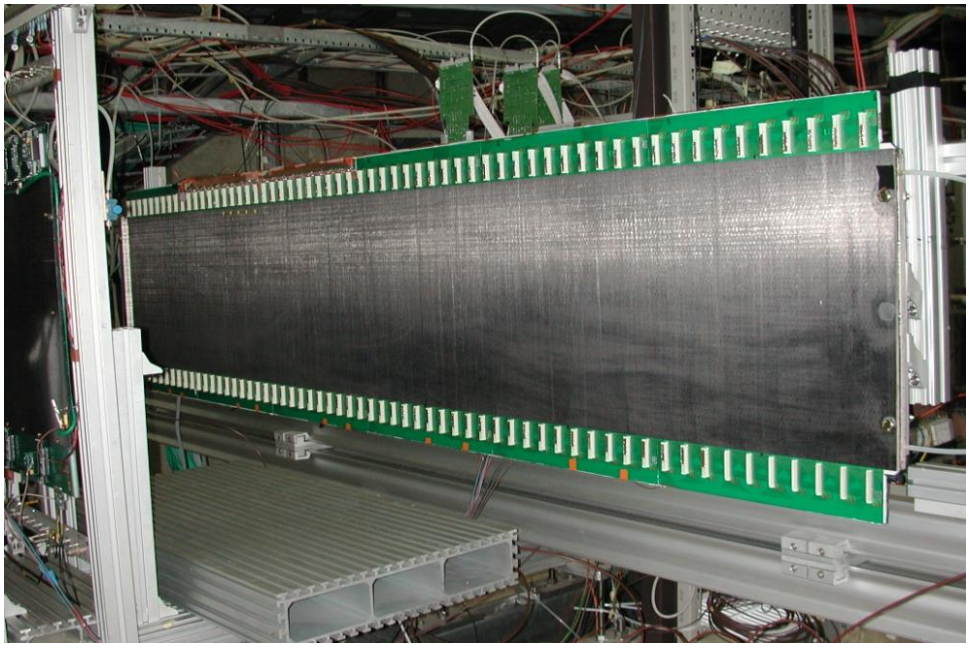

Figure 25: Tracking chamber slat. Figure taken from [CDS02].

4. The Muon Trigger

The Muon Trigger Chambers [ALI99, ALI00] consists of two stations (see Figure 19), with two planes of 18 single-gap Resistive Plate Chambers (RPC) each (Figure 26). They are situated behind the muon filter wall at 16 m and 17 m from the interaction point. The size of each plane is 6 x 6 m^2.

Each RPC is made of two low-resistive backelite electrodes, separated by 2 mm of gas, two graphite films under high voltage and readout strip planes in the x and y directions. The gas is a mixture of Ar, $C_2H_2F_4$, i-butane and SF_6. The chamber response is fast with a signal rise time of approximately 2 ns and a time resolution in the order of 1-2 ns.

The trigger system [ALI99, ALI00, ALI03] is able to identify single muon and dimuon tracks for a certain p_T cut. The first requirement for a track to trigger is that it has to be detected in at least three out of four of the trigger chamber planes. The local trigger algorithm then performs operations separately on both the bending and non-bending plane. The p_T of the track is found by measuring its deflection (see Figure 27).

Tracks with infinite p_T would show no deviation and therefore a larger deviation in the y-direction indicates a lower p_T for the track.The correspondence between the particle's deflection in the bending plane and its p_T has been determined and tabulated in the Look-Up Tables (LUT). The p_T cut is applied firstly by fast specialized circuits and then secondly by fast processors which apply a more precise cut. If the p_T-value is above the required cut, the trigger is activated. The charge of the track can also be determined by the trigger system by measuring the bending direction. This makes it possible to determine if the tracks are positive or negative single muon tracks, or like and unlike sign dimuons.

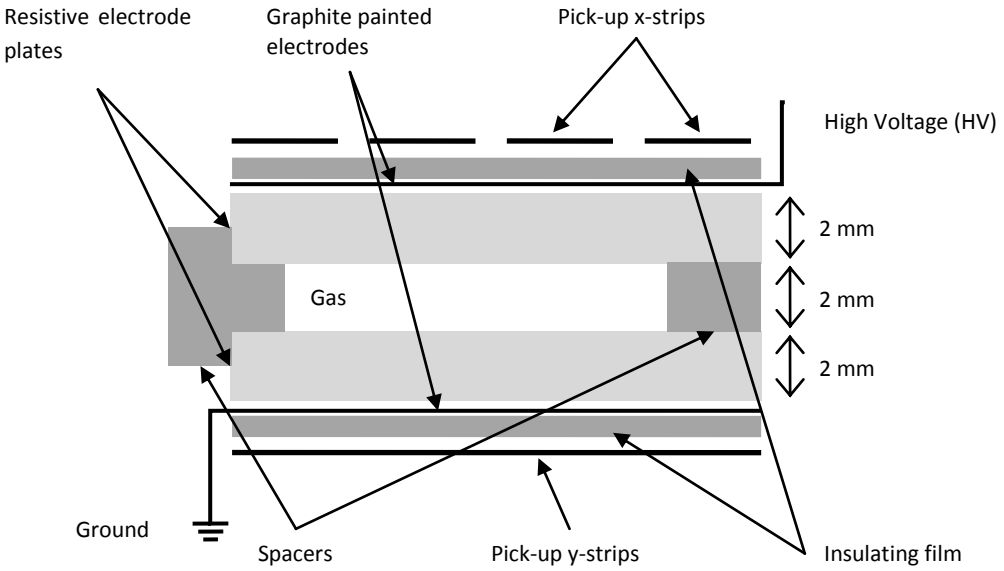

Figure 26: Resistive Plate Chamber (RPC).

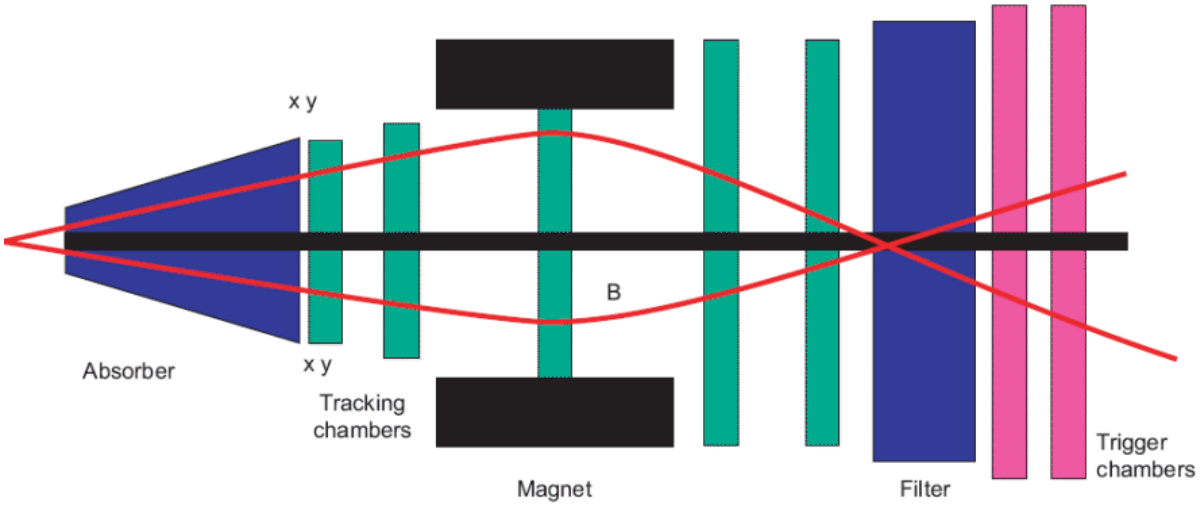

Figure 27: The trigger principle for the Muon Trigger chambers. Tracks with infinite p_T would show no deviation. Therefore a larger deviation in the y-direction indicates a lower p_T for the track. Figure taken from [ALI08]

There are thus six possible trigger types of which five can be sent to the Central Trigger Processor (CTP) (see section D.1) at a time during data taking: single muon tracks with low or high p_T , as well as like and unlike sign muon pairs with low or high p_T. This is summarized in Table 2.

Table 2: Triggers available for the Muon Trigger system.

	Single	Unlike	Like
Low p_T	MSL	MUL	MLL
High p_T	MSH	MUH	MLH

5. Alignment of the Muon Spectrometer

In order to track the particles crossing the Muon Spectrometer accurately it is essential that the positions of the chambers and their elements are known precisely [Sto08b]. There are two methods that can be used in order to align the Muon Spectrometer to the correct position during the installation phase. The first method is to make a photogrammetric measurement of the detection elements. This gives the relative position of the elements in an arbitrary coordinate system. It is performed in the maintenance position. The in-plane adjustment system of each element is used to correct its relative position.

The second method is a theodolite measurement which is performed both in the maintenance and acquisition position and gives the correct position of the chambers in the ALICE correlated coordinate system. The in-plane adjustment system of the half plane is used to correct the position, and thus the position of the chambers.

But when switching on the magnets the initial positioning will be disturbed due to the magnetic forces and thermal expansion of the chambers and their supports. The Geometry Monitoring System (GMS) [TG+05], illustrated in Figure 28 below, is used to measure the deformations and the relative displacements of the rigid modules of the tracking system. The GMS is an array of 460 optical

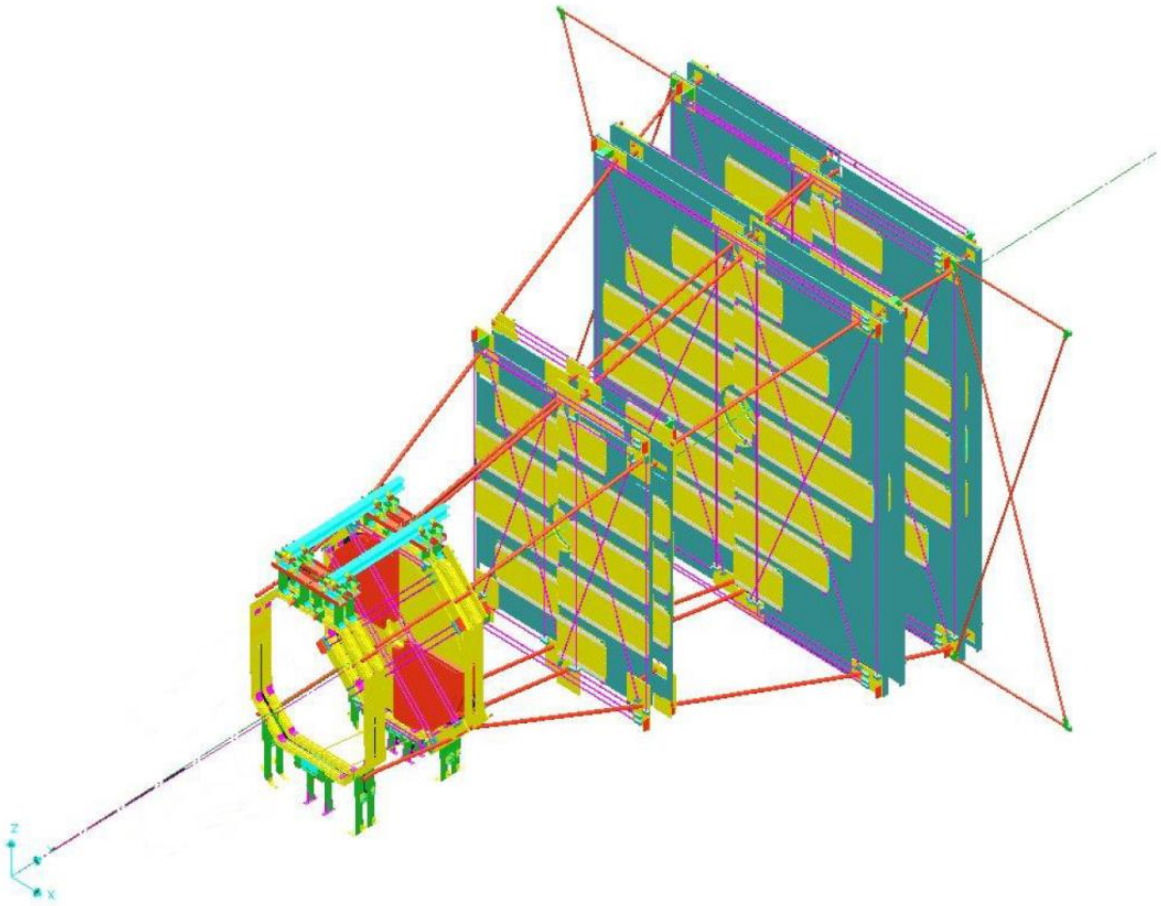

Figure 28: The Geometry Monitoring System (GMS). The red lines are optical lines. Figure taken from [TG+05].

sensors located on platforms at each corner of the tracking chambers onto which an optical image is projected. By analysing this image the displacement can be measured and corrected.

The alignment of the tracking chambers is carried out using the MILLEPEDE package [BK02]. MILLEPEDE is able to accurately determine the vast number of alignment parameters by applying a linear least squares fit to a sample of tracks collected with no magnetic field in the dipole or solenoid magnet.

6. Acceptance and efficiency: effect of alignment

In order to study the properties of the QGP the Muon Spectrometer must be able to trigger, track and identify muons. The Muon Spectrometer is capable of measuring single muons and dimuons, thereby determining the production of heavy flavour via the muonic decay channel, giving information on the formation and characteristics of the QGP. Also for determining the production of the $W^{\pm}$ bosons it is required that the Muon Spectrometer must be able to make accurate measurements in the high-p_T region.

To make these measurements it is necessary to take into account the acceptance (A) and efficiency (ε) of the detector. The observed distributions are the cross sections folded with the detector acceptance and efficiency [Sto08a]:

$$\frac{d^2N}{dp_T dy} = \frac{d^2\sigma}{dp_T dy} \times \mathcal{L}t \times A \times \varepsilon \qquad \text{(III—1)}$$

where $\mathcal{L}t$ is the integrated luminosity. This equation is similar to Equation I—5, p. 7.

The acceptance and efficiency ($A \times \varepsilon$) have to be determined either from data or simulation which model the detector response and therefore requires that information on the detector response during data taking is accurately known. The global efficiency of the Muon Spectrometer is influenced by a number of factors, including the intrinsic efficiency of its Tracking and Trigger Chambers and the efficiency of the tracking and triggering algorithms.

To determine the tracking efficiency the status of each electronic channel and the residual misalignment of the chambers and detection elements (DEs) have to be taken into account. This can be done by running a simulation using the same conditions for reconstruction as were the case during data taking. The change in the tracking efficiency from run to run can be controlled by using the same number of events in the simulation run as the number of events that occurred in the same run during data taking. Thereby the response of the channels is weighted as a function of time [A+12a]. For example in 2010 the typical tracking efficiency was usually around 93 % [A+12a]. The trigger efficiency was determined directly from data and the typical values were around 96 % [A+11, Sto08a]. These efficiencies were used in the simulations to give a realistic description of the detector response.

The ratio between the number of reconstructed events over the number of generated events in the simulation then gives the product $A \times \varepsilon$. For instance, in the case of heavy flavour decay muon production at forward rapidity in pp at $\sqrt{s_{NN}}$ = 7 TeV during 2010 the average value of the global $A \times \varepsilon$ was close to 90 % [A+12a]. However for 2011 data taking the tracking efficiency changed due

to changes in the detector elements (DEs). Chapter IV.C.1 will give more details on the efficiencies during the 2011 Pb-Pb period

In this present study the interest is in the role the alignment (or misalignment) of the Muon Spectrometer plays in the efficiency (inefficiency) in the high-p_T region where single muons from $W^{\pm}$ boson decays are measured. Any misalignment of the detection elements could result in the incorrect determination of the particle p_T and consequently affect the trigger decision. This means there is a possible systematic error in the particle p_T and the trigger selection. Therefore it is important to understand the effects of the alignment of the chambers and DEs on the efficiency in order to do an accurate analysis and account for all the necessary corrections to the results.

For that reason, before it is possible to do a complete study of the $W^{\pm}$ boson, the effect of the alignment of the chambers and DEs of the Muon Spectrometer has to be determined.

D. ALICE Online Data Taking

ALICE studies a variety of physics observables under different beam conditions. The task of the ALICE trigger, Data Acquisition (DAQ) and High Level Trigger (HLT) [2] systems is to select physics events of interest, provide efficient access to these events for the execution of high-level trigger algorithms and archive the data to permanent storage for later analysis.

1. Central Trigger Processor (CTP)

The ALICE Central Trigger Processor (CTP) [ALI03] is designed to choose events which fulfil a selection of different characteristics. This selection needs to occur at rates which can be scaled down to suit physics requirements and the restrictions imposed by the bandwidth of the Data Acquisition (DAQ) system and the High Level Trigger (HLT). The trigger needs to be able to make optimum use of the subdetectors, which are busy for different periods, and to perform trigger selections in different running modes, either pp, Pb-Pb, p-Pb or Pb-p.

Trigger detectors such as the Muon Trigger send a signal to the CTP when an event occurs. These signals are called trigger inputs. The CTP then sends a signal, called a trigger signal, to the readout detectors via Local Trigger Units (LTU) which act as the interfaces between the CTP and the readout detectors. The ALICE trigger is a 3-level trigger system and therefore there can be three consecutive trigger inputs – two fast level trigger inputs, Level 0 (L0) and Level 1 (L1) followed by the final level, Level 2 (L2), and also three trigger signals – L0, L1 and L2a (accepted) or L2r (rejected) message. Trigger detectors could also be readout detectors [TCWG13].

There can also different trigger classes, where combinations of trigger and readout detectors are grouped together depending on the physics of interest [Ant08].

2. Data Acquisition (DAQ) and High Level Trigger (HLT)

The data acquisition (DAQ) architecture [ALI03] is illustrated in Figure 29. The detectors receive the trigger signals and associated information from the CTP through a dedicated LTU interfaced to a Timing, Trigger and Control (TTC) system. The frontend readout electronics (FERO) of the detectors are interfaced to the ALICE Detector Data Links (DDL). Event fragments produced by the detectors are injected on the DDLs.

The DAQ Read-Out Receiver Cards (D-RORC) are hosted by the Local Data Concentrators (LDCs). In the LDCs the event fragments are logically assembled into sub-events. The LDCs can take data isolated from the global system for a test or calibration run or it can ship the sub-events to the Global Data Collectors (GDCs), where the whole events are built. The D-RORCs have two DDL channels which can either both be used as input from the detector or one can be used as input and the other one as output to the H-RORC of the High Level Trigger (HLT) [ALI03]. In the latter case data is copied to the HLT for software triggering or data compression by the Front End Processors (FEP).

The event building network is a standard communication network which supports the TCP/IP protocol. This network is also used to distribute the HLT decisions from the HLT LDCs to the detector LDCs where the decision to accept or reject sub-events are applied. The HLT can run in three different modes: Mode A where the HLT makes no decision, Mode B where the HLT makes a decision but it is not applied and Mode C where the decision is applied. In order to avoid busy machines slowing down the system the event distribution manager (EDM) checks the occupancy of the GDCs and tells the LDCs to dispatch events to the machines that are not crowded.

After the GDCs collect these sub-events and assemble these into whole events they record the events to the Transient Data Storage (TDS) at the experimental area. The data files on the TDS are migrated to the Permanent Data Storage (PDS) at the computing centre by the TDS Managers (TDSM).

Other services needed by the DAQ system, such as control of the database, are performed by the DAQ Services Servers (DSS). The Detector Algorithms (DA) and Data Quality Monitoring (DQM) are also run by additional servers which are connected to the event building network.

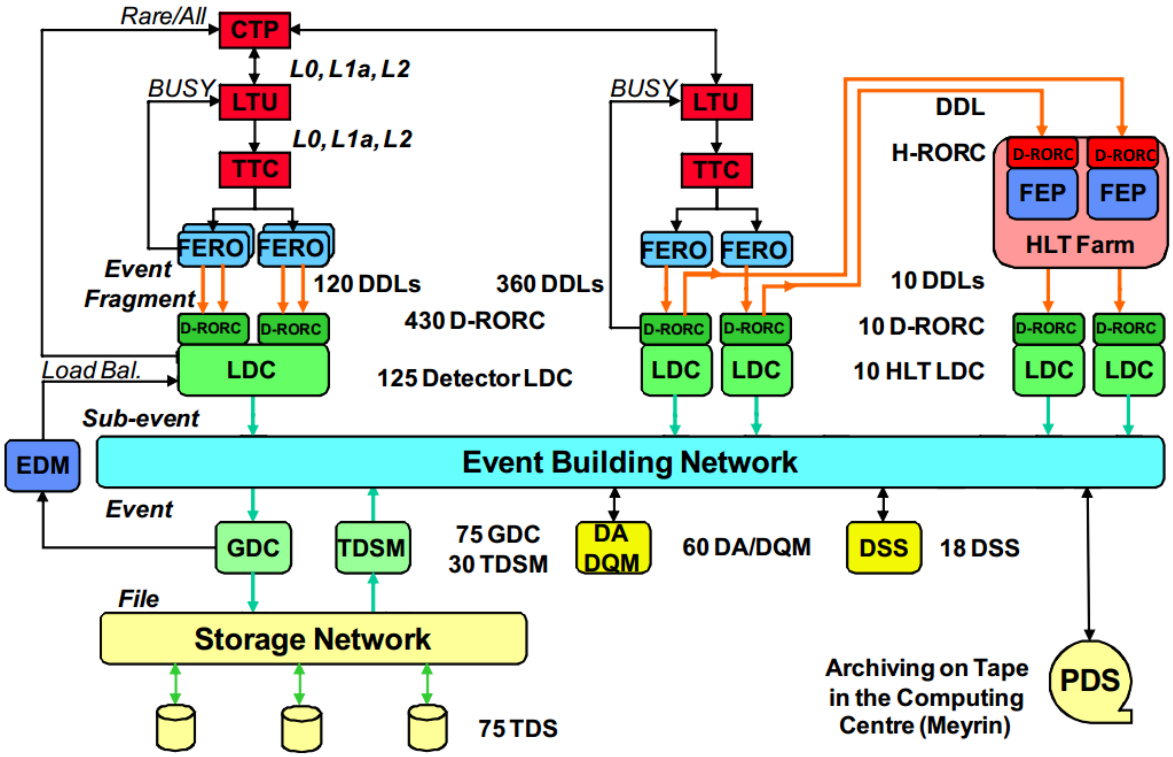

Figure 29: The Data Acquisition (DAQ) architecture. Figure from [ALI10]

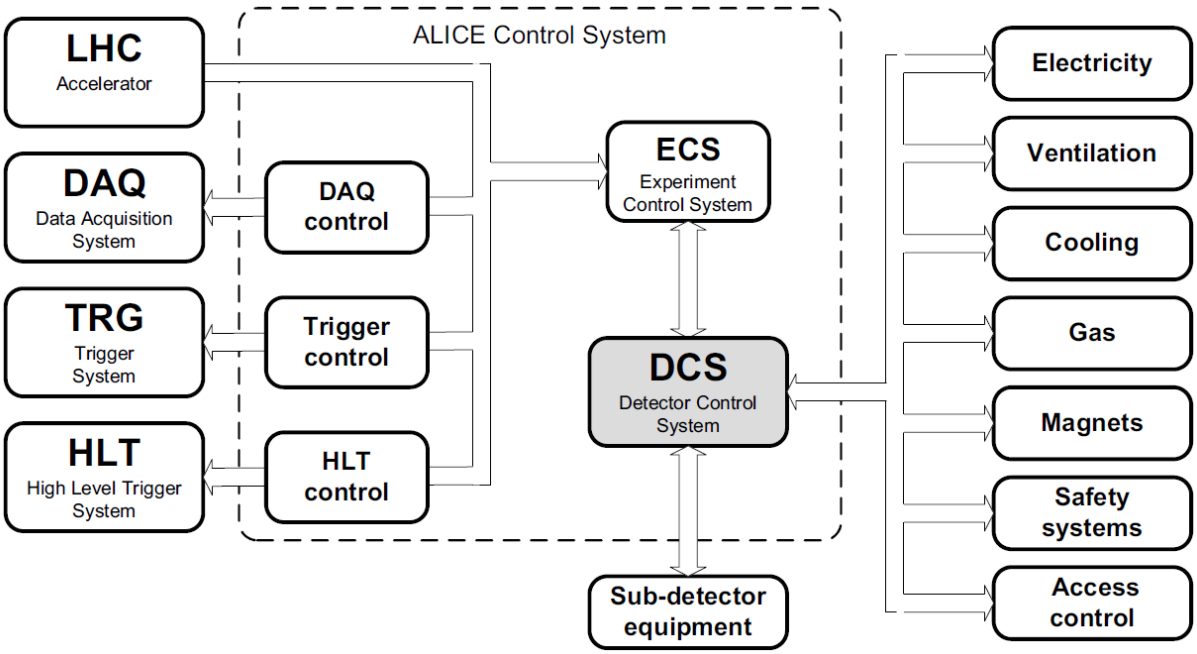

Figure 30: The ALICE Control System context. Picture from [ALI03]

3. Detector Control

The ALICE Detector Control System (DCS) [ALI03] is designed to assure a high running efficiency by reducing downtime to a minimum. It maximizes the number of readout channels operational at any time, and measures and stores all parameters necessary for efficient analysis of the physics data. The control and monitoring is provided in such a way that the whole experiment can be operated from the ALICE Control Room (ACR).

Figure 30 shows that the ALICE Control System [ALI03] includes all control activities in the ALICE experiment. The Experimental Control System (ECS) is responsible for the synchronization between the various systems. The DCS is the interface between the ALICE Control System, the various services (e.g. cooling, gas, magnets, etc.) and the individual detectors.

The ECS is responsible for the “partitioning” of the experiment, whereby a part of the experiment can be operated separately from the rest of the experiment. This is achieved by implementing Finite State Machines (FSMs) [ALI03] which are used by all the other systems interacting with the ECS. A FSM is an intuitive, generic mechanism which models the functionality of equipment or a sub-system.

The Muon Tracker component of the Detector Control System (MCH_DCS) is used to make changes to the FSM of the Muon Tracker, i.e. to include or exclude parts of the detector, and to change the state of the detector. There are four main states [Sui09]:

- In STANDBY the High Voltages (HV) and Low Voltages (LV) are switched off. The HV are used for powering the CPC of the Trigger Chambers, and the LV powers the FEE and the CROCUS.
- In STANDBY_CONFIGURED the LV are switched on, i.e. the FEE and the CROCUS and the HV are also switched on at a value of ~600 V in order to be able to quickly move into BEAM_TUNING.

- In BEAM_TUNING the LV are on and the HV are at an intermediate value where there is no gain due to particles crossing the detector (~1200 V). This mode is used for pedestal and electronic calibration runs. In these runs the pedestals are measured and the thresholds computed in order to correct for the gain dispersion and noise, so that the impact points can be accurately determined [Cha08].
- In READY the LV are on and the HV are at their full value (~1600 V) – this is the mode in which the detector needs to be ready for physics runs and for data taking.

The commands issued by the operator to change the state of the detector from the Detector Control Agent (DCA) are simply GO_STBY_CONFIGURED, GO_BEAM TUNING, GO_READY and GO_STANDBY (Figure 31).

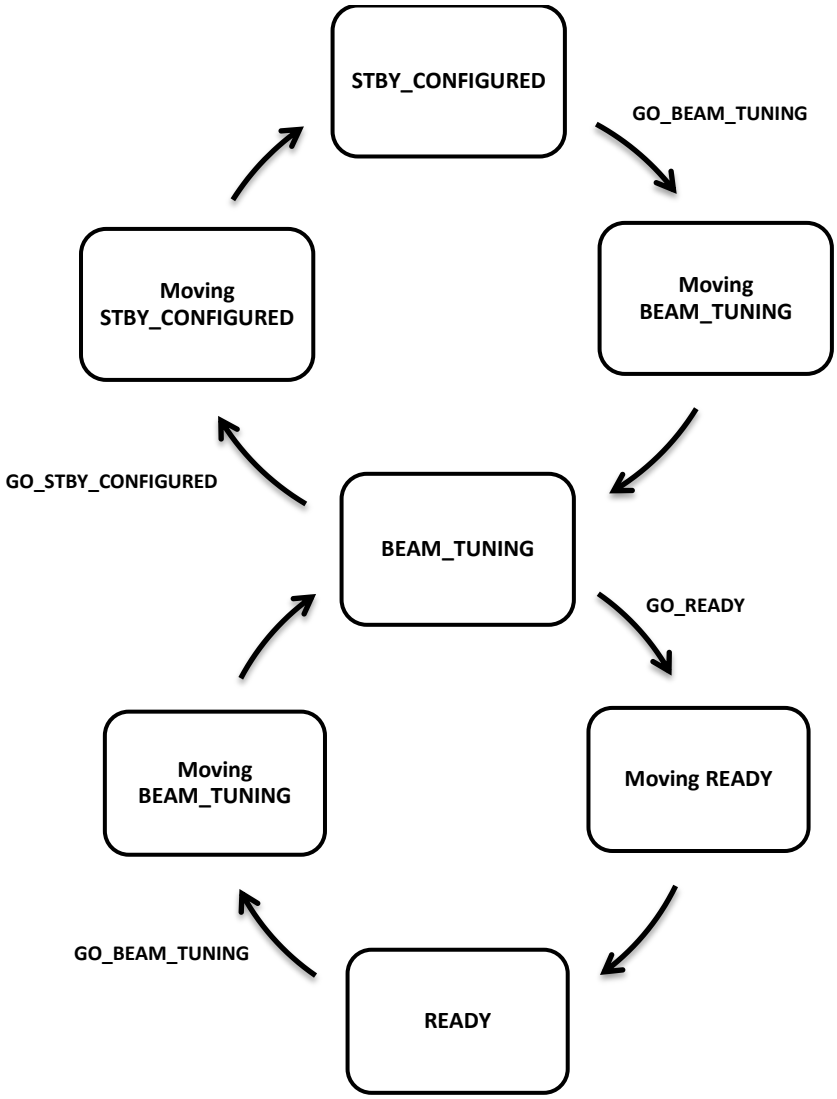

Figure 31: Representation of three of the four states of the Muon Tracker (MCH) and commands of the Detector Control Agent (DCA).

4. ALICE and the LHC: LHC beam modes, Handshakes and Filling Schemes

The LHC has two general modes: the accelerator mode and the beam mode [LHC11a]. The accelerator mode provides an overview of the machine activity (e.g. proton or ion physics,

shutdown, etc.) and the beam mode provides the state of the machine with regard to the machine cycle (e.g. injection, ramp, etc.) Only the modes related to proton and ion physics which are important during ALICE data taking will be described below.

The LHC is in the BEAM SETUP accelerator mode when the machine is being setup with one or two beams. The beam modes during this accelerator mode are described in Table 3 and some are also shown in Figure 32:

Table 3: Some of the Beam modes of the LHC relevant to ALICE. Table adapted from [LHC11a].

Beam mode	Description
SETUP	Possibly beam in transfer lines with transfer line dumps in. Includes pre-injection plateau and injection plateau - no beam in ring.
CYCLING	Pre-cycle before injection following access, recovery, etc. The objective of this mode is to reset the magnetic history of the machine and prepare the machine for a new cycle.
INJECTION PROBE BEAM	If either ring 1 or ring 2 will be injected with or have safe beam circulating. In this mode a number of checks will be done for the different accelerator sub-systems before injecting higher intensities. The aim will be to establish a circulating safe beam with a given lifetime.
INJECTION SETUP BEAM	During the INJECTION PROBE BEAM we will be able to make measurements with very limited precision. In order to make more precise measurements before filling for physics, a SETUP BEAM will be used. This beam will be wholly representative of the physics beam to follow, just with fewer bunches to stay below the damage threshold
INJECTION PHYSICS BEAM	At this stage the machine has been optimized. It proved to be able to have circulating beam with appropriate lifetime and it is ready to accept higher intensities needed for physics. Within this mode, prior to high intensity beam injection, a pilot beam will be injected since the accelerator will be empty when this mode is reached.
PREPARE RAMP	Injection from SPS complete, preparing for ramp of the beam energy which is at an energy of 450 GeV per beam.
RAMP	Ready to ramp or ramping or immediate post ramp.
FLAT TOP	Ramp finished: beam is at required energy - pre-squeeze checks.
SQUEEZE	Preparing for or squeezing of the beams: Beams are focussed by adjusting the emittance and β^* is brought to the required value (1 m) to ensure collisions, thereby raising the intensity of the beam.
ADJUST	Preparing for collisions or adjusting beams after the squeeze. Possible to enter this mode from STABLE BEAMS. Possible to enter this mode at the end of STABLE BEAMS without the intention of going back into physics.
STABLE BEAMS	Stable conditions with collisions in the experiments, backgrounds and life time under control. Small adjustment of beam parameters permitted. In case of slow degradation all the experiments are warned and the ADJUST mode is entered when all the experiments have confirmed they are ready.
UNSTABLE BEAMS	Emergency mode entered from stable beams in case of sudden beam degradation. The UNSTABLE BEAMS mode may be entered without prior warning to the experiments. UNSTABLE BEAMS mode can be entered from ADJUST only if the accelerator mode is MD. This transition has been requested for Roman Pots calibration or special machine protection tests. In this case, a special key has to be turned in the control room of the experiment to disable, temporarily, the protection interlock, and has to be put back in position after the tests are finished.
BEAM DUMP	Requested or emergency dump. It will be verified that all the machine protection equipment performed correctly, together with the LBDS system via the XPOC analysis.
RAMP DOWN	Ramp down and cycling after programmed dump at end of physics fill.

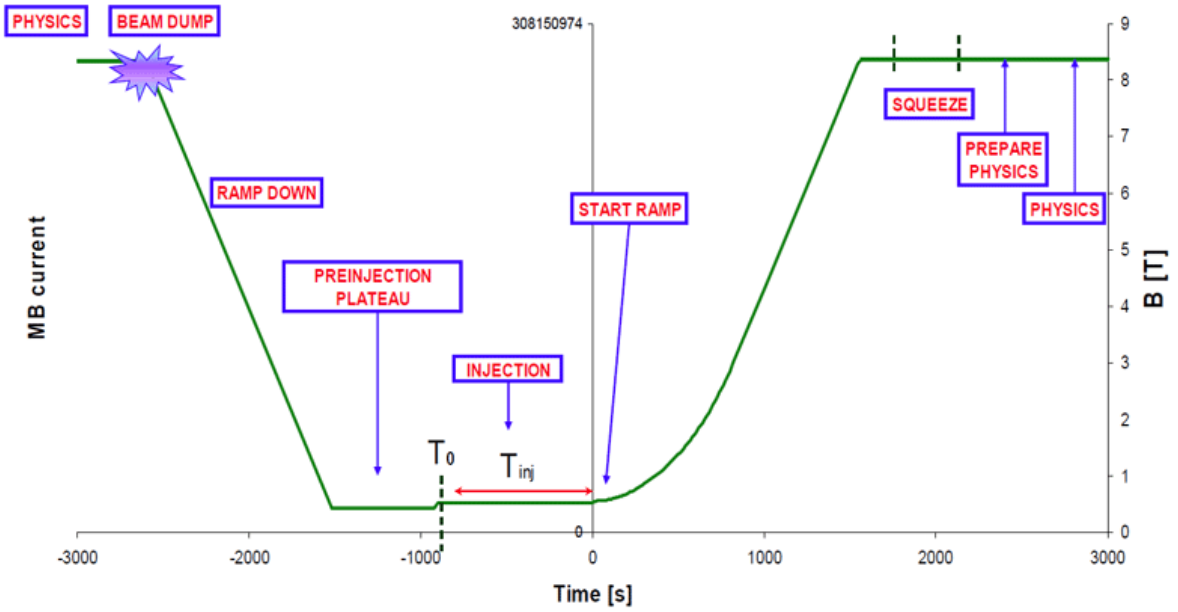

Figure 32: Magnetic field of the LHC during operation with some of the beam phases shown. When the magnets are ramped up the beam energy increases and when they are ramped down the beam energy decreases. Figure taken from [LHC12]

There is a Handshake protocol which is a communication protocol between the LHC and the LHC experiments [LHC11b]. This informs the experiments about critical actions to be performed during the INJECTION, ADJUST and BEAM DUMP PHASES and to get confirmation that the detectors are ready for action.

E.g. for the INJECTION and ADJUST PHASES the sequence of messages exchanged between the LHC and ALICE are the following in both cases:

1. The LHC sends the WARNING message to ALICE at least ten minutes before the phase starts.
2. ALICE replies PREPARE to indicate the message was received and all the sub-detectors are brought to SAFE mode.
3. ALICE replies READY as soon as the sub-detectors are ready to start the phase, i.e. ALICE is in Global SAFE.
4. When LHC gets the READY message from all the experiments, it sends the READY message to ALICE and changes to the appropriate beam mode and the next phase starts. This can either be the INJECTION PROBE BEAM or INJECT AND DUMP or CIRCULATE AND DUMP phases.
5. As soon as this phase is over the LHC sends the OK message to ALICE and the next beam mode is moved into. After INJECTION follows PREPARE RAMP and the machine will RAMP to FLAT TOP. This means that the beam energy is brought to the required value by “ramping up” the superconducting magnets of the LHC. FLAT TOP is followed by ADJUST where the path of the beam is adjusted to enable collisions and after ADJUST follows STABLE BEAMS in which collisions occur in ALICE according to a specific filling scheme and physics interest.
6. LHC then sends the final message, STANDBY.
7. ALICE replies with the VETO message which signals the end of the phase.

The sequence of messages is similar for the BEAM DUMP PHASE and the TRANSFER LINE SETUP.

The pedestal and calibration runs for the Muon Tracker are performed in between PREPARE RAMP and ADJUST. A pedestal run also needs to be performed the RAMP DOWN phases (see Figure 33). This can be done by the DCS shifter on request of the shift leader if the Data Quality Management (DQM) plots show any irregularities.

Depending on the interaction rate measured by the V0 a certain partition of detectors may be turned on and the right configuration needs to be chosen for the specific filling scheme. The shift leader (SL) has the responsibility to ensure that data taking is achieved efficiently, that all detectors join the global run in time and the configuration of the experiment is correct [ALIRC12]. Other duties include checking the event sizes and busy time, especially for the Muon Tracker and if needed ramping up or down the magnets. He or she must also insure that the target luminosity is reached. Furthermore it is crucial that the ALICE clock (local time) is in sync with the LHC (beam time).

DAQ and DCS are in charge of organizing the subdetectors and ensuring through time sharing and avoiding time overlap that all physics goals are reached. The Muon Tracker (MCH) could sometimes have HV trips. These cause high busy time and event sizes which lead to the run being stopped. Therefore it is important for the MCH shifter to exclude channels which are prone to trip from the FSM and to keep an eye on the busy time during his shift. If there are LV of HV trips during a run, this will cause high busy time, resulting in the shift leader having to stop and restart the run. If this does not solve the problem the MCH may be removed from the run all together.

To summarize the procedure that must be followed at ALICE during PHYSICS runs we give an example of the order of the LHC beam modes and some of the responsibilities of ALICE in Figure 33.

For every period there are different filling schemes [LPC12b] implemented by the LHC according to the requirements of the physics being studied at that time. The filling scheme names are given according to the following guidelines: <spacing>_<Nb>b_<IP1/5>_<IP2>_<IP8>_<code>.

- The <spacing> refers to the characteristic bunch spacing used with respect to time, e.g. 25 or 50 ns.
- <Nb> is the total number of bunches.
- <IP1/5>, <IP2> and <IP8> are the expected number of colliding bunch pairs in Interaction Point 1 or 5 (IP1/5), etc.
- The <code> is a suffix to encode variants of a filling scheme.

E.g. the filling scheme name 200ns_358b_356_336_0_24bpi15inj_IONS tells us that the bunch spacing was 200 ns; each beam had a total number of 358 bunches, the expected number of colliding bunch pairs in IP1/5 were 356, in P2 it was 336 and in IP8 it was 0. The code tells us there were 24 bunches per injection (bpi), with 15 injections and this was for IONS (Pb-Pb) physics.

Depending on the physics requirements, different trigger classes are in use, e.g. Minimum Bias (MB), or RARE triggers, such as those of the Muon Trigger (described in Chapter III.C.4).

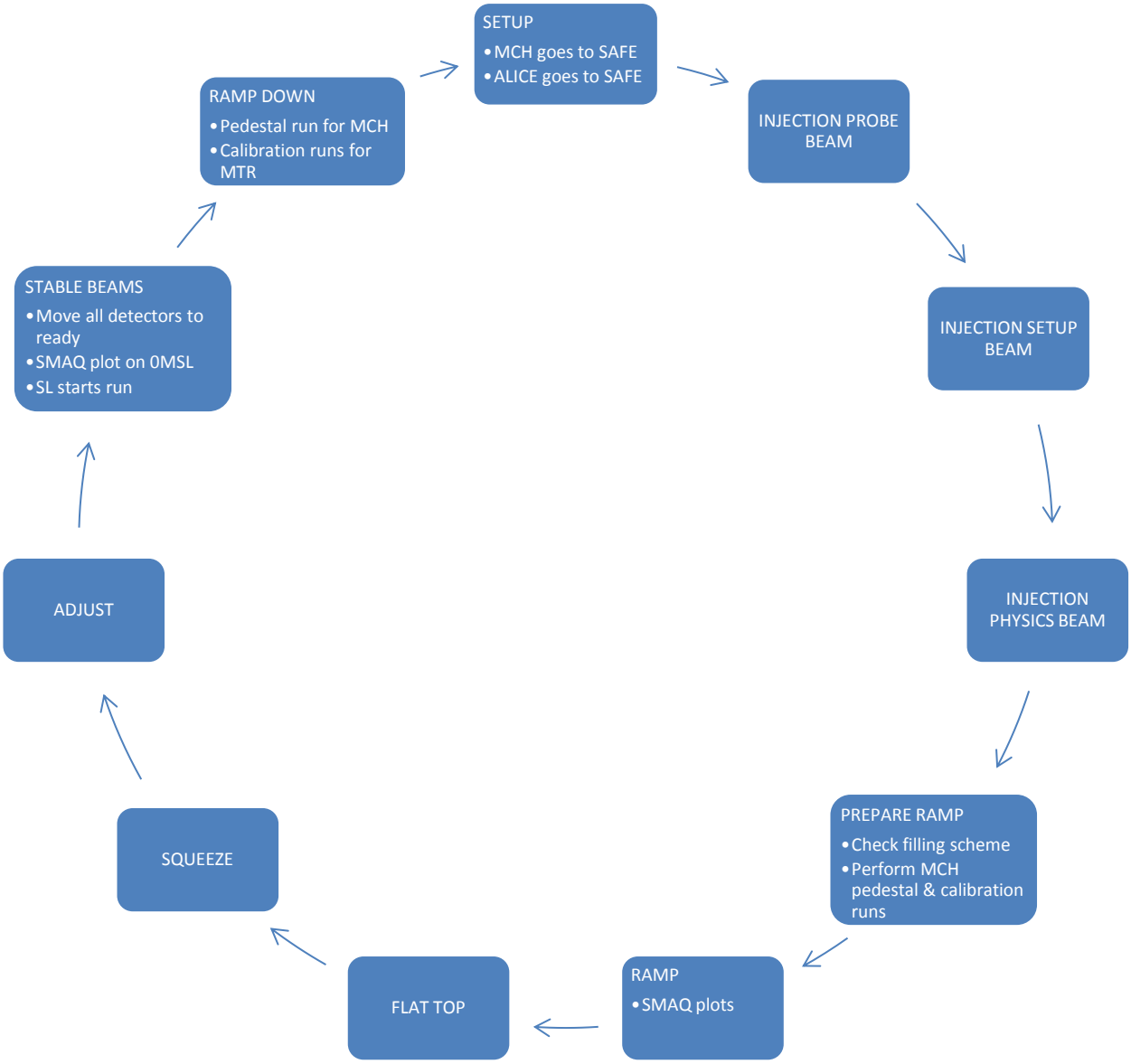

Figure 33: LHC Beam modes with some ALICE responsibilities

Chapter IV. Simulation and Analysis

This chapter is dedicated to the simulation and analysis in this study. The aim of this study is to see what the effect of the alignment of the chambers and detector elements (DEs) of the Muon Spectrometer will be on the measurement of the $W^{\pm}$ boson. Before the techniques used in the simulation and data analysis can be described it is necessary to first give an introduction on the AliROOT [ALI11a] offline framework used to simulate, reconstruct and analyse data in ALICE. Therefore section A will describe the AliROOT framework and how the simulation and analysis is accomplished. This is followed by section B which will give the details of the simulation sample used in the alignment study and the technique used to analyse it. Section C gives the information on the Pb-Pb data sample which was obtained during data taking in 2011 and describes the analysis technique used in the study of data reconstructed using different alignment information of the Muon Spectrometer.

A. AliROOT: Offline Framework

AliROOT [ALI11a] is the set of software tools used by the ALICE collaboration to process data. It is based on the Object Oriented programming language, C++ [C++13] and uses the ROOT [ROO13] framework developed at CERN. The objectives of the AliRoot framework are threefold. Firstly it provides the simulation of the primary hadronic collisions and the response of the ALICE detector. Secondly it reconstructs the raw physics data from simulated and real events and lastly it performs the analysis of the reconstructed data.

This is all done by applying the principles of reusability (it should be easy to use the same code in different modules and classes) and modularity (separating the functionality into independent and interchangeable modules). Figure 34 shows a schematic of all the components of AliROOT. These two principles minimize the amount of unused or rewritten user code, and maximize the participation of physicists. The STEER module is the core of the system and directs the run management and contains the general interface and base classes. The different detector groups can work at the same time on the system with minimum interference because their codes are independent from each other. An Object Oriented programming language which defines a class hierarchy is the natural choice to achieve this modular structure.

1. Simulation

Using Monte Carlo event generators, such as PYTHIA [S+06] and HIJING [GW94] hadronic collisions can be simulated. These generators are interfaced into AliROOT in a transparent way to the users. Transport packages like GEANT4 [A+03] and FLUKA [FSFR05] can then be chosen by the user to simulate the detector response. This is done simply by loading the preferred shared library without having to change the code.

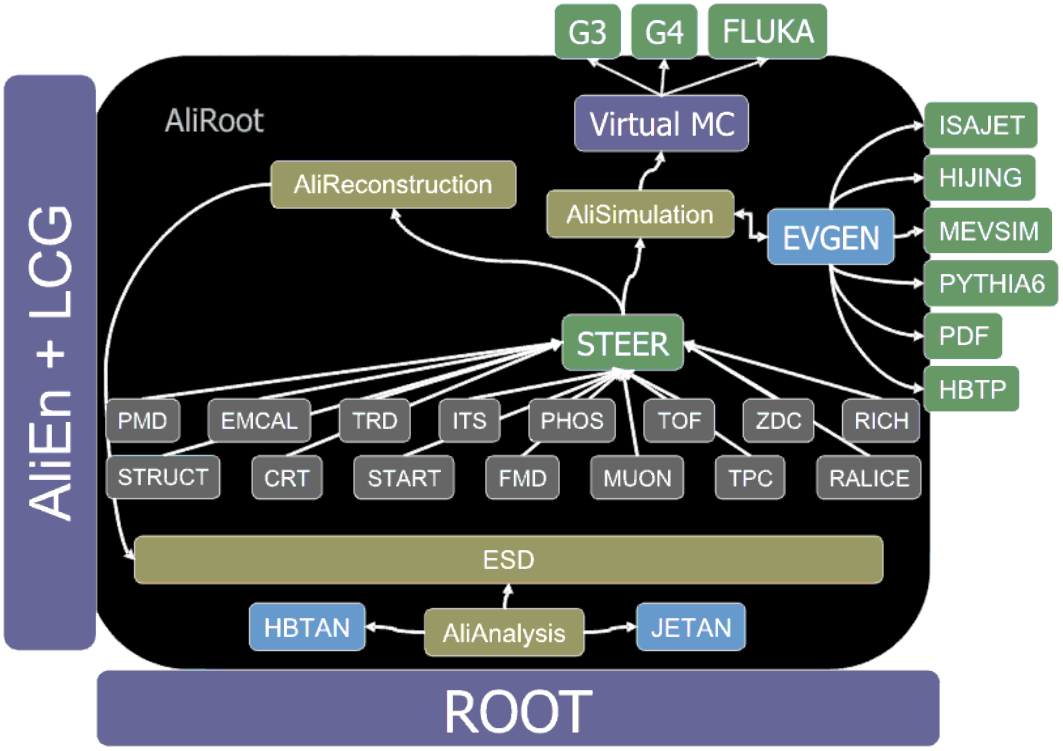

Figure 34: The AliROOT framework. Figure taken from [ALI11a]

The data processing framework is schematically shown in Figure 35. The left side shows the simulation phase and the right side the reconstruction phase. In the simulation phase Monte Carlo truth is broken down to reproduce the detector response, while in the reconstruction phase the raw data (either real or simulated) are reconstructed to retrieve the kinematics of the detected particles.

Event generators simulate the primary interactions, giving a kinematic tree. This tree contains all the produced Monte Carlo "particles" with their kinematic properties, such as momentum and energy. It also keeps track of the production history by storing the relationship (mother-daughter) between particles and their production vertexes. The transport package then carries each particle into the detectors, where its energy is deposited. The point where this "particle" loses its energy and the energy itself is what is referred to as a *hit*. These *hits* also contain the information on ("know") which particle generated them ("track labels").

In the next step the hits are broken down (disintegrated) into *digits* using the information about the specific detector response. The information on the parent track is lost and the spatial position is translated into the corresponding detector readout element, e.g. strips, pads, etc. There are two kinds of *digits*: either *"summable digits"* with close to zero-thresholds or *"digits"* with real thresholds. The *"summable digits"* can be summed when different events are superimposed (merged). Event merging is used to embed a signal event in a signal-free underlying event and this allows reuse of the underlying events in order to economize computing resources. "D*igits"* on the

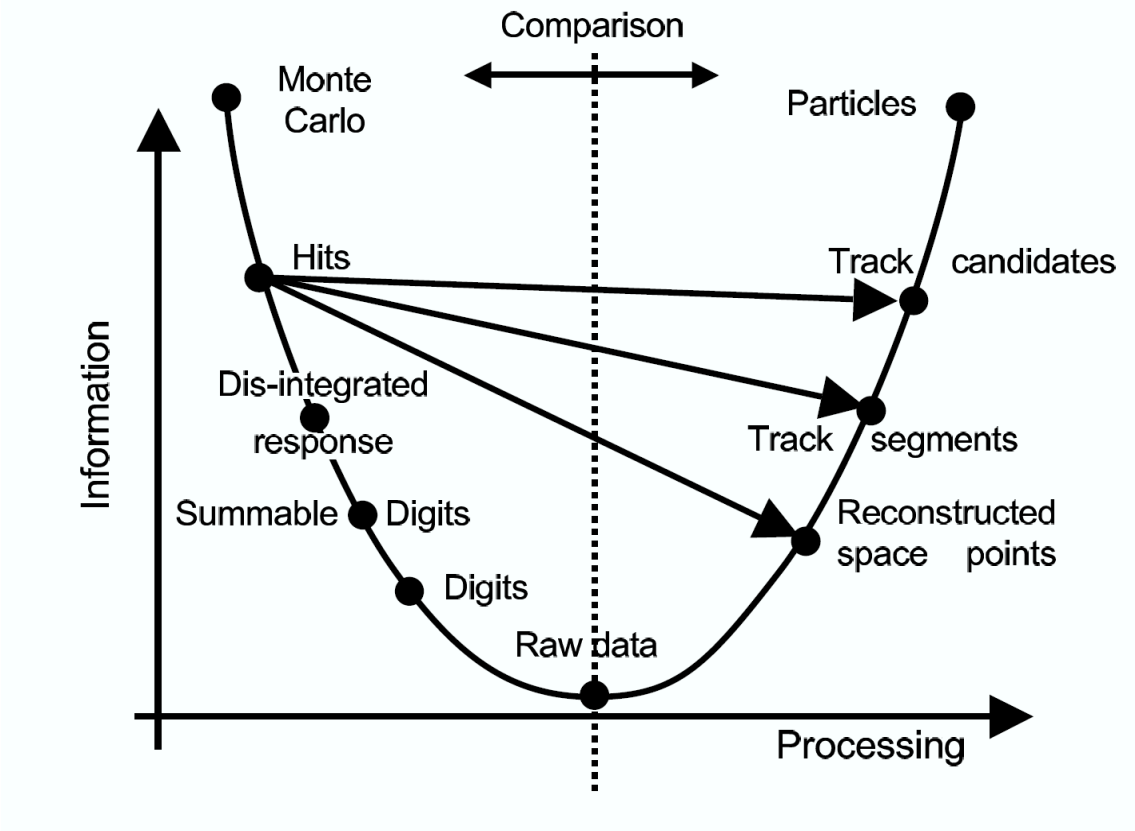

Figure 35: Schematic of the data processing in AliROOT. Figure taken from [ALI11a]

other hand are similar to what you would have in real data taking and can be used to estimate the expected data size. The "*digits*" are then converted into raw data. "*Digits*" and raw data differ in that *digits* still have the information on the Monte Carlo particle which generated it, while raw data do not; and digits are stored in ROOT classes, while raw data are stored in binary format. The simulation process is highlighted in Figure 36 which illustrates the different steps from Monte Carlo particle generation up to the creation of digits and raw data. It also shows the different responsibilities of the AliROOT modules.

The Virtual Monte Carlo (VMC) allows running different Monte Carlo simulations without having to change the user code. The VMC also provides the interface to construct the geometries of the detectors. Figure 37 shows a schematic representation of the VMC and how it fulfils these responsibilities by interfacing with the generators, different transport packages and detector geometries. The C++ macro used to configure the simulation is usually named Config.C. It creates and configures the Monte Carlo object, the generator object and the detector modules (Figure 37). Extracts from the Config.C files used in the simulation alignment study of this work are shown in the next section (Insert 1) and a complete configuration file can be found in the Appendix.

2. Reconstruction

The reconstruction chain can then start during which the raw data (real or simulated) are converted to track candidates and stored as Event Summary Data (ESD). This ROOT[8] file contains all the output of the reconstruction necessary for physics studies. These include fields necessary to identify the

[8] A ROOT file is a file in which ROOT stores information.

event, such as event number, run number, etc.; primary vertex information estimated by for instance the SPD; and arrays of tracks from the various detectors. The size of the ESD is roughly one order of magnitude smaller than the raw data. Figure 38 shows the reconstruction framework and indicates the processes from digits or raw data to ESD. The different components of AliROOT responsible for the reconstruction are also shown.

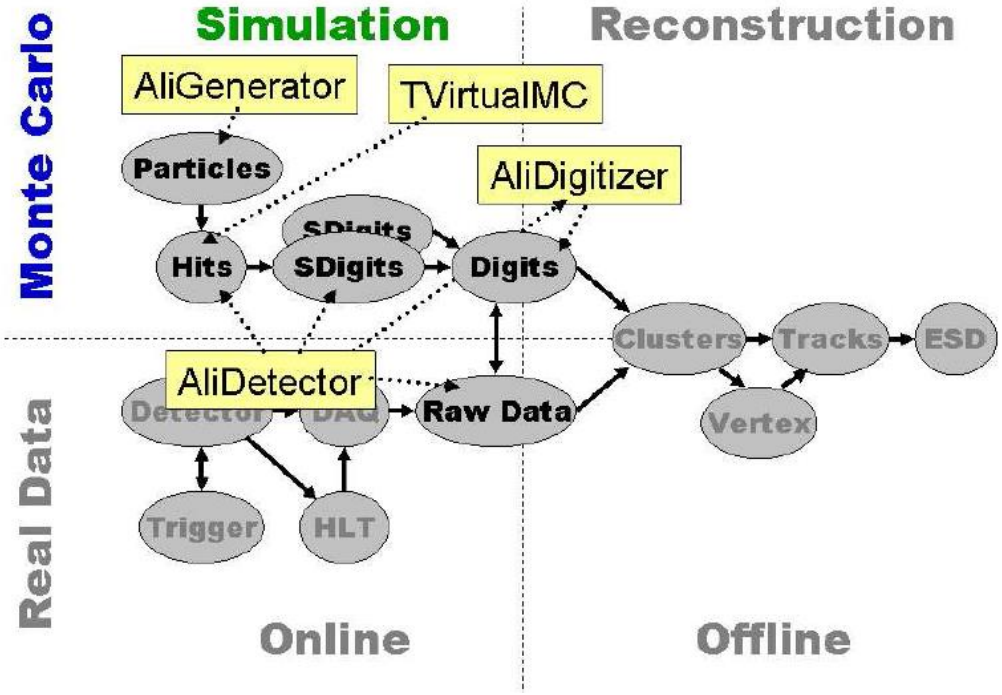

Figure 36: Simulation Framework. Figure from [ALI11a]

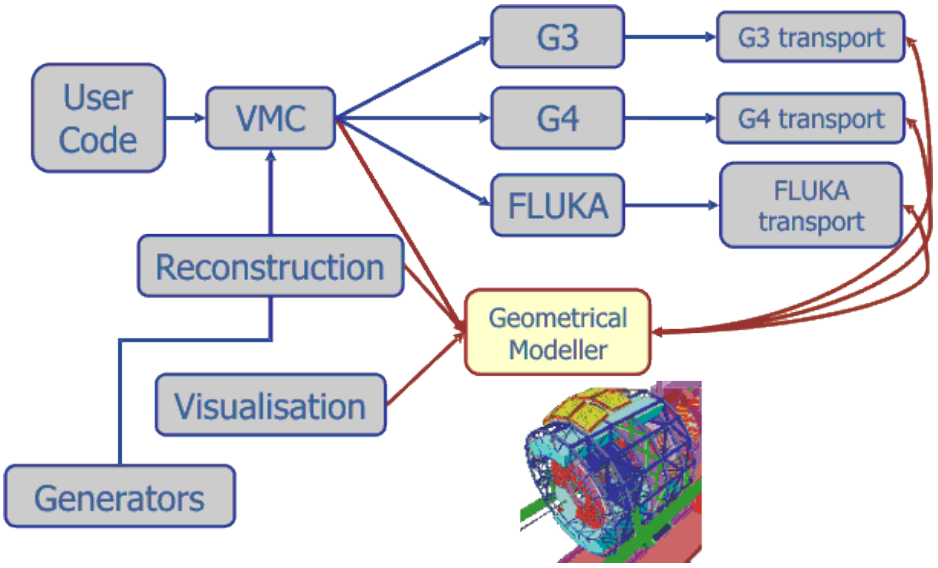

Figure 37: The Virtual Monte Carlo (VMC). Figure taken from [ALI11b]

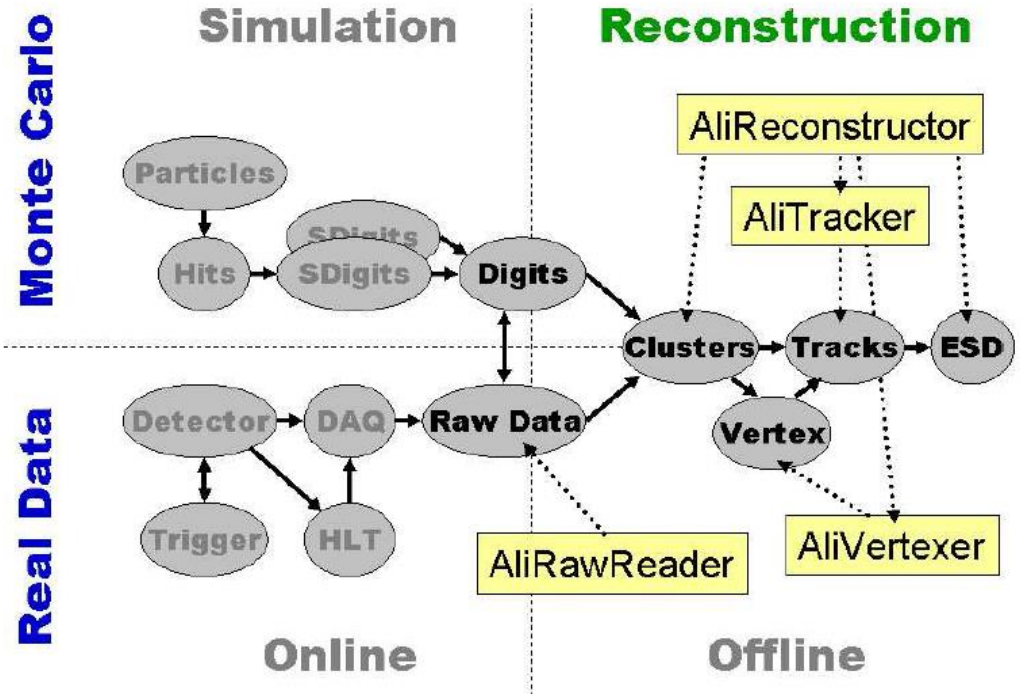

Figure 38: Reconstruction Framework. Figure taken from [ALI11a]

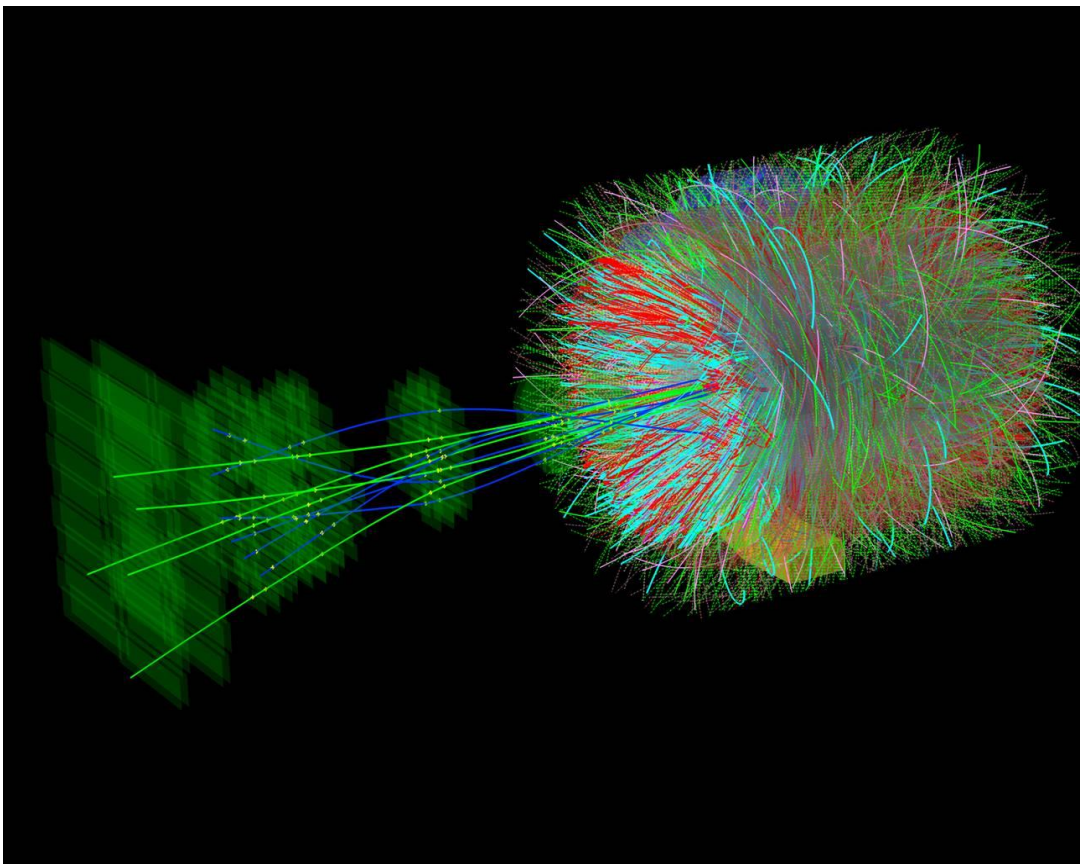

Figure 39: Pb-Pb event from the LHC in 2011 detected and reconstructed by ALICE. The grey cylindrical transparent object represents the TPC. Tracks detected by the TPC are shown in red and tracks detected by the SPD in white. Figure taken from [ALI13b].

A very important aspect of the reconstruction is the use of the correct calibration and alignment information. The Offline Condition Database (OCDB) [Car09] is the place where the calibration and alignment data is stored. It is a set of entries in the AliEn file catalogue that point to the physical entities containing the calibration and alignment data. The OCDB contains ROOT objects stored in ROOT files. These objects are run dependent and can be identified by a path name in the AliEn file catalogue and their validity for a certain run range. When running the simulation and reconstruction the AliCDBManager can access the OCDB and retrieve the data containing the conditions which were present during a certain data taking period. These conditions can be stored either on the grid or local storages for further use. An example of how this is achieved is shown in the simulation (sim.C) and reconstruction (rec.C) macros in Insert 2 and Insert 3, respectively.

Figure 39 shows a reconstruction of tracks produced during an event in a Pb-Pb collision at ALICE in 2011.

3. Analysis

a) From ESD to AOD

The analysis starts with the ESD. For an analysis related to a specific physics objective, only certain relevant information is necessary. For instance in heavy flavour muon studies only the muon tracks and some information on the vertex are of importance. The selection of the relevant data is done through a train of "analysis tasks" whereby Analysis Object Data (AOD) files are created. For a specific analysis activity further reconstruction passes may be requested, producing new ESD and AOD files which are then called *Pass 1*, *Pass 2*, etc. These are then the files which users can easily use for their own analysis. Within ALICE there are several Physics Working Groups (PWGs) and each one requires some sets of AODs per event for their specific analysis needs. AOD files are generated at different computing centres and stored on their storage elements, while access is granted to all ALICE collaborators.

b) Event and track selection

Users can analyse the AOD files at their own institute with ease using the ALICE Grid [FK04] which will be described in the next subsection (Chapter IV.A.4). Different cuts, depending on the purpose of the specific analysis, may be applied to the events and tracks stored in the AODs in order to reduce background.

The selection cuts applied to events for a single muon analysis in the Muon Spectrometer are shown in Table 4 and will be described below:

- Firstly a "Physics Selection" is applied to the events at ESD level. Only events which satisfy a certain quality criteria of the detector response are considered. This already reduces beam-induced background in the creation of the AODs. Quality Assurance (QA) checks are then performed on the AOD files and only events in runs that pass the analysis quality criteria (see Table 8, p. 70) are selected for the analysis.
- The next part of the selection process is applied by requiring that events triggered the specific trigger class of interest. For Pb-Pb events in single muon studies in the Muon Spectrometer this would for instance be the CPBI1MSL-B-NOPF-MUON trigger class for low-

p_T muons and the CPBI1MSH-B-NOPF-MUON trigger class for high-p_T muons (see Chapter III.D.1, p. 47 for details on trigger classes).

- Some other event cuts, such as requiring the centrality of the event to be within a certain region (e.g. 0 – 80 %) and the vertex of the interaction to have been reconstructed by the SPD could also be implemented.

Table 4: Selection cuts applied to events and tracks in the analysis of the simulation of pp collisions at $\sqrt{s_{NN}}$ = 8 TeV and of Pb-Pb data collected at $\sqrt{s_{NN}}$ = 2.76 TeV.

	Selection Cut	Simulation analysis	Data analysis
Event	Physics Selection	None	MSH
	Centrality	None	0 – 100 %
	Vertex reconstructed	None	Yes
Track	Pseudorapidity (η)	$-4 < \eta < -2.5$	$-4 < \eta < -2.5$
	Exit angle at front absorber (θ_{abs})	$171° < \theta_{abs} < 178°$	$171° < \theta_{abs} < 178°$
	Trigger Matching	Apt ~ 0.5 GeV/c	Hpt ~ 4.2 GeV/c
	p x DCA	5σ	Run and θ_{abs} dependent (between 5 - 6 σ)

In the studies conducted at forward rapidity using the data recorded by the Muon Spectrometer, there are various cuts which are also applied to the muon tracks in order to further reduce background. Table 4 contains a summary of these cuts and the values used in the present simulation and data analysis:

- These include cuts which are related to the geometrical acceptance of the detector. For the Muon Spectrometer these cuts correspond to the pseudorapidity (η) range of $-4 < \eta < -2.5$ and the polar angle of the track measured at the end of the front absorber (θ_{abs}) has to be between $171° < \theta_{abs} < 178°$.
- Then a cut is specified which requires the track in the Tracking Chambers to match a track in the Trigger Chambers with a certain p_T threshold. This is a very efficient way of reducing the hadronic background which are absorbed by the iron wall. The p_T threshold can be chosen as either All-p_T (Apt), Low-p_T (Lpt) or High-p_T (Hpt). These thresholds vary for different data taking periods, but for LHC11h the Apt cut threshold was p_T > 0.5 GeV/c, the Lpt threshold was p_T > 1.7 GeV/c and the Hpt threshold was p_T > 4.2 GeV/c. The effects of using different p_T thresholds were studied in parallel by Senosi [Sen12].
- The correlation between momentum (p) and Distance of Closest Approach (DCA) can be used to remove tracks not originating from the interaction vertex [A+12a]. The DCA is the distance between the interaction vertex and the extrapolated muon track, in the plane containing the vertex and perpendicular to the beam direction (see Figure 40). Due to multiple scattering of the muons in the front absorber their DCA distribution is expected to be a Gaussian function with a width proportional to $\frac{1}{p}$ and dependent on the material in the front absorber. Particles which do not follow this trend can be rejected by applying a p x DCA cut at $n\sigma$, where σ is obtained from a Gaussian fit to the p x DCA distribution and n is a factor (usually 5 or 6) dependent on certain run conditions during the period. Since the front absorber is made of different materials (see Figure 21, p. 40), σ is different for two regions

of θ_{abs}, $171° < \theta_{abs} < 172°$ and $172° < \theta_{abs} < 178°$. This has to be taken into account when applying the cut. These tracks which do not satisfy the cut are either fake tracks (tracks not associated to a single particle traversing the Muon Spectrometer) or beam-induced background (particles produced due to interactions between the beam and gas in the beam-pipe near the IP). For further details on the effect of the p x DCA cut see [Sto12, LZ12a].

4. The ALICE Grid

Because ALICE is an international collaboration the computing resources and skills are unsurprisingly distributed worldwide, making a centralized solution impossible. In order to deal with the high data acquisition rate (1.25 GB/s) in heavy-ion collisions and vast amount of data (5 PB/year) to be stored and a very high amount of CPU power required, the Grid project [FK04] was developed. Through a hierarchy of computing centers which are called *Tiers* (See Figure 41), every collaborator has equal access to data and resources. *Tier 0* is located at CERN where the raw data are stored. *Tier 1*'s are the major computing centers of ALICE, at CERN and other facilities, where a backup of the raw-data is kept and the reconstruction task is performed. *Tier 2*'s are the small regional centers, particularly involved in Monte Carlo simulation and data analysis. *Tier 3*'s are the university departmental local clusters or user workstations where mainly private analysis and small Monte Carlo production can be performed [FK04].

The Alice Environment (AliEn) [BPSG04] provides access to the Grid resources, as well as a functional computing environment in a transparent way to the user, without compromising the stability of the ALICE software core. A central service manages the tasks, with computing resources defined as "remote queues". Input and output associated to a job can be registered in a virtual file system (the AliEn file catalogue) in which a virtual file name is associated to the file. This enables a user in an

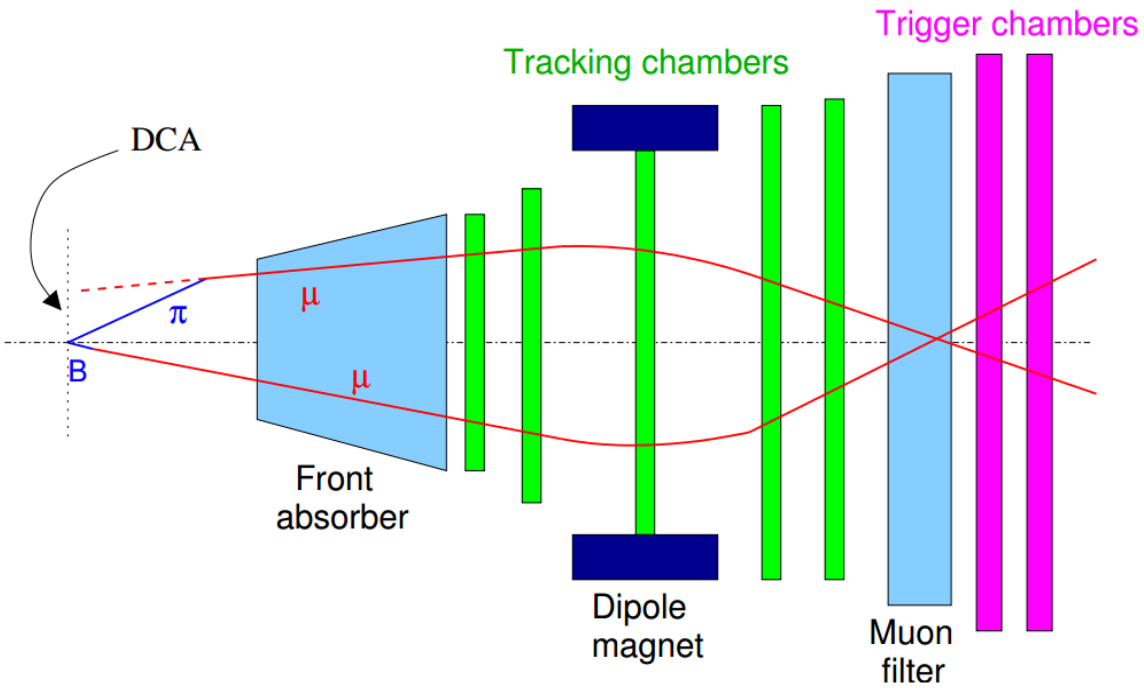

Figure 40: Schematic of the Muon Spectrometer showing the Distance of Closest Approach (DCA). Figure from [Sto10]

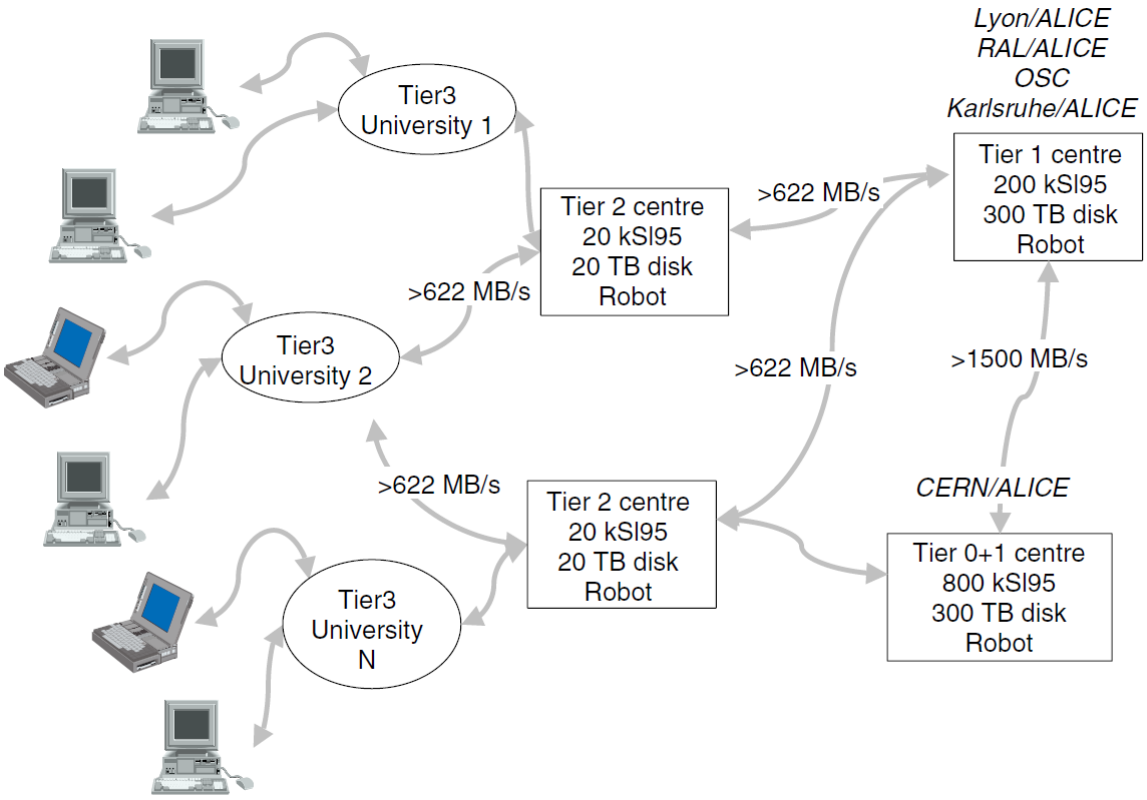

Figure 41: The ALICE Grid structure. Figure taken from [A+08].

analysis process to extract datasets from the AliEn file catalogue. The tasks are split according to the datasets location, in an effort to maximize resource usage and minimize data movement. After the task has been executed the output files are registered to the file catalogue and are made available to the user.

The system is monitored by the MonALISA framework [Mon13], which stands for Monitoring Agents using a Large Integrated Services Architecture. It is developed by Caltech and its partners and is able to provide complete monitoring, control and global optimization services for complex systems. The MonALISA repository for ALICE contains information on AliEn jobs and the storage elements (SE), as well as production information on real data and Monte Carlo simulations.

B. Alignment Study using Simulation

Since the alignment of the tracking chambers and detector elements (DEs) of the Muon Spectrometer is a crucial step for single muon analyses [Sto08b, A+12a], it is necessary to first conduct an investigation on the effect the alignment might have on the $W^{\pm}$ boson analysis. In a preliminary study different residual misalignment scenarios and an ideal scenario were simulated and reconstructed. The details of how the simulation sample used in the analysis was produced will now be given and later the analysis method used will be described.

1. Simulation Sample

The simulation samples were generated with PYTHIA 6.4.21 [SMS06] using AliRoot. The configuration file (Config.C) used in the simulations was similar to the one used in the previous

performance study by Conesa del Valle [CdV07], but with some important changes: the centre-of-mass energy was lowered from $\sqrt{s_{NN}}$ = 14 TeV to 8 TeV and the newer CTEQ5L [CTE13b] Parton Distribution Function (PDF) was used, instead of the older CTEQ4L [CTE13a] PDF. During 2012 pp collisions were carried out at this centre-of-mass energy of $\sqrt{s}$ = 8 TeV at the LHC and the simulations were therefore also done at $\sqrt{s}$ = 8 TeV in order to later compare to results from 2012 pp data analysis. This comparison was not attempted in this study because the 2012 pp data were still being prepared for analysis. Because the aim of the simulation was to provide a signal for the $W^{\pm}$ boson, the process

$$p + p \rightarrow W^{\pm} + X$$

(referred to as process kPyW in PYTHIA) was activated in the simulation in each of the events. Also the semi-muonic decay of the $W^{\pm}$ boson

$$W^{\pm} \rightarrow \mu^{\pm} + x$$

was enforced in each event. This single muon was also set to be generated within the acceptance of the Muon Spectrometer,

$$-4.0 < \eta < -2.5$$

which corresponds to a polar angle of $171° < \theta < 178°$.

We can calculate what the expected number of muons from $W^{\pm}$ boson decays would have been in the pp collisions for 2012 using Equation I—5, p. 7. The production cross section of the $W^{\pm}$ boson in pp collisions at 8 TeV is given by PYTHIA as $\sigma_{pp}^{W^{\pm}}$ = 16 nb. The branching ratio for $W^{\pm} \rightarrow \mu^{\pm}\nu$ is 10.57 % according to Figure 15, p. 30. The integrated luminosity and detector acceptance and efficiency was assumed to be $\int \mathcal{L}\,dt$ = 10 pb^{-1} and 80 % respectively [Lop12, BS12]. Therefore the number of expected muons is given by:

$$N_{\mu^{\pm} \leftarrow W^{\pm}}^{obs} = \int \mathcal{L}\,dt\,(A \times \varepsilon)\sigma_{pp}^{W^{\pm}} BR_{W^{\pm} \rightarrow \mu^{\pm}\nu} \qquad \text{(IV—1)}$$

$$\approx 5000$$

There were 5000 events generated in each simulation and 500 simulation files were produced giving a total of 2,5 M events. This was done in order to have large statistics with which to determine the performance of the detector and to study different alignment cases by measuring the distributions of $W^{\pm}$ bosons [Bos13].

Parts of the configuration file used for the ideal scenario, Config.C, are shown in Insert 1. Only the most important commands are shown. (The complete Config.C, sim.C and rec.C macros are given in Appendix A).

The reconstruction of the generated raw data was then completed for several different cases. In the first case an ideal scenario is used. This assumes a 100 % efficient detector with no dead channels or detector elements (DEs) in the tracking and triggering chambers and a 100 % trigger efficiency. The detector is also assumed to be perfectly aligned. See Chapter III.C.5 for details on the alignment of the Muon Spectrometer.

Insert 1: Extracts of the Config.C file used to steer and configure the Simulation of the pp collisions.

```
void Config() {
  // Set random seed
  gRandom->SetSeed(seed);
   // Create transporter
   new TGeant3TGeo("C++ Interface to Geant3");
   //Create RunLoader
   AliRunLoader* rl=0x0;
   rl = AliRunLoader::Open("galice.root", AliConfig::GetDefaultEventFolderName(), "recreate");
    // Set External decayer
   TVirtualMCDecayer *decayer = new AliDecayerPythia();
   decayer->SetForceDecay(kAll);
   decayer->Init();
   gMC->SetExternalDecayer(decayer);
   // Set up transporter parameters
   gMC->SetProcess("DCAY",1);
   gMC->SetCut("CUTGAM", cut);
   // Create and set up event simulator for W production (Zaida Config.)
   AliGenPythia *gener = new AliGenPythia(1);
   gener->SetProcess(kPyW);
   gener->SetStrucFunc(kCTEQ5L);
   gener->SetEnergyCMS(8000.);
   gener->SetCutOnChild(1);
   gener->SetChildPtRange(1.0,1000.);
   gener->SetThetaRange(171.0,178.0);
   gener->SetNumberOfAcceptedParticles(1); //need a muon inside
   gener->SetPdgCodeParticleforAcceptanceCut(13); //the muon arm acceptance
   gener->SetForceDecay(kWToMuon);
   gener->Init();
   // Define all materials and detectors
   AliBODY *BODY = new AliBODY("BODY", "Alice envelop");
```

Insert 2: Extracts from the sim.C file used to run the simulation for the Ideal case.

```
void sim(Int_t nev=5000) {
  AliSimulation simulator;
  simulator.SetTriggerConfig("MUON");
  simulator.SetMakeSDigits("MUON");
```

```
 simulator.SetMakeDigits("MUON");
 simulator.SetMakeDigitsFromHits("");
 simulator.SetRunQA("MUON:ALL");
 // Default = Ideal OCDB
 simulator.SetDefaultStorage("alien://folder=/alice/simulation/2008/v4-15-Release/Ideal");
 // CTP (muon standalone)
 simulator.SetSpecificStorage("GRP/CTP/Config", "
          alien://folder=/alice/cern.ch/user/b/bogdan/prod2011/cdb");
 // Vertex and Mag.field from OCDB
 simulator.SetSpecificStorage("GRP/GRP/Data","alien://folder=/alice/data/2011/OCDB");
 simulator.UseMagFieldFromGRP();
 simulator.Run(nev);
}
```

Insert 3: Extracts of the rec.C file used to run the reconstruction for the ideal case.

```
void rec() {
  AliReconstruction reco;
 reco.SetRunLocalReconstruction("MUON");
 reco.SetRunTracking("MUON");
 reco.SetRunVertexFinder(kFALSE);
 reco.SetFillESD("MUON");
 reco.SetRunQA("MUON:ALL");
 // Default = raw OCDB
 reco.SetDefaultStorage("alien://Folder=/alice/data/2011/OCDB");
 reco.SetDefaultStorage("alien://Folder=/alice/simulation/2008/v4-15-Release/Ideal");
 //tracking
 reco.SetSpecificStorage("MUON/Align/Data","alien://folder=/alice/simulation/2008/v4-15-Release/Ideal");
 // CTP
reco.SetSpecificStorage("GRP/CTP/Config","alien://folder=/alice/cern.ch/user/b/bogdan/prod2011/cdb");
// GRP from local OCDB
 reco.SetSpecificStorage("GRP/GRP/Data",Form("local://%s",gSystem->pwd()));
 reco.Run();
}
```

Also 11 other cases are reconstructed which correspond to realistic scenarios. The true status of the detector during the 2011 data taking period is incorporated into the reconstructions. The realistic configuration of the detector is retrieved from the OCDB and used in the simulation. Therefore it includes the effects caused by the dead channels and faulty DEs from the 2011 period. Furthermore in each case different residual misalignments for the chambers and DEs are introduced (See Table 1

for the number of chamber modules and DEs). For each case a random residual misalignment scenario is used. The values of the resolution of the alignment of the detector element (DE) and chambers of the Muon Spectrometer are shown in Table 5 and Table 6, respectively. In each misalignment case each detector element (DE) was shifted randomly within the value of the resolution in the x- and y-directions and in the angle ϕ (rotation around z-axis). The chambers of the detector were also moved randomly within the values of their resolution in the x-, y-, z-directions and rotations around these axes.

Table 5: Resolution of the alignment of the detector elements (DEs) of the Muon Spectrometer. Table courtesy of J. Castillo [Cas12]

Detector elements	X (μm)	Y (μm)	Φ(/Z)
	125	125	0.0125°

Table 6: Resolution of the alignment of the chambers of the Muon Spectrometer. Table courtesy of J. Castillo [Cas12].

Chambers	X (μm)	Y (μm)	Z (μm)	Θ(/X)	Ψ(/Y)	Φ(/Z)
	300	300	500	0.010°	0.005°	0.005°

The macro used to run the reconstruction, rec.C (See Insert 3) is responsible for loading the correct OCDB objects for the specific run conditions, as well as the alignment of the Muon Spectrometer. Therefore each rec.C file for the different residual misalignment cases retrieves its random alignment conditions from a different OCDB object especially created for the purpose of testing the effects of the alignment.

2. Alignment Analysis of Simulation

Looking at Table 4 on p. 61 for a summary of the selection cuts used in the analyses, we see that none were applied to the simulation events. For these simulations the focus was solely on the generation of $W^{\pm}$ boson signals via the single muon decay channel in the Muon Spectrometer and therefore no reconstruction in the central barrel or global detectors were done. Thus no physics selection could be done, as is usually the case in pp simulations and data analyses, since this requires information from the SPD and V0. No requirement that the vertex must have been reconstructed was applied for the same reason and since these are simulated pp and not Pb-Pb events, centrality is not applicable.

Various selection cuts were applied in order to reduce the background. These are the cuts also shown in Table 4 and include the geometrical cuts on pseudorapidity (η) and θ_{abs} as well as the Apt trigger matching and p x DCA cut.

These cuts were applied by implementing the "AliMuonTrackCuts" class. This class is described in detail on the ALICE Twiki page [Sto13a]. In the analysis the cuts were specified as shown in Insert 4.

Insert 4: Line of code to implement the selection cuts in the analysis using AliMuonTrackCuts.

```
fMuonTrackCuts->SetFilterMask(AliMuonTrackCuts::kMuEta|AliMuonTrackCuts::kMuThetaAbs|
        AliMuonTrackCuts::kMuPdca|AliMuonTrackCuts::kMuMatchApt);
```

After the cuts were applied the transverse momentum (p_T) and pseudo-rapidity (η) distributions were extracted using the analysis task "AliAnalysisTaskSingleMu" given in Appendix A. In the analysis on the Grid, version v5-33-02b of ROOT and v5-03-24-AN of AliROOT was used. The results obtained from these analyses will be shown and discussed in Chapter V.A.

C. Alignment Study on Pb-Pb Data

1. Experimental Measurements

The data analysis was carried out on Pb-Pb data collected during period LHC11h[9] at $\sqrt{s_{NN}}$ = 2.76 TeV. The LHC beam filling scheme at that time was 200ns_358b_356_336_0_24bpi15inj_IONS. This tells us that the number of interacting bunches per collision at ALICE were 336 and the rate of hadronic collisions for that period was about 1 kHz which gives a luminosity of 33.5 × 10^{25} $cm^{-2}s^{-1}$ [TOA11].

Only unlike single muons with high-p_T were considered. The active Trigger Class Code used in this analysis is CPBI1MSH-B-NOPF-MUON[10]. The requirement for this trigger is a signal on both V0A and V0C detectors and on at least three of the four planes of the Muon Trigger Chambers and a minimum muon transverse momentum of p_T > 4.2 GeV/c. The number of events passing these conditions gives a data sample of 22.9 M Pb-Pb events, corresponding to an integrated luminosity of roughly L_{int} = 94.44 μb^{-1} (See Figure 42). The number of events during the different stages of the analysis is shown in Table 7. The HLT was in mode C, which means that the HLT decision was applied, but this is only of importance for the TPC and has no influence on the data recorded by the Muon Spectrometer. The currents of the L3 and dipole magnet were +30 kA and +6 kA, respectively.

Table 7: Number of events in the *Pass 1* and *Pass 2* data samples during the different stages of the analysis.

Number of events and integrated luminosity of data samples			
	Pass 1	***Pass 2***	L_{int}
Single Muon High Trigger (MSH)	22.4 M	22.9 M	94.44 μb^{-1}
QA and Physics Selection	17.7 M	17.9 M	73.91 μb^{-1}
Event and Track Selection	3.5 M	3.6 M	----

The alignment of the tracking chambers was carried out by the MILLEPEDE package [BK02] which is able to accurately determine the large number of alignment parameters using a general linear least squares fit of a number of tracks. This alignment is done at the beginning of the data taking period by analyzing physics tracks with the dipole and L3 magnets switched off.

[9] The scheme used to name the periods of data taking starts with LHC11a, LHC11b, etc. for pp runs and LHC11h is the period with Pb-Pb runs.

[10] CPBI1MSH-B-NOPF-MUON: CPBI = Class for Pb-Pb Interaction, MSH = Muon Single High, B = two filled bunches crossing, NOPF = absence of past-future protection conditions; an alias for this class is kMUSHPB (U = Unlike)

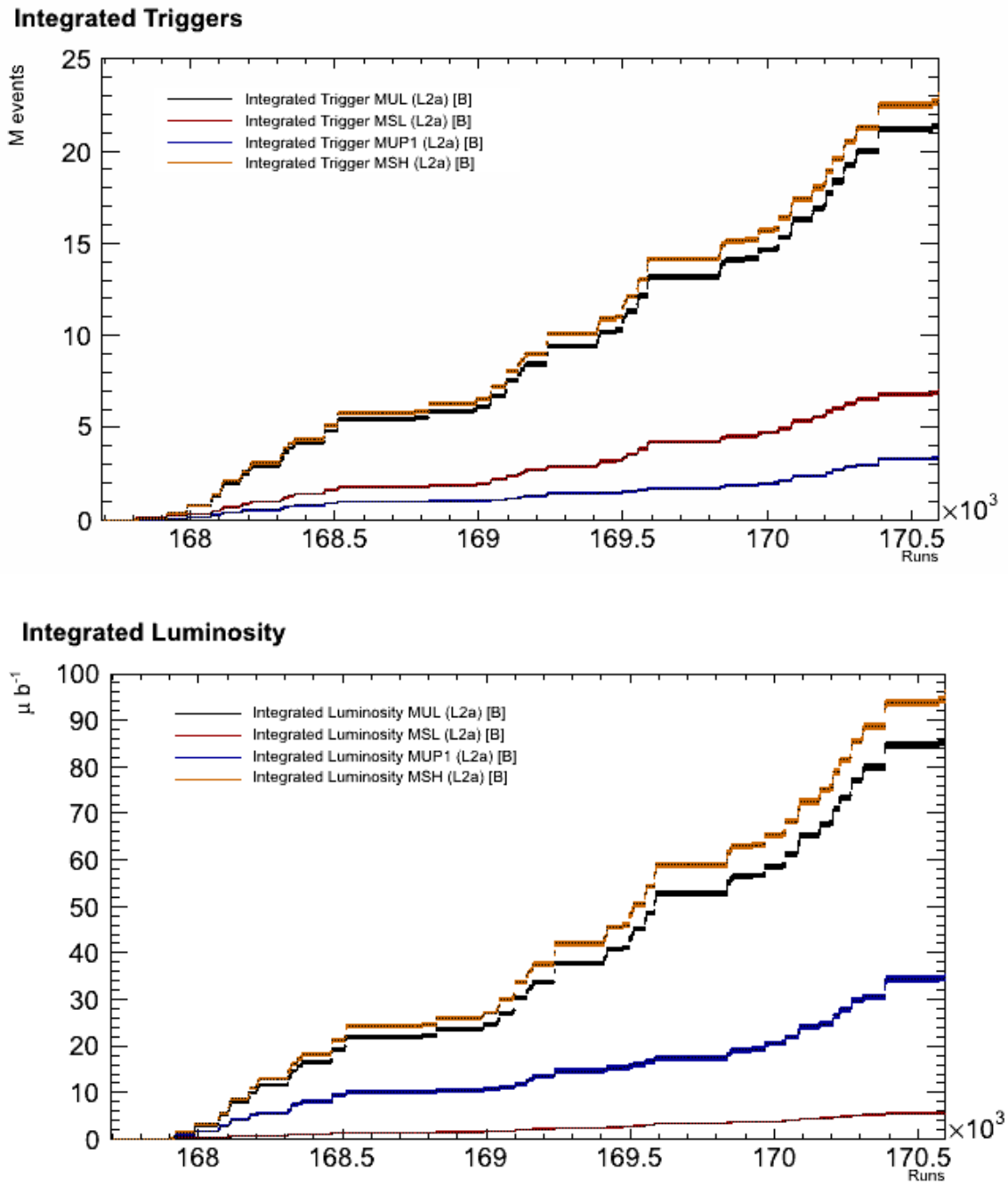

Figure 42: Integrated trigger events (above) and integrated luminosity (below) for different triggers during LHC11h. The orange line shows the Integrated MSH trigger events and luminosity measurements. Figures taken from [TOA11].

The ESD files which contain the first reconstruction of the raw data used the original alignment information stored in the OCDB. By extracting from these ESDs the information relevant to single muon and dimuon studies, the *Pass 1 Muon* AODs were created. After an improvement of the resolution of the alignment of the tracking chambers, the ESDs were later again reconstructed with the refitted alignment and new analysis files, *Pass 2 Muon* AODs, were created for muon studies. These two data sets (hereafter referred to only as *Pass 1* and *Pass 2*) will be analysed in this alignment study to test the effect of the new improved alignment.

Furthermore a Quality Assurance (QA) study had been completed on both the LHC11h *Pass 1* and *Pass 2* data [Had12]. Runs were first selected using the ALICE Logbook [ALI13a] according to the criteria shown in Table 8. These selections check the quality of the physics runs during the LHC11h period. The Muon Trigger and Tracker, SPD and V0 were required to have been included in the run as read-out detectors and their measurements had to be of good quality, as well as the overall data taking quality. The importance of including the SPD and V0 as read-out is the fact that they provide valuable information on the vertex used in the analysis. The data transport had to be successfully completed and only runs with a duration of more than 10 min were considered.

The list of runs passing these requirements is shown in Appendix B. This QA study showed that some of the runs from LHC11h only had Minimum Bias trigger information and other runs had no centrality trigger information. There was also a run (169420) which showed a 15 % loss of efficiency in one of the chambers (Chamber 1 of the Muon Tracker). It was decided therefore not to analyse these runs in order to achieve the best results. Also for *Pass 2* there were two new runs which had not been reconstructed for *Pass 1* (168356 and 170315). These two runs were therefore also not included in the analysis of *Pass 2* since the aim of this study was to check the differences due to the alignment only and not the total difference between *Pass* 1 and *Pass* 2.

In the end, a total of 129 runs were analysed and 17.9 M Pb-Pb events passed the QA and MSH (Muon Single High) trigger requirements. This corresponds to an integrated luminosity of L_{int} = 73.91 μb^{-1} [Aph13].

Table 8: Conditions of the Quality Assurance (QA) imposed on runs from LHC11h.

Quality Assurance Run Conditions	
Period:	LHC11h
Run Type:	PHYSICS
Detectors:	At least [MUON_TRG & MUON_TRK & SPD & V0] as Readout
MUON_TRK Quality Flag:	Good run
MUON_TRK Shuttle Done:	DONE
Beam:	Yes
GDC mStream Recording:	Yes
MUON_TRG Quality Flag:	Good run
V0 Quality Flag:	Good run
Shuttle Done:	Yes
MUON_TRG Shuttle Done:	DONE
V0 Shuttle Done:	DONE
Data Taking Quality Flag:	Good run
SPD Quality Flag:	Good run
SPD Shuttle Done:	DONE
Duration:	[10 m..]
GRP Shuttle Done:	DONE

According to the QA analysis the Muon Tracker showed good efficiency and increased for *Pass 2* compared to *Pass 1* due to the fact that two of the detector elements (slats DE 710 and 915) had been recovered with the new reconstruction [Had12]. During runs 168203 – 170593 there was an approximate 10 % loss of efficiency on Chamber 3 of the Muon Tracker for both *Pass 1* and *Pass 2*. The average efficiency for the Muon Tracker for *Pass 1* and *Pass 2* was determined using an embedding technique in simulation [A+12c, Pil12d]. It was found to be around 86.8 % at high-p_T for

Pass 1 and improved slightly for *Pass 2*, around 87.3 %. The average values for the efficiencies of the Muon Trigger and Tracker Chambers for LHC11h are summarized in Table 9.

The efficiency of the Muon Trigger according to the QA analysis was more than 95 % and stable during the data taking period LHC11h [Had12]. It is the same for both *Pass 1* and *Pass 2.* The Trigger efficiency can also be evaluated using simulation and gives on average the same result, but shows a dependence on centrality with an efficiency of 98 % in peripheral events and 94.5 % in central collisions [Pil12d].

Table 9: The Muon Trigger and Muon Tracker Chamber efficiencies for data taking period LHC11h for *Pass 1* and *Pass 2*.

	Pass 1	***Pass 2***
Muon Trigger	95 % [Had12]	95 % [Had12]
Muon Tracker	86.8 % [Pil12d]	87.3 % [Pil12d]

By using the embedding technique in a realistic simulation which includes all the electronic problems of the Muon Tracker for each run and plugging the Muon Trigger efficiency measured from data into the simulation, the global $A \times \epsilon$ correction can be found [Pil12a]. A signal is embedded into a real event to reproduce the effects induced by the high particle multiplicity in Pb-Pb collisions. The reconstructed signal is then compared to the generated signal in the acceptance of the Muon Spectrometer . The results give the $A \times \epsilon$ correction and show a global systematic uncertainty for the detector response of 3.5 % and also a 1 % systematic uncertainty due to the centrality dependence of the efficiency [Pil12a]. The systematic uncertainties relevant to this study are shown in Table 10.

There is also a systematic uncertainty caused by the alignment of the chambers of the Muon Spectrometer. This was determined using the same method used in this dissertation's preliminary simulation study on the effect of the alignment. Simulating randomly generated residual misalignments, of the same order of magnitude as in the data and comparing these residual cases to the real (unknown) residual misalignment, the systematic uncertainty in the high p_T region was found to be dependent on the p_T. The uncertainty can be given by 1 % × p_T (in GeV/c) [A+12a, Pil12a].

Table 10: Systematic uncertainties in the measurements in Pb-Pb collisions for 2011.

	Systematic Uncertainty
Detector response	3.5 % [Pil12a]
Centrality dependence of efficiency	1 % [Pil12a]
Alignment	1 % × p_T (in GeV/c) [A+12a, Pil12a]

2. W± Boson Data-Analysis

Event selection was done as is shown in Table 4, p. 61. As was already mentioned, only events which triggered the MSH trigger were selected. Furthermore the full centrality range from 0 – 100 % was selected and it was required that the vertex had been reconstructed.

The same selection cuts were applied to the tracks as for the misalignment case, with some differences which will be mentioned here. The same geometrical acceptance cuts were applied, but the track measured in the tracking chamber was this time required to match a track in the trigger chamber above the high p_T (Hpt) threshold. The p x DCA cut was once again used to remove fake tracks and also beam-induced background tracks (beam-gas) which do not point to the interaction vertex (see discussion in Chapter IV.A.b).

After these event and track selections only 3.54 M events remained for *Pass 1* and 3.67 M for *Pass 2* in the data sample (Table 7). This reduction from number was to be expected, seeing as usually only half of the tracks detected in the Muon Trigger match a track in the Muon Tracker and the η, θ_{abs} and p x DCA cuts also further remove the unwanted background such as beam-gas and fake tracks.

The p_T and η distributions were then extracted. The analysis task used is the same one given in Appendix A with some modifications in order to apply the event and track selections differently. This Analysis Task was developed for the specific purpose of analysing Single Muon tracks and is called "AliAnalysisTaskSingleMu". It is derived from the "AliVAnalysisMuon" class and uses the "AliAnalysisMuonUtility" which contains methods to handle either ESDs or AODs [Sto12]. ROOT v5-34-05 and AliROOT v5-04-35-AN were used to analyse the data on the Grid. The results obtained from this analysis will be shown in Chapter V.B.

Chapter V. Results and Discussion

In the Introduction it was mentioned that the alignment of the Muon Spectrometer plays a crucial role in the analysis (Chapter I.C). The Muon Spectrometer was then described in detail in Chapter III.C and the different methods used to determine the alignment of the detector were discussed. The effect of the alignment on the measurement of observables needs to be determined through simulation and data analyses in order to give a full account of the efficiency of the detector. This relates to the systematic uncertainty in the measurements. This chapter will give the results of the two studies which were done concerning the alignment of the Muon Spectrometer of ALICE and its effects on measuring the $W^{\pm}$ boson.

In the first study the systematic error due to the uncertainty in the alignment of the detector is predicted by analysing simulations of pp collisions at $\sqrt{s}$ = 8 TeV. In these simulations the production of the $W^{\pm}$ boson and subsequent decay in the single muon channel is explicitly set in each event. The tracks "measured" by the detector are then reconstructed using different conditions for the alignment and status of the Muon Spectrometer. The variation of the different misaligned cases will be used to determine the systematic uncertainty in the measurements.

Secondly a comparison is made between two different reconstructions of Pb-Pb data collected at $\sqrt{s_{NN}}$ = 2.76 TeV during the LHC11h data taking period. *Pass 1* AODs were reconstructed in December 2011 with the best information available at the time on the alignment of the detector. Later the alignment of the detector was better understood and a new reconstruction was performed in July 2012. Thus *Pass 2* AODs refitted to the new alignment information were also made available for analysis. By studying the difference in the distributions of the original *Pass 1* and refitted *Pass 2* AOD data sets, the effect of the "new alignment" can be determined.

A. Alignment Study from pp Simulation

The study of the effects of the alignment of the Muon Spectrometer is comprised of comparing the p_T and η distributions, as well as the charge asymmetry (ratio $\frac{\mu^+}{\mu^-}$) of different alignment cases for pp collisions at $\sqrt{s}$ = 8 TeV. In an ideal case a 100 % efficient (no dead channels or dead detector elements) and a perfectly aligned detector is used in the simulation and reconstruction of events. The other alignment cases are realistic cases which incorporate the true status of the detector (dead channels, etc.) during the 2011 data taking period and each case also includes a different residual misalignment of the chambers and detector elements (DEs). The values for the resolution of the alignment of the chambers and DEs were given in Chapter IV.B.1, p. 67 in Table 5 and Table 6, respectively. The residual misalignment is randomly generated for each chamber and DE, within the alignment resolution of that chamber or DE.

The ideal case was first compared to only one realistic residual misalignment case (sometimes called "residual" or "realistic" case) in order to see what the effect of the realistic configuration of the detector is on the simulation and reconstruction. The ideal and realistic residual misalignment case do not show any remarkable differences at the generation level (not shown in this study), as was studied by Senosi [Sen, Sen12]. The selection cuts shown in Table 4 of Chapter IV.B.2, p. 61 were applied to the reconstructed tracks in order to reduce background as was mentioned before.

1. Transverse momentum (p_T) distributions

After reconstruction of the Monte Carlo data clear differences can be seen between the ideal and realistic residual case in their p_T distributions. The p_T distributions of all reconstructed muon tracks are shown in Figure 43 for the ideal case and in Figure 44 for the residual case. In all figures the errors which are shown are only statistical ones. The different muon sources are indicated in the legends of these figures. The contributions from the decay of $W^{\pm}$ bosons are represented by the turquoise open ($\mu^+ \leftarrow W^+$) and turquoise closed ($\mu^- \leftarrow W^-$) markers. This is the dominant contribution in the simulation because the production of $W^{\pm}$ bosons is activated for each event and its decay to a single muon in the acceptance range of the spectrometer is explicitly set in the simulation.

Other processes, such as the decay of heavy flavour (mesons containing c and b quarks) and light mesons (π, K) therefore contribute much less to the simulation. "Secondary" decays of π, K inside the front absorber (See Chapter III.C.a)) can also lead to some muons, not originating from the $W^{\pm}$ boson, being detected. Sometimes hadrons can also pass through the iron wall and are then incorrectly reconstructed as muons. These muons from other sources than the $W^{\pm}$ boson are produced at low p_T and will therefore not influence an analysis in the high-p_T region. The tracks labelled "$\mu^+ \leftarrow \mathrm{Unidentified}$" are fake tracks which are not produced in the simulation and although there are some reconstructed at high-p_T they can safely be ignored in the analysis since their contribution is negligible.

In Figure 43 it can clearly be seen that there is a difference between the shape of the p_T distributions of the $\mu^+ \leftarrow W^+$ and $\mu^- \leftarrow W^-$ in the ideal case. This difference in shape will be discussed at a later stage, but we can already mention that it is due to the net isospin available in the pp collisions and parity violation effects which were discussed in Chapter II.E.4 and 5, respectively.

Comparing the ideal case (Figure 43) to the residual case (Figure 44) we see that the shapes of the p_T distributions change considerably in the residual case. For the residual case the peaks are broader than the peaks of the ideal case. Also for the residual case there are more $\mu^+ \leftarrow W^+$ than $\mu^- \leftarrow W^-$ in the high-p_T region (40 – 80 GeV/c), where in the ideal case this was the other way around. These differences will be discussed further for the p_T distributions of $\mu^+ \leftarrow W^+$ and $\mu^- \leftarrow W^-$ separately.

Next, ten other realistic residual misalignment cases (case 0 – 9) were generated following the same method as for the first realistic case. For each case the misalignment is generated randomly and each reconstruction is therefore different. This gives a total of one ideal case and 11 realistic residual cases. The selection cuts were applied to the reconstructed tracks in the same manner as before. This time only the muons decaying directly from $W^{\pm}$ bosons were selected using Monte Carlo mother-daughter[11] information, since it is the effect on the distributions of the $W^{\pm}$ boson that we want to investigate.

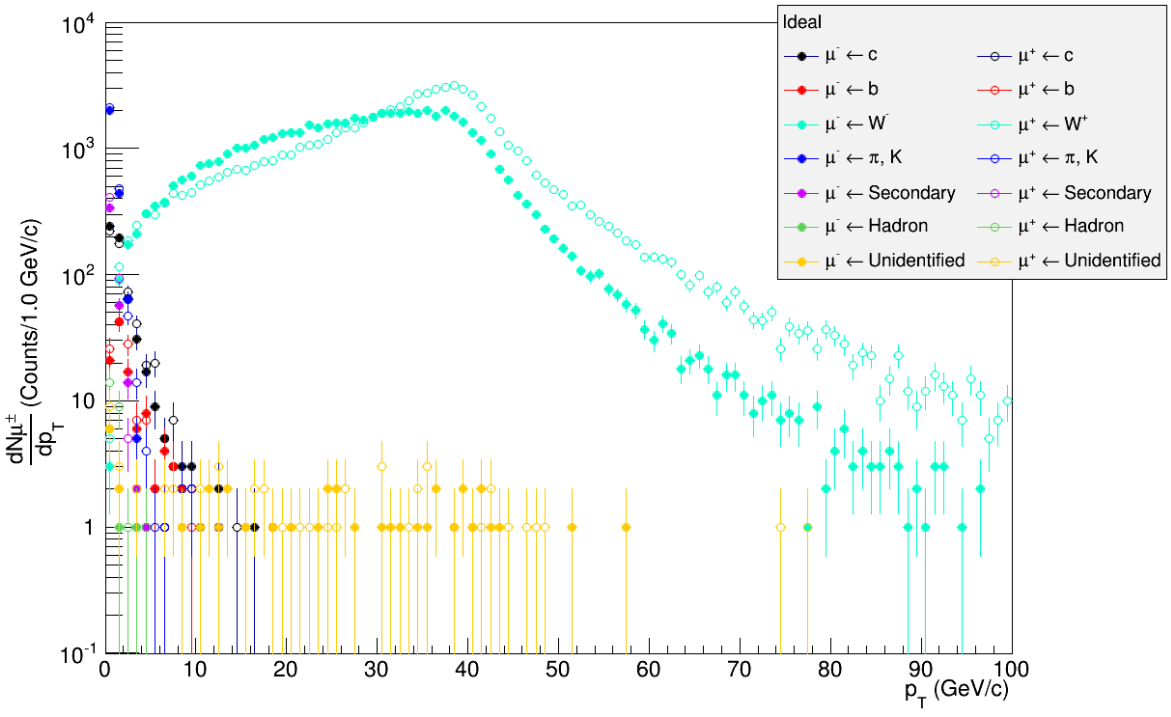

Figure 43: Simulation of the p_T distributions of different $\mu^{\pm}$ sources for an ideal case carried out with PYTHIA at $\sqrt{s}$ = 8 TeV.

[11] The muon is the "daughter" of another particle – the "mother". The code checks in the kinematics tree, which stores all the particles created in the simulation with their relation to other particles, to see if the "mother" is a $W^{\pm}$ boson. If the mother is not a $W^{\pm}$ boson it rejects the muon and does not consider it for further analysis.

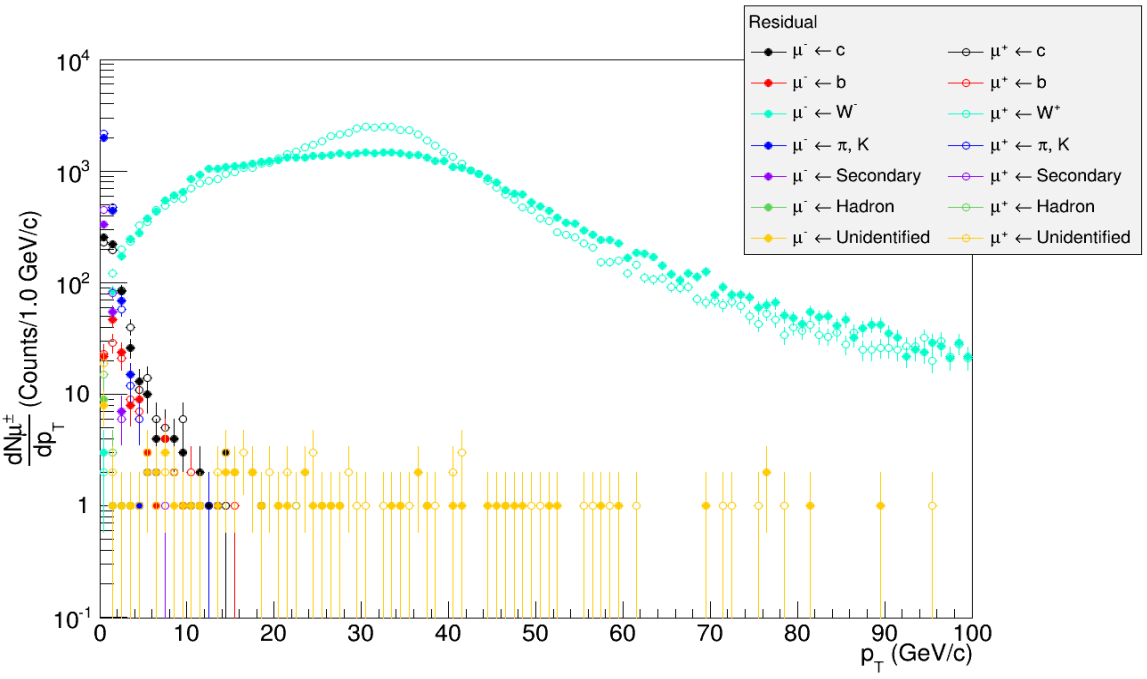

Figure 44: Simulation of the p_T distributions of different $\mu^{\pm}$ sources for the realistic residual case carried out with PYTHIA at $\sqrt{s}$ = 8 TeV.

The p_T distributions of $\mu^+ \leftarrow W^+$ and $\mu^- \leftarrow W^-$ for the ideal (red markers), first realistic residual misalignment case (black) and the 10 other misalignment cases (case 0 - 9) are normalized to the number of events and shown in Figure 45 and Figure 46 respectively. Take note that one of these residual cases is the same one used before in Figure 44 and is named the "residual" case (black markers), while "case 0" to "case 9" are also ten other residual misalignment cases.

In Figure 45 the p_T distributions of $\mu^+ \leftarrow W^+$ show that for the ideal case has a narrow distribution with a sharp peak at around p_T = 40 GeV/c leaning to the right-hand side. This is approximately half the $W^{\pm}$ boson mass and is the expected value for the p_T of the muons due to conservation of energy and momentum (see Chapter I.B.7, p. 7). The distributions of the residual cases are broader than the ideal case and shifted to various values between 30 < p_T < 40 GeV/c. Their peaks are also less pronounced than the peak of the ideal case. The variation in the shapes of the distributions of the different misalignment cases shows the systematic uncertainty caused by the alignment of the detector.

In Figure 46 the p_T distribution of $\mu^- \leftarrow W^-$ the ideal case also has a peak at around p_T = 40 GeV/c, similar to the ideal case of $\mu^+ \leftarrow W^+$. But here the ideal case has a broader peak leaning to the left-hand side. This difference in the shape of the $\mu^+ \leftarrow W^+$ and $\mu^- \leftarrow W^-$ distributions is due to the polarization effects caused by parity violation which was explained in Chapter II.E.5, p. 28. By further comparing the $\mu^+ \leftarrow W^+$ and $\mu^- \leftarrow W^-$ distributions, we see that more μ^+ than μ^- are produced. This is expected in pp collisions because of the net isospin available in the collisions. More u than d valence quarks are available in the collision, resulting in the formation of more W^+ than W^- bosons (see the discussion in Chapter II.E.4, p. 27 on charge asymmetry).

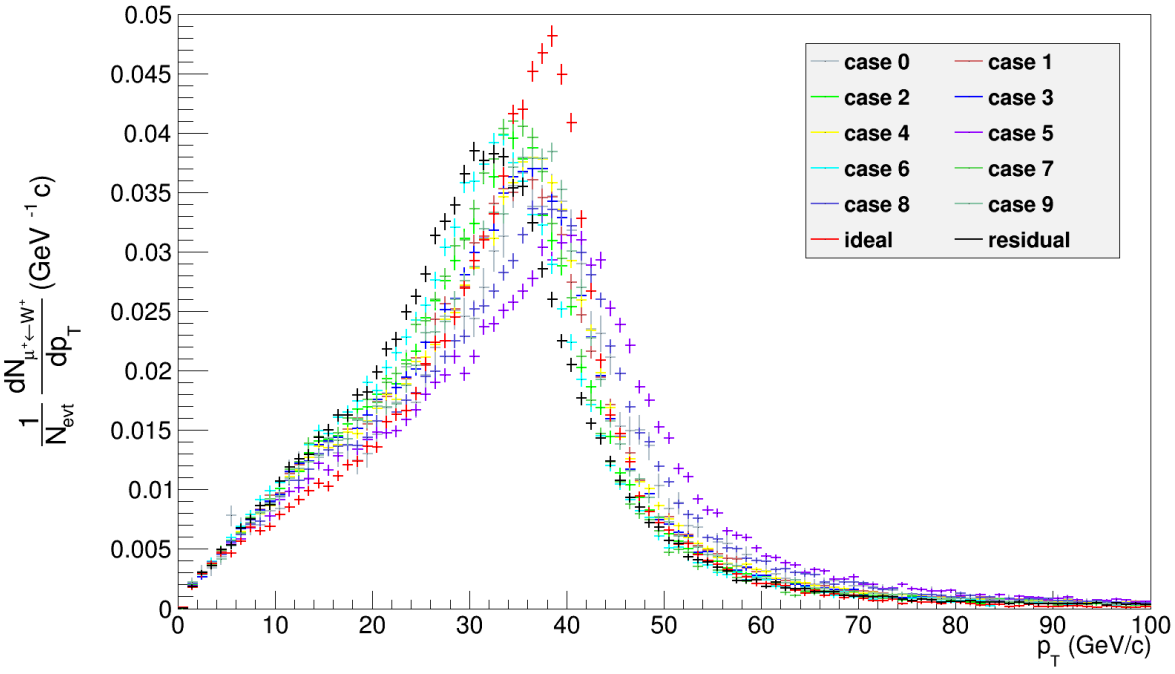

Figure 45: The p_T distributions of $\mu^+ \leftarrow W^+$ simulated in pp collisions at $\sqrt{s}$ = 8 TeV using PYTHIA. The red markers show the ideal case, the black markers the first residual case, while the other coloured markers (case 0 – 9) are for 10 different misalignment cases.

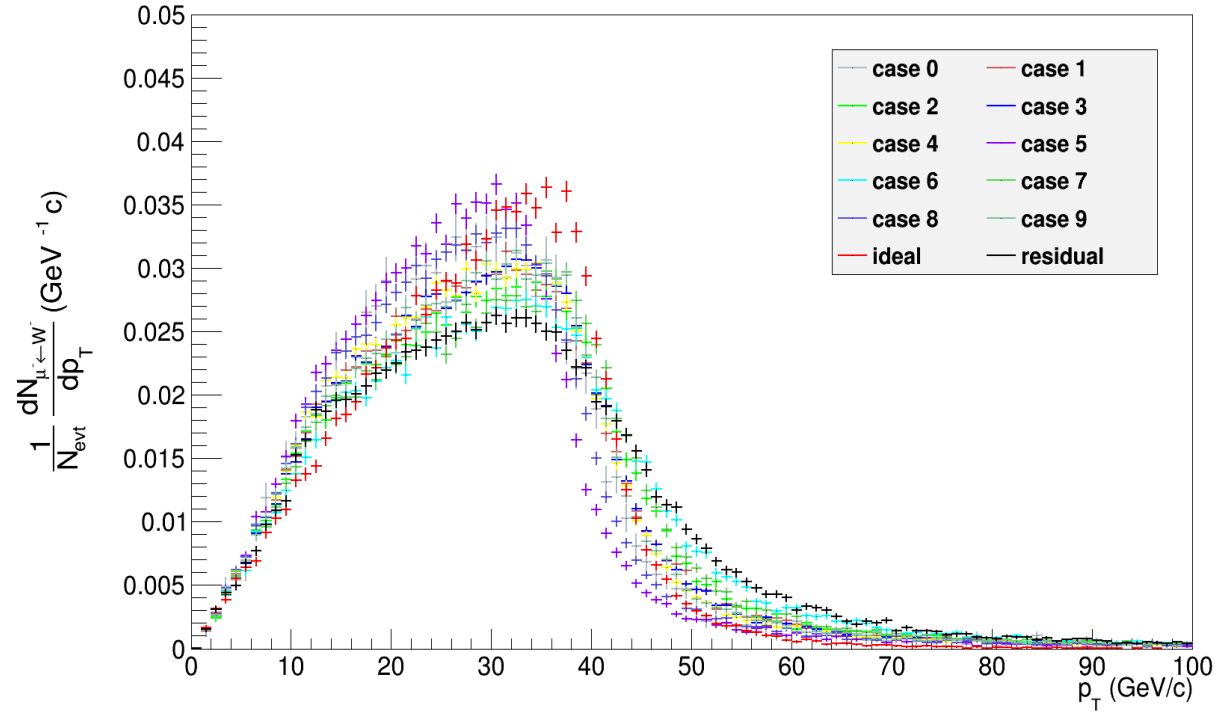

Figure 46: The p_T distributions of $\mu^- \leftarrow W^-$ simulated in pp collisions at $\sqrt{s}$ = 8 TeV using PYTHIA. The red markers show the ideal case, the black markers the first residual case, while the other coloured markers (case 0 – 9) are for 10 different misalignment cases.

For the $\mu^- \leftarrow W^-$ distributions, the residual cases have mostly wider and flatter peaks than the ideal case. The shapes of the distributions of the residual cases are also shifted with respect to the shape of the ideal case. As was mentioned for the p_T distributions of $\mu^+ \leftarrow W^+$ of the different misalignment cases, the variation (spread) in the shapes of the $\mu^- \leftarrow W^-$ distributions shows the systematic uncertainty caused by the alignment of the detector.

Figure 47 shows the normalized p_T distributions of $\mu^+ \leftarrow W^+$ and $\mu^- \leftarrow W^-$ for the ideal case (red) and two other residual cases, "case 5" (purple) and "residual" (black). These two cases show the largest deviation from the ideal case and are therefore shown here to illustrate the worst case scenarios the misalignment may have on the results.

The performance study by Conesa Del Valle [CdV07] made a prediction on the differential production cross sections of $\mu^\pm \leftarrow W^\pm$ as a function of p_T which is shown in Figure 48. In this present study the differential production cross sections is not determined by normalizing to the predicted cross section of 20.9 nb^{-1}, as was done in the performance study [CdV07]. For the present simulation study the same configuration file of the performance study was used (see Insert 1, p. 65) but with some important changes: the centre-of-mass energy was lowered from $\sqrt{s}$ = 14 TeV to 8 TeV and the newer CTEQ5L Parton Distribution Function (PDF) was used, instead of the old CTEQ4L PDF. Therefore any comparison between the present study and the performance study can only be qualitative and not quantitative. These changes could cause the differences between the shapes observed in this study and the performance study. The predicted differential production cross section is somewhat comparable to the results of the ideal case of this study. The exception is the fact that $\mu^- \leftarrow W^-$ dominates over $\mu^+ \leftarrow W^+$ in the region 10 < p_T < 35 GeV/c in the present study, which is not the case in the performance study.

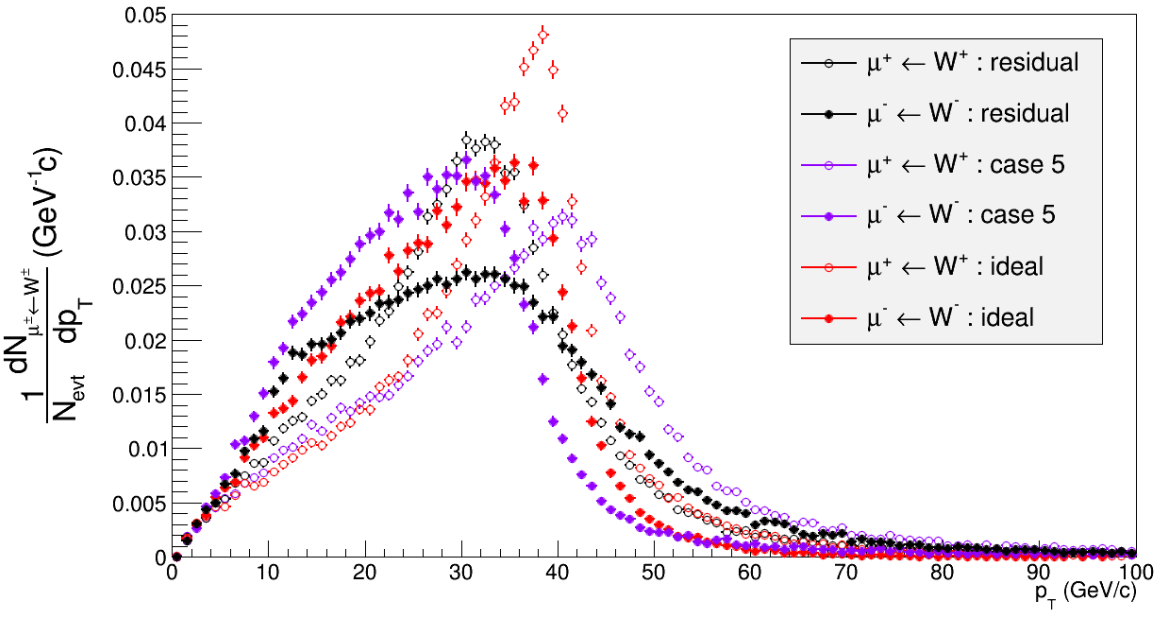

Figure 47: The p_T distributions of $W^\pm$ boson muonic decays simulated in pp collisions at $\sqrt{s}$ = 8 TeV using PYTHIA.

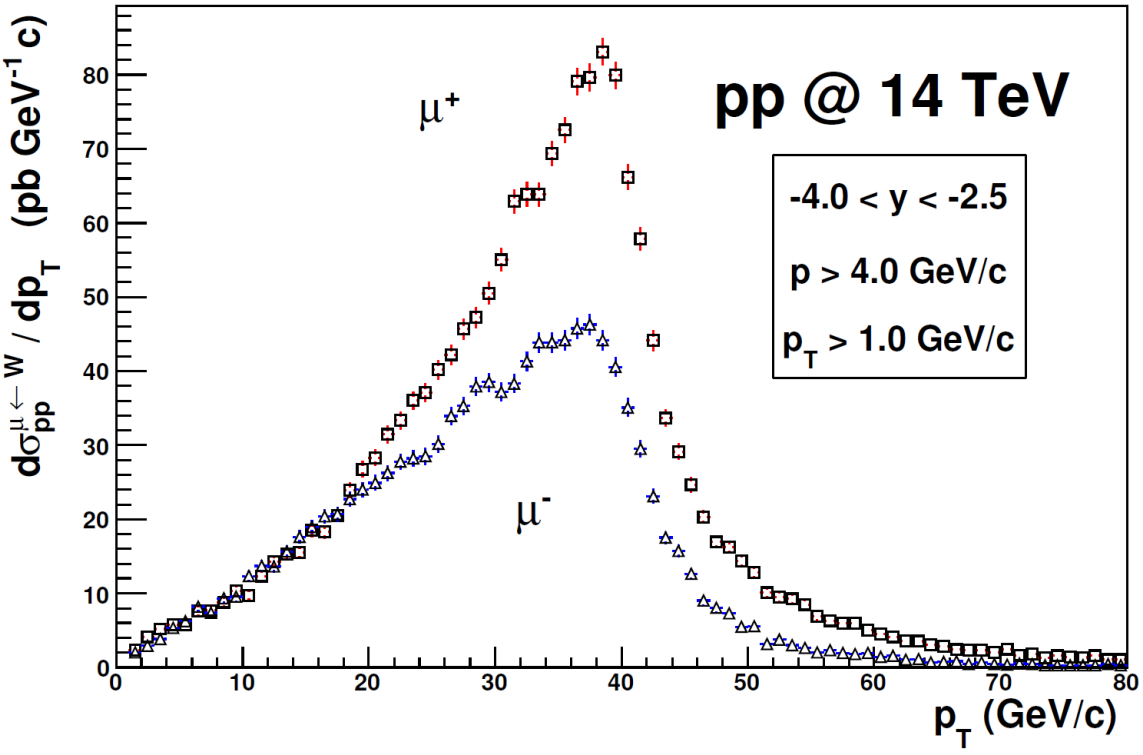

Figure 48: Predicted differential production cross section from $W^{\pm}$ boson muonic decays in the ALICE Muon Spectrometer acceptance as a function of p_T in pp collisions at $\sqrt{s}$ = 14 TeV. Squares represent μ^+ and triangles μ^-. Figure taken from [CMAF06].

2. Charge asymmetry

Figure 49 shows the ratio $\frac{\mu^+ \leftarrow W^+}{\mu^- \leftarrow W^-}$ (charge asymmetry) for the ideal (red) and different misalignment cases as a function of p_T. For the ideal case the charge asymmetry is higher than unity at low-p_T (p_T < 5 GeV/c) and drops below one between 5 < p_T < 30 GeV/c (see Figure 50 for a magnification of this area). This drop below unity is observed because more $\mu^- \leftarrow W^-$ than $\mu^+ \leftarrow W^+$ are produced in this region, as can clearly be seen in Figure 43. The charge asymmetry for the ideal case is larger than one from around p_T = 30 GeV/c and continues to grow at higher p_T since more $\mu^+ \leftarrow W^+$ than $\mu^- \leftarrow W^-$ occur here, also according to Figure 43. Therefore because the decay of $W^{\pm}$ boson is expected to dominate the single muon spectra in the high-p_T region (see Chapter II.F) an increase in the charge asymmetry will indicate the production of $W^{\pm}$ bosons in pp collisions.

The different misalignment cases show a large spread (variation) between 25 < p_T < 40 GeV/c. This spread becomes even greater for p_T > 40 GeV/c and starts to scatter considerably for p_T > 60 GeV/c. This leads to a high systematic uncertainty in measurements inside these regions, which have to be taken into account when conducting $W^{\pm}$ boson studies. The systematic uncertainty is 50 % between 25 < p_T < 40 GeV/c and grows even much worse for p_T > 40 GeV/c.

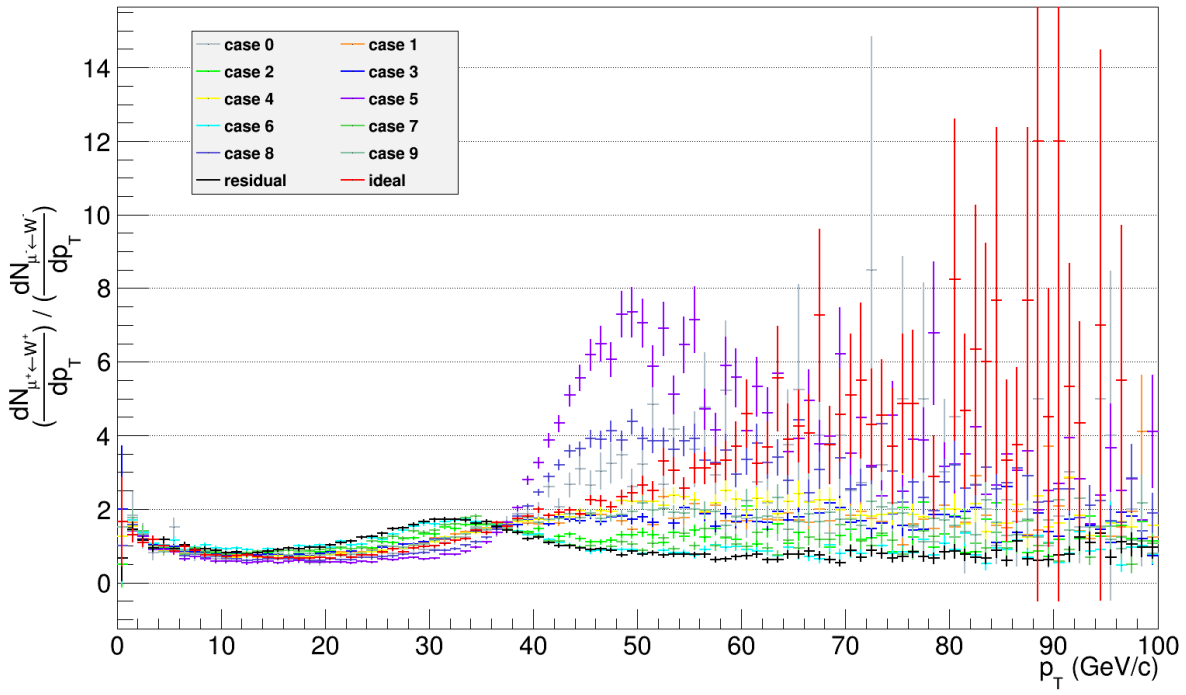

Figure 49: The ratio $\frac{\mu^+\leftarrow W^+}{\mu^-\leftarrow W^-}$ (charge asymmetry) as a function of transverse momentum (p_T) simulated in pp collisions at $\sqrt{s}$ = 8 TeV using PYTHIA. The red markers show the ideal case, while the other coloured markers are for the 11 different misalignment cases.

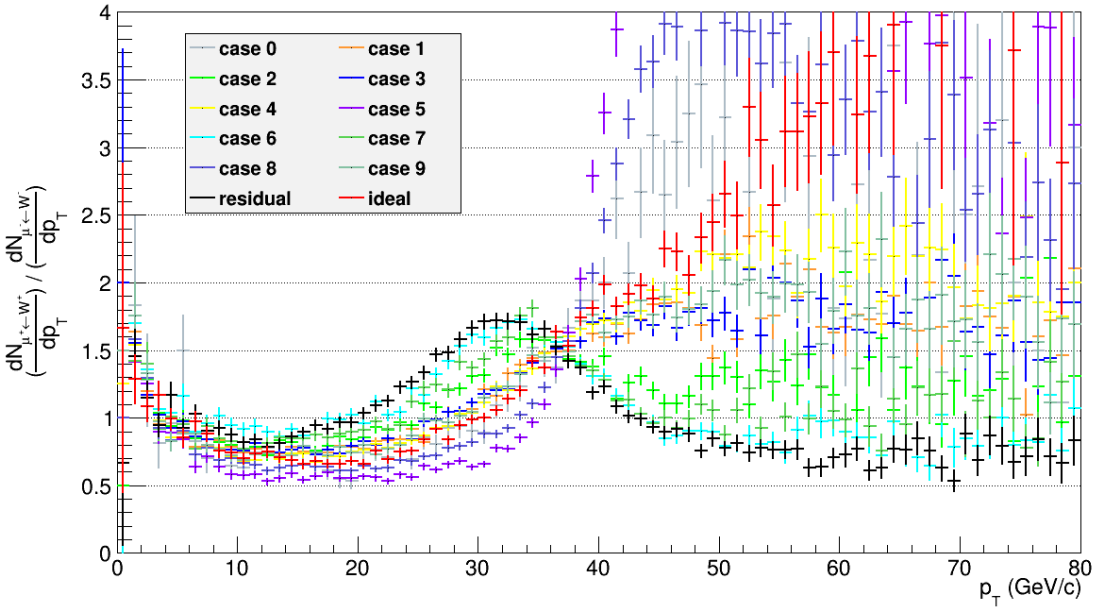

Figure 50: A magnification of the ratio $\frac{\mu^+\leftarrow W^+}{\mu^-\leftarrow W^-}$ (charge asymmetry) as a function of transverse momentum (p_T) simulated in pp collisions at $\sqrt{s}$ = 8 TeV using PYTHIA. The range 0 < p_T < 80 GeV/c is shown to clarify the charge asymmetry in this region. Note that some points fall outside of the charge asymmetry range (0, 4) from p_T > 40 GeV/c.

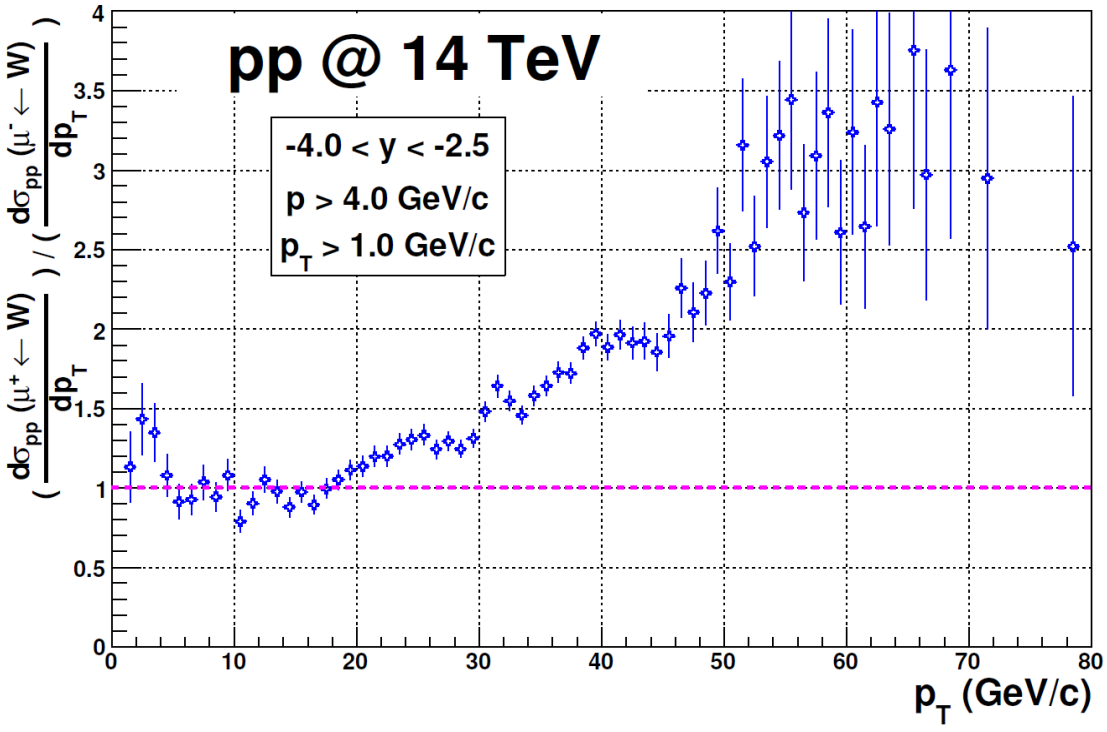

Figure 51: The single muon charge asymmetry for the $W^{\pm}$ boson in the ALICE Muon Spectrometer acceptance as a function of p_T for pp collisions at $\sqrt{s}$ = 14 TeV. Figure from [CMAF06].

An attempt to compare the charge asymmetry results of this study to the previous performance study [CdV07] was also made. Once again, it is important to note the differences between this study and the performance study, already mentioned before in the discussion of the p_T distributions (p. 74). These include differences in centre-of-mass energy and choice of PDF, and therefore the comparison can only be qualitative, and not quantitative. The trend for the ideal case (see Figure 50 red markers) is somewhat similar to the predicted charge asymmetry contribution from $W^{\pm}$ (shown in Figure 51) in the sense that both show charge asymmetry greater than one below p_T = 5 GeV/c. But in Figure 50 the ideal case is less than one for 5 < p_T < 30 GeV/c and only reaches values above unity for p_T > 30 GeV/c, while in Figure 51 the charge asymmetry remains close to one for 5 < p_T < 20 GeV/c and grows above one for p_T > 20 GeV/c. The residual cases do not compare well at all, especially for p_T > 40 GeV/c: either rising too sharply in "case 5" or decreasing below unity for "residual", with the other cases somewhere in between.

3. Pseudorapidity (η) distributions

The η distributions of $\mu^{\pm} \leftarrow W^{\pm}$ were also considered in this analysis. Firstly the difference between the ideal and one realistic case with residual misalignment was examined. The same realistic residual misalignment case ("residual"), used when studying the p_T distributions, was also used here. Figure 52 shows the η distributions of $\mu^{\pm} \leftarrow W^{\pm}$ for the ideal case, while Figure 53 shows the realistic "residual" case.

Comparing the η distributions of $\mu^{+} \leftarrow W^{+}$ and $\mu^{-} \leftarrow W^{-}$ for the ideal case one can see that there are more μ^{+} than μ^{-} produced at higher rapidity. This is once again due to the fact mentioned

earlier that more u than d valence quarks are available in the pp collisions, since the proton consists of 2 u valence and only 1 d valence quark. The effect of parity violation of the weak interaction can also be observed by examining the different slopes of the $\mu^+ \leftarrow W^+$ and $\mu^- \leftarrow W^-$ decays. The slopes suggest that $\mu^+ \leftarrow W^+$ were preferably produced closer to mid-rapidity and $\mu^- \leftarrow W^-$ to higher rapidity (see discussion in Chapter II.E.5, p. 28).

There is also a small difference seen between the ideal and residual case, which will later be discussed separately for the $\mu^+ \leftarrow W^+$ and $\mu^- \leftarrow W^-$ distributions. The peculiar drop the -2.6 < η < -2.5 bin seen in both the ideal and residual case will also be discussed soon.

Figure 54 shows the differential production cross section of $\mu^\pm \leftarrow W^\pm$ as a function of rapidity (y) predicted by the performance study [CdV07, CMAF06] in the whole rapidity range -5 < y < 5. It indicates the region ALICE is able to measure: -4.0 < y < -2.5. Rapidity and pseudorapidity are the same in the ALICE reference frame as was discussed in Chapter I.C, p. 8. Therefore the results of the present study can be qualitatively compared to that of the previous performance study. The slopes show some agreement in the fact that the $\mu^+ \leftarrow W^+$ distribution increases faster than the $\mu^- \leftarrow W^-$ distribution. But where Figure 54 shows the crossing between $\mu^+ \leftarrow W^+$ and $\mu^- \leftarrow W^-$ to be at y = -4.0 this present study shows it to be at around y = -3.2. The differences could simply be related to the differences introduced in the new configuration file of this study.

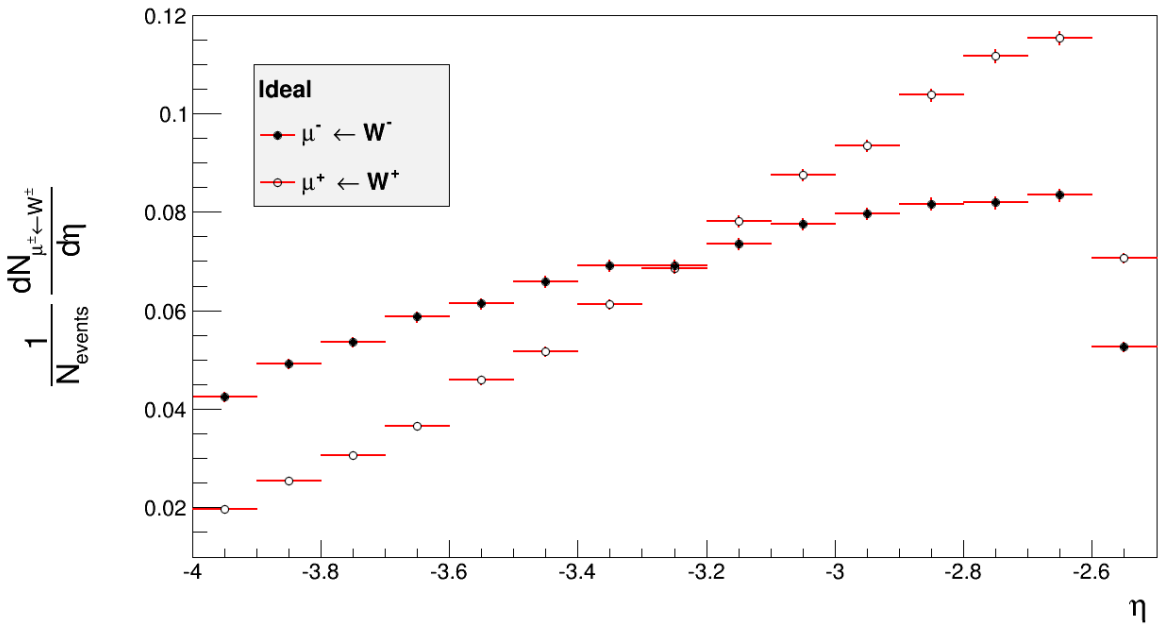

Figure 52: The η distributions of $\mu^\pm \leftarrow W^\pm$ for the ideal case simulated in pp collisions at $\sqrt{s}$ = 8 TeV using PYTHIA.

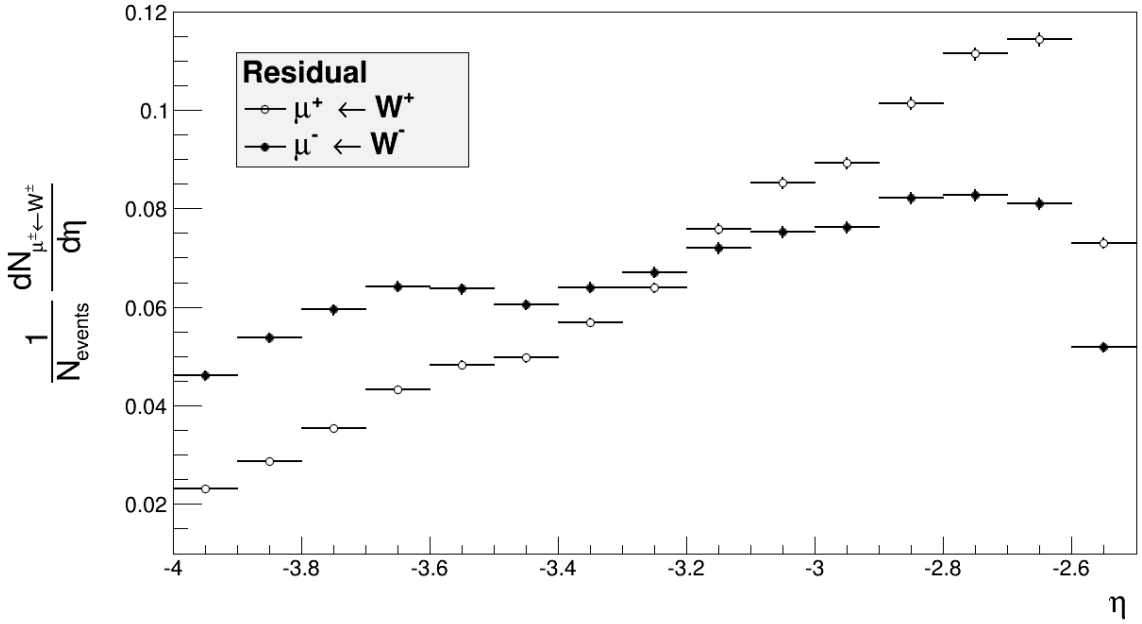

Figure 53: The η distributions of $\mu^{\pm} \leftarrow W^{\pm}$ for the first residual case simulated in pp collisions at $\sqrt{s}$ = 8 TeV using PYTHIA.

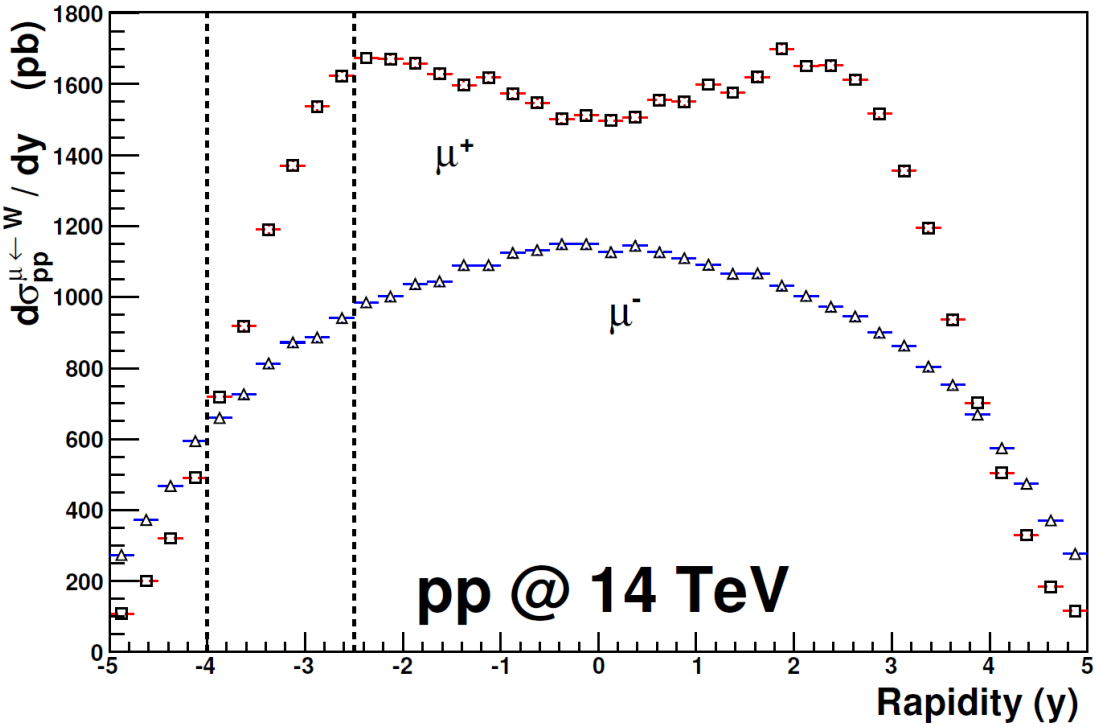

Figure 54: Predicted differential production cross section of $\mu^{\pm} \leftarrow W^{\pm}$ as a function of rapidity (y) in pp collisions at $\sqrt{s}$ = 14 TeV. Figure from [CMAF06].

Comparison between the ideal case and the 11 different misalignment cases are shown in Figure 55 and Figure 56, for the $\mu^{+} \leftarrow W^{+}$ and $\mu^{-} \leftarrow W^{-}$ distributions respectively. There are only small changes observed in the trends of the ideal and residual cases, with the biggest differences between -3.6 < η < -2.9. Here the residual cases drop below the ideal case. This is thought to be only due to

the differences between the ideal (100 % working channels, etc.) and realistic status (dead channels, etc.) of the detector, and not caused by the different alignments [duT12, Pil12c]. It can be seen that the variations between the η distributions of the residual cases are not as prominent as was the case for the residual p_T distributions and therefore the effect of the alignment can be safely ignored.

All the η distributions show the same peculiar drop in the -2.6 < η < -2.5 bin for which there are at least two possible explanations. It could be because of the constraint set in the simulation on the $\mu^{\pm} \leftarrow W^{\pm}$ to be within the acceptance of the Muon Spectrometer $171° < \theta < 178°$ (see Config.C in Insert 1, p. 65). This could give a reduction in the yield at the edges of the η distributions because particles produced just outside of the acceptance of the Muon Spectrometer, which could have entered into the spectrometer due to multiple scattering, are not taken into account.

The other explanation is that it could be a real effect caused by the acceptance and efficiency ($A \times \epsilon$) of the Muon Spectrometer (see Chapter III.C.5, p. 45 for a description of the Muon Spectrometer acceptance and efficiency) This effect would show in the reconstruction of simulated and of real data since both uses the same detector configuration in the reconstruction.

At this stage it is not possible to tell which of the two possibilities causes this strange effect, but later examining the η distributions of real data will shed some light on whether this behaviour was caused by the constraints set on the simulation or the true configuration of the spectrometer, or possibly both [Sto13b].

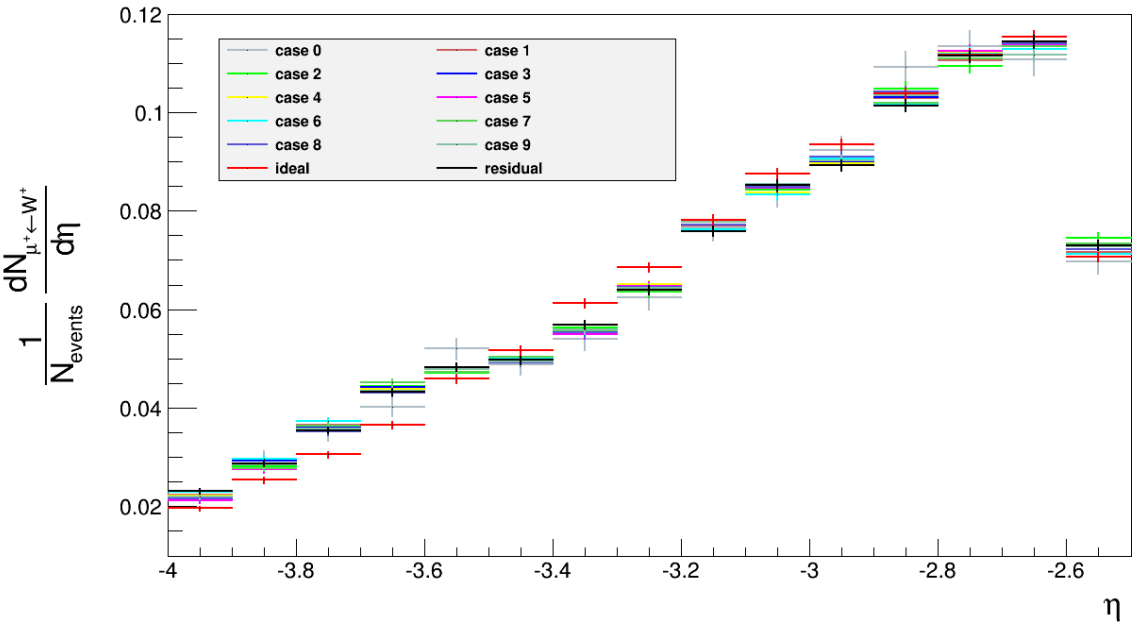

Figure 55: The η distributions of $\mu^{+} \leftarrow W^{+}$ simulated in pp collisions at $\sqrt{s}$ = 8 TeV using PYTHIA. The red data points show the ideal case, while the other coloured markers are for the 11 different misalignment cases.

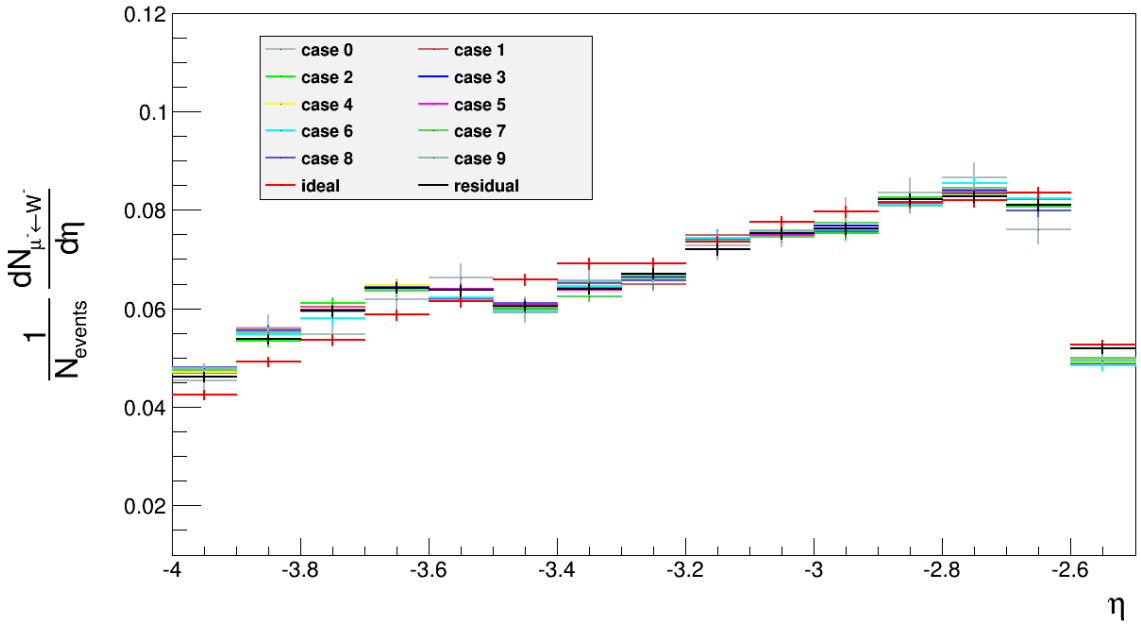

Figure 56: The η distribution for $\mu^- \leftarrow W^-$ simulated in pp collisions at $\sqrt{s}$ = 8 TeV using PYTHIA. The red data points show the ideal case, while the other coloured markers are for the 11 different misalignment cases.

4. Summary

The results from the simulation alignment study shows that the alignment of the Muon Spectrometer does have an influence on the p_T distributions of single muons decaying from the $W^{\pm}$ boson ($\mu^{\pm} \leftarrow W^{\pm}$) and also on the charge asymmetry (ratio $\frac{\mu^+ \leftarrow W^+}{\mu^- \leftarrow W^-}$). The distributions of the different misalignment cases are spread out due to the uncertainty in the alignment, resulting in a large systematic error in future measurements, especially at values of p_T > 40 GeV/c.

The effects of the alignment on the η distributions are minimal and can consequently be ignored. Differences between the ideal and residual cases are rather due to the differences between the ideal (100 % efficient detector with no dead channels, etc.) and realistic status (inefficiencies with some dead channels, etc. - as was the case during 2011) of the detector. There is a strange drop observed in the η distributions in the -2.6 < η < -2.5 bin, which could be due to the simulation configuration (constraints set on $\mu^{\pm} \leftarrow W^{\pm}$ to be within the acceptance of the Muon Spectrometer) or the real status of the detector. It will be interesting to see whether this strange behaviour is also observed at in the data analysis.

Some of the results of this study can be compared to the predictions made in the previous performance study by Conesa Del Valle [CdV07], although they can only be compared qualitatively due to differences between the configuration of the simulation and reconstruction in the two cases. The ideal case does resemble somewhat the predictions made, while the misalignment cases show clear differences. Further investigation could explain these discrepancies better [Sen], but will not be attempted in this study.

B. Alignment Study on Pb-Pb data

The simulation study of the alignment has already shown an important systematic uncertainty in the high-p_T region. It is important to also check the effect of alignment on the measurement of $W^{\pm}$ bosons in a Pb-Pb data study. A comparison between data recorded during Pb-Pb collisions at $\sqrt{s_{NN}}$ = 2.76 TeV and reconstructed with previous alignment files (*Pass 1*) and data reconstructed with an improved alignment (*Pass 2*) will test the effect of the alignment. The runs analysed are shown in Appendix B and are the same for both *Pass 1* and *Pass 2*. The details of which runs were chosen can be found in Chapter IV.C.1.

The method used to analyse the Pb-Pb data from LHC period LHC11h at $\sqrt{s_{NN}}$ = 2.76 TeV is described in 0. The same cuts were applied to both Pass 1 and Pass 2, and are also discussed in that section and summarized in Table 4. The original data (*Pass 1*) and the data refitted with an improved alignment (*Pass 2*) are compared for the p_T distributions, the ratio of $\frac{\mu^+}{\mu^-}$ (charge asymmetry) and the η distributions. In all cases *Pass 1* is shown in blue and *Pass 2* in red. The ratio $\frac{Pass\ 2}{Pass\ 1}$ is shown in purple at the bottom of the figures and magnifications in the region 0 < p_T < 40 GeV/c are also shown for clarification. The difference between the Pass 1 and Pass 2 ratio of $\frac{\mu^+}{\mu^-}$ (charge asymmetry) is also closely examined since it can give an indication of the production of $W^{\pm}$ bosons. In all cases the error which is shown is purely statistical. The systematic errors can be found in Table 10. The η distributions of both Pass 1 and Pass 2 are also studied to see if they are influenced by the new alignment and to check the strange behaviour observed in the simulation analysis.

Furthermore comparisons are made to the performance study by Conesa Del Valle [CdV07, CMAF06] for the p_T distributions and the charge asymmetry.

1. Transverse momentum (p_T) distributions

The *Pass 1* and *Pass 2* p_T distributions of the yield of all single $\mu^{\pm}$ ($\frac{dN_{\mu^{\pm}}}{dp_T}$) are plotted in Figure 57 and an enlargement of the ratio $\frac{Pass\ 2}{Pass\ 1}$ in the region 0 < p_T < 40 GeV/c is given in Figure 58. For both *Pass 1* and *Pass 2* the shapes of the distributions are similar. There is a high concentration of tracks at low values of p_T and there seems to be a slight increase or "bump" in the high-p_T region, 20 – 40 GeV/c. This could be a hint that $W^{\pm}$ bosons were produced in the collisions (see Chapter I.B.7, p. 7). But the number of tracks observed at high p_T is limited, making it impossible to draw any definite conclusions.

The shapes of the p_T distributions in Figure 57 show a good qualitative comparison to the predicted total single muon distribution (black points shown in Figure 59) of the performance study [CdV07]. The performance study predicted much more statistics than this study, because the predictions were made under assumptions of a centre-of-mass energy of $\sqrt{s_{NN}}$ = 5.5 TeV, twice as high as the current $\sqrt{s_{NN}}$ = 2.76 TeV and a higher integrated luminosity of 5 x 10^{32} cm^{-2} and not just 94.44 μb^{-1}. Also since PYTHIA cannot simulate Pb-Pb collisions, the simulation was done by combining weighted p-p, n-n and p-n collisions [CdV07].

Table 11: Total number of tracks which satisfy the cuts in the analysis.

	Pass 1	Pass 2	Pass 2 / Pass 1	Increase
$\mu^{\pm}$	3545210	3667026	1.034	3.4 %
μ^{+}	1809264	1887392	1.043	4.3 %
μ^{-}	1735932	1779621	1.025	2.5 %

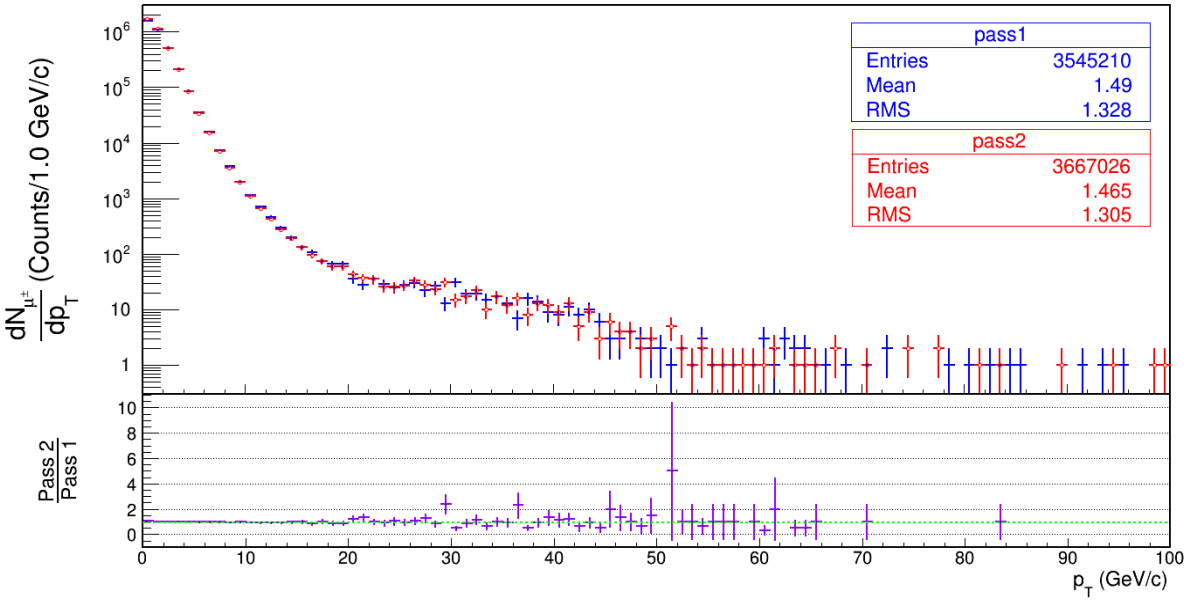

Figure 57: The *Pass 1* (blue) and *Pass 2* (red) p_T distributions of $\mu^{\pm}$ for Pb-Pb data collected at $\sqrt{s_{NN}}$ = 2.76 TeV from data taking period LHC11h. The ratio $\frac{Pass\ 2}{Pass\ 1}$ is shown in purple.

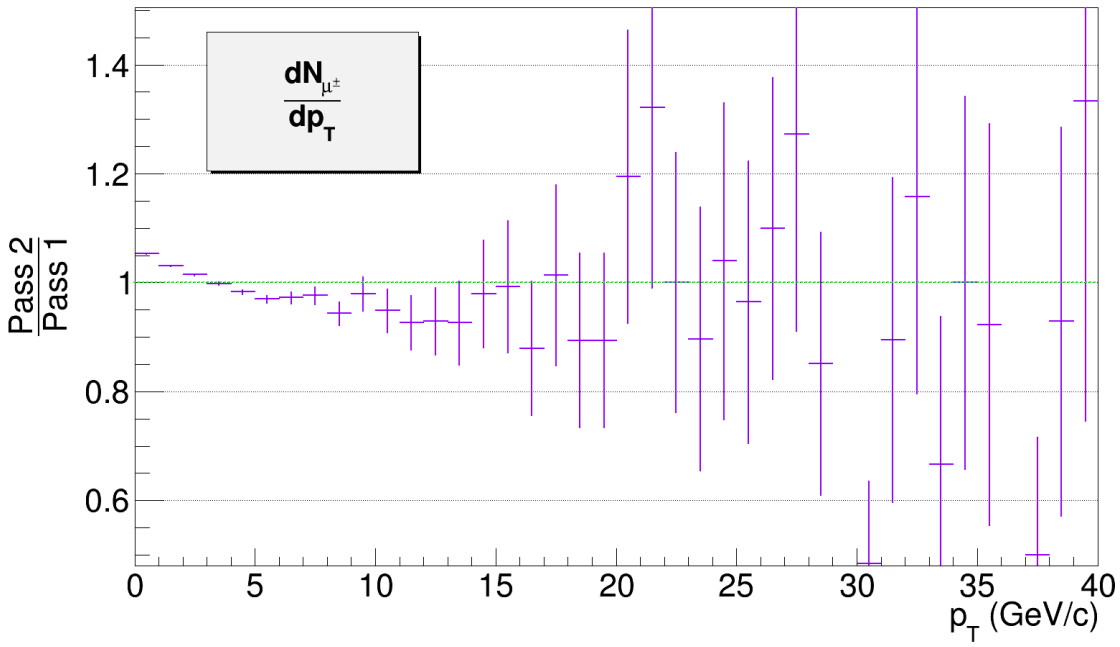

Figure 58: Ratio of $\frac{Pass\ 2}{Pass\ 1}$ for the p_T distributions of $\mu^{\pm}$ for Pb-Pb data collected at $\sqrt{s_{NN}}$ = 2.76 TeV from data taking period LHC11h.

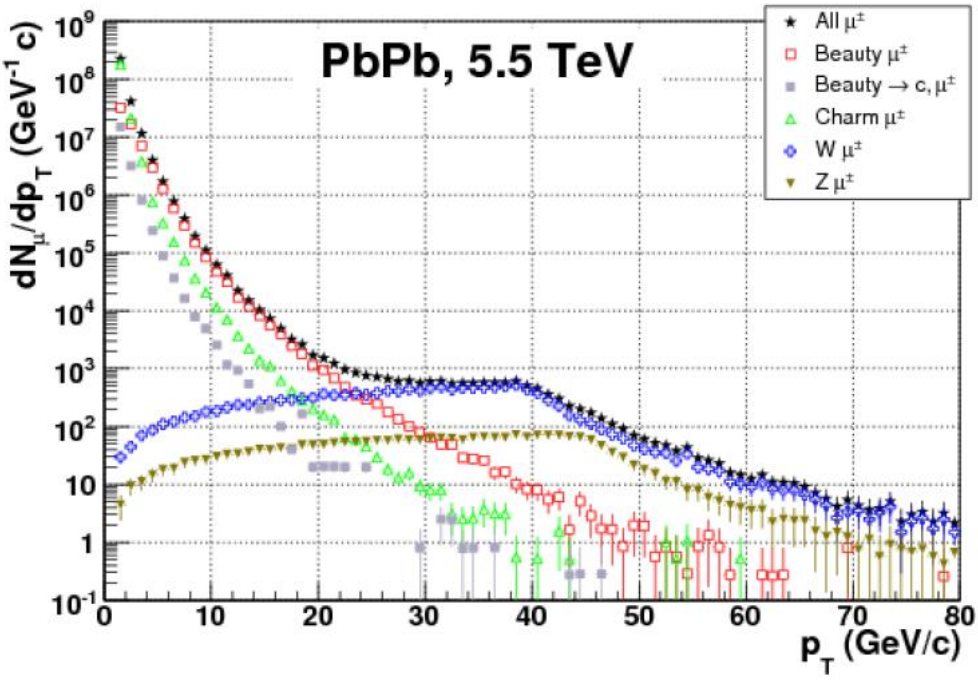

Figure 59: Estimated number of reconstructed muons as a function of p_T for Pb-Pb collisions at 5.5 TeV. Figure taken from [CMAF06].

More tracks were analysed for *Pass 2* than for *Pass 1* (The different values for the number of tracks analysed are summarized in Table 11). This is because the ratio $\frac{Pass\ 2}{Pass\ 1}$ is larger than unity for p_T < 5 GeV/c as can be seen in Figure 58. This shows that the yield of *Pass 2* is higher than the yield of *Pass 1* in this low p_T region by about 5 % and since in this region both yields are very high (10^4 - 10^6) it causes the difference in the total number of tracks for *Pass 1* and *Pass 2* of 3.4 %. It can also be seen that between 5 < p_T < 15 GeV/c the ratio drops below one, but since the yield is much lower in this region than in the p_T < 5 GeV/c region, it does not play such an important role. The limited statistics for both *Pass 1* and *Pass 2* at values of p_T > 30 GeV/c causes a significant scatter in the ratio with large statistical errors.

The p_T distributions of the yield of μ^+ ($\frac{dN_{\mu^+}}{dp_T}$) for *Pass 1* and *Pass 2* are shown in Figure 60, and the ratio $\frac{Pass\ 2}{Pass\ 1}$ is shown in Figure 61. There are also more tracks for *Pass 2* than for *Pass 1*, which the ratio $\frac{Pass\ 2}{Pass\ 1}$ shows us once again comes from the p_T < 5 GeV/c region. Both distributions show the same shape. Here there is not the same increase (or plateau) observed in the high-p_T region (20 < p_T <40 GeV/c), as was the case for the $\mu^{\pm}$ distributions. Lack of statistics leads to a scatter in the ratio and there is even an empty bin at p_T = 36 GeV/c since there are no tracks in *Pass 1* for this bin.

The p_T distributions of the yield of μ^- ($\frac{dN_{\mu^-}}{dp_T}$) for *Pass 1* and *Pass 2* are shown in Figure 62, and the ratio $\frac{Pass\ 2}{Pass\ 1}$ is shown in Figure 63. And yet again there are more tracks in *Pass 2* than in *Pass 1* for the similar reason as explained before. *Pass 1* and *Pass 2* have similar trends and show an increase in the yield in the region 20 < p_T < 40 GeV/c. These differences in the yields of the μ^+ and μ^- in this region could be an indirect result of the production of $W^{\pm}$ bosons. This will be discussed later when

examining the ratio $\frac{\mu^+}{\mu^-}$ (charge asymmetry). The ratio $\frac{Pass\ 2}{Pass\ 1}$ shows the same scatter at higher values of p_T due to the lack of statistics, similar to the μ^- scenario.

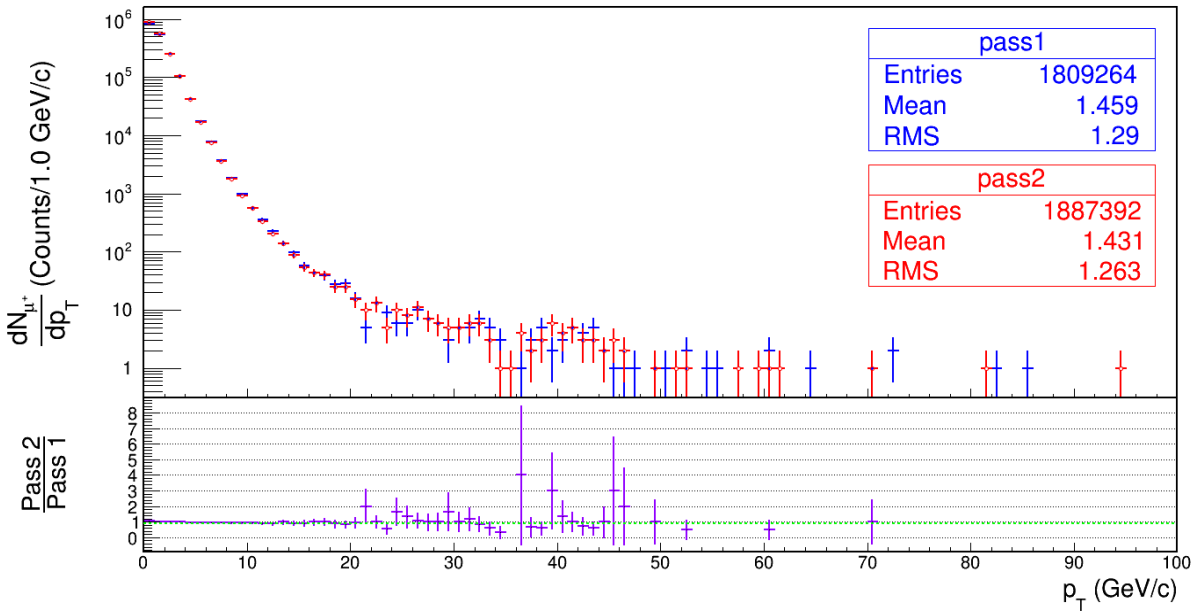

Figure 60: The *Pass 1* (blue) and *Pass 2* (red) p_T distributions of μ^+ for Pb-Pb data collected at $\sqrt{s_{NN}}$ = 2.76 TeV from data taking period LHC11h. The ratio $\frac{Pass\ 2}{Pass\ 1}$ is shown in purple.

.

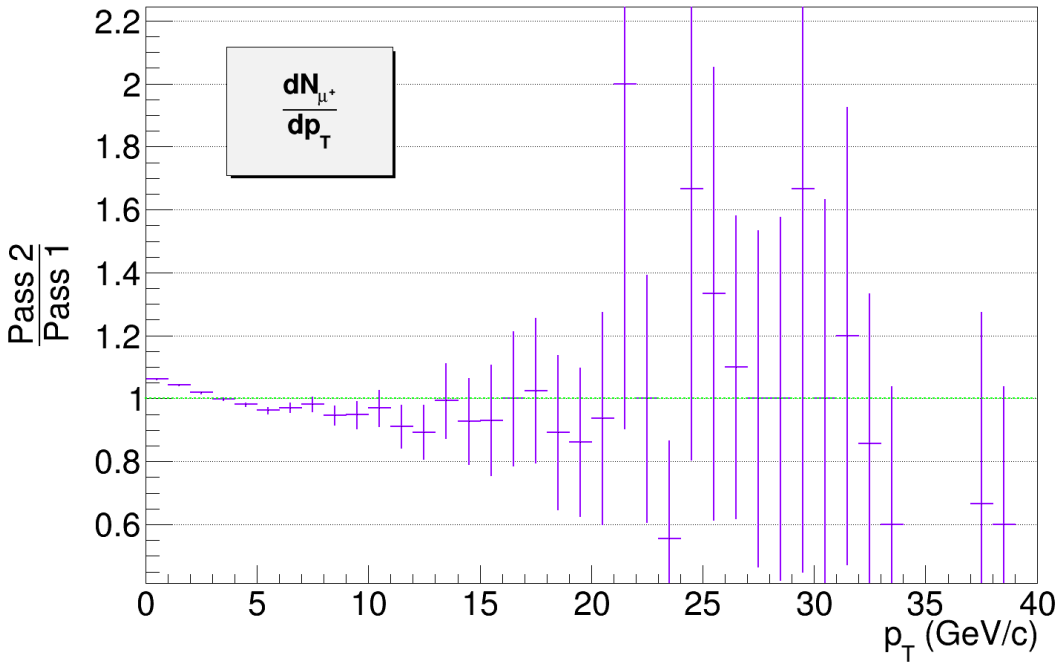

Figure 61: Ratio of $\frac{Pass\ 2}{Pass\ 1}$ for the p_T distributions of μ^+ for Pb-Pb data collected at $\sqrt{s_{NN}}$ = 2.76 TeV from data taking period LHC11h.

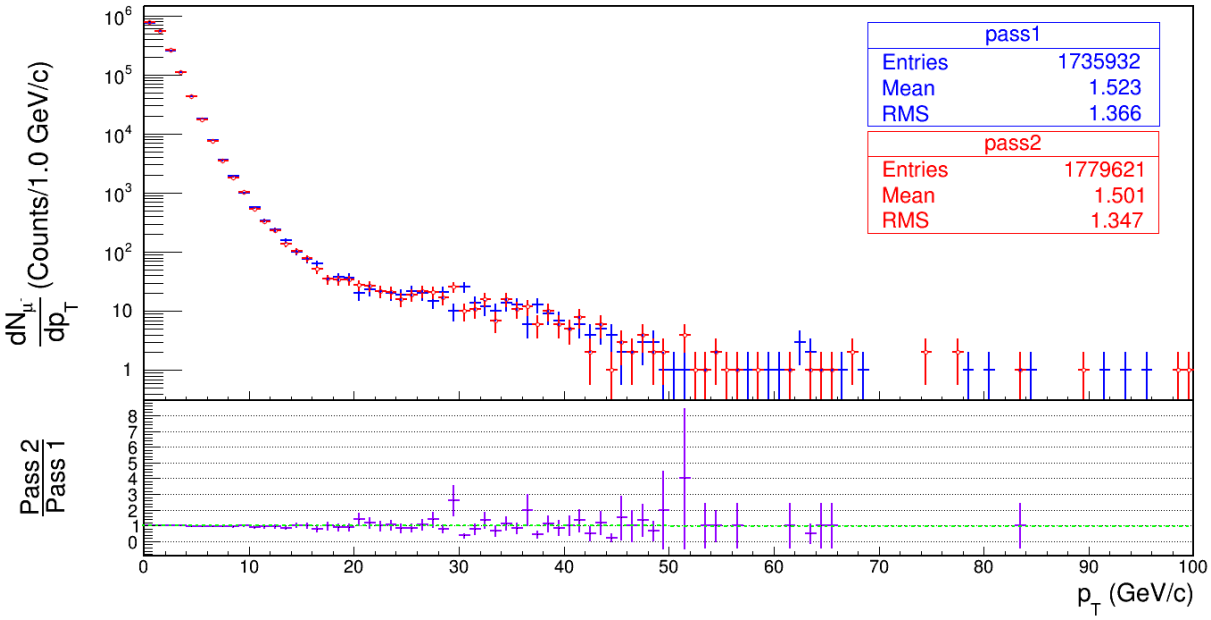

Figure 62: The *Pass 1* (blue) and *Pass 2* (red) p_T distributions of μ^- for Pb-Pb data collected at $\sqrt{s_{NN}}$ = 2.76 TeV from data taking period LHC11h. The ratio $\frac{Pass\ 2}{Pass\ 1}$ is shown in purple.

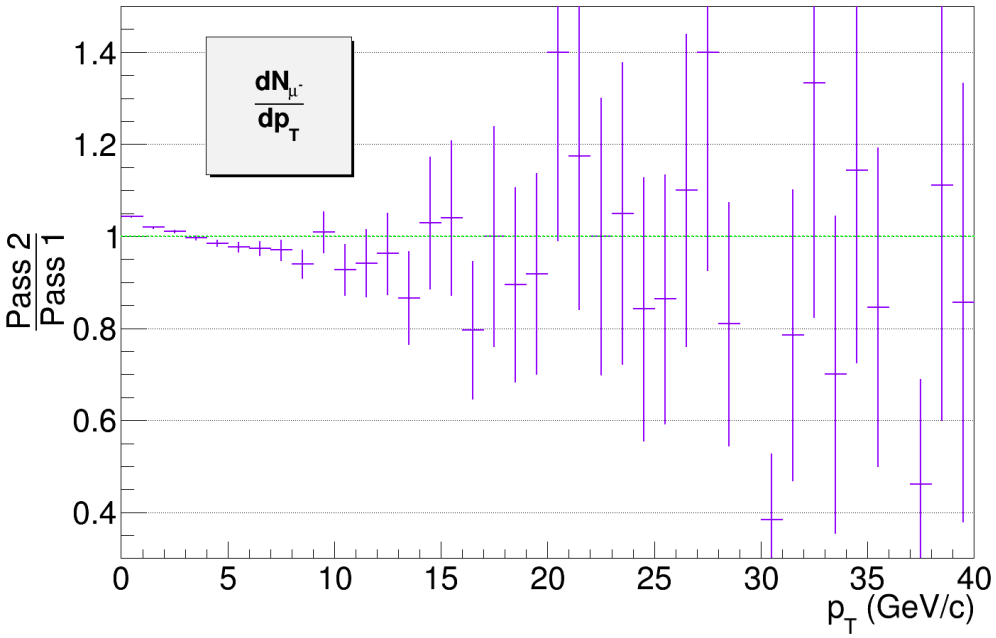

Figure 63: Ratio of $\frac{Pass\ 2}{Pass\ 1}$ for the p_T distributions of μ^- for Pb-Pb data collected at $\sqrt{s_{NN}}$ = 2.76 TeV from data taking period LHC11h.

The comparison between the number of tracks analysed for *Pass 1* and *Pass 2* for the three different cases ($\mu^{\pm}$, μ^+ and μ^-) are summarized in Table 11. It shows that there are consistently more tracks for *Pass 2* than for *Pass 1*. This increase was also seen in a similar study by Zhu and Li [ZL12a]. In that study the total number of tracks were less than in this study for both *Pass 1* and *Pass 2*, but this can be attributed to job efficiency on the grid, i.e. some of their analysis jobs may have finished with errors, resulting in data being lost.

Finally it is also evident from the analysis of the p_T distributions of *Pass 1* and *Pass 2* that there is not a notable difference for the new alignment used in *Pass 2.*

2. Charge asymmetry

Figure 64 shows the ratio $\frac{\mu^+}{\mu^-}$ (charge asymmetry) for *Pass 1* and *Pass 2*. Both Pass1 and Pass2 show very similar trends. The ratios are slightly above unity for p_T < 2 GeV/c (more μ^+ than μ^-) and then remain close to unity (μ^+ and μ^- the same) for 2 < p_T < 10 GeV/c. Next the ratios drop below one (more μ^- than μ^+) at around p_T = 10 GeV/c and then continue to be negative. For p_T > 35 GeV/c the lack in statistics causes the scattering of the data points and it is hard to say anything conclusive for this region.

As was mentioned earlier when the difference in the p_T distributions was noticed, this charge asymmetry in the high-p_T region (20 < p_T < 40 GeV/c) could indicate the production of $W^{\pm}$ bosons. This is due to the fact that in Pb-Pb collisions the production of W^- is favoured over W^+ because of the isospin content of the colliding Pb nuclei. Therefore in this high-p_T region (approximately half the $W^{\pm}$ boson mass) where $\mu^{\pm} \leftarrow W^{\pm}$ are the dominating contribution to the total p_T distribution, more μ^- than μ^+ should be detected. For further explanation see Chapter II.E.4, p. 27.

The shape of the charge asymmetry shown in this analysis does remarkably resemble that of the performance study by Conesa del Valle [CdV07] given in Figure 66, even with the limitations in the statistics. This qualitative comparison would suggest that $W^{\pm}$ bosons were indeed detected through its semi-muonic decay channel during the Pb-Pb data taking period.

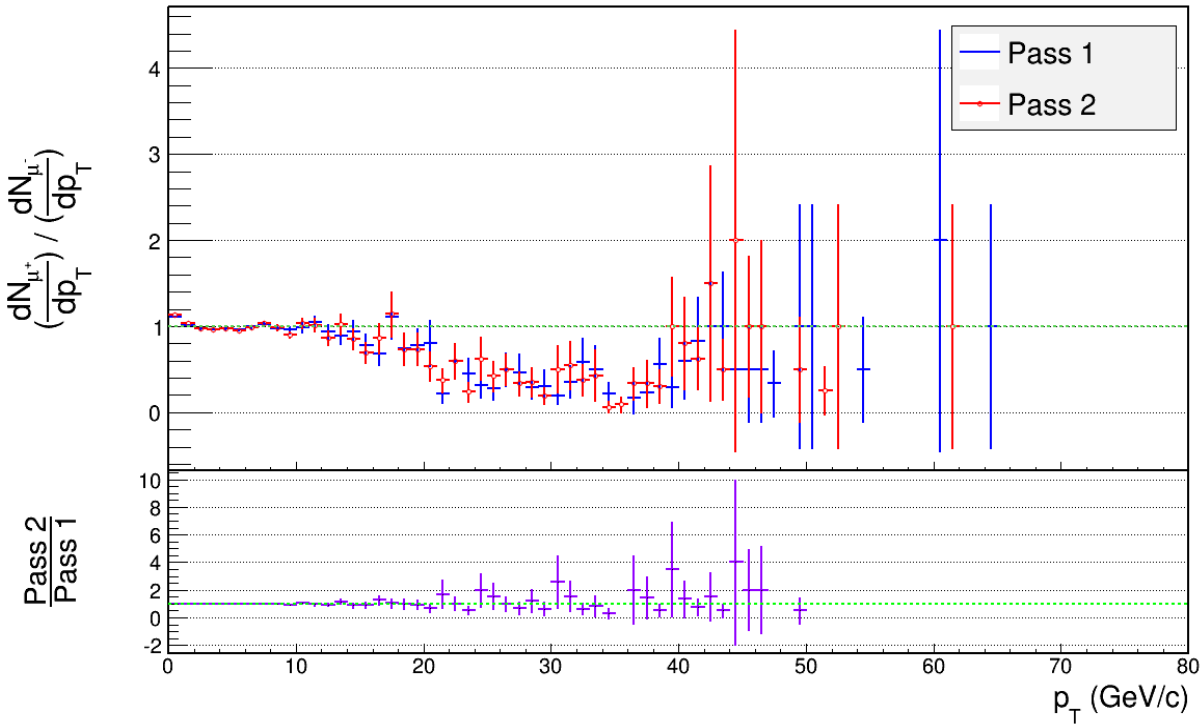

Figure 64: The ratio of $\frac{\mu^+}{\mu^-}$ (charge asymmetry) as a function of p_T for LHC11h *Pass 1* (blue) and for *Pass 2* (red). The ratio $\frac{Pass\ 2}{Pass\ 1}$ is shown in purple

The ratio $\frac{Pass\ 2}{Pass\ 1}$ is magnified in Figure 65 and is only slightly above one for p_T < 5 GeV/c and close to unity for p_T < 10 GeV/c. At higher values of p_T the ratio becomes too scattered to make any clear comparison.

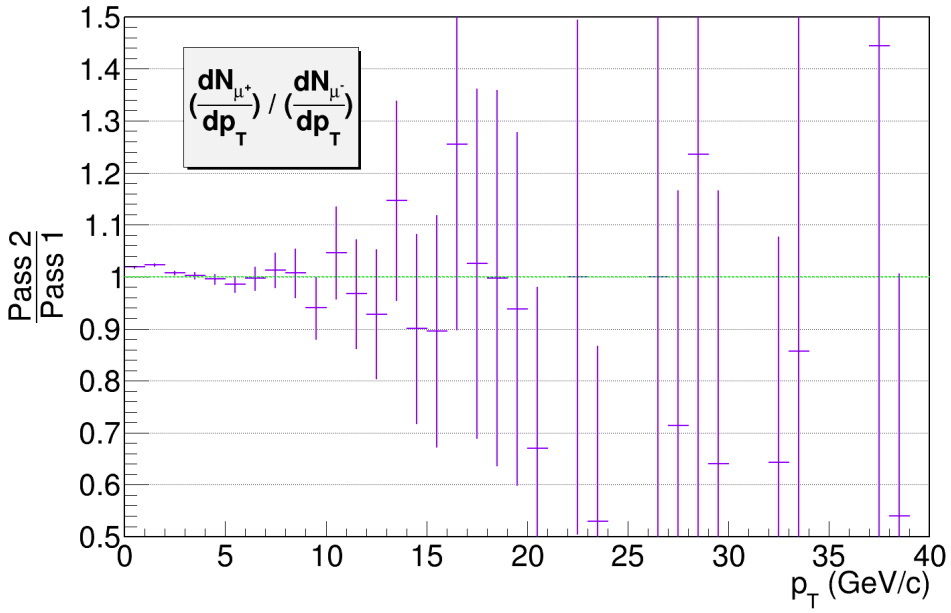

Figure 65: Ratio of $\frac{Pass\ 2}{Pass\ 1}$ for the charge asymmetry of μ^- for Pb-Pb data collected at $\sqrt{s_{NN}}$ = 2.76 TeV from data taking period LHC11h.

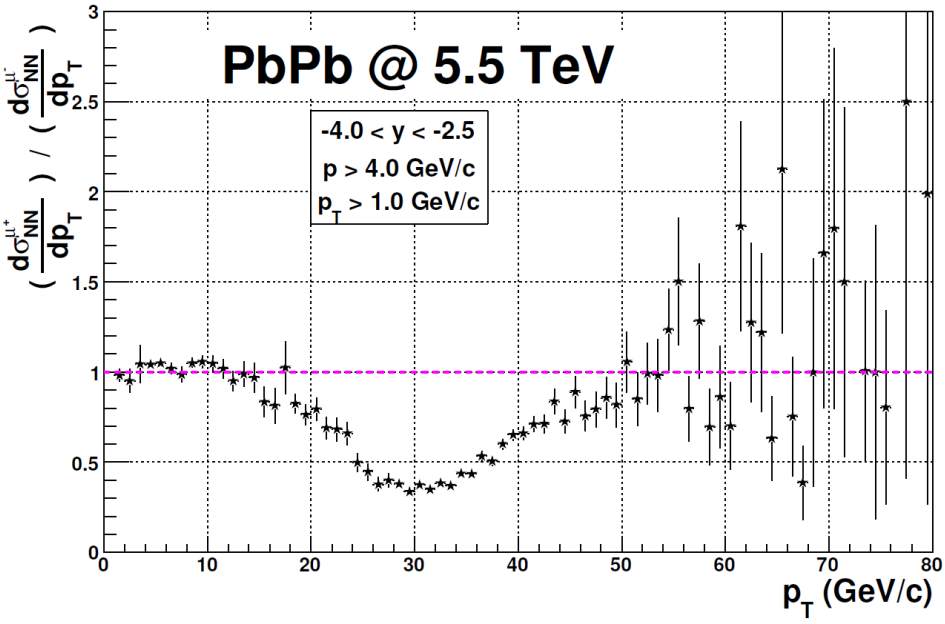

Figure 66: Single muon charge asymmetry (ratio of $\frac{\mu^+}{\mu^-}$) as a function of p_T for Pb-Pb collisions at $\sqrt{s_{NN}}$ = 5.5 TeV in the ALICE Muon Spectrometer acceptance. Figure from [CdV07]

3. Pseudorapidity (η) distribution

The η distributions of $\mu^{\pm}$ (Figure 67) show that the trends for both *Pass 1* and *Pass 2* are the same, but slightly lower for *Pass 1* than for *Pass 2*. This is due to the larger number of tracks for *Pass 2* than for *Pass 1* already mentioned before. The differences between the *Pass 1* and *Pass 2* distributions are relatively small and only increases somewhat in the bins between -4 < η < -3.2. In bin -4 < η < -3.9 the largest difference is observed, where the number of tracks is less than in bin -3.9 < η < -3.8 for *Pass 1* and more for *Pass 2*, respectively.

Furthermore the trends of both distributions are decreasing (higher number of tracks at η = -4, than at η = -2.5), which is opposite to the behavior seen in the η distributions extracted from the pp simulation of $\mu^{+} \leftarrow W^{+}$ and $\mu^{-} \leftarrow W^{-}$ (Figure 55 and Figure 56, p. 84). This decrease is also observed in the similar study by Zhu and Li when extracting the single muons which trigger the high-p_T trigger (MSH trigger) from LHC11h *Pass 1* and *Pass 2* [ZL12a]. In that study the single muon tracks which satisfy the low-p_T trigger (MSL trigger) are also studied and the η distributions of these single muons show an increasing trend. This difference in the trends between MSH and MSL triggered tracks is related to the kinematics of the tracks, as there is an interplay between p_T and η. Tracks with high p_T will mostly be detected at mid-rapidity and tracks with low p_T will mostly be detected at higher rapidity [Sto13b].

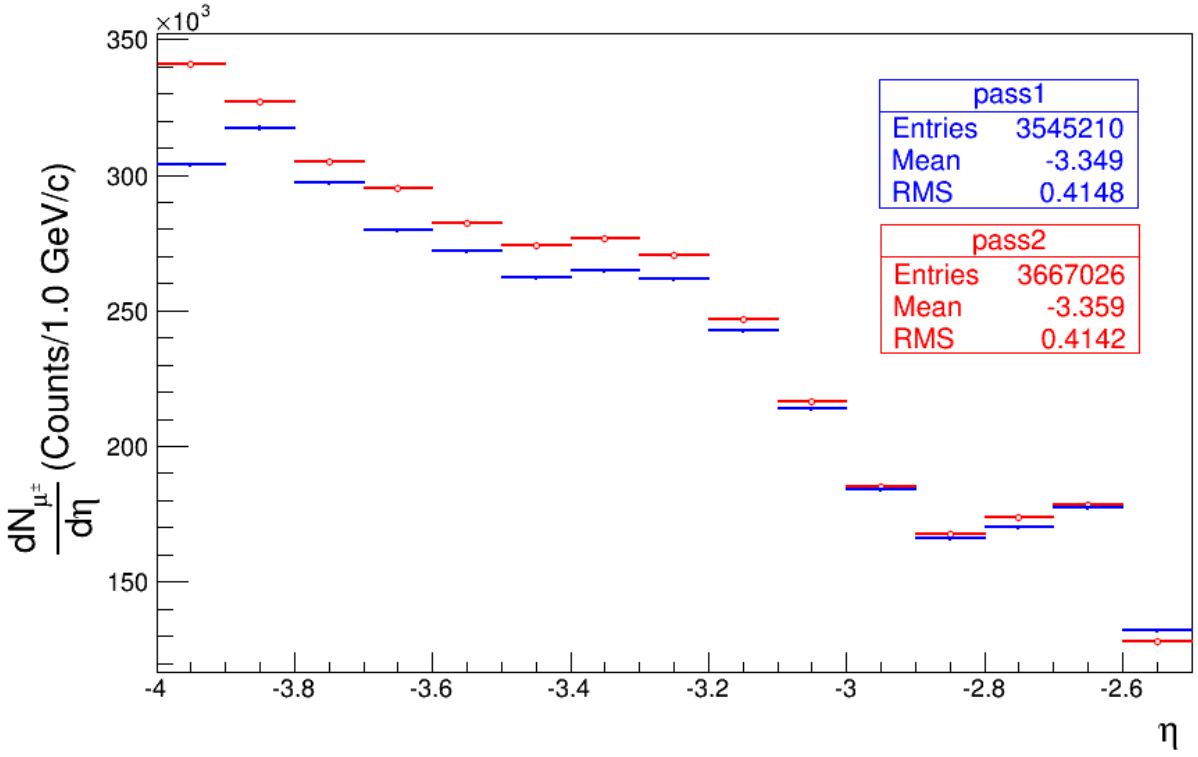

Figure 67: The *Pass 1* (blue) and *Pass 2* (red) η distributions of $\mu^{\pm}$ for Pb-Pb data collected at $\sqrt{s_{NN}}$ = 2.76 TeV from data taking period LHC11h.

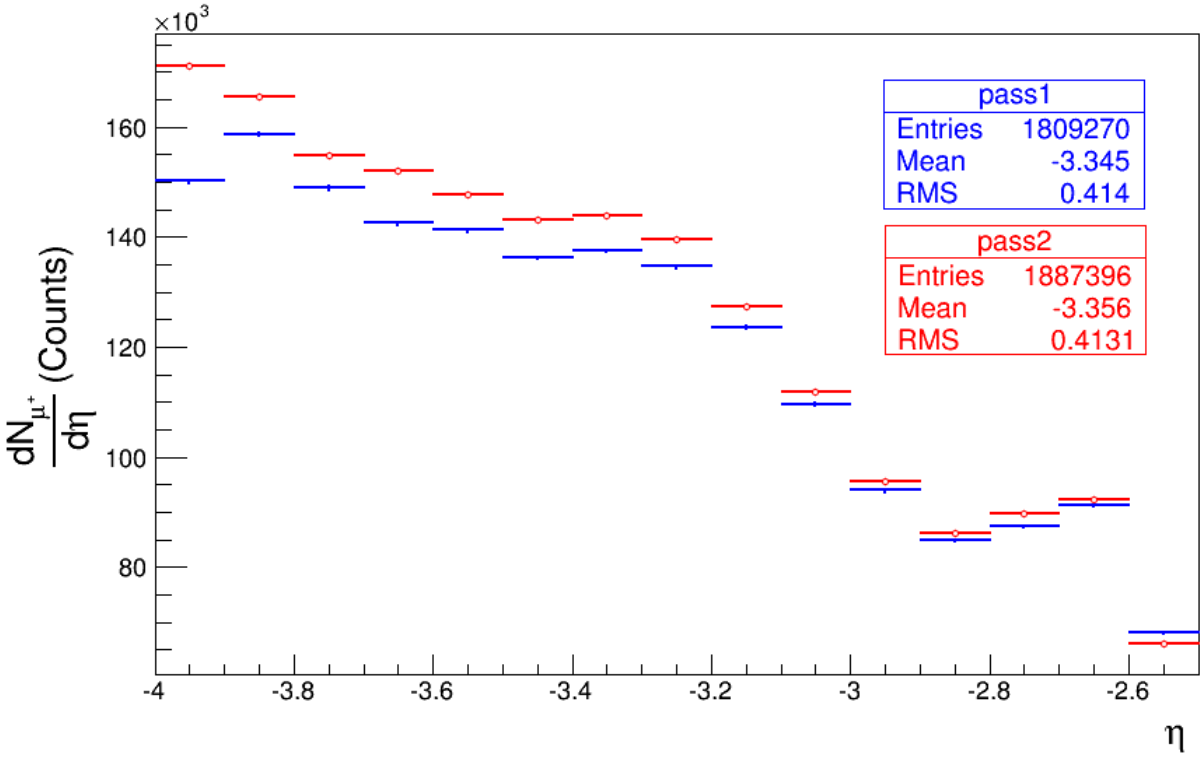

Figure 68: The *Pass 1* (blue) and *Pass 2* (red) η distributions of μ^+ for Pb-Pb data collected at $\sqrt{s_{NN}}$ = 2.76 TeV from data taking period LHC11h.

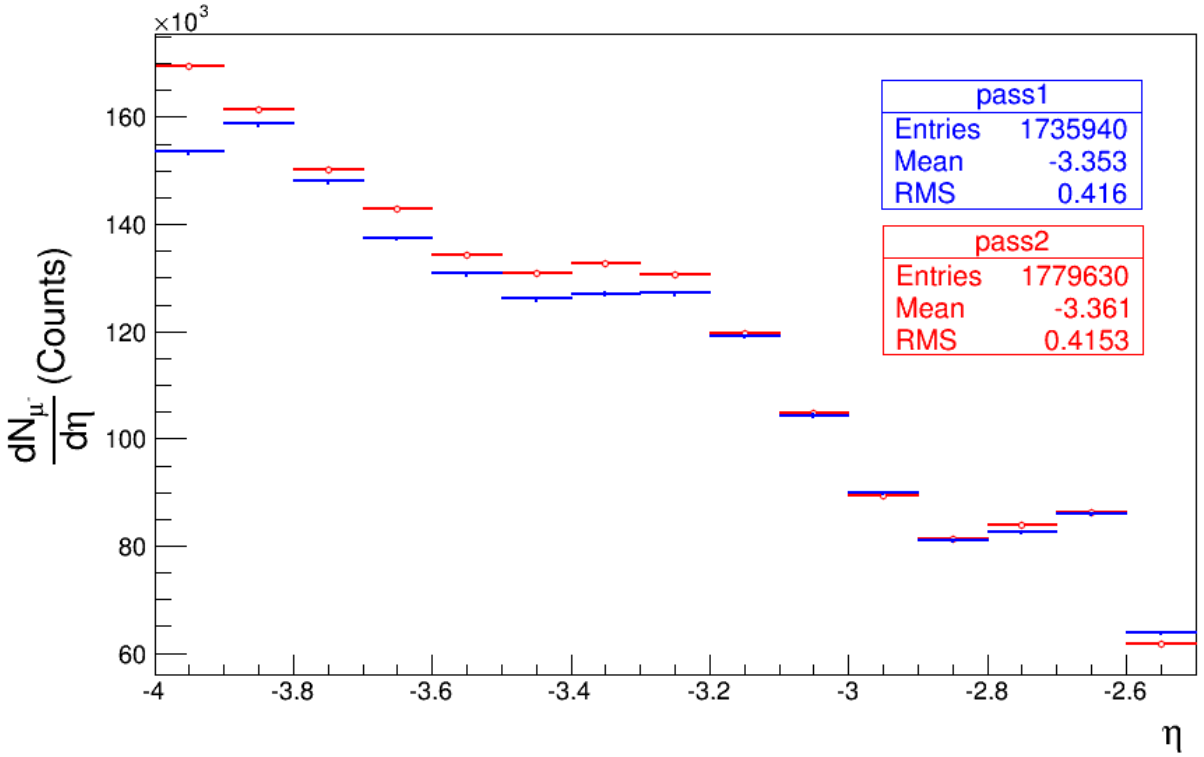

Figure 69: The *Pass 1* (blue) and *Pass 2* (red) η distributions of μ^- for Pb-Pb data collected at $\sqrt{s_{NN}}$ = 2.76 TeV from data taking period LHC11h.

Another interesting observation can be made in the region between -2.9 < η < -2.5. Here we see that the number of tracks increases from -2.9 < η < -2.6, and then drops in bin -2.6 < η < -2.5. This drop in bin -2.6 < η < -2.5 could be related to the drop also observed in the same bin of the simulation sample (Figure 55 and Figure 56, p. 84), which would mean that there is indeed a real effect caused by the acceptance and efficiency ($A \times \epsilon$) of the spectrometer (See discussion in section A.3, p. 81). But this could also be seen, not as a drop in bin -2.6 < η < -2.5, but rather as an enhancement in bins -2.8 < η < -2.6, which could also be related to the status of the detector (dead channels, etc.) [Sto13b]. Unfortunately this could not be compared further to the study by Zhu and Li [ZL12a], since the sizes of bins in that study are too large (0.3) compared to this study (0.1) to draw any meaningful conclusions.

4. Possible W± boson extraction

The $W^{\pm}$ boson signal can be extracted in the high-p_T region by applying a fit to the background distribution in the low-p_T region, extrapolating this fit to the high-p_T region and then subtracting this from the p_T distribution. This fit can be made between different regions in the low p_T region, e.g. (7, 13), (8, 15) and it is still not known which fit give the correct contribution from charm and beauty decays. Unfortunately the statistics are limited due to the fact that the luminosity achieved in 2011 was lower than at first expected, and thus insufficient for a meaningful $W^{\pm}$ boson study. Therefore it was decided not to try and extract the $W^{\pm}$ boson signal in this study.

Once the $W^{\pm}$ boson can be extracted from the measurements, it could be possible to calculate the nuclear modification factor, R_{AA}. For this calculation (see Chapter II.D.5) a pp reference also at $\sqrt{s_{NN}}$ = 2.76 TeV is needed. Unfortunately the statistics for these pp runs are also limited and it is impossible to extract a meaning $W^{\pm}$ boson signal from them as well.

5. Summary

The results of the alignment study using the original alignment (*Pass 1*) and improved alignment (*Pass 2*) of Pb-Pb data collected in collisions at $\sqrt{s_{NN}}$ = 2.76 TeV, shows that the effect of the alignment is limited on the p_T distributions, the ratio of $\frac{\mu^+}{\mu^-}$ (charge asymmetry) and the η distributions.

The lack of statistics makes it hard to make any definite conclusions in the high-p_T region, but the charge asymmetry does show remarkable resemblance to the prediction made by the performance study of Conesa del Valle [CdV07].

The peculiar drop which was observed in the -2.6 < η < -2.5 bin for the simulation study was also observed here, and it would seem that this is then an effect caused by the configuration of the detector, i.e. the acceptance and efficiency ($A \times \epsilon$). Although in the simulation the drop could be more pronounced since tracks which could have entered the spectrometer via multiple scattering, etc. from just outside of the acceptance range were never even generated in the simulation due to the restraint set in the configuration file for the muons to be inside the acceptance of the spectrometer.

Chapter VI. Summary and Conclusions

A. Summary

In Chapter I the reader was introduced to the prediction by lattice Quantum Chromodynamics (lQCD) that under conditions of extreme energy density and temperature a deconfined state of matter, known as the quark-gluon plasma (QGP), can be formed. These conditions can be attained during heavy-ion collisions, such as Pb-Pb collisions, carried out at the CERN Large Hadron Collider (LHC). There are various methods available to study the QGP which are employed by the ALICE, ATLAS and CMS experiments at the CERN LHC.

One of these available methods is measuring heavy quarks (charm and bottom) leptonic decay products. Heavy quarks are hard probes created early in the collisions due to their large mass. They undergo all the phases of the transition and are affected by the properties of the QGP because they interact via the strong force. By measuring the nuclear modification factor, R_{AA} in Pb-Pb collisions, and using pp collisions as reference, the effects of the deconfined medium on the heavy quarks can be determined. The R_{AA} is not only dependent on the hot nuclear matter effects caused by the formation of the QGP, but also by the cold nuclear matter effects present in the dense Pb nuclei. Therefore these cold matter effects also need to be studied further using p-Pb and Pb-p collisions as references.

Another method of studying the effects of the QGP is by measuring the $W^{\pm}$ boson leptonic decay products. The ALICE central barrel measures electrons in the mid-rapidity region ($|y| < 0.9$) and the Muon Spectrometer is able to measure the semi-muonic decay channel at forward rapidity ($2.5 < y < 4$) down to p_T values of $\sim$ 0.5 GeV.c. The $W^{\pm}$ boson which is created at the high energies available at the LHC is an excellent observable of the initial state of the collision because it is formed early in the collision and does not interact strongly with the QGP. Therefore it is not affected by the QGP and can be used as a reference when studying effects on other probes. There are many reasons to study the $W^{\pm}$ boson. It can be used as a standard candle in luminosity measurements and thereby to measure detector performances; it provides information on the Parton Distribution Functions (PDFs) of the quarks at small Bjorken-x values in pp collisions; it can be used to study the cold nuclear modification effects such as nuclear shadowing in p-A collisions; and it is a medium blind reference for the effects induced by the QGP on other probes in Pb-Pb collisions.

The importance of the alignment of the chambers and detector elements (DEs) of the Muon Spectrometer was also discussed and it was determined that in order to do a comprehensive study of muons at high transverse momentum (high-p_T) the effects caused by any misalignment have to be fully understood. These effects result in a systematic uncertainty in the measurements, which will influence any single muon study, such as the study of $W^{\pm}$ boson production at high-p_T.

VI. Summary and Conclusions

Chapter II gave the theoretical background involved in studying the QGP. The Standard Model of elementary particles and some properties of the theory of Quantum Chromodynamics (QCD) were discussed. The formation of the QGP was looked at and the observables available to study the QGP were stated. Some of the aspects in heavy flavour physics were also elaborated on, with special emphasis on hot nuclear matter effects in A-A collisions, such as heavy quark energy loss. The definition of the nuclear modification factor R_{AA} was given and it was discussed extensively. Chapter II also focussed on the electroweak theory and the $W^{\pm}$ boson production mechanisms. The charge asymmetry of $W^{\pm}$ boson production in pp and Pb-Pb collisions was explained, as well as the effects of parity violation in the leptonic decay of the $W^{\pm}$ boson. Lastly the different muon sources contributing to the single muon spectra at LHC energies were briefly discussed.

The LHC and ALICE were described in Chapter III with special emphasis on the Muon Spectrometer. The methods of aligning the Muon Tracker Chambers were discussed and the Muon Trigger system explained. The online data taking systems (CTP, DAQ, HLT and DCS) were also illustrated and the procedures employed in the ALICE Control Room (ACR) during data taking were looked at.

Chapter IV introduced the offline framework AliROOT. This set of software tools is built up from the ROOT framework and is based on object orientated programming in order to achieve modularity and re-usability. Its purpose is to simulate the hadronic collisions using event generators such as Pythia and HIJING, to reconstruct the events by integrating with transport packages like Geant4 and to analyse the reconstructed data. The analysis is realized by the ALICE Grid which provides the user access to the data in a transparent way by the use of the ALICE environment (AliEN) and can be monitored easily using MonALISA. The different selection cuts which can be applied to data were also discussed.

This chapter then showed the simulation and analysis techniques used in the production of $W^{\pm}$ boson signal for an ideal alignment and several different misalignments. The simulation was performed at $\sqrt{s}$ = 8 TeV with PYTHIA 6.4.21 and specific restraints were set in the configuration file (Config.C) used in the simulation and reconstruction. Selection cuts were then applied to the muon tracks during the analysis and the p_T distributions and charge asymmetry, as well as the η distributions of the muons decaying from $W^{\pm}$ bosons were extracted.

Next, the conditions during the data taking for Pb-Pb collisions at $\sqrt{s_{NN}}$ = 2.76 TeV in 2011 (LHC11h) were given. The particulars of the trigger class used in the analysis were also revisited. The Quality Assurance (QA) selection process which required the data runs to meet certain criteria was then taken into account and some runs were rejected due to the QA results. The efficiencies of the Muon Tracker and Muon Trigger were found to be roughly 87 % and 95 %, respectively. Afterwards selection cuts were applied to the original (*Pass 1*) and refitted (*Pass 2*) data and the p_T distributions, charge asymmetry and η distributions of muon tracks passing the cuts were examined.

The results of both the simulation alignment study and the data analysis were shown and discussed in Chapter V. Some interesting observations and conclusions were made from the results of the simulation alignment study and the data analysis. These conclusions will now be given in the next section.

B. Conclusions

To conclude, a preliminary alignment study was completed on $W^{\pm}$ boson signal obtained from pp simulations generated at $\sqrt{s}$ = 8 TeV with PYTHIA 6.4.21. This was done to first determine the effect of the misalignment of the Muon Spectrometer chambers and detector elements (DEs) on a single muon analysis of $W^{\pm}$ bosons.

After applying selection cuts to the simulated pp data, the ideal and residual cases could be compared. Significant changes for both of the p_T distributions of $\mu^+ \leftarrow W^+$ and $\mu^- \leftarrow W^-$ were observed. For both of the p_T distributions of $\mu^+ \leftarrow W^+$ and $\mu^- \leftarrow W^-$ the peaks of the residual misalignment cases are shifted and wider compared to the ideal case. The charge asymmetry $\frac{\mu^+ \leftarrow W^+}{\mu^- \leftarrow W^-}$ of the residual cases showed a large spread between 25 < p_T < 40 GeV/c, which became even worse in the range p_T > 40 GeV/c. Therefore, from this preliminary analysis it was concluded that the alignment will have an effect on the study of high-p_T single muons decaying from $W^{\pm}$ bosons. The p_T distributions and especially the charge asymmetry showed remarkable changes under different misalignments. This confirmed that the misalignment of the Muon Spectrometer chambers and DEs does indeed result in a systematic uncertainty of around 50 % in the region 25 < p_T < 40 GeV/c and even larger than 50 % in the high-p_T region where the $W^{\pm}$ boson will be measured (p_T > 40 GeV/c).

In contrast to this, it was found that the alignment did not affect the η distributions severely, but that the small changes observed in the η distributions are only caused by the differences between the ideal (100 % efficient with no dead channels or missing DEs) and realistic (true efficiency and dead channels and missing DEs from LHC11h included) status of the Muon Spectrometer. None the less, the η distributions did show a strange behaviour in the -2.6 < η < -2.5 bin. There is a significant drop of ~ 36 % for $\mu^+ \leftarrow W^+$ and ~ 37 % for $\mu^- \leftarrow W^-$ compared to the -2.7 < η < -2.6 bin observed in this range, which could be caused either by the simulation configuration or by a true acceptance and efficiency ($A \times \epsilon$) effect of the spectrometer. It was decided to study this further in the Pb-Pb collisions analysis, to determine whether this is a real effect observed in data as well.

Comparison was also made between the results of this study and that of the performance study which predicted the outcome of $W^{\pm}$ boson studies in pp simulations at $\sqrt{s}$ = 14 TeV. The two studies do show some similar trends in the p_T distributions, charge asymmetry $\frac{\mu^+ \leftarrow W^+}{\mu^- \leftarrow W^-}$ and the η distributions for the ideal case. But since there are differences in the centre-of-mass energies, as well as the PDFs used in the simulations, the comparison can only be done qualitatively and not quantitatively. The residual cases do not compare well to the prediction at all, which proves that the performance of the Muon Spectrometer is influenced by the residual misalignment of the Muon Spectrometer chambers and DEs.

In order to check the effect of alignment on data, a study on Pb-Pb collisions at $\sqrt{s_{NN}}$ = 2.76 TeV from 2011 (LHC11h) was conducted. Original data (*Pass 1*) and data which had been refitted to an improved alignment (*Pass 2*) were compared. The efficiency of the Muon Trigger Chambers are the same for *Pass 1* and *Pass 2* at around 95 %, while the efficiency of the Muon Tracker increased slightly from 86.8 % to 87.3 %. Unfortunately the statistics are limited in the high-p_T region, making it difficult to compare the two data sets in the region of interest of this study. With the low statistics the comparison between *Pass 1* and *Pass 2* showed that the effect due to the improvement in the

alignment is negligible in the high-p_T region for the p_T distributions of $\mu^{\pm}$, μ^{+} and μ^{-}. The charge asymmetry $\frac{\mu^{+}}{\mu^{-}}$ is similarly unchanged in this region. However in the low-p_T region where much more statistics are available, there is a difference in the number of tracks for *Pass 1* and *Pass 2,* with more tracks for *Pass 2,* than for *Pass 1*. Therefore the improvement in alignment, results in more muons being reconstructed at low p_T, while at high p_T with the limited number of muons being detected, there does not seem to be an obvious improvement. But, since the low p_T muons determine the baseline of the muons decaying from c and b quarks, which has to be taken into account at high p_T, this should have an effect on the final number of $W^{\pm}$ bosons being measured. Later studies with more statistics and better improvements on the alignment might give extra insights into the effect of alignment on the detector performance.

The η distributions for *Pass 1* and *Pass 2* are also not significantly different, with the trends being similar in both cases. The drop in the -2.6 < η < -2.5 bin which was observed in the η distributions of the misalignment simulations was also seen in the data analysis and it proved that the acceptance and efficiency ($A \times \epsilon$) of the Muon Spectrometer influences the η distributions in this region. This effect still requires further investigation and comparison to other ongoing studies might clarify this behaviour.

The shapes of the charge asymmetry in *Pass 1* and *Pass 2* are similar to that of the prediction of the performance study, which would suggest that $W^{\pm}$ bosons were detected.

It was decided not to yet attempt a complete $W^{\pm}$ boson analysis due to the lack of statistics. This further requires the determination of the background from muons decaying from heavy flavour (c, b) by applying a fit in the low-p_T region and subtracting that from the total p_T distribution. This method is currently being studied and refined. Also, seeing as the statistics in the range 30 < p_T < 80 GeV/c were limited the extraction of a meaningful $W^{\pm}$ boson signal and therefore also of the nuclear modification factor R_{AA} was deemed to be improbable at this stage.

C. Outlook

The way forward is to analyse Pb-Pb data from 2012 in order to cross-check any new results to this analysis. Once enough statistics have been accumulated a complete $W^{\pm}$ boson study can be done. With enough statistics the background from charm and bottom decays can be subtracted using a fit in the low-p_T region and extrapolating their contribution to high-p_T. Other methods to extract the $W^{\pm}$ boson yield have been used by CMS [CMS12] and a similar approach has been tested in ALICE in a preliminary study [ZL12a, ZL12b]. This method fits the p_T distribution of the Pb-Pb data to two different components: the first being the shape of the $W^{\pm}$ boson muonic decays simulated in pp events and the second being the background from charm and bottom modelled by a modified Rayleigh function with three parameters. Once the production cross section of the $W^{\pm}$ boson can be obtained from these analyses, it could be used as a standard candle for luminosity measurements and to evaluate the detector performance. The production cross sections of the $W^{\pm}$ boson could also provide information on the quark Parton Distribution Function (PDF).

Furthermore, there has recently been a new improvement on the *Pass 2* data. The same alignment is used in the new reconstruction, but the resolution has been further improved by removing the mono-cathode clusters in the reconstruction [Pil12b]. The focus of this study was to show the

improvement only due to alignment, but it could be further extended to study the complete improvement from *Pass 1* to these newer *Pass 2* data sets. This study also showed that in the low-p_T region the alignment does have an effect on the p_T distributions and therefore should influence heavy flavour and quarkonium studies. Indeed in J/Ψ studies *Pass 2* gives approximately 2300 more J/Ψ's than in *Pass 1* [Val12].

A measurement of the nuclear modification factor R_{AA} could also be made in the future. Unfortunately the pp reference which is needed to calculate the R_{AA} is currently still unavailable, due to the fact that pp statistics in 2011 (LHC11c and LHC11d) are too poor to have a precise measurement. The pp reference could be obtained either from analysing data from 2012 or from using theoretical models validated on ATLAS and CMS data. Once the Pb-Pb data can be compared to the pp reference, the R_{AA} can be determined. This can help to understand the modifications of the nuclear PDFs in the lead nucleus compared to the proton. Comparison could also be made to results on $W^{\pm}$ boson production by ATLAS and CMS as well as to the results from other studies in ALICE using the electron decay channel at mid-rapidity.

The LHC completed several p-Pb runs in 2013 and analyses are underway which will enable checking the contribution of cold nuclear effects to the nuclear modification factor. These analyses will give more information on the quark PDFs and cold nuclear matter effects, such as nuclear shadowing and absorption.

Currently the LHC is scheduled for upgrades until 2015 giving an opportunity to focus on preparing and analysing the data obtained thus far. When the LHC will hopefully restart at its nominal energies of $\sqrt{s_{NN}}$ = 14 TeV for pp and $\sqrt{s_{NN}}$ = 5.5 TeV for Pb-Pb the luminosities reached will provide sufficient statistics to further study $W^{\pm}$ boson production at ALICE, thereby enabling further studies into the initial conditions of the interaction and the properties of the QGP.

Appendix A. Simulation and Reconstruction files

A. Configuration file (Config.C) used in Ideal Case

```
// Config file MUON + ITS (for vertex) for PDC06
// Tuned for p+p min biais and quarkonia production (AliGenMUONCocktailpp)
// Remember to define the directory and option
// gAlice->SetConfigFunction("Config('$HOME','box');");
// april 3rd: added L3 magnet
#if !defined(__CINT__) || defined(__MAKECINT__)
#include <Riostream.h>
#include <TRandom.h>
#include <TDatime.h>
#include <TSystem.h>
#include <TVirtualMC.h>
#include <TGeant3TGeo.h>
#include "STEER/AliRunLoader.h"
#include "STEER/AliRun.h"
#include "STEER/AliConfig.h"
#include "PYTHIA6/AliDecayerPythia.h"
#include "PYTHIA6/AliGenPythia.h"
#include "TDPMjet/AliGenDPMjet.h"
#include "STEER/AliMagFCheb.h"
#include "STRUCT/AliBODY.h"
#include "STRUCT/AliMAG.h"
#include "STRUCT/AliABSOv3.h"
#include "STRUCT/AliDIPOv3.h"
#include "STRUCT/AliHALLv3.h"
#include "STRUCT/AliFRAMEv2.h"
#include "STRUCT/AliSHILv3.h"
#include "STRUCT/AliPIPEv3.h"
#include "ITS/AliITSv11Hybrid.h"
#include "TPC/AliTPCv2.h"
#include "TOF/AliTOFv6T0.h"
#include "HMPID/AliHMPIDv3.h"
#include "ZDC/AliZDCv3.h"
#include "TRD/AliTRDv1.h"
```

A. Simulation and Reconstruction files

```
#include "TRD/AliTRDgeometry.h"
#include "FMD/AliFMDv1.h"
#include "MUON/AliMUONv1.h"
#include "PHOS/AliPHOSv1.h"
#include "PHOS/AliPHOSSimParam.h"
#include "PMD/AliPMDv1.h"
#include "T0/AliT0v1.h"
#include "EMCAL/AliEMCALv2.h"
#include "ACORDE/AliACORDEv1.h"
#include "VZERO/AliVZEROv7.h"
#endif

//--- Functions ---
class AliGenPythia;
void ProcessEnvironmentVars();

static Int_t runNumber = 0;
TDatime dt;
static UInt_t seed = dt.Get();

// Comment line
static TString comment;

void Config()
{
  // Get settings from environment variables
   ProcessEnvironmentVars();

   gRandom->SetSeed(seed);
   cerr<<"Seed for random number generation= "<<seed<<endl;

   //=======================================================================
 //  Libraries required by geant321
#if defined(__CINT__)
   gSystem->Load("liblhapdf");      // Parton density functions
   gSystem->Load("libEGPythia6");   // TGenerator interface
   gSystem->Load("libpythia6");     // Pythia
   gSystem->Load("libAliPythia6");  // ALICE specific implementations
   gSystem->Load("libgeant321");
#endif
   new TGeant3TGeo("C++ Interface to Geant3");
```

A. Simulation and Reconstruction files

```
//  Create the output file
  AliRunLoader* rl=0x0;
  cout <<"Config.C: Creating Run Loader ..."<< endl;
  rl = AliRunLoader::Open(
            "galice.root", AliConfig::GetDefaultEventFolderName(), "recreate");
  if (rl == 0x0) {
  gAlice->Fatal("Config.C","Can not instatiate the Run Loader");
  return;
  }
  rl->SetCompressionLevel(2);
  rl->SetNumberOfEventsPerFile(10000);
  gAlice->SetRunLoader(rl);

//=======================================================================
// Set External decayer
  TVirtualMCDecayer *decayer = new AliDecayerPythia();
  decayer->SetForceDecay(kAll);
  decayer->Init();
  gMC->SetExternalDecayer(decayer);

//=======================================================================
// ******* GEANT STEERING parameters FOR ALICE SIMULATION *******
  gMC->SetProcess("DCAY",1);
  gMC->SetProcess("PAIR",1);
  gMC->SetProcess("COMP",1);
  gMC->SetProcess("PHOT",1);
  gMC->SetProcess("PFIS",0);
  gMC->SetProcess("DRAY",0);
  gMC->SetProcess("ANNI",1);
  gMC->SetProcess("BREM",1);
  gMC->SetProcess("MUNU",1);
  gMC->SetProcess("CKOV",1);
  gMC->SetProcess("HADR",1);
  gMC->SetProcess("LOSS",2);
  gMC->SetProcess("MULS",1);
  gMC->SetProcess("RAYL",1);

  Float_t cut = 1.e-3;       // 1MeV cut by default
  Float_t tofmax = 1.e10;
```

```
   gMC->SetCut("CUTGAM", cut);
   gMC->SetCut("CUTELE", cut);
   gMC->SetCut("CUTNEU", cut);
   gMC->SetCut("CUTHAD", cut);
   gMC->SetCut("CUTMUO", cut);
   gMC->SetCut("BCUTE",  cut);
   gMC->SetCut("BCUTM",  cut);
   gMC->SetCut("DCUTE",  cut);
   gMC->SetCut("DCUTM",  cut);
   gMC->SetCut("PPCUTM", cut);
   gMC->SetCut("TOFMAX", tofmax);

//  W production (Zaida Config.)

   AliGenPythia *gener = new AliGenPythia(1);

   gener->SetProcess(kPyW);
   gener->SetStrucFunc(kCTEQ5L);
   gener->SetEnergyCMS(8000.);
   gener->SetPtRange(0,1.e10);
   gener->SetYRange(-12.0,12.0);
   gener->SetPhiRange(0., 360.);
   gener->SetPtHard(0.,-1.0);

   gener->SetCutOnChild(1);
   gener->SetChildPtRange(1.0,1000.);
   gener->SetThetaRange(171.0,178.0);
   gener->SetNumberOfAcceptedParticles(1); //need a muon inside
   gener->SetPdgCodeParticleforAcceptanceCut(13); //the muon arm acceptance
   gener->SetOrigin(0.,0., 0.);  //vertex position
   gener->SetSigma(0.0, 0.0, 0.0);       //Sigma
   gener->SetForceDecay(kWToMuon);
   gener->SetTrackingFlag(1);
   gener->Init();

 //============================================================
 // Field (L3 0.5 T) outside dimuon spectrometer
 //AliMagF *field = new AliMagF("Maps","Maps", 2, 1., 1., 10., AliMagF::k5kG);
   //   AliMagF *field = new AliMagF("Maps","Maps", -1., -1., AliMagF::k5kG,AliMagF::kBeamTypepp, 7000/2.0);
   //TGeoGlobalMagField::Instance()->SetField(field);
```

A. Simulation and Reconstruction files

```
rl->CdGAFile();


Int_t iABSO  = 1;
Int_t iACORDE= 0;
Int_t iDIPO  = 1;
Int_t iEMCAL = 0;
Int_t iFMD   = 1;
Int_t iFRAME = 1;
Int_t iHALL  = 1;
Int_t iITS   = 0;
Int_t iMAG   = 1;
Int_t iMUON  = 1;
Int_t iPHOS  = 0;
Int_t iPIPE  = 1;
Int_t iPMD   = 0;
Int_t iHMPID = 0;
Int_t iSHIL  = 1;
Int_t iT0    = 0;
Int_t iTOF   = 0;
Int_t iTPC   = 0;
Int_t iTRD   = 0;
Int_t iVZERO = 1;
Int_t iZDC   = 0;

//=================== Alice BODY parameters =============================
AliBODY *BODY = new AliBODY("BODY", "Alice envelop");

if (iMAG)
{
   //=================== MAG parameters ============================
   // --- Start with Magnet since detector layouts may be depending ---
   // --- on the selected Magnet dimensions ---
   AliMAG *MAG = new AliMAG("MAG", "Magnet");
}

if (iABSO)
{
   //=================== ABSO parameters ============================
   AliABSO *ABSO = new AliABSOv3("ABSO", "Muon Absorber");
}
if (iDIPO)
```

```
{
   //================== DIPO parameters ============================
   AliDIPO *DIPO = new AliDIPOv3("DIPO", "Dipole version 3");
}
if (iHALL)
{
   //================== HALL parameters ============================
   AliHALL *HALL = new AliHALLv3("HALL", "Alice Hall");
}
if (iFRAME)
{
   //================== FRAME parameters ============================
   AliFRAMEv2 *FRAME = new AliFRAMEv2("FRAME", "Space Frame");
         FRAME->SetHoles(1);
}
if (iSHIL)
{
   //================== SHIL parameters ============================
   AliSHIL *SHIL = new AliSHILv3("SHIL", "Shielding Version 3");
}
if (iPIPE)
{
   //================== PIPE parameters ============================
   AliPIPE *PIPE = new AliPIPEv3("PIPE", "Beam Pipe");
}
if (iITS)
{
   //================== ITS parameters ============================
         //AliITS *ITS  = new AliITSv11Hybrid("ITS","ITS v11Hybrid");
         AliITS *ITS  = new AliITSv11("ITS","ITS");
}
if (iTPC)
{
  //============================ TPC parameters ====================
   AliTPC *TPC = new AliTPCv2("TPC", "Default");
}

if (iTOF) {
   //================== TOF parameters ============================
         AliTOF *TOF = new AliTOFv6T0("TOF", "normal TOF");
}
```

A. Simulation and Reconstruction files

```
  if (iHMPID)
  {
     //================== HMPID parameters ===========================
     AliHMPID *HMPID = new AliHMPIDv3("HMPID", "normal HMPID");
  }
  if (iZDC)
  {
     //================== ZDC parameters ============================
     AliZDC *ZDC = new AliZDCv3("ZDC", "normal ZDC");
     ZDC->SetSpectatorsTrack();
     ZDC->SetLumiLength(0.);
  }
  if (iTRD)
  {
     //================== TRD parameters ============================
     AliTRD *TRD = new AliTRDv1("TRD", "TRD slow simulator");
     AliTRDgeometry *geoTRD = TRD->GetGeometry();
    // Partial geometry: modules at 0,1,7,8,9,16,17
    // starting at 3h in positive direction
   geoTRD->SetSMstatus(2,0);
   geoTRD->SetSMstatus(3,0);
   geoTRD->SetSMstatus(4,0);
   geoTRD->SetSMstatus(5,0);
   geoTRD->SetSMstatus(6,0);
   geoTRD->SetSMstatus(11,0);
   geoTRD->SetSMstatus(12,0);
   geoTRD->SetSMstatus(13,0);
   geoTRD->SetSMstatus(14,0);
   geoTRD->SetSMstatus(15,0);
   geoTRD->SetSMstatus(16,0);
  }
  if (iFMD)
  {
     //================== FMD parameters ============================
          AliFMD *FMD = new AliFMDv1("FMD", "normal FMD");
 }

  if (iMUON)
  {
     //================== MUON parameters ===========================
     // New MUONv1 version (geometry defined via builders)
```

A. Simulation and Reconstruction files

```
            AliMUON *MUON = new AliMUONv1("MUON", "default");
            // activate trigger efficiency by cells
            MUON->SetTriggerEffCells(1);  // not needed if raw masks
   }
   if (iPHOS)
   {
      //==================== PHOS parameters ===========================
    AliPHOS *PHOS = new AliPHOSv1("PHOS", "noCPV_Modules123");
   }
   if (iPMD)
   {
      //==================== PMD parameters ============================
      AliPMD *PMD = new AliPMDv1("PMD", "normal PMD");
   }
   if (iT0)
   {
      //==================== T0 parameters =============================
      AliT0 *T0 = new AliT0v1("T0", "T0 Detector");
   }
   if (iEMCAL)
   {
      //==================== EMCAL parameters ============================
      AliEMCAL *EMCAL = new AliEMCALv2("EMCAL", "EMCAL_COMPLETEV1");
   }
    if (iACORDE)
   {
      //==================== ACORDE parameters ============================
      AliACORDE *ACORDE = new AliACORDEv1("ACORDE", "normal ACORDE");
   }
    if (iVZERO)
   {
      //==================== ACORDE parameters ============================
      AliVZERO *VZERO = new AliVZEROv7("VZERO", "normal VZERO");
   }
}

Float_t EtaToTheta(Float_t arg){
  return (180./TMath::Pi())*2.*atan(exp(-arg));
}

void ProcessEnvironmentVars()
```

A. Simulation and Reconstruction files

```
{
   // Random Number seed
   if (gSystem->Getenv("CONFIG_SEED")) {
            seed = atoi(gSystem->Getenv("CONFIG_SEED"));
   }
   // Run number
   if (gSystem->Getenv("DC_RUN")) {
     runNumber = atoi(gSystem->Getenv("DC_RUN"));
   }
}
```

B. Simulation file (sim.C) used in Ideal Case

```
void sim(Int_t nev=5000) {

  AliSimulation simulator;
// simu run/run (no RejectList)
  simulator.SetTriggerConfig("MUON");
  simulator.SetMakeSDigits("MUON");
  simulator.SetMakeDigits("MUON");
  simulator.SetMakeDigitsFromHits("");
  simulator.SetRunQA("MUON:ALL");
  simulator.SetRunHLT("");

// Default = Ideal OCDB
  simulator.SetDefaultStorage("alien://folder=/alice/simulation/2008/v4-15-Release/Ideal");

 // CTP (muon standalone)
  simulator.SetSpecificStorage("GRP/CTP/Config", "alien://folder=/alice/cern.ch/user/b/bogdan/prod2011/cdb");

// Vertex and Mag.field from OCDB
//  simulator.UseVertexFromCDB();
  simulator.SetSpecificStorage("GRP/GRP/Data","alien://folder=/alice/data/2011/OCDB");
  simulator.UseMagFieldFromGRP();

  TStopwatch timer;
  timer.Start();
  simulator.Run(nev);
  timer.Stop();
  timer.Print();
}
```

C. Reconstruction file (rec.C) used for Ideal Case

```
void rec() {
  AliReconstruction reco;
// run/run (No RejectList)
  reco.SetCleanESD(kFALSE);
  reco.SetWriteAlignmentData();

  reco.SetRunLocalReconstruction("MUON");
  reco.SetRunTracking("MUON");
  reco.SetRunVertexFinder(kFALSE);
  reco.SetFillESD("MUON");
  reco.SetRunQA("MUON:ALL");

// Default = raw OCDB
  reco.SetDefaultStorage("alien://Folder=/alice/data/2011/OCDB");
 reco.SetDefaultStorage("alien://Folder=/alice/simulation/2008/v4-15-Release/Ideal");
//tracking
  reco.SetSpecificStorage("MUON/Align/Data","alien://folder=/alice/simulation/2008/v4-15-Release/Ideal");

// CTP
reco.SetSpecificStorage("GRP/CTP/Config","alien://folder=/alice/cern.ch/user/b/bogdan/prod2011/cdb");
//  reco.SetSpecificStorage("GRP/CTP/Config","alien://folder=/alice/cern.ch/user/b/bastid/OCDB");  // for test
// GRP from local OCDB
 reco.SetSpecificStorage("GRP/GRP/Data", Form("local://%s",gSystem->pwd()));

  TStopwatch timer;
  timer.Start();
  reco.Run();
  timer.Stop();
  timer.Print();
}
```

Appendix B. Quality Assurance (QA) Run Lists

QA LHC11h *Pass 1* and *Pass 2*			
Run	Comments	Run	Comments
167706		168362	
167713		168458	
167806		168460	
167807		168461	
167808		168464	
167813		168467	
167814		168511	
167818		168512	
167915		168514	
167920		168777	
167921		168826	
167985		168992	
167986		169035	
167987		169040	
167988		169044	
168066		169045	
168069		169091	
168076		169094	
168107		169099	
168108		169138	
168115		169144	
168172		169145	
168173		169148	
168175		169156	
168181		169160	
168203		169167	
168205		169236	
168206		169238	
168207		169411	
168208		169415	
168212		169417	
168213		169418	
168310		169419	
168311		169420	15% loss efficiency on Chamber 1
168318		169475	
168322		169498	
168325		169504	
168341		169506	
168342		169512	
168356	Not in *Pass 1*	169515	
168361		169550	

B. Quality Assurance (QA) Run Lists

169553		170155	
169554		170159	
169555		170162	MB, but no MUON, Centrality Trigger
169557		170163	
169586		170193	
169587		170203	
169588		170204	
169590		170207	
169683	MB, but no MUON, Centrality Trigger	170228	
169835		170230	
169837		170264	Not reconstructed
169838		170267	Not reconstructed
169846		170268	
169855		170269	
169858		170270	
169859		170306	
169923	Not reconstructed	170308	
169965		170309	
169969		170311	
170027		170312	
170036		170313	
170040		170315	Not in *Pass 1*
170081		170387	
170083		170388	
170084		170389	MB, MUON, but no Centrality Trigger
170085		170390	MB, MUON, but no Centrality Trigger
170088		170572	
170089		170593	
170091			

All the runs without comments were considered for the analyses and all the runs with comments were not considered for the analyses.

Appendix C. Analysis task

```
/**************************************************************************
 * Copyright(c) 1998-2007, ALICE Experiment at CERN, All rights reserved. *
 *                                                                        *
 * Author: The ALICE Off-line Project.                                    *
 * Contributors are mentioned in the code where appropriate.              *
 *                                                                        *
 * Permission to use, copy, modify and distribute this software and its   *
 * documentation strictly for non-commercial purposes is hereby granted   *
 * without fee, provided that the above copyright notice appears in all   *
 * copies and that both the copyright notice and this permission notice   *
 * appear in the supporting documentation. The authors make no claims     *
 * about the suitability of this software for any purpose. It is          *
 * provided "as is" without express or implied warranty.                  *
 **************************************************************************/

/* $Id: AliAnalysisTaskSingleMu.cxx 55545 2012-04-04 07:16:39Z pcrochet $ */

//-----------------------------------------------------------------------------
/// \class AliAnalysisTaskSingleMu
/// Analysis task for single muons in the spectrometer.
/// The output is a list of histograms and CF containers.
/// The macro class can run on AODs or ESDs.
/// In the latter case a flag can be activated to produce a tree as output.
/// If Monte Carlo information is present, some basics checks are performed.
///
/// \author Diego Stocco
//-----------------------------------------------------------------------------

#define AliAnalysisTaskSingleMu_cxx

#include "AliAnalysisTaskSingleMu.h"

// ROOT includes
#include "TROOT.h"
#include "TH1.h"
#include "TH2.h"
#include "TAxis.h"
#include "TCanvas.h"
#include "TLegend.h"
#include "TMath.h"
#include "TObjString.h"
#include "TObjArray.h"
#include "TF1.h"
#include "TStyle.h"
//#include "TMCProcess.h"
#include "TArrayI.h"
#include "TPaveStats.h"
#include "TFitResultPtr.h"

// STEER includes
#include "AliAODEvent.h"
#include "AliAODTrack.h"
#include "AliAODMCParticle.h"
#include "AliMCEvent.h"
#include "AliMCParticle.h"
#include "AliESDEvent.h"
#include "AliESDMuonTrack.h"
#include "AliVHeader.h"
#include "AliAODMCHeader.h"
#include "AliStack.h"
```

C. Analysis Task

```
// ANALYSIS includes
#include "AliAnalysisManager.h"

// CORRFW includes
#include "AliCFContainer.h"
#include "AliCFGridSparse.h"
#include "AliCFEffGrid.h"

// PWG includes
#include "AliVAnalysisMuon.h"
#include "AliMergeableCollection.h"
#include "AliCounterCollection.h"
#include "AliMuonTrackCuts.h"


/// \cond CLASSIMP
ClassImp(AliAnalysisTaskSingleMu) // Class implementation in ROOT context
/// \endcond


//_____________________________________________________________________________
AliAnalysisTaskSingleMu::AliAnalysisTaskSingleMu() :
  AliVAnalysisMuon(),
  fThetaAbsKeys(0x0)
{
  /// Default ctor.
}

//_____________________________________________________________________________
AliAnalysisTaskSingleMu::AliAnalysisTaskSingleMu(const char *name, const
AliMuonTrackCuts& cuts) :
  AliVAnalysisMuon(name, cuts),
  fThetaAbsKeys(0x0)
{
  //
  /// Constructor.
  //
  TString thetaAbsKeys = "ThetaAbs23 ThetaAbs310";
  fThetaAbsKeys = thetaAbsKeys.Tokenize(" ");
}


//_____________________________________________________________________________
AliAnalysisTaskSingleMu::~AliAnalysisTaskSingleMu()
{
  //
  /// Destructor
  //

  delete fThetaAbsKeys;
}

//_____________________________________________________________________________
void AliAnalysisTaskSingleMu::MyUserCreateOutputObjects()
{

  TH1* histo = 0x0;
  TString histoName = "", histoTitle = "";

  Int_t nVzBins = 40;
  Double_t vzMin = -20., vzMax = 20.;
  TString vzName("Vz"), vzTitle("Vz"), vzUnits("cm");

  histoName = "hIpVtx";
  histo = new TH1F(histoName.Data(), histoName.Data(), nVzBins, vzMin, vzMax);
  histo->SetXTitle("v_{z} (cm)");
  AddObjectToCollection(histo, kIPVz);
```

```
  Int_t nPtBins = 100;
  Double_t ptMin = 0., ptMax = 100.;
  TString ptName("Pt"), ptTitle("p_{t}"), ptUnits("GeV/c");

  Int_t nEtaBins = 25;
  Double_t etaMin = -4.5, etaMax = -2.;
  TString etaName("Eta"), etaTitle("#eta"), etaUnits("");

  Int_t nPhiBins = 36;
  Double_t phiMin = 0.; Double_t phiMax = 2.*TMath::Pi();
  TString phiName("Phi"), phiTitle("#phi"), phiUnits("rad");

  Int_t nChargeBins = 2;
  Double_t chargeMin = -2., chargeMax = 2.;
  TString chargeName("Charge"), chargeTitle("charge"), chargeUnits("e");

  Int_t nThetaAbsEndBins = 2;
  Double_t thetaAbsEndMin = -0.5, thetaAbsEndMax = 1.5;
  TString thetaAbsEndName("ThetaAbsEnd"), thetaAbsEndTitle("#theta_{abs}"),
thetaAbsEndUnits("a.u.");

  Int_t nMotherTypeBins = kNtrackSources;
  Double_t motherTypeMin = -0.5, motherTypeMax = (Double_t)kNtrackSources - 0.5;
  TString motherType("MotherType"), motherTypeTitle("motherType"),
motherTypeUnits("");

  Int_t nbins[kNvars] = {nPtBins, nEtaBins, nPhiBins, nVzBins, nChargeBins,
nThetaAbsEndBins, nMotherTypeBins};
  Double_t xmin[kNvars] = {ptMin, etaMin, phiMin, vzMin, chargeMin, thetaAbsEndMin,
motherTypeMin};
  Double_t xmax[kNvars] = {ptMax, etaMax, phiMax, vzMax, chargeMax, thetaAbsEndMax,
motherTypeMax};
  TString axisTitle[kNvars] = {ptTitle, etaTitle, phiTitle, vzTitle, chargeTitle,
thetaAbsEndTitle, motherTypeTitle};
  TString axisUnits[kNvars] = {ptUnits, etaUnits, phiUnits, vzUnits, chargeUnits,
thetaAbsEndUnits, motherTypeUnits};

  AliCFContainer* cfContainer = new AliCFContainer("SingleMuContainer","Container
for tracks",kNsteps,kNvars,nbins);

  for ( Int_t idim = 0; idim<kNvars; idim++){
    histoTitle = Form("%s (%s)", axisTitle[idim].Data(), axisUnits[idim].Data());
    histoTitle.ReplaceAll("()","");

    cfContainer->SetVarTitle(idim, histoTitle.Data());
    cfContainer->SetBinLimits(idim, xmin[idim], xmax[idim]);
  }

  TString stepTitle[kNsteps] = {"reconstructed", "generated"};

  TAxis* currAxis = 0x0;
  for (Int_t istep=0; istep<kNsteps; istep++){
    cfContainer->SetStepTitle(istep, stepTitle[istep].Data());
    AliCFGridSparse* gridSparse = cfContainer->GetGrid(istep);

    currAxis = gridSparse->GetAxis(kHvarMotherType);
    for ( Int_t ibin=0; ibin<fSrcKeys->GetEntries(); ibin++ ) {
      currAxis->SetBinLabel(ibin+1, fSrcKeys->At(ibin)->GetName());
    }
  }

  AddObjectToCollection(cfContainer, kTrackContainer);

  fMuonTrackCuts->Print("mask");
}
```

```
//_____________________________________________________________________________
void AliAnalysisTaskSingleMu::ProcessEvent(TString physSel, const TObjArray&
selectTrigClasses, TString centrality)
{
  //
  /// Fill output objects
  //

//   if ( GetVertexSPD()->GetNContributors() < fMinNvtxContirbutors ) return;

  Double_t ipVz = GetVertexSPD()->GetZ();
  Double_t ipVzMC = 0;
  if ( IsMC() ) {
    if ( fMCEvent ) ipVzMC = fMCEvent->GetPrimaryVertex()->GetZ();
    else if ( fAODEvent ) {
      AliAODMCHeader* aodMCHeader = (AliAODMCHeader *)fAODEvent-
>FindListObject(AliAODMCHeader::StdBranchName());
      if ( aodMCHeader ) ipVzMC = aodMCHeader->GetVtxZ();
    }
  }

  for ( Int_t itrig=0; itrig<selectTrigClasses.GetEntries(); ++itrig ) {
    TString trigClassName = ((TObjString*)selectTrigClasses.At(itrig))-
>GetString();
    ((TH1*)GetMergeableObject(physSel, trigClassName, centrality, "hIpVtx"))-
>Fill(ipVz);
  }

//   Bool_t isPileupFromSPD = ( fAODEvent && ! fAODEvent->GetTracklets() ) ?
InputEvent()->IsPileupFromSPD(3, 0.8, 3., 2., 5.) : InputEvent()-
>IsPileupFromSPDInMultBins(); // Avoid break when reading Muon AODs (tracklet info
is not present and IsPileupFromSPDInMultBins crashes
//   if ( isPileupFromSPD ) return;

  Double_t containerInput[kNvars];
  AliVParticle* track = 0x0;

  for ( Int_t istep = kStepReconstructed; istep<=kStepGeneratedMC; ++istep ) {
    Int_t nTracks = ( istep == kStepReconstructed ) ? GetNTracks() :
GetNMCTracks();
    for (Int_t itrack = 0; itrack < nTracks; itrack++) {
      track = ( istep == kStepReconstructed ) ? GetTrack(itrack) :
GetMCTrack(itrack);

      Bool_t isSelected = ( istep == kStepReconstructed ) ? fMuonTrackCuts-
>IsSelected(track) : ( TMath::Abs(track->PdgCode()) == 13 );
      if ( ! isSelected ) continue;

      // In W simulations with Pythia, sometimes muon is stored twice.
      // Remove muon in case it has another muon as daugther
      if ( istep == kStepGeneratedMC ) {
        Int_t firstDaughter = GetDaughterIndex(track, 0);
        if ( firstDaughter >= 0 ) {
          Bool_t hasMuonDaughter = kFALSE;
          Int_t lastDaughter = GetDaughterIndex(track, 1);
          for ( Int_t idaugh=firstDaughter; idaugh<=lastDaughter; idaugh++ ) {
            AliVParticle* currTrack = GetMCTrack(idaugh);
            if ( currTrack->PdgCode() == track->PdgCode() ) {
              hasMuonDaughter = kTRUE;
              break;
            }
          }
          if ( hasMuonDaughter ) {
            AliDebug(1, Form("Current muon (%i) has muon daughter: rejecting it",
itrack));
            continue;
          }
        }
```

```
      }

      Int_t trackSrc = ( istep == kStepReconstructed ) ? GetParticleType(track) :
RecoTrackMother(track);

      Double_t thetaAbsEndDeg = 0;
      if ( istep == kStepReconstructed ) {
        Double_t rAbsEnd =  ( fAODEvent ) ? ((AliAODTrack*)track)-
>GetRAtAbsorberEnd(): ((AliESDMuonTrack*)track)->GetRAtAbsorberEnd();
        thetaAbsEndDeg = TMath::ATan( rAbsEnd / 505. ) * TMath::RadToDeg();
      }
      else {
        thetaAbsEndDeg = ( TMath::Pi()-track->Theta() ) * TMath::RadToDeg();
      }
      Int_t thetaAbsBin = ( thetaAbsEndDeg < 3. ) ? kThetaAbs23 : kThetaAbs310;

      containerInput[kHvarPt]         = track->Pt();
      containerInput[kHvarEta]        = track->Eta();
      containerInput[kHvarPhi]        = track->Phi();
      containerInput[kHvarVz]         = ( istep == kStepReconstructed ) ? ipVz :
ipVzMC;
      containerInput[kHvarCharge]     = track->Charge()/3.;
      containerInput[kHvarThetaAbs]   = (Double_t)thetaAbsBin;
      containerInput[kHvarMotherType] = (Double_t)trackSrc;

      for ( Int_t itrig=0; itrig<selectTrigClasses.GetEntries(); ++itrig ) {
        TString trigClassName = ((TObjString*)selectTrigClasses.At(itrig))-
>GetString();
        if ( istep == kStepReconstructed && ! TrackPtCutMatchTrigClass(track,
trigClassName) ) continue;
        ((AliCFContainer*)GetMergeableObject(physSel, trigClassName, centrality,
"SingleMuContainer"))->Fill(containerInput,istep);
      } // loop on selected trigger classes
    } // loop on tracks
  } // loop on container steps
}


//_____________________________________________________________________________
void AliAnalysisTaskSingleMu::Terminate(Option_t *) {
  //
  /// Draw some histograms at the end.
  //

  AliVAnalysisMuon::Terminate("");

  if ( ! fMergeableCollection ) return;

  TString physSel = fTerminateOptions->At(0)->GetName();
  TString trigClassName = fTerminateOptions->At(1)->GetName();
  TString centralityRange = fTerminateOptions->At(2)->GetName();
  TString furtherOpt = fTerminateOptions->At(3)->GetName();

  TString minBiasTrig = "";
  TObjArray* optArr = furtherOpt.Tokenize(" ");
  TString currName = "";
  for ( Int_t iopt=0; iopt<optArr->GetEntries(); iopt++ ) {
    currName = optArr->At(iopt)->GetName();
    if ( currName.Contains("-B-") ) minBiasTrig = currName;
  }
  delete optArr;

  furtherOpt.ToUpper();

  AliCFContainer* cfContainer = static_cast<AliCFContainer*> (
GetSum(physSel,trigClassName,centralityRange,"SingleMuContainer") );
  if ( ! cfContainer ) return;
```

```
  AliCFEffGrid* effSparse = new AliCFEffGrid(Form("eff%s", cfContainer-
>GetName()),Form("Efficiency %s", cfContainer->GetTitle()),*cfContainer);
  effSparse->CalculateEfficiency(kStepReconstructed, kStepGeneratedMC);

  AliCFGridSparse* gridSparseArray[3] = {effSparse->GetNum(), effSparse->GetDen(),
effSparse};
  TString gridSparseName[3] = {cfContainer->GetStepTitle(kStepReconstructed),
cfContainer->GetStepTitle(kStepGeneratedMC), "Efficiency"};

  Int_t srcColors[kNtrackSources] = {kBlack, kRed, kSpring, kTeal, kBlue, kViolet,
kMagenta, kOrange};
//  TString allSrcNames = "";
//  for ( Int_t isrc=0; isrc<kNtrackSources; ++isrc ) {
//    if ( ! allSrcNames.IsNull() ) allSrcNames.Append(" ");
//    allSrcNames += fSrcKeys->At(isrc)->GetName();
//  }

  TCanvas* can = 0x0;
  Int_t xshift = 100;
  Int_t yshift = 100;
  Int_t igroup1 = -1;
  Int_t igroup2 = 0;

  Bool_t isMC = furtherOpt.Contains("MC");
  Int_t firstSrc = ( isMC ) ? 0 : kUnidentified;
  Int_t lastSrc  = ( isMC ) ? kNtrackSources - 1 : kUnidentified;
  if ( ! isMC ) srcColors[kUnidentified] = 1;

  TString histoName = "", histoPattern = "", drawOpt = "";
  ////////////////
  // Kinematics //
  ////////////////
  TCanvas* canKine[3] = {0x0, 0x0, 0x0};
  TLegend* legKine[3] = {0x0, 0x0, 0x0};

  TString varTitle[kNvars] =
{"Pt","Eta","Phi","Vz","Charge","ThetaAbsEnd","MotherType"};

//   for ( Int_t isrc = firstSrc; isrc <= lastSrc; ++isrc ) {
  for ( Int_t isrc = kWbosonMu; isrc <= kWbosonMu; ++isrc ) {
    for ( Int_t icharge=0; icharge<2; ++icharge ) {
      for ( Int_t igrid=0; igrid<1; ++igrid ) {
        if ( gridSparseArray[igrid]->GetEntries() == 0. ) break;
        if ( gridSparseArray[igrid]->IsA() != AliCFEffGrid::Class() ) {
          SetSparseRange(gridSparseArray[igrid], kHvarEta, "", -3.999, -2.501);
          SetSparseRange(gridSparseArray[igrid], kHvarMotherType, "", isrc+1,
isrc+1, "USEBIN");
          SetSparseRange(gridSparseArray[igrid], kHvarCharge, "", icharge+1,
icharge+1, "USEBIN");
        }
        if ( ! canKine[igrid] ) {
          igroup1++;
          igroup2 = 0;
          currName = Form("%s_proj_%s", GetName(), gridSparseName[igrid].Data());
          canKine[igrid] = new
TCanvas(currName.Data(),currName.Data(),igroup1*xshift,igroup2*yshift,600,600);
          canKine[igrid]->Divide(1,1);
          legKine[igrid] = new TLegend(0.6, 0.6, 0.8, 0.8);
          igroup2++;
        }
        for ( Int_t iproj=0; iproj<1; ++iproj ) {
          canKine[igrid]->cd(iproj+1);
//           if ( ( iproj == kHvarPt || iproj == kHvarVz ) &&
gridSparseArray[igrid]->IsA() != AliCFEffGrid::Class() ) gPad->SetLogy();
          TH1* projHisto = gridSparseArray[igrid]->Project(iproj);
         projHisto->SetName(Form("%s_%s_%s_%s", varTitle[iproj].Data(),
gridSparseName[igrid].Data(), fSrcKeys->At(isrc)->GetName(), fChargeKeys-
>At(icharge)->GetName()));
```

C. Analysis Task

```
//        projHisto->SetName(Form("proj%i_%s_src%i_charge%i", iproj,
gridSparseName[igrid].Data(), isrc, icharge));
          if ( projHisto->GetEntries() == 0 ) continue;
          Bool_t isFirst = ( gPad->GetListOfPrimitives()->GetEntries() == 0 );
          drawOpt = isFirst ? "e" : "esames";
          //if ( isrc == kUnidentified && ! drawOpt.Contains("same") ) isMC =
kFALSE;
          //if ( ! isMC ) srcColors[kUnidentified] = 1;
         projHisto->SetLineWidth(2);
         projHisto->SetLineColor(33);
          projHisto->SetMarkerColor(1);
          projHisto->SetMarkerStyle(20+4*icharge);
         /// Divide histogram by number of events not number of tracks.
//       TH1* projHistoNorm = projHisto->DrawNormalized(drawOpt.Data());
//           projHisto->Draw(drawOpt.Data());
         TString selKey = ( physSel == kPhysSelPass ) ? "yes" : "no";
         TString evtSel = Form("trigger:%s/selected:%s", trigClassName.Data(),
selKey.Data());
         Double_t sum = fEventCounters->GetSum(evtSel.Data());
         fEventCounters->Print();
         projHisto->Scale(1/sum);
         projHisto->Draw(drawOpt.Data());
          gPad->Update();
          TPaveStats* paveStats = (TPaveStats*)projHisto->FindObject("stats");
          if ( paveStats ) paveStats->SetTextColor(srcColors[isrc]);
          if ( iproj == 0 ) {
            TString legEntry = fChargeKeys->At(icharge)->GetName();
            if ( isMC ) legEntry += Form(" %s", fSrcKeys->At(isrc)->GetName());
            legKine[igrid]->AddEntry(projHisto,legEntry.Data(), "lp"); /// Made
change here from projHisto to projHistoNorm
          }
        } // loop on projections
      } // loop on grid sparse
    } // loop on mu charge
  } // loop on track sources


  for ( Int_t igrid=0; igrid<3; igrid++ ) {
    if ( ! canKine[igrid] ) continue;
    canKine[igrid]->cd(1);
    legKine[igrid]->Draw("same");
    if ( gridSparseArray[igrid]->IsA() == AliCFEffGrid::Class() ) continue;
    SetSparseRange(gridSparseArray[igrid], kHvarCharge, "", 1,
gridSparseArray[igrid]->GetAxis(kHvarCharge)->GetNbins(), "USEBIN"); // Reset range
  } // loop on container steps */


  ///////////////////////
  // Event statistics //
  ///////////////////////
  printf("\nTotal analyzed events:\n");
  TString evtSel = Form("trigger:%s", trigClassName.Data());
  fEventCounters->PrintSum(evtSel.Data());
  printf("Physics selected analyzed events:\n");
  evtSel = Form("trigger:%s/selected:yes", trigClassName.Data());
  fEventCounters->PrintSum(evtSel.Data());

  TString countPhysSel = "any";
  if ( physSel.Contains(fPhysSelKeys->At(kPhysSelPass)->GetName()) ) countPhysSel =
"yes";
  else if ( physSel.Contains(fPhysSelKeys->At(kPhysSelReject)->GetName()) )
countPhysSel="no";
  countPhysSel.Prepend("selected:");
  printf("Analyzed events vs. centrality:\n");
  evtSel = Form("trigger:%s/%s", trigClassName.Data(), countPhysSel.Data());
  fEventCounters->Print("centrality",evtSel.Data(),kTRUE);
}
```

References

[A+03] S. Agostinelli et al., "*GEANT4 – A Simulation Toolkit*" *Nucl. Instrum. Meth. A*506, 250-303, 2003. http://www.sciencedirect.com/science/article/pii/S0168900203013688

[A+05a] J. Adams et al. (STAR Collaboration), "*Experimental and theoretical challenges in the search for the quark-gluon plasma: The STAR collaboration's critical assessment of the evidence from RHIC collisions*" *Nucl. Phys. A*757, 102–183, 2005. arXiv: nucl-ex/0501009

[A+05b] K. Adcox et al. (PHENIX Collaboration), "*Formation of dense partonic matter in relativistic nucleus nucleus collisions at RHIC: Experimental evaluation by the PHENIX collaboration,*" *Nucl. Phys. A*757, 184–283, 2005. arXiv: nucl-ex/0410003

[A+05c] I. Arsene et al. (BRAHMS Collaboration), "*Quark gluon plasma and color glass condensate at RHIC? The perspective from the BRAHMS experiment,*" *Nucl. Phys. A*757, p. 1–27, 2005. arXiv:nucl-ex/0410020

[A+06] B. Alessandro et al. (ALICE Collaboration), "*ALICE: Physics performance report, Volume II*", *Jour Phys. G: Nucl. Part. Phys.* 32:1295-2040, 2006. http://iopscience.iop.org/0954-3899/32/10/001/

[A+08] K. Aamodt et al. (ALICE Collaboration), "*The ALICE Experiment at the CERN LHC,*" *J. Instrum.* 3, S08002, 2008. http://iopscience.iop.org/1748-0221/3/08/S08002/

[A+11] K. Aamodt et al. (ALICE Collaboration), "*Rapidity and transverse momentum dependence of inclusive J/psi production in pp collisions at √s = 7 TeV,*" *Phys. Lett. B*704, 442-455, 2011. arXiv:1105.0380

[A+12a] B. Abelev et al. (ALICE Collaboration), "*Heavy flavour decay muon production at forward rapidity in proton–proton collisions at √s = 7 TeV,*" *Phys. Lett. B*708, 265–275, 2012. arXiv:1201.3791

[A+12b] B. Abelev et al. (ALICE Collaboration), "*Production of Muons from Heavy Flavor Decays at Forward Rapidity in p-p and Pb-Pb collisions at √(s_NN) = 2.76 TeV,*" *Phys. Rev. Lett.* 109, 112301, 2012. arXiv:1205.6443

[A+12c] B. Abelev et al. (ALICE Collaboration), "*J/Psi Suppression at Forward Rapidity in Pb-Pb Collisions at √(s_NN) = 2.76 TeV,*" *Phys. Rev. Lett.* 109, 072301, 2012. arXiv:1202.1383

[A+94] L. Ahle et al. (E-802 Collaboration), "*Global transverse energy distributions in Si+A1, Au at 14.6A GeV/c and Au+Au at 11.6A GeV/c,*" *Phys. Lett. B*332, 258-264, 1994. http://inspirehep.net/record/374156/hepdata

References

[ADMP04] C. Anastasioua, L. Dixon, K. Melnikov and F. Petriello, "*High-precision QCD at hadron colliders: Electroweak gauge boson rapidity distributions at NNLO*," *Phys. Rev. D*69, 094008, 2004. arXiv:hep-ph/0312266

[AEGH97] J. F. Amundson, O. J. Eboli, E. M. Gregores and F. Halzen, "*Quantitative Tests of Color Evaporation: Charmonium Production,*" *Phys. Lett. B*390, 323-328, 1997. arXiv:hep-ph/9605295

[ALI00] ALICE Collaboration, "*Addendum to the Technical Design Report of the Dimuon Forward Spectrometer,*" CERN / LHCC 2000–046, 2000. https://aliceinfo.cern.ch/secure/system/files/documents/technical_coordination/tdr2-main.pdf

[ALI03] ALICE Collaboration, "*Technical Design Report of the Trigger, Data Acquisition, High-Level Trigger and Control System,*" CERN-LHCC-2003-062, ALICE-TDR-10, 2003. http://cds.cern.ch/record/684651

[ALI08] ALICE Collaboration (CERN), "*The ALICE Dimuon Spectrometer*", 2008. http://aliceinfo.cern.ch/Public/en/Chapter2/Chap2_dim_spec.html.

[ALI10] ALICE DAQ Project & ALICE ECS Project, "*ALICE DAQ and ECS Manual", ALICE-INT-2010-001,* 2010.

[ALI11a] ALICE Collaboration, "*ALICE Offline Pages,*" http://aliceinfo.cern.ch/Offline/AliRoot. 2011

[ALI11b] ALICE Collaboration, "*Particle Transport and Detector Simulation,*" 2011. http://aliweb.cern.ch/Offline/Activities/Simulation/ParticleTransport.html.

[ALI13a] ALICE Collaboration, "*ALICE Electronic Logbook,*" 2013. https://alice-logbook.cern.ch.

[ALI13b] ALICE Collaboration, "*ALICE Figure Repository,*" ALICE Collaboration, 2013. https://aliceinfo.cern.ch/Figure/

[ALI99] ALICE Collaboration, "*Technical Design Report of the Dimuon Forward Spectrometer*", CERN/LHCC 99–22," 1999. https://edms.cern.ch/document/470838/1%20

[ALIRC12] ALICE Run Coordination, "*The ALICE guide to Shift Leadership",* 2012-08-21. https://twiki.cern.ch/twiki/pub/ALICE/WebHome/sl-guide_2012_pp_latest.pdf

[Ant08] F. Antorini, "*Naming scheme for ALICE trigger classes, v. 0.1 (draft),*" 2008-06-30. http://aliweb.cern.ch/Offline/Activities/TriggerPattern.html

[Aph13] L. Aphecetche, *Private communication: Luminosity*, 2013.

References

[ASW05] N. Armesto, C. A. Salgado and U. A. Wiedemann, "*Low-p_T collective flow induces high-p_T jet quenching*" *Phys. Rev. D*72, 064910, 2005. arXiv:hep-ph/0411341

[B+05] B. B. Back et al. (PHOBOS Collaboration), "*The PHOBOS perspective on discoveries at RHIC,*" *Nucl. Phys. A*757, 28–101, 2005. http://0-www.sciencedirect.com.innopac.up.ac.za/science/article/pii/S0375947405005282

[B+12] J. Beringer et al. (Particle Data Group), "*Gauge and Higgs Bosons*," *Phys. Rev. D*86, 2012.

[Bay02] G. Baym, "*RHIC: From dreams to beams in two decades,*" *Nucl.Phys. A*698, XXIII-XXXII, 2002. arXiv:hep-ph/0104138

[BBB+03] M. Bedjidian, D. Blaschke, G. T Bodwin et al, "*Hard probes in heavy ion collisions at the LHC: heavy flavour physics",* 2003. arXiv:hep-ph/0311048

[BDM+97] R. Baier, Y. L. Dokshitzer, A. H. Mueller, S. Peigne and D. Schiff, "*Radiative energy loss of high energy quarks and gluons in a finite-volume quark-gluon plasma*," *Nucl. Phys. B*483, 291–320, 1997. arXiv:hep-ph/9607355

[Bet07] S. Bethke, "*Experimental Tests of Asymptotic Freedom*," *Prog. Part. Nucl. Phys.* 58, p351-386, 2007. arXiv:hep-ex/0606035

[BF95] E. Braaten and S. Fleming, "*Color-Octet Fragmentation and the Psi' Surplus at the Fermilab Tevatron,*" *Phys. Rev. Lett.* 74, 3327-3330, 1995. http://dx.doi.org/10.1103/PhysRevLett.74.3327

[Bjo82] J. D. Bjorken, "*Energy loss of energetic partons in quark - gluon plasma: Possible extinction of high p(t) jets in hadron - hadron collisions",* 1982. FERMILAB-PUB-82-059-THY.

[BK02] V. Blobel and C. Kleinwort, "*A New Method for the High-Precision Alignment of Track Detectors,*" 2002. arXiv:hep-ex/0208021

[BNL12] Brookhaven National Laboratory, "*BNL Newsroom,*" 2012. http://www.bnl.gov/bnlweb/pubaf/pr/photos/2012/07/rhic_graphics_fig1-hr.jpg.

[Bos13] F. Bossù, *Private communication: Simulation of events*, 2013

[BPSG04] P. Buncic, A. J. Peters, P. Saiz and J. Grosse-Oetringhaus, "*The architecture of the AliEn system,*" in *CHEP 2004*, Interlaken, Switzerland, 2004.

[BS12] N. Bastid, D. Stocco, "*Status of W analysis in the semi-muonic decay channel*" PWG-HF HFM meeting 2012-02-06. https://indico.cern.ch/getFile.py/access?contribId=0&resId=0&materialId=slides&confId=176058

References

[C++13] C++ Resources Network, "*Welcome to cplusplus.com,*" 2013. http://www.cplusplus.com/info/.

[C+04] F. Carminati et al. (ALICE Collaboration), "*ALICE: Physics performance report, Volume I,*" *Jour. Phys. G: Nucl. Part. Phys.* 30, 2004.

[Car09] F. Carminati for the ALICE Collaboration, "*The Offline Conditions DB framework*", 2009. http://aliweb.cern.ch/Offline/Activities/ConditionDB.html.

[Cas12] J. Castillo, *Private communication: Resolution of the Muon Spectrometer,* 2012.

[CDS02] CERN Document Server (CDS) "*ALICE Dimuon: Slat chamber prototype under test at PS.*" ALICE-PICT-MUON-2002-001, 2002. http://cds.cern.ch/record/790000/files/muon-2002-001.jpg

[CDS07] CERN Document Server (CDS) "*Installation of station 1 of the tracking chambers of the ALICE Muon Spectrometer,"* 2007. http://cds.cern.ch/record/1046255/files/muon-2007-008.jpg ALICE-PICT-MUON-2007-008

[CdV07] Z. Conesa del Valle, "*Performance of the ALICE muon spectrometer. Weak boson production and measurement in heavy-ion collisions at LHC.*" PhD Thesis, University of Nantes, Universitat Autónoma de Barcelona, 2007.

[CER04] CERN, "*CERN Photo Lab,*" 2004. http://cds.cern.ch/collection/CERN%20PhotoLab?ln=en.

[CER09a] CERN, "*Accelerators and Technology Sector,*" 2009. https://espace.cern.ch/acc-tec-sector/default.aspx.

[CER09b] CERN, "*The Large Hadron Collider: The LHC Guide,*" 2009. http://home.web.cern.ch/about/accelerators/large-hadron-collider.

[CF07] A. Capella and E. G. Ferreiro, "*J/psi suppression and the nuclear absorption decrease with increasing energy,*" *Phys.Rev.C*76, 064906, 2007.

[Cha08] V. Chambert for the ALICE Collaboration, "*The electronics of ALICE Dimuon tracking chambers,*" 2008. http://inspirehep.net/record/809184

[CL86] W. E. Caswell and G. Lepage, "*Effective Lagrangians for bound state problems in QED, QCD, and other field theories,*" *Phys. Lett. B*4(167), 437-442, 1986.

[CMAF06] Z. Conesa del Valle, G. Martinez Garcia, L. Aphecetche and C. Finck, "*Production of W vector bosons in p+p and Pb+Pb collisions at LHC energies. W detection in the ALICE muon spectrometer.",ALICE-INT-2006/021,* 2006.

References

[CMS12] CMS Collaboration, "Study of W boson production in PbPb and pp collisions at sNN = 2.76 TeV," *Phys. Lett. B*715, 66, (2012).

[Coo05] A. M. Cooper-Sarkar, "Low-x physics and W and Z production at LHC," arXiv: hepex/0512228, 2005.

[Cor04] T. M. Cormier on behalf of the ALICE - USA Collaboration, "*Jet physics in ALICE with a proposed electromagnetic calorimeter,*" *Eur. Phys. J. C*34, s333 - s345, 2004.

[Cre11] M. Creutz, "*Confinement, chiral symmetry and the lattice,*" *Acta Physica Slovaca 1*(61), 1 - 127, 2011.

[CTE13a] The Coordinated Theoretical-Experimental Project on QCD (CTEQ) "*CTEQ4 Parton Distribution Function Sets*", 2013. http://www.phys.psu.edu/~cteq/CTEQ4Table/

[CTE13b] The Coordinated Theoretical-Experimental Project on QCD (CTEQ) "*CTEQ5 Parton Distribution Function Sets*", 2013. http://www.phys.psu.edu/~cteq/CTEQ5Table/

[Das13] I. Das, "*Dimuon Forward Spectrometer: Tracking chambers,*" ALICE Twiki Page, 2013. https://twiki.cern.ch/twiki/bin/viewauth/ALICE/MuonTracking.

[dEn03] D. d'Enterria, "*Hard scattering cross sections at LHC in the Glauber approach: from pp to pA and AA collisions*," arXiv:nucl-ex/0302016, 2003.

[DK01] Y. L. Dokshitzer and D. E. Kharzeev, "*Heavy quark colorimetry of QCD matter,*" *Phys. lett. B*519, 199–206, 2001.

[DKT91] Y. L. Dokshitzer, V. A. Khoze and S. I. Troian, "*On specific QCD properties of heavy quark fragmentation ('dead cone'),*" *J. Phys. G*17, 1602–1604, 1991.

[DLP06] A. Dainese, C. Loizides and G. Paic, "*Leading-particle suppression and surface emission in nucleus-nucleus collisions.,*" *Acta Phys. Hung.*A27, 245–249, 2006.

[duT12] P. J. W. du Toit, "*Analysis of W boson with ALICE: Efffect of alignment on W boson analysis,*" *South African Institute of Physics (SAIP) Conference 2012*, Pretoria, South Africa, 2012.

[EKS99] K. Eskola, V. Kolhinen and C. Salgado, "*The scale dependent nuclear effects in parton distributions for practical applications,*" *Eur.Phys.J. C*9, 61-68, 1999. arXiv:hep-ph/9807297

[Fer13] Fermilab, "*Science at Fermilab*," Fermilab, 2013. http://www.fnal.gov/pub/inquiring/matter/madeof/index.html.

[FK04] I. Foster and C. Kesselman, "*The Grid: Blueprint for a New Computing Infrastructure,*" 2nd ed., San Francisco, CA: Morgan and Kaufmann, 2004.

References

[FM04] S. Frixione and M. Mangano, "*How accurately can we measure the W cross section?*" *JHEP05:056,* 2004. arXiv:hep-ph/0405130

[FSFR05] A. Ferrari, P. R. Sala, A. Fass and J. Ranft, "*FLUKA: A multi-particle transport code (progam version 2005),*" *CERN-2005-010*, 2005. http://cds.cern.ch/record/898301

[Gag10] M. Gagliardi, "*Quarkonium and heavy flavour physics with ALICE at the LHC,*" W*orkshop on discovery physics at the LHC*, Kruger National Park, South Africa, 2010.

[GdC07] R. Granier de Cassagnac, "*Quarkonium suppression from SPS to RHIC (and from p+A to A+A),*" *Nucl.Phys.A* 783, 293-300, 2007. arXiv:nucl-ex/0610003

[GM70] R. J. Glauber and G. Matthias, "*High-Energy Scattering of protons by nuclei.,*" *Nucl. Phys. B*21, 135-137, 1970. http://inspirehep.net/record/61160?ln=pt

[GRB04] L. Grandchamp, R. Rapp and G. E. Brown, "*In-medium effects on charmonium production in heavy-ion collisions*," *Phys. Rev. Lett.* 92, 212301, 2004. arXiv:hep-ph/0306077

[Gri04] D. Griffiths, "*Introduction to Elementary Particles*", WILEY-VCH, 2004.

[GV97] S. Gavin and R. Vogt, "*Charmonium suppression by comover scattering in Pb+Pb collisions,*" *Phys. Rev. Lett.* 78, 1006–1009, 1997. arXiv:hep-ph/9606460

[GW73] D. J. Gross and F. Wilczek, " *Ultraviolet behavior of non-abelian gauge theories.,*" *Phys. Rev. Lett.*30, 1343–1346, 1973. http://inspirehep.net/record/81238?ln=sv

[GW94] M. Gyulassy and X.-N.Wang, "*HIJING 1.0: A Monte HIJING 1.0: A Monte Carlo Program for Parton and Particle Production in High Energy Hadronic and Nuclear Collisions*," *Comput. Phys. Commun. 83,* 307, 1994. arXiv:nucl-th/9502021

[Had12] C. Hadjidakis, "*QA for the selection of good physics runs for muon physics*," ALICE Twiki page, 2012. https://twiki.cern.ch/twiki/bin/viewauth/ALICE/QAForTheSelectionOfGoodPhysicsRunsForMuonPhysics

[Han01] S. Hands, "*The phase diagram of QCD,*" *Contemp. Phys.* 42, 209–225, 2001. arXiv:physics/0105022

[Hil13] C. E. Hill, "*Ion and electron sources",* 2013 http://linac2.home.cern.ch/linac2/seminar/seminar.htm

[HJ00] U. Heinz and M. Jacob, "*Evidence for a New State of Matter: An Assessment of the Results from the CERN Lead Beam Programme,*" 2000. arXiv:nucl-th/0002042

References

[Ian11] E. Iancu, "*QCD in heavy ion collisions*,", *European School of High–Energy Physics 2011 (ESHEP2011)*, Cheile Gradistei, Romania, 2011. arXiv:1205.0579

[Kar01] F. Karsch, "*Lattice QCD at High Temperature and Density", Lect.Notes Phys.* 583, 209-249, 2002. arXiv:hep-lat/0106019

[Kar06] F. Karsch, "*Lattice simulations of the thermodynamics of strongly interacting elementary particles and the exploration of new phases of matter in relativistic heavy ion collisions,*" *J. Phys.: Conf. Ser.* 46, 122 - 131, 2006. arXiv:hep-lat/0608003

[KL03] F. Karsch and E. Laermann, "*Thermodynamics and in-medium hadron properties from lattice QCD"* prepared for *"Quark-Gluon Plasma III", R.Hwa (ed.),* 2003. arXiv:hep-lat/0305025

[Koc95] V. Koch, "*Introduction to Chiral Symmetry*," TAPS workshop, Bosen, Germany, 1995. arXiv:nucl-th/9512029

[KT99] D. Kharzeev and R. L. Thews, "*Quarkonium formation time in a model-independent approach." Phys. Rev. C*60(4), 41901, 1999. arXiv:nucl-th/9907021

[LHC11a] Large Hadron Collider project, "*Functional specification: LHC Modes, LHC Modes", LHC-OP-ES-0005 rev 1.4,* 2011. https://edms.cern.ch/file/865811/1.1/LHC-OP-ES-0005-10-10.pdf

[LHC11b] Large Hadron Collider project, "*Functional specification: LHC - Experiments Handshake Protocol over DIP", LHC-OP-ES-0019 rev 4,* 2011. https://edms.cern.ch/file/1031913/4/LHC-OP-ES-0019-V4.pdf

[LHC12] LHC Portal, "*LHC portal*," 2012. http://www.lhcportal.com/

[LHC13] LHC, "*LHC Performance and Statistics*," 2013. https://lhc-statistics.web.cern.ch/LHC-Statistics

[LIN08] Linac 2, "*CERN Hadron Linacs,*" http://linac2.home.cern.ch/linac2/.

[Lop12] X. B. Lopez, "*Preliminary luminosity request and corresponding triggers for pp 2012 Muon Physics*" ALICE Trigger Meeting, 2012-02-03 https://indico.cern.ch/getFile.py/access?contribId=4&resId=0&materialId=slides&confId=175225

[LPC12a] LHC Project Coordination (LPC), "*LHC Programme Coordination web pages*," 2012. http://lpc.web.cern.ch/lpc/.

[LPC12b] LHC Project Coordination (LPC), "*LHC Filling schemes*"2012 http://lpc.web.cern.ch/lpc/fillingschemes.htm

References

[LZ12a] S. Li and J. Zhu, *"Analysis of simulations with W signals", PWG-MUON Meeting,* 2012-03-06. https://indico.cern.ch/getFile.py/access?contribId=2&resId=0&materialId=slides&confId=180591

[Mar06a] G. Martinez, "*Introduction to the experimental study of hadronic matter in heavy ion collisions. The Quark Gluon Plasma*", HDR Thesis," 2006. http://tel.archives-ouvertes.fr/tel-00370481.

[Mar06b] B. R. Martins, "*Nuclear and Particle Physics: An Introduction*", London: John Wiley & Sons Ltd., 2006.

[McL03] L. McLerran, "*Rhic physics: The quark gluon plasma and the color glass condensate: Four lectures," BARC Workshop "Mesons and Quarks"*, Mumbai, India, 2003. arXiv:hep-ph/0311028

[MNR92] M. L. Mangano, P. Nason and G. Ridofli, "*Heavy quark correlations in hadron collisions at next-to-leading order," Nucl. Phys. B*373, 295, 1992. http://inspirehep.net/record/30595?ln=fr

[Mon13] MonALISA, "*MonALISA: Monitoring Agents using a Large Integrated Services Architecture*," 2013. http://monalisa.cacr.caltech.edu/monalisa.htm.

[MRST00] A. D. Martin, R. G. Roberts, W. J. Stirling and R. S. Thorne, "*Parton distributions and the LHC: W and Z production," Eur. Phys. J.* C14, 133, 2000. arXiv:hep-ph/9907231

[MS86] T. Matsui and H. Satz, "*J/psi suppression by quark-gluon plasma formation," Phys. Lett. B*178, 416, 1986. http://inspirehep.net/record/230496?ln=en

[NO06] Z. Nussinov and G. Ortiz, "*Sufficient symmetry conditions for Topological*," 2006. arXiv:cond-mat/0605316.

[Nob13] Nobelprize.org, "*All Nobel Prizes in Physics*", 2013 http://www.nobelprize.org/nobel_prizes/physics/laureates/

[PES09] H. Paukkunen, K. Eskola and C. Salgado, "*EPS09 - Global NLO analysis of nuclear PDFs and their uncertainties," PoS High-pTphysics09,* 019, 2009. arXiv:0903.1956

[Pil12a] P. Pillot, "*Measurement of heavy-flavour decay muon production at forward rapidity in Pb-Pb collisions at √(s_NN) = 2.76 TeV with ALICE*", International workshop on heavy quark production in heavy-ion collisions, 2012-11-15 https://indico.cern.ch/getFile.py/access?contribId=22&sessionId=20&resId=0&materialId=slides&confId=182856

[Pil12b] P. Pillot, "*Improvement of the muon resolution*" PWG-MUON meeting, 2012-10-30. https://indico.cern.ch/getFile.py/access?contribId=0&resId=0&materialId=slides&confId=215069

[Pil12c] P. Pillot, *Private communication: Tracking Efficiencies*, 2012 and 2013.

[Pil12d] P. Pillot, "*MUON tracking performances", MUON Workshop*, iThemba LABS, Somerset West, South Africa, 2012. http://indico.tlabs.ac.za/contributionDisplay.py?contribId=2&sessionId=13&confId=21

[PS+02] J. Pumplin, D. Stump, J. Huston, H. Lai, P. Nadolsky and W. Tung, "*New Generation of Parton Distributions with Uncertainties from New Generation of Parton Distributions with Uncertainties*," *JHEP* 0207:012, 2002. MSU-HEP-011101, arXiv:hep-ph/0201195

[ROO13] The ROOT Team, "*ROOT: A Data Analysis Framework*," 2013. http://root.cern.ch.

[S+06] T. Sjöstrand, S. Mrenna, P. Skands, "*PYTHIA 6.2 Physics and Manual*," JHEP 0605:026 2006. arXiv:hep-ph/0603175.

[Sat00] H. Satz, "*Colour Deconfinement in Nuclear Collisions,*" *Rept. Prog. Phys.* 63, 1511, 2000. arXiv:hep-ph/0007069

[Sat06] H. Satz, "*Colour Deconfinement and Quarkonium Binding*," *J. Phys. G32: R25,* 2006. arXiv:hep-ph/0512217

[Sat07] H. Satz, "*Quarkonium binding and dissociation: The spectral analysis of the QGP*," *Nucl. Phys. A*783, 249-260, 2007. arXiv:hep-ph/0609197

[Sen] K. J. Senosi, "*Analysis of Monte-Carlo generated data for W boson production in the semi-muonic channel using the ALICE detector",*MSc Dissertation, University of Cape Town to be published.

[Sen12] K. J. Senosi, "*Analysis of Monte-Carlo generated data for W boson production in the semi-muonic channel using the ALICE detector",* SAIP Conference 2012

[Sre07] M. Srednicki, "*Quantum Field Theory*", Cambridge University Press, 2007.

[STA10] STAR Collaboration, "*The Search for QGP*," 2010. http://www.star.bnl.gov/~gorbunov/main/node5.html

[Sto08a] D. Stocco, "*Efficiency determination of the Muon Spectrometer trigger chambers from real data,* ALICE Internal Note ALICE-INT-2008-004, 2008.

References

[Sto08b] D. Stocco, "*Development of the ALICE Muon Spectrometer: preparation for data taking and heavy flavour measurement*", PhD Thesis, Università Di Torino, 2008.

[Sto10] D. Stocco, "*Update on the single-muon analysis", PWG-MUON Meeting,* 2010-09-29. https://indico.cern.ch/getFile.py/access?contribId=3&resId=0&materialId=slides&confId=108663

[Sto12] D. Stocco, "*Analysis code development", PWG-MUON Meeting,* 2012-10-08. https://indico.cern.ch/getFile.py/access?contribId=4&resId=0&materialId=slides&confId=211557

[Sto13a] D. Stocco, "*MuonTrackCuts,*" ALICE Twiki Page, 2013. https://twiki.cern.ch/twiki/bin/viewauth/ALICE/MuonTrackCuts#AliMuonTrackCuts_AN1.

[Sto13b] D. Stocco, *Private communication: Analysis of LHC11h Pass 1 and Pass 2,* 2013.

[Sui09] C. Suire, "*MCH Shifter Tutorial DAQ,*" ALICE Twiki Page, 2009. https://twiki.cern.ch/twiki/pub/ALICE/MCHDocDAQ/MCH_ShifterTutorial_DAQ.pdf.

[TCG05] A. Tricoli, A. M. Copper-Sarkar and C. Gwenlan, "*Uncertainties on W and Z production at LHC,*" *ATLAS-PHYS-CONF-2005-008,* 2005. arXiv:hep-ex/0509002

[TCWG13] ALICE Trigger Coordination Working Group, "*ALICE Trigger Coordination*," 2013-02-10. https://twiki.cern.ch/twiki/bin/viewauth/ALICE/TriggerCoordination.

[TG+05] R. Tieulent, A. Grigoryan, J.-Y. Grossiord, H. Gulkanyan, J.-C. Ianigro, V. Kakoyan, P. Pillot, H. Vardanyan, "*The Geometry Monitoring System of the ALICE Dimuon Spectrometer – Overview*" CERN-ALICE-INT-2005-009 http://www.opensourceinstruments.com/GMS/PRR.pdf

[The94] R. L. Thews, "Formation time scales for quarkonia in a deconfining medium," DPF '94, Albuquerque, NM, 1994. arXiv:hep-ph/9409209

[TOA11] J. Thäder, K. Oyama, F. Antinori "PbPb 2011 Trigger Summary," 2011-12-14. https://indico.cern.ch/getFile.py/access?contribId=0&resId=0&materialId=slides&confId=166147

[Val12] L. Valencia Palomo, "J/Psi in Pb-Pb 2011: pass1 vs pass2" MUON Meeting 2012-09-03 https://indico.cern.ch/getFile.py/access?contribId=1&resId=0&materialId=slides&confId=206160

[WAH+57] C. S. Wu, E. Ambler, R. W. Hayward, D. Hoppes and R. P. Hudson, "Experimental test of parity conservation in beta decay," *Phys. Rev.,* no. 105(4), 1413, 1957. http://www-sk.icrr.u-tokyo.ac.jp/~masato/class/parity-violation-paper.pdf

References

[Wie00] U. A. Wiedemann, "Gluon radiation off hard quarks in a nuclear environment: opacity expansion," *Nucl.Phys. B588,* 303-344, 2000. arXiv:hep-ph/0005129

[ZL12a] J. Zhu and S. Li, *Single Muon Analysis in Pb-Pb and p-Pb collisions: PWG-HF HFM Meeting:,* 2012-09-24. https://indico.cern.ch/getFile.py/access?contribId=0&resId=0&materialId=slides&confId=208934

[ZL12b] J. Zhu and S. Li, "W -> μ Analysis at Forward Rapidity in Pb-Pb Collisions at 2.76 TeV with ALICE," *APW-Puebla 2012*, Puebla, 2012-12-01. https://indico.cern.ch/getFile.py/access?contribId=32&sessionId=2&resId=0&materialId=slides&confId=204583